Multi-distributed activation energy model for wood pyrolysis : modelling strategy applied to experimental kinetics of different particle sizes

Yong Tian

Yong Tian. Multi-distributed activation energy model for wood pyrolysis : modelling strategy applied to experimental kinetics of different particle sizes. Chemical and Process Engineering. Université Paris-Saclay, 2021. English. NNT : 2021UPAST033 . tel-03254294

Thèse de doctorat

NNT :2021UPAST033

Multi-distributed activation energy model for wood pyrolysis : modelling strategy applied to experimental kinetics of different particle sizes

Thèse de doctorat de l'université Paris-Saclay

Ecoles doctorales n°579 : sciences mécaniques et énergétiques,
matériaux et géosciences (SMEMAG)

Spécialité de doctorat: Génie des Procédés

Unité de recherche: Université Paris-Saclay, CentraleSupélec,

Laboratoire de Génie des Procédés et Matériaux. 91190, Gif-sur-Yvette, France.

Thèse présentée et soutenue à Paris-Saclay, le 15 avril 2021, par

Yong TIAN

Composition du Jury

Mme. Marie-Laurence Giorgi Professeure, CentraleSupélec, Université Paris-Saclay	Présidente du jury
M. Ian Turner Professeur, Queensland University of Technology	Rapporteur & examinateur
M. Patrick Rousset Chercheur, Montpellier Université d'Excellence	Rapporteur & examinateur
M. Anthony Dufour Chargé de recherche, Université de Lorraine	Examinateur
Mme Dorothée Laurenti Chargée de recherche, Université Lyon I	Examinatrice
M. Patrick Perré Professeur, CentraleSupélec, Université Paris-Saclay	Directeur de thèse

université
PARIS-SACLAY

ÉCOLE DOCTORALE
Sciences mécaniques et
énergétiques, matériaux
et géosciences (SMEMAG)

Titre : **Modèle d'énergie d'activation multi distribuée pour la pyrolyse du bois: stratégie de modélisation appliquée à la cinétique expérimentale de particules de différentes tailles**

Mots clés : Pyrolyse, DAEM, TG, pseudo-composant, pondération, taille des particules

Résumé : La pyrolyse de la biomasse lignocellulosique est une méthode efficace pour la production de bio-liquide et de gaz de synthèse. Le modèle de multidistribuée d'énergie d'activation (DAEM) est un outil robuste de modélisation de la cinétique de pyrolyse. Pourtant, sa stratégie optimale concernant le nombre et la forme des distributions reste une question ouverte. Parallèlement, des développements supplémentaires sont nécessaires pour étendre la capacité du modèle à prédire l'effet de la taille des particules. Ce travail vise à établir une stratégie DAEM robuste et universelle pour la modélisation de la pyrolyse, puis de l'appliquer à la cinétique de pyrolyse de particules de différentes tailles.

Après les identifications sur la base de données d'apprentissage, les modèles sont systématiquement testés avec une base de données de validation. Pour la modélisation, une stratégie optimale a été définie en testant une grande diversité de nombre et forme des distributions. Trois distributions avec des formes pertinentes garantissent une bonne prédiction avec une concision appropriée. La combinaison de deux fonctions gaussiennes et d'une fonction exponentielle s'est révélée la plus performante des combinaisons DAEM testées, et plus performante également que les schémas classiques du premier et du n-ième ordre. Par la suite, ce choix de modèle DAEM (deux gaussiennes + une exponentielle) a été utilisé pour déterminer les paramètres intrinsèques de la poudre d'épicéa et de peuplier. La qualité de la prédiction cinétique a permis, pour la première fois, de déterminer également les enthalpies de réaction à partir des signaux DSC. Des analyses expérimentales d'échantillons multiéchelles ont révélé les effets de la taille, avec notamment une plus grande carbonisation liée aux réactions secondaires. Cela se traduit par la corrélation négative entre perte de masse et composition élémentaire.

Les identifications ont fourni des paramètres cinétiques du modèle DAEM pour différentes tailles, à partir desquels des profils de dévolatilisation et des indices synthétiques sont extraits pour montrer l'effet de la taille sur les trois pseudos composants. La capacité de prédiction du modèle a été vérifiée sur trois tailles d'échantillons par des expériences additionnelles effectuées avec des essais isothermes.

Enfin, les corrélations entre la masse résiduelle adimensionnelle et la composition élémentaire nous ont permis de déterminer la composition des réactions secondaires, constituée principalement de carbone. La composition élémentaire du charbon peut donc être prédite en utilisant la différence de cinétique entre une poudre fine et une taille donnée.

Title : **Multi-distributed activation energy model for wood pyrolysis : modelling strategy applied to experimental kinetics of different particle sizes**

Keywords : Pyrolysis, DAEM, TG, pseudo-component, trade-off, particle size

Abstract : Pyrolysis of lignocellulosic biomass is an effective method for the bio-liquid and syngas productions. The multi-distributed activation energy model (DAEM) is a comprehensive tool for modelling pyrolysis kinetics. Yet, its optimal strategy regarding distribution number and shape is still an open question. Meanwhile, further developments are needed to extend the model's ability to predict the effect of particle size. This work aims to establish a robust and universal DAEM strategy for pyrolysis modelling, which is applied to the pyrolysis kinetics of different particle sizes.

To assess the models, a validation database was systematically employed after identification on the learning database. A trade-off strategy was defined by testing multi-distribution DAEMs with various distribution number and shape. Three-distribution with relevant shapes ensured good prediction with suitable conciseness, and the combination of two-Gaussian plus one exponential distributions further gave the best trade-off between prediction capacity and numerical complexity. This model showed superiority compared to other DAEMs, first-order and nth-order schemes, being determined as the optimal numerical tool in this work. Afterward, two Gaussian + one exponential DAEM distributions were employed to determine intrinsic parameters for spruce and poplar powder. The quality of kinetics prediction allowed, for the first time, the enthalpies of reaction to be also determined from the DSC signals. Experimental analyses of multi-scale samples revealed the effects of particle size with carbonization enhancements, being further evidenced by the negative correlation between mass loss and elemental compositions. The DAEM identifications provided solid kinetic parameters for different sizes, from which devolatilization profiles and synthetic indices are extracted to show the effect of size on three pseudo-components. The prediction ability of the model was checked by further experiments performed at different time-temperature patterns with several particle sizes. Finally, correlations between dimensionless residual mass (DRM) and element compositions allowed us to determine the composition of secondary charring, which consists mainly of carbon. The elemental composition of char can therefore be predicted using the difference of kinetics between fine powder and a given particle size.

Acknowledgements

It has been a very memorable and irreplaceable experience to complete this Ph.D. process in LGPM, many people come to my help for overcoming the difficulties in work and life. First of all, I'd like to thank Prof. Patrick Perré, my supervisor, his important guidance and rigorous attitude are priceless to achieve the major accomplishments. Working with him is very inspiring and profitable, his creativity and efficiency really have profound influence on me. I sincerely thank for his supervisions and supports.

I would like to express my gratitude to the LGPM team. Many thanks to Pin LU, who helped me in project application and tomography analysis, he also helped a lot when I stayed in Pomacle. I also thank Jamila for her supports in TG set-up and following experiments. My thanks to Barbara, Clarisse, and Vincent for their assistance in elementary analysis, many thanks to Cédric for helping composition analysis, thanks to Nathalie for SEM visualizing, thanks to Sébastien for sample manufacturing. Thanks to the kind people in the lab that helped me with daily problems: Corinne, Magali, Elisabeth, Sandra. I also thank my fellow PhDs/post-doc for their supports: Wenbiao JIANG, Minghao YANG, Wangshu CHEN, Li GONG, Jing ZHANG, Yuanyuan HE, Sufang LI, Yan GAO, Menasa, Andrea, Angéla, Jérôme....

I'd like to thank all the members of the jury, thank Mr. Ian Turner and Mr. Patrick Rousset for accepting as the reporters, and thank Ms. Marie-Laurence Giorgi, Ms. Dorothée Laurenti and Mr. Anthony Dufour for examining the manuscript.

I specially thank Dan ZHU for our happy and precious memories in France. Thanks to the friends who travelled and climbed with me: Chao WU, Lei ZHOU, Peng WEI, Ye LI, Di ZHOU, Mark, Fredric, Loic,Nico....

Special thanks to the Chinese Scholarship Council (CSC) for their financial support, it has been a very precious opportunity, thanks to the Chinese government and Chinese Embassy that keep us safe.

A great thank to my parents, who have provided much support and understanding during my study in France, they always encourage me and remined me about my health and happiness.

Content

List of symbols

Normal symbols

A	Pre-exponential factor	s^{-1}
C_p	Specific heat capacity	$J \cdot kg^{-1} \cdot K^{-1}$
D_f	Degree of freedom	-
D_m	Maximum deviation	%
$\overline{\overline{\mathbf{D}_{eff}}}$	effective diffusivity tensor	$m^2 \cdot s^{-1}$
E	Activation energy	J
E_0	Mean activation energy in distribution	J
E_{min}	Minimum activation energy	J
f	Distribution function	J^{-1}
H	Reaction enthalpy factor	$KJ \cdot kg^{-1}$
$\dot{H}_{pyro}$	Pyrolysis enthalpy	J^{-1}
j_k	Diffusive flux of component k	$kg \cdot m^{-2} \cdot s^{-1}$
J_q	Heat flux	$W \cdot m^{-2}$
k	Reaction rate constant	s^{-1}
m	Wood mass	g
n	Number of interval length	-
N_d	Distribution number	-
n_g	Interval number in gamma distribution	-
N_p	Number of increment point	-
P	Pressure	Pa
R	Gas constant	$J \cdot kg^{-1} \cdot K^{-1}$
R_L	Local residual of DTG	$g \cdot s^{-1}$
$\dot{S}$	Heat source due to reaction	J^{-1}
t	Reaction time	s

T	Temperature	$K\ or\ ℃$
t_f	Final reaction time	s
V	Volatile mass from a reaction	g
V_{max}	Weighting factor	-
W	Heat flux	W
X	Conversion rate	%

Greek symbols

α	Shape parameter in gamma distribution	-
β	Rate parameter in gamma distribution	-
λ	Thermal conductivity	$W \cdot m^{-1} \cdot K^{-1}$
σ	Standard deviation	J^{-1}
Γ	Gamma function	-
μ	Dynamic viscosity	$kg \cdot m^{-1} \cdot s^{-1}$
ρ	Density	$kg \cdot m^{-3}$
τ	Time constant	s

Subscripts

b	Bound water
$blank, 1/2$	Blank heat flux
c	Char
cal	Calculation data
exp	Experimental data
i	Reaction number
j	Distribution number
r	Remaining content

R	Residue
w	Wood
v	Volatiles

Superscript

n	relative to distribution n
∞	Total potential volatile production
j	Distribution number

Abbreviations

DAEM	Distributed activation energy model
DML	Dimensionless mass loss
DRM	Dimensionless residual mass
DSC	Differential Scanning Calorimeter
DTG	Differential Thermogravimetry
OF	Objective function
RSS	Residual sum of square
RMSE	Root mean square error
SD	Standard deviation
TGA	Thermogravimetric Analysis

General introduction

Worldwide industrial developments consume vast amount of energy sources, especially the traditional, non-renewable fossil fuels. Meanwhile their scarcity and environmental issues such as global warming increase the demand for alternative energy sources more than ever. In this context, bioenergy is globally promoted due to its merits of being renewable, carbon neutral and environmentally friendly [1].

Pyrolysis is a very promising thermochemical technology to converts biomass under anaerobic conditions into bio-oil, biochar, and gaseous products. It is also the initial step before two major thermochemical technologies: combustion and liquification, making it the key link in the BtL (biomass to liquid) industrial chain. For kinetic investigations, thermogravimetric (TG) technology is the most direct and efficient method to detect mass loss during a given temperature/time profile in real time. Besides, differential scanning calorimetry (DSC) can monitor the heat flux alongside the whole reaction history. When used simultaneously, these two technologies allow a more comprehensive analysis of pyrolysis kinetics, and facilitate the subsequent model simulations.

Biomass pyrolysis is a sophisticated phenomenon concerning both chemical (reactions) and physical (heat and mass transfer) processes. Modelling of biomass pyrolysis is quite essential for both kinetic analyses and industrial process optimization. The distributed activation energy model (DAEM) is a comprehensive numerical tool for pyrolysis kinetics. It assumes biomass pyrolysis to occur as series of independent and parallel reactions with continuous activation energies, which account for the inherent non-uniformity of chemical bonds. The activation energies are subject to single or multiple statistic distributions, among which the multiple-distribution DAEM turns to provide more accurate descriptions. And the concepts of pseudo-components inside multi-distributions DAEM correspond well with chemical meanings of biomass constituents (i.e. hemicellulose, cellulose, and lignin).

Distribution shapes inside DAEM represent diverse kinetic behaviours. Symmetric distributions like Gaussian and logistic have been widely employed [2]. Meanwhile, due to the asymmetric behaviour during the initial and final stages of thermal decomposition, asymmetric distributions attract growing attentions including Weibull and Gamma distributions [3]. The number of multiple-distribution scheme decides simulation accuracy and numerical complexity as well. It is a key factor that profoundly affects computational implementations. Apparently, an optimal strategy in distribution shape and number is quite crucial for model applicability (numerical complexity, prediction ability and simulation accuracy). On the other hand, model implementation always involves the kinetic identifications, in which multiple temperature profiles effectively reduce parameter uncertainties. This is a key point of the modelling strategy: the quality of fitting is just an indirect indication of the model quality. The real quality of the model should be assessed on a validation database, that must be different from the learning database. However, this crucial validation stage is barely conducted in relevant researches.

Numerous factors could affect pyrolysis kinetics including heating rate, temperature, residence time, particle size and gas atmosphere [4]. Among them, particle size of raw material strongly affects the mechanisms and is, at the same time, a key characteristic of different reactor types. Particle size changes the intricate coupling between heat and mass transfer, thermo-activated reaction, heterogenous reactions between volatiles and solid phase, enthalpy transfer by change of phase. These facts greatly encourage relevant kinetic researches with comprehensive models to be conducted. Meantime, heat flux is crucial for handling thermal overshoot and temperature runaways in industrial processes. As benefits of the prediction potential of multiple-distribution DAEM, it is therefore also worthwhile to further apply the model to the determination of reaction enthalpies.

(1) Trade-off strategy of distribution number and shape in multiple-distribution DAEM

(2) Intrinsic mechanism of wood powder with two-Gaussian + one exponential DAEM, including the analysis of the heat flux to extract reaction enthalpies

(3) Effect of particle size in TG analyses and corresponding DAEM simulations.

(4) Model prediction regarding mass loss and char composition for different particle sizes

To achieve these research goals, this thesis will apply thermogravimetric apparatus, together with the developments of multiple-distribution DAEM. The two mutual-supported research approaches are illustrated in Figure 1. Experimental works are performed by thermogravimetric apparatus (TG/ DSC) and characterization methods (elementary analysis, scanning electron microscope, and tomography imaging). In the meantime, the model strategy is determined in an extensive trade-off process. Learning and validation databases include dynamic and static tests, respectively, which ensure a reliable identification/verification strategy for multiple-distribution DAEM. This provides accurate predictions and simulations of pyrolysis kinetics at various conditions (dynamic/static temperature programs, different particle sizes and different crucible types). Further the optimal model strategy is applied for kinetic determination and relevant predictions.

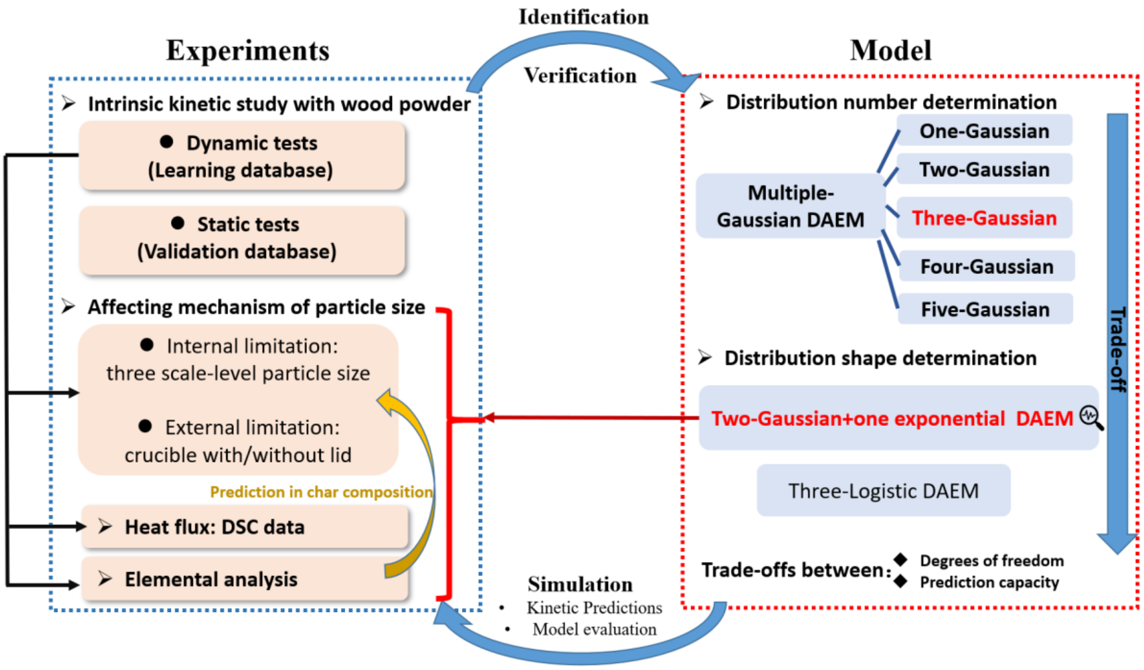

Figure 1. Research scheme of both experiments and modelling work in thesis

This thesis starts with background review in Chapter 1. Introductions on both biofuel and biomass are made for basic understanding, with a specific attention to the structure of wood. Conversion technologies in biomass industry are introduced thereafter.

Chapter 2 reviews the existing theories in biomass pyrolysis kinetics. The DAEM formulations and relevant concepts are presented in detail. Factors affecting the pyrolysis kinetics are also reviewed.

In Chapter 3, experimental protocols and analytical techniques in research are presented, fundamental characteristics of wood samples are also displayed.

Chapter 4 presents the determination strategy regarding both distribution number and shape inside multiple-distribution DAEM. The trade-off investigations between numerical complexity and predication ability are conducted among different DAEMs. This allows us to identify the best strategy (two Gaussian plus one exponential distributions), which will be used in the rest of the work.

Chapter 5 applies the two-Gaussian + one exponential DAEM in the pyrolysis mechanism of spruce and poplar powder, and exhibits the intrinsic kinetics concerning both mass loss and heat flux. The strategy of extracting enthalpy factors from DSC signals is presented. And the prediction abilities are also checked in Van Krevelen diagram and the control of temperature rise.

Chapter 6 studies the effects of particle size with both experimental and numerical investigations. Six types of wood samples will provide sufficient thermogravimetric data including five sample shapes and two reactor conditions. The mechanisms affected by particle size are explained by transfer-induced secondary charring. The variation trends in the DAEM model will be analysed by synthetic parameters computed from the model parameters. Model’s prediction potential in mass loss will be verified for different particle shapes and further extended to determine the char compositions using kinetic differences between wood powder and given particles.

Chapter 7 will give the overall conclusions and perspectives.

This work aims to contribute to fundamental kinetic study of wood pyrolysis, specifically in the numerical strategy of three-distribution DAEM and the mechanisms with varied particle size. With credible schemes in model strategy, the detailed information in gas-solid phase variation patterns get potentials in precise kinetic determinations and predictions. Thanks to the validation stage systematically proposed in the work, the kinetic parameters could be useful for further applications, including upscaling in industrial reactors.

Chapter 1. Context

1.1 Biomass and biofuel

Biomass refers to the mass of living organisms, including plants, animals, and microorganisms, or, from a biochemical perspective, cellulose, lignin, sugars, fats, and proteins [5]. Biomass is the fourth largest source of energy in the world after coal, petroleum and natural gas, providing about 14% of the world's primary energy consumption [6]. In the background that fossil fuels are anticipated to deplete within 40-50 years and cause environmental damages such as the global warming, acid rain and urban smog [7], biomass shows vast advantages of being renewable, carbon-neutral in its lifecycle, serving as an optimal alternative energy to cope with greenhouse gas, air pollution and fossil fuel depletions [8].

Biofuel refers to solid, liquid and gaseous fuels that are derived from renewable sources such as biomass, animal fats, plantations or waste oils [9]. For example, biofuel can include bioethanol, bio-butanol, biodiesel, vegetable oil, bio-methanol, pyrolysis oil, biogas (CH_4), and bio-hydrogen. As a promising substitute energy source, biofuel helps relieve pressure from depleting energy situation, decrease external energy dependence and avoid heavily environmental problems. In 2018, the share of biofuel reached a newly high 5.6% in total primary energy supply [10]. Generally, biofuel is classified into three generations based on the origin of biomass sources. The first-generation is derived from food crops like corn, wheat, sugar beet and oil seeds, usually in form of bio-diesel and bio-ethanol. Yet, the production of first-generation biofuel inevitably encounters conflicts with food and makes it less promising. The second-generation biofuel is produced from non-food biomass of lignocellulosic feedstock materials, which include by-products (cereal straw, sugar cane bagasse, forest residues), wastes (organic components of municipal solid wastes), and dedicated feedstocks (purpose-grown vegetative grasses, short rotation forests and other energy crops) [11]. The second-generation biofuel has no direct conflicts with food feedstocks, also it shows advantages in wide resource range and sustainable supply. However, lignocellulosic biomass has multiple physical characteristics that require complex transformation chain to produce biofuel. The third-generation biofuel is mainly derived from algae or seaweed, they convert solar energy into chemical energy of bio-oil, carbohydrate, and proteins. Algae has a high photosynthetic efficiency, and it can help in water treatment by consuming nutrient such as nitrogen and phosphorus. Its major components are protein, lipid and soluble polysaccharide [12], which favor low energy input in exchange for high hydrocarbon content in bio-oil. But the difficulties in production, harvesting and pretreatment remains important issues to the mass production of biofuel. Moreover, the algae technology requires large amount of water and nutrient within cultivation cycle [13].

1.2 Wood

1.2.1 Physical structure

Wood is one of the mostly used materials in man's history, its mechanical properties make it very useful as construction and civil material. Wood is strongly orthotropic, its three material directions: longitudinal, radial, and tangential present contrasted characteristics. Physical cell wall structures are formed in wood by secondary growth, endowing properties like water transportation, wood rigidity and strength, their typical honeycomb-like structure are evenly distributed in longitudinal direction [14-16]. As shown in figure 1.1, the cell wall consists of several different layers with different chemical compositions and microfibril orientation. The outer layer of lamella is made of pectic substances [17], which provides adhesions between wood cells. Primary cell wall is made up with randomly distributed microfibrillars cellulose, hemicellulose, and lignin. Three inner layers are classified into S_1, S_2 and S_3 layers with different orientation [16, 18]. They all consist of microfibrillars, hemicellulose and lignin with an ordered pattern. S_1 is homogeneous but very thin (0.1-0.35μm). S_2 is the thickest layer (1-10μm) which represents about 80% of the total cell wall thickness [19]. S_3 is the most inner layer (0.5-1.1μm) that contacts which lumen structure.

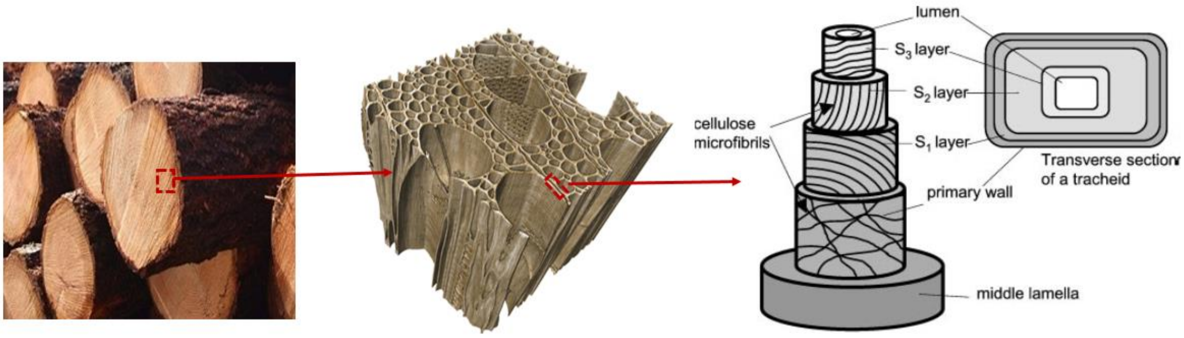

Figure 1.1- Multiscale structures of wood (high resolution tomography figure from [20] and illustration figure of cell wall from [17])

1.2.2 Chemical structure

Major macromolecules present in the cell wall consist of cellulose, hemicellulose, lignin (chemical structure in figure 1.2). In addition, the extractives and inorganic matters (alkali metal minerals) also exist. Their contents differ among species and part of tree, where the highest levels are encountered in heartwood [21]. Nonetheless, the fundamental knowledge on organic and inorganic components can help build the essential understanding in wood conversion processes.

Cellulose is widely described as saturated linear polysaccharide, the chemical formula is often written as $(C_6H_{10}O_5)_n$, where n is polymerization degree. It consists of linear chains of (1,4)-D-glucopyranose units with molecular weight around 100,000 [22]. It occupies about 40%-50% in wood (around 42% in softwood and 45% in hardwood) [21]. Cellulose usually gets fibrous structures and it is presented in cell wall of plant and in pure form in cotton fibre. Four known crystal structures of cellulose were reported: cellulose I to IV, differing in crystal structure and amorphous proportion [23]. As a consequence of its high degree of polymerization, crystallinity degree and its orientation, cellulose contributes mainly to the strength of wood fibre as well as in the stems of plants [24].

Hemicellulose mainly consists of polysaccharides deriving from sugars (glucose, mannose, xylose, and arabinose), methylglucuronic and galaturonic acides, its average molecular weight is lower than 30,000. It constitutes around 28% in softwood and 35% in hardwood [25]. Hemicellulose in hardwoods are mainly in the form of acetylglucuronoxylan (15-30%), and other components like galactose, arabinose, rhamnose, glucuronic acid and acetyl groups; meanwhile in softwood, hemicellulose mainly consists of galactoglucomannan (5-8%) and glucomannan (10-15%) [26]. Polysaccharides in hemicellulose are heterogeneously branched, and non-covalently bonded to the surface of cellulose microfibril [22]. It provides matrix for cellulose and links fibrous cellulose and amorphous lignin. The less stable chemical structures make hemicellulose more reactive than cellulose, and its thermal decomposition products are more complicated than those of cellulose.

Lignin presents as three-dimensional organic structure with highly cross-linked macromolecules [27]. Its irregular phenolic polymer consists of more than four substituted phenyl propane, and the highly branched poly- aromatic polymers endow lignin with aromatic nature. Lignin accounts for 23%-33% in softwood and 16%-25% in hardwood, it is insoluble in water and stable in nature. Different substitution patterns of aromatic rings exist in woody lignin, including: p-hydroxyphenyl (H), guaiacyl (4-hydroxy-3-methoxyphenyl, G) and syringyl (3,5-dimethoxy-4-hydroxyphenyl, S). Usually, softwood contains more G groups and less H groups, while hardwood mainly consists of G and S groups. These monomers are linked together through various kinds of ether linkages (C−O) and condensed (C−C) bonds, leading to a heterogeneous chemical structure for lignin [28, 29]. Typical lignin structures mainly comprise syringyl units that interconnected through β-O-4, β-1 and β-β interunit bonds [30]. The polyphenolic component in lignin plays the role of cement [31], which holds the micro-fibrils with relatively high structural rigidity.

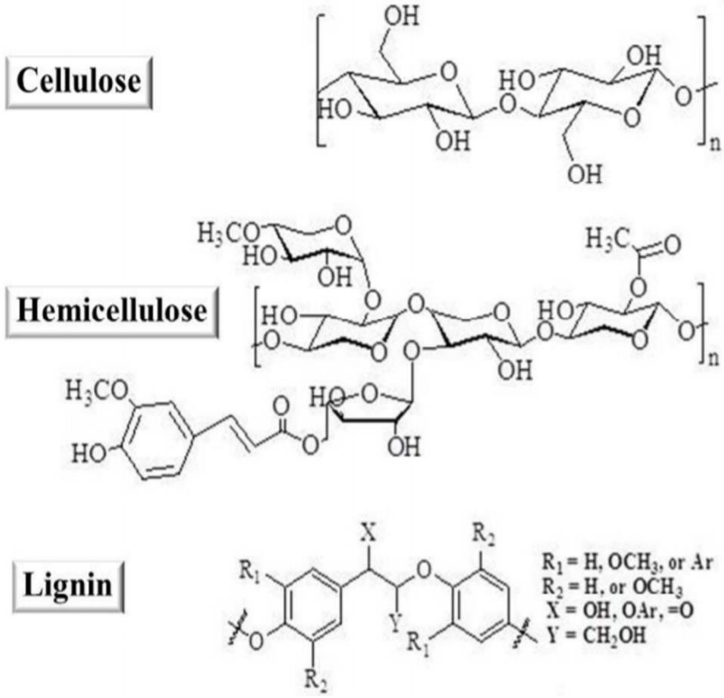

Figure 1.2- Chemical structures of cellulose, hemicellulose and lignin [32]

The inorganic materials in biomass are usually in forms of mineral matters, including silicates, oxyhydroxides, sulphates, phosphates, carbonates, chlorides, and nitrates. SiO_2, CaO and K_2O are the major inorganic components in biomass [24]. They are often retained in biochar or ash after thermal treatments of biomass. Inorganic’s contents are usually less than 1% in softwood and can be higher than 15% in herbaceous biomass [33].

The extractives in biomass are defined by their solubility in polar or non-polar solvents (water, ethanol, benzene, and toluene), they commonly consist of various saccharides, proteins, lipids, fats, etc. The extractives act as energy reserves and protection material from insect.

1.3 Biomass conversion technologies

Modern industry meets the needs to convert biomass into energy forms of solid, liquid, gaseous chemical products, and efficient heat for power generation. Generally, industrial processes need to deal with biomass feedstocks that are varied in energy density, size, moisture content and intermittent supply [34]. Moreover, the requirements of high energy density and easy transportability in bio-fuels put more emphasis on the efficient conversion technologies. As shown in figure 1.3, the existing biomass conversion technologies can be classified into two basic categories: biochemical processes and thermo-chemical processes. Producible bio-energy depends much on the chemical/physical properties and the efficiency of extraction technologies. It is scientists' great interest to maximize the yield of applicable energies from biomass. Herein, some presentative technologies will be introduced.

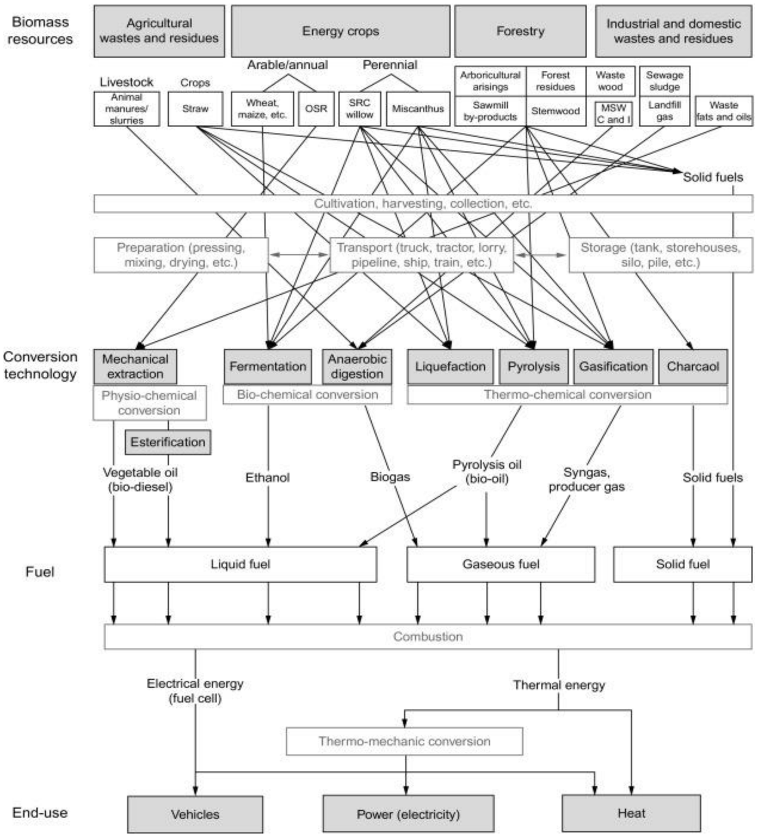

Figure 1.3- Biomass technologies for producing biofuel [35]

1.3.1 Biochemical technology

Biochemical conversion is an environmentally friendly method for producing chemical products, in which biogas (hydrogen or methane) and ethanol, are produced by bioprocesses.

The present discussions will focus on the existing technologies that produce these two forms of products.

1.3.1.1 Fermentation

Biohydrogen, as target product, can be produced in dark fermentation by strictly anaerobic or facultative anaerobic bacteria [36]. The anaerobic bacteria grow on carbohydrate rich substrates (including glucose, starch, and cellulose), and gives organic fermentation end products, hydrogen and carbon dioxide [6]. Carbohydrates in biomass are the preferred organic carbon sources for hydrogen productions, the major process and reactions involved in dark fermentation are shown in figure 1.4. The CSTR (continuously stirred tank reactor) is the most used bio-reactor for the continuous hydrogen productions of dark fermentation process, where biomass can be well suspended in the mixed liquor and keep the same composition as the effluent [37].

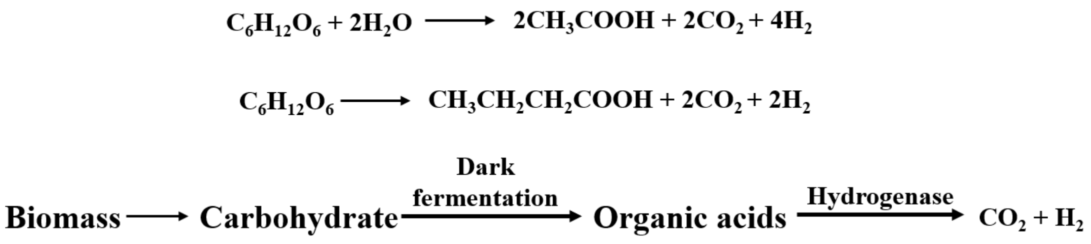

$$C_6H_{12}O_6 + 2H_2O \longrightarrow 2CH_3COOH + 2CO_2 + 4H_2$$

$$C_6H_{12}O_6 \longrightarrow CH_3CH_2CH_2COOH + 2CO_2 + 2H_2$$

$$\text{Biomass} \longrightarrow \text{Carbohydrate} \xrightarrow{\text{Dark fermentation}} \text{Organic acids} \xrightarrow{\text{Hydrogenase}} CO_2 + H_2$$

Figure 1.4- Major reactions and dark fermentation process [6]

Another application of the fermentation is to produce ethanol. The bio-ethanol plants usually use the feedstocks of sugarcane, sugar beet juice, corn or wheat for the first generation [38]. First it requires the pre-treatment of raw biomass material (enzymatic hydrolysis, acid hydrolysis, extraction, saccharification and polysaccharides), simple sugar is obtained and sent for subsequent fermentations, where hydrolysate and yeasts (*Saccharomyces cerevisia*) are added for the process initiation. The major reactions during the fermentations are:

$$C_{12}H_{22}O_{11} + H_2O \xrightarrow{invertase} C_6H_{12}O_6(Glucose) + C_6H_{12}O_6(Fructose)$$

$$C_6H_{12}O_6(Glucose) \xrightarrow{zymase} 2CH_3CH_2OH(Ethanol) + 2CO_2$$

1.3.1.2 Photosynthesis process

The phototrophic organisms usually apply purple bacteria, green bacteria, cyanobacteria, and algae [6]. They convert water molecules into hydrogen ion (H^+) and oxygen, the H^+ is subsequently converted by hydrogenase enzymes into H_2 under anaerobic conditions [39]. Direct bio-photolysis is sensitive to oxygen and suffers from limited conversion efficiency, the use of oxygen absorbers and heterocystous cyanobacteria is therefore encouraged in relevant processes [6]. In contrast, the indirect bio-photolysis overcomes the problems by separating spatially oxygen evolution and hydrogen evolution [40]. One typical fixed-bed reactor of the photosynthesis process is shown in figure 1.5. The hydrogen is produced by means of batch operation, and this unit can be further coupled with fuel cells [6].

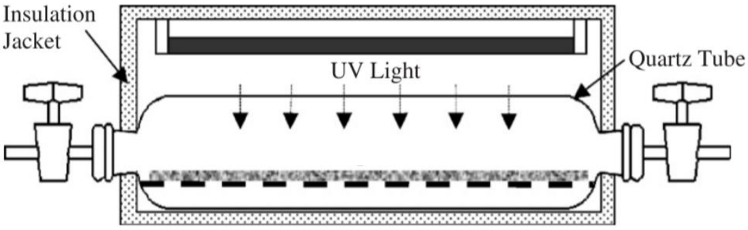

Figure 1.5- Fixed bed reactor for photosynthesis process [41]

1.3.1.3 Anaerobic digestion

Anaerobic microorganisms digest the organic material for producing biogas (methane), which can be used for electricity and heat production (figure 1.6). The microorganisms involve the degradation of organic material, and they usually require high concentration of wet biomass matters in the absence of oxygen [42]. Anaerobic digestion process can deal with organic waste such as livestock manure, crops, sewage sludge and solid waste. And the after-process material can be utilized as fertilizer, or bedding material.

The bio-reactor is an airtight container called digester, which ranges in size from around 1 m^3 (small household unit) to as large as 2000 m^3 (large commercial installation) [43]. Depending on different feedstocks and process systems, the biogas products usually contain methane with contents of 55%-75%, while the state-of-art technology can produce biogas containing 95% methane [42].

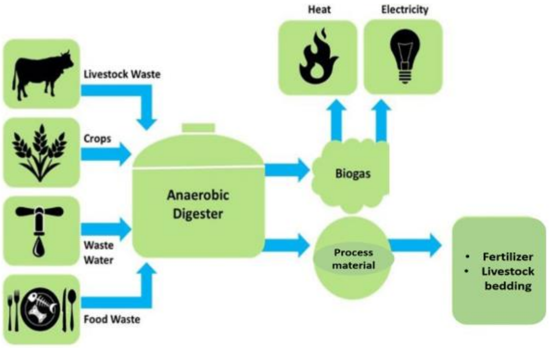

Figure 1.6- Flowchart of anaerobic digestion process [44]

1.3.2 Thermo-chemical technology

Industrial technologies present four choices for biomass thermal conversions: combustion, gasification, pyrolysis, and liquefaction. These technologies are in different stages of development, and herein emphasis will be put on the research subject: pyrolysis.

1.3.2.1 Combustion

Combustion is an old technology which has been used since ancient time, the biomass burns in air and converts the chemical energy into heat. As the main way of bioenergy production, it responds over 90% of the global bioenergy [45]. In modern industry, heat from biomass combustion is usually converted into mechanical power or electricity, figure 1.7 shows one representative combustion process that aims for power generation. Power plants produced electricity in the range of 100-3000 MW by biomass combustion, and the co-firing with coal attracts more interests because of their high conversion efficiency [46]. Also the on-site co-generation of heat and electricity is a practical way to elevate energy efficiency and produce cheap fuels from biomass [45].

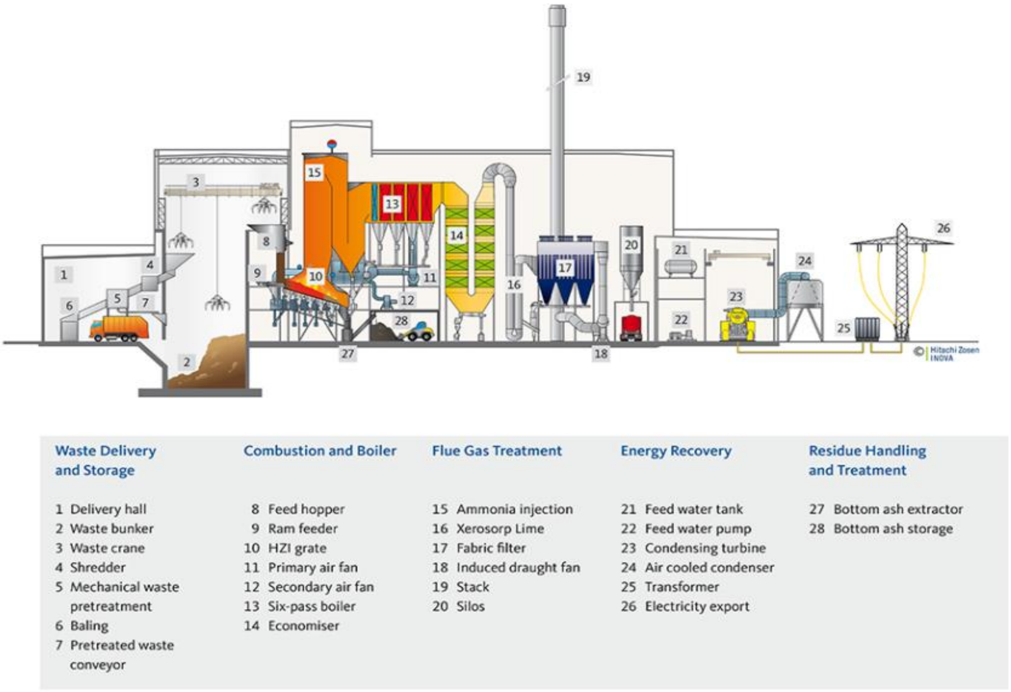

Figure 1.7- Industrial biomass combustion process for power generation [47]

1.3.2.2 Liquefaction

Hydrothermal liquefaction converts biomass into liquid biofuel under specific conditions including solvent media, high pressure (5-25 MPa) and proper temperature (250-500 ºC) [48]. Main products from liquefaction are bio-crude, char, water-soluble material, and gases. Figure 1.8 illustrates an example of hydrothermal liquefaction of lignocellulose biomass [49, 50]. The process started by decomposing biomass into reactive molecules that can repolymerize into hydrophobic and oil compounds, then the rearrangement via condensation, cyclization, and polymerization will produce new larger, hydrophobic macromolecules [51].

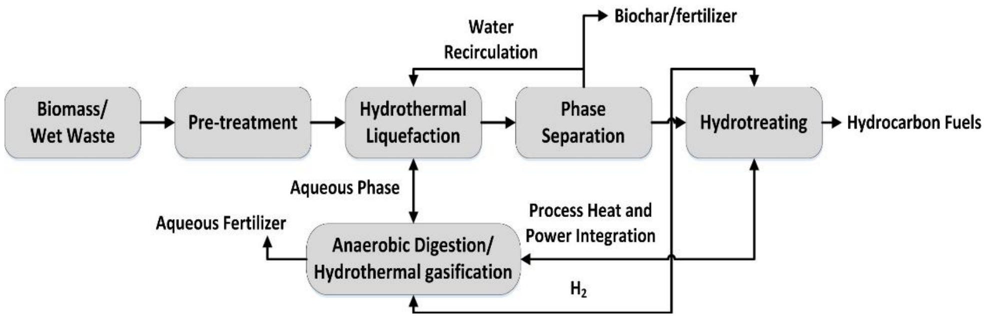

Figure 1.8- Flow chart of hydrothermal liquefaction process of biomass [49, 50]

1.3.2.3 Gasification

Gasification is a thermo-chemical process that converts biomass into gaseous fuel under an oxygen-deficient environment. It removes part of oxygen in biomass and increases energy density by either dehydration or decarboxylation [52]:

$$\text{Dehydration: } C_mH_nO_q \rightarrow C_mH_{n-2q} + qH_2O$$

$$\text{Decarbooxylation: } C_mH_nO_q \rightarrow C_{m-\frac{q}{2}}H_n + \frac{q}{2}CO_2$$

The versatility of gasification is that it can be used for producing syngas, hydrogen, or other liquid fuel [53]. Meantime, it is usually linked with co-gasification, where the high content of moisture in biomass favours syngas production and methanol synthesis [54]. Also, the cogeneration of gaseous fuel from biomass gasification can potentially produce bioenergy onsite. As shown in figure 1.9, the major types of industrial gasifiers are: fixed bed gasifier (updraft, downdraft and cross draft) and fluidized-bed gasifier (bubbling fluidized-bed and circulating fluidized-bed) [55].

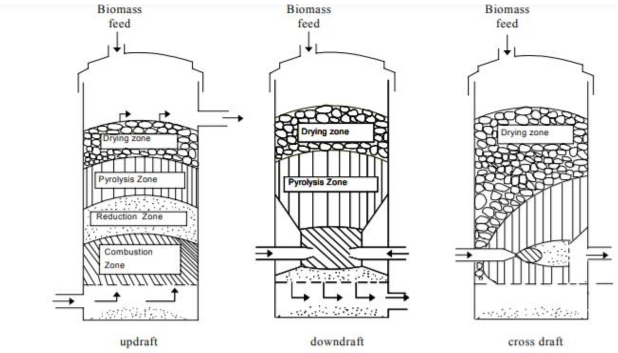

i) Fixed Bed Gasifiers

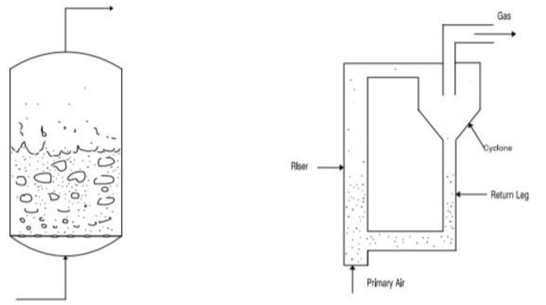

a) Bubbling Fluidized Bed **b) Circulating Fluidized Bed**

ii) Fluidized Bed Gasifiers

Figure 1.9-Major types of biomass gasifier [55]

1.3.2.4 Pyrolysis

Pyrolysis is a thermal decomposition route under an oxygen-free atmosphere. Overall, endothermic behaviour of biomass pyrolysis demand heat from 207 to 434 kJ/kg [56]. Polymers in three main components (hemicellulose, cellulose, and lignin) will melt and depolymerize into small-molecular vapours, which further condense into so-called bio-oil. Incondensable gases (including CO, CH_4, CO_2, H_2) also escape from decomposition. The final solid residual is rich in carbon, known as bio-char. Figure 1.10 illustrates a brief progress during biomass pyrolysis, the general stages during the temperature increase are: (1) Primary reactions including the removal of surface water and partial depolymerization. (2) Major mass loss (80% to 90%) of the main reaction period that relate to hemicellulose and cellulose decomposition. (3) Hot volatile inside biomass undergoes secondary reaction, homogeneously in the vapor phase and heterogeneously over the char surface. (4) The tertiary products only generate at high temperature with low yield, mainly including the cracking reactions that produce small-molecular gases.

Bio-oil from pyrolysis is a dark-brown liquid, it can be directly used in boiler or blend with vacuum gas oil in fluid catalytic cracking (FCC) units of oil refineries. Biochar can be either burned in the pyrolysis units for self-supply heat or used as reducing agent in metallurgical industry [57]. The un-condensable gas has high calorific value, which can be re-circulated into reactor for heat supply, or flow to downstream process like Fisher-Tropsch process.

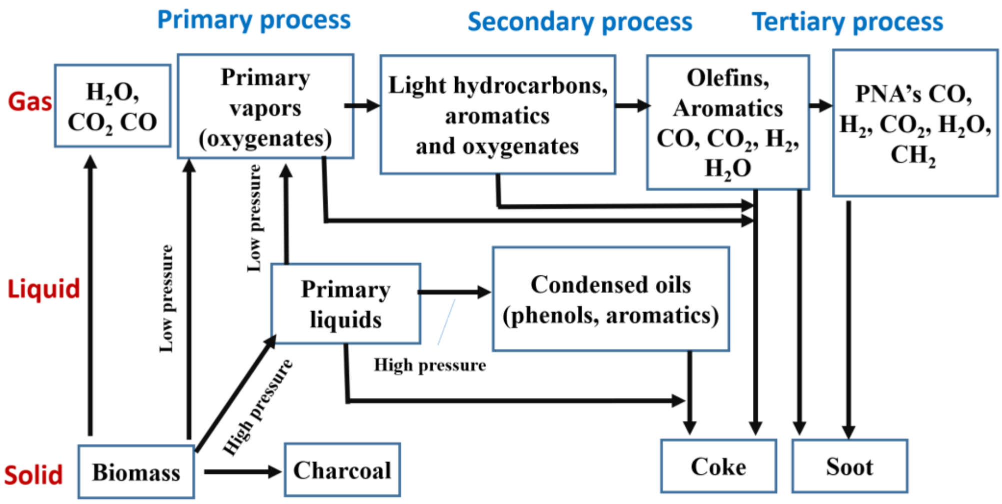

Figure 1.10- Flowchart of biomass pyrolysis process [58]

Industrial application of biomass pyrolysis encourages reactor developments including fixed bed, fluidized bed, rotating furnace, ablative and vacuum reactors [59], leading to considerable flexibility among products' yields and compositions. Three typical classifications depending on heating rates can be assigned as: Slow, fast, and flash pyrolysis. The basic parameters of these techniques are summarized in table 1.1.

Table 1.1. Main features of different types of pyrolysis technology

Type	Heating rate °C/min	Pyrolysis temperature (°C)	Residence time (feedstock)	Representative reactor	Main product
Slow pyrolysis	5-7	227-927	>1 h	fixed bed	char
Fast pyrolysis	300-800	327-627	0.5-10 s	fluidized bed	bio-oil
Flash pyrolysis	>1000	327-927	<2s	fluidized bed	pyrolytic gas

*Data are cited from literatures [60] and [61]

Fluidized bed reactor is widely applied in industrial biomass pyrolysis. It realizes the fast and direct heating of biomass by the high-flow heat carrier that are either high temperature gas or fine solid particles. The common schematic plot of fluidized bed reactor is shown in figure 1.11.

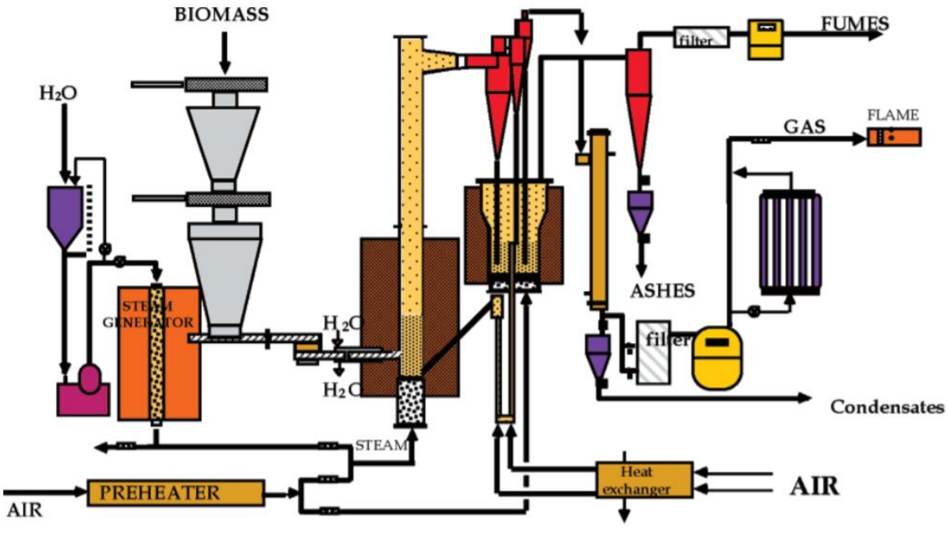

Figure 1.11- Schemes and industrial fluidized bed process [62]

Volatile yields are effectively promoted by the rapid heating, high temperature and short residence time, with bio-oil yield up to 75 wt.% and higher heating value of 17 MJ/kg [60]. Generally, small particle size is strictly required to fulfil requirements of fluidization velocity, the corresponding pre-treatment and downstream cyclone separation are usually indispensable [63]. On the other hand, surface area and heat transfer efficiency that link to particle size can affect product composition and yield.

Increasing developments have been also employed on the fixed-bed reactor (figure 1.12). Stable biomass layer and indirect heating method make a slow heating rate for raw material, resulting in high char yield. There are two main motivations for developing fixed-bed reactor: (1) succinct reactor design that ensure reliable and economical process; (2) liquid product that is easy for phase separations, being preferable to acquire special chemicals from bio-oil.

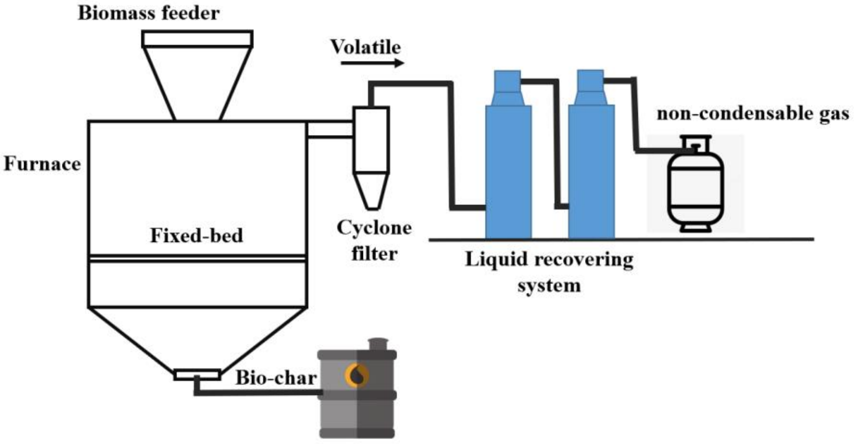

Figure 1.12- Fixed-bed reactor of biomass pyrolysis (adapted from [64])

Fixed bed generally deals with large particle sizes and large batch quantity. Temperature gradients are intense inside biomass bed, where near-wall portions turn to have higher temperatures than those in reactor centre. Transport phenomena become more significant in both macroscopic feedstock bed and microscopic single particle inside fixed bed reactor. Indeed, the particle size plays a crucial role in both fast and slow pyrolysis technologies, specific investigations should therefore be conducted for better process implement and control.

Chapter 2. Literature reviews

2.1 Chemical kinetic models of biomass pyrolysis

Significant efforts are required in kinetics models that is to create powerful tools in simulating reactor performances, understanding product evolution and optimizing process controls [65]. Pyrolysis involves complex sets of sequential and parallel unimolecular and bimolecular reactions [66], being quite demanding for detailed descriptions. Nonetheless, extensive kinetics schemes have been established over decades, from single-component, lumped-reaction models to the distributed activation energy model (DAEM), involving both nucleation behaviour and reactivity distribution. The most common kinetics models in biomass pyrolysis will be reviewed hereafter.

2.1.1 Single-component kinetics

Single-component (or one-stage) kinetics is the simplest global model. This macroscopic scheme treats biomass as one component which transforms into products with three categories: char, tar, and gas. The primary devolatilization and secondary charring are often included together. Additional measurements of product yields and thermogravimetric data are normally needed for model inputs. Figure 2.1 shows a typical single-component mechanism with three parallel reactions, it was first put forward by Shafizadeh and Chin [67] and then widely applied in early researches. The reaction competitions among three product classes are also indicated, where the liquid formation competes with both char and gaseous products at different temperature levels [68].

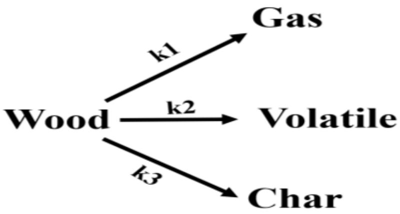

Figure 2.1- Overall pyrolysis mechanism by Shafizadeh and Chin [67]

The one-component mechanism provides reasonable agreement with experimental observations and meaningful ideology for an overall description of numerous reactions during biomass pyrolysis. That is why many subsequent models have been developed based on this scheme, in which reaction mechanisms are coupled with transfer formulations. For instance, Di Blasi [69, 70] coupled the one-component scheme with conservation law and momentum transfer by Darcy law, the 2D model was designed to investigate the effects of particle shrinkage and permeabilities in pyrolytic products' distribution.

Alternatively, a global mechanism [71, 72] further coupled secondary reaction mechanism with primary volatile. As shown in figure 2.2, reactive volatile matters from primary reactions convert with two competitive routes into permanent gases and refractory condensable materials, and the latter reaction is responsible for carbon deposition in solid phase.

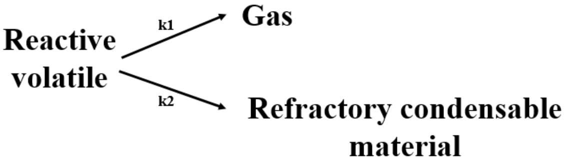

Figure 2.2- One-component scheme of secondary reaction mechanism [71, 72]

Still, one has to admit that one-component scheme is poorly constructed especially when dealing with analytical chemistry [73], and there still exists difficulties in determining kinetic constants after coupling secondary reactions or transfer phenomenon. Low values of activation energies could arise from the occurrence of different reactions in different temperature intervals [74]. Moreover, the scheme is based on the analysis of existing experimental data, its global kinetics will possibly fail when predicting different heating profiles, especially when covering a higher temperature which is not included in the database of parameter identification [75, 76]. These limitations are the motivations for further developments of multi-component mechanisms to better represent complexed reactions.

2.1.2 Multi-component kinetics

Multiple-component (or multi-stage) mechanisms consist of several parallel reaction zones or pseudo-components, among which interactions are supposed as inactive. The mechanism schemes read as follows:

$$C_i \xrightarrow{k_i} V_i, \quad i \in [1, m]$$

$$\frac{dC_i}{dt} = k_i C_i^{n_i}, \qquad k_i = A_i e^{\frac{-E_i}{RT}}$$

Where i is the component number, C_i is decomposable chemical component, V_i is corresponding lumped volatile products. k_i is reaction rate constant that involves the pre-exponential factor (A_i) and the activation energy (E_i). m is the number of pseudo-components, and n_i is the reaction order involving in each decomposition reaction.

One general pathway is to assume biomass to be a superimposition of several lignocellulosic components, it's a semi-global mechanism that involves sequential multi-step reactions of solid phase (C_i) and volatile (V_i) (figure 2.3). Number of reactants or reaction steps are manually chosen based on the complexity of kinetics.

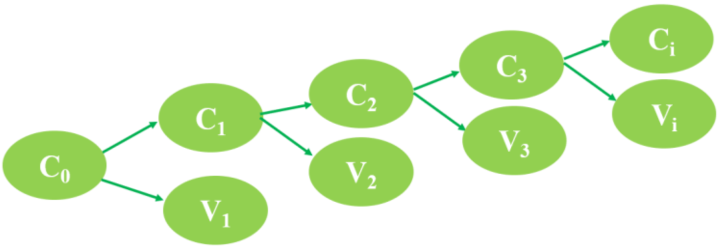

Figure 2.3- Scheme of sequential multi-step kinetics in biomass pyrolysis [77]

Subsequently, the majority of multi-component schemes incorporate three main constituents in biomass (i.e. hemicellulose, cellulose, and lignin). Usually, they are supposed to decompose through non-interaction reactions with independent kinetic parameters [78, 79]. The superposition of three simultaneous decompositions results in the final thermogravimetric behaviours.

One representative multi-component scheme was proposed by Miller and Bellan [80] that described individual biomass component with intermediate steps and interactions (Figure 2.4). Essentially, every chemical component still follows the single-component mechanism with limited reactions, and their combined mechanisms give birth to the final multi-component scheme.

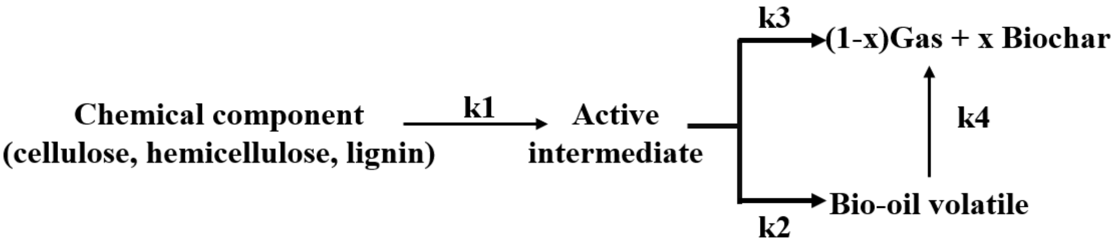

Figure 2.4- Multi-component scheme proposed by Miller and Bellan [80]

Kinetic works of specific chemical components have been further developed within the main frame of multi-component kinetic. Sub-kinetic of cellulose is mostly investigated due to its largest proportion in lignocellulosic biomass. Based on the scheme in figure 2.4, modifications have been made by considering the role of secondary reactions. Figure 2.5 shows one modified model proposed by Diebold [81] where all reactions are assumed to be first-order and irreversible. Cellulose first converts into active cellulose, primary char, and water. Active cellulose further decomposes by three pathways: cracking directly into secondary gases, devolatilization into primary vapor or dehydrations into char and water.

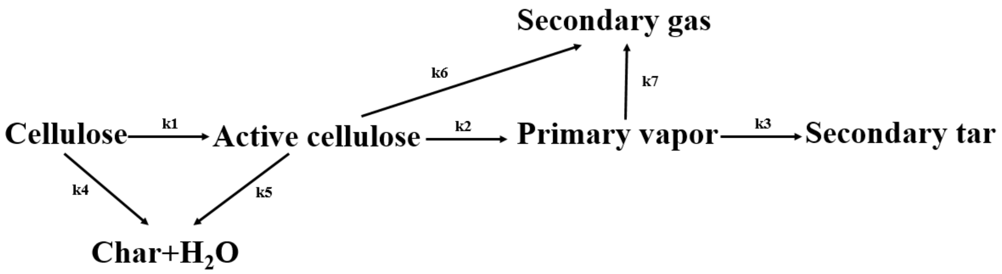

Figure 2.5- Cellulose pyrolysis kinetic model by Diebold [81]

Hydroxyacetaldehyde is found as cellulose's primary decomposition product through ring scission, and its formation competes with char generation [82]. Banyasz [83] proposed a relevant mechanism for fast pyrolysis in figure 2.6, which mainly accounts for the release of formaldehyde, hydroxyacetaldehyde, CO and CO_2. Formaldehyde and CO are indicated as the products of secondary reactions and levoglucosan in tar is major source for hydroxyacetaldehyde.

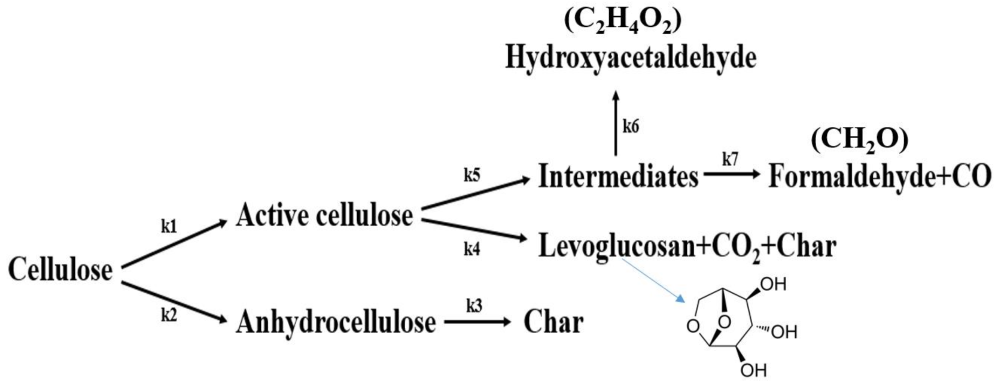

Figure 2.6- Cellulose pyrolysis kinetic model by Banyasz [83]

Andrés [84, 85] used a fragmentation pathway for cellulose (figure 2.7), which describes the primary reaction of ring fragmentation and secondary reaction of charring. Here, $(1-\chi_1)$ is the amount of initial fragmentation primary products, including hydroxyacetaldehyde (HAA), 5-hydroxymethyl-furfural (HMFU). χ_1 stands for the content in secondary product.

$$\mathbf{Cellulose} \xrightarrow{k} (1-\chi_1) * (0.95HAA + 0.25GLYOX + 0.2CH_3CHO + 0.25HMFU + 0.2C_3H_6O + 0.16CO_2 + 0.23CO + 0.9H_2O + 0.1CH_4 + 0.61Char)$$
$$+\chi_1 * \ (5.5Char + 4H_2O + 0.5CO_2 + H_2)$$

Figure 2.7- Cellulose pyrolysis kinetic model by Andrés [84, 85]

Concerning the sub-kinetic of hemicellulose, adapted schemes were proposed by Ranzi [65] to include secondary charring (figure 2.8a and 2.8b). The scheme shows that hemicellulose first decomposes without mass loss into two active hemicellulose HCA1 and HCA2. HCA1 further decomposes by two competition reactions between sugar formation (xylose) and fragmentation (figure 2.8a). On the other hand, HCA2 accounts for the secondary charring (figure 2.8b), which takes place among previous fragmentation products of both HCA1 and HCA2.

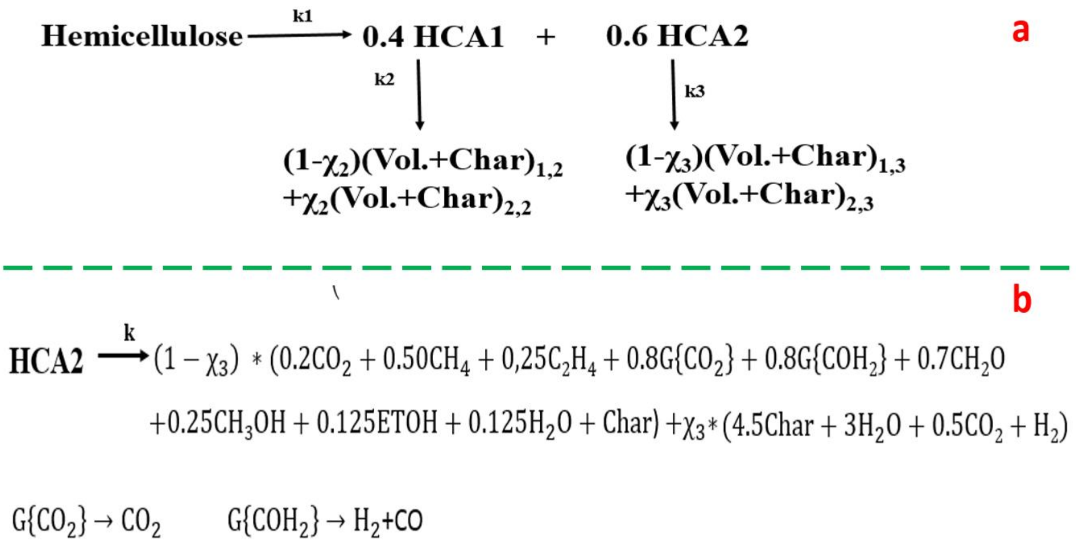

Figure 2.8- Hemicellulose pyrolysis scheme and HCA2 decomposition scheme [65]

Lignin decomposes over a broader temperature range, because its various oxygen functional groups have different degrees of stability. A simple illustration of lignin's decomposition scheme is shown in figure 2.9.

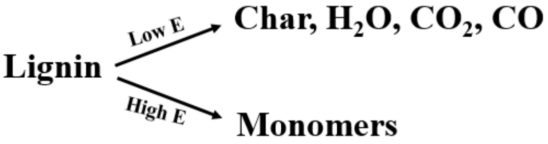

Figure 2.9- Lignin pyrolysis scheme [86]

The release of primary volatile component is mostly attributed to cleavage of propyl chains, linkages between monomers and methoxy substituents of aromatic rings. Then, a secondary charring occurs from the rearrangement of char skeleton in polycyclic aromatic structures [86].

Gauthiere [87, 88] considered lignin decomposition as a combination of three components : LIG-C (lignin components rich in carbon), LIG-H (lignin components rich in hydrogen) and LIG-O (lignin components rich in oxygen). As shown in figure 2.10, LIG-C first decomposes into volatile, char and another carbon-rich lignin (LIG-CC), further secondary reactions occur to produce volatile and char. LIG-H and LIG-O components first transform into volatile and OH-rich lignin, subsequently the OH-rich lignin undergoes secondary reactions to produce sinapaldehyde (FE2MACR), volatile and char. Lignin tends to favor char formation due to its high content of aromatic rings.

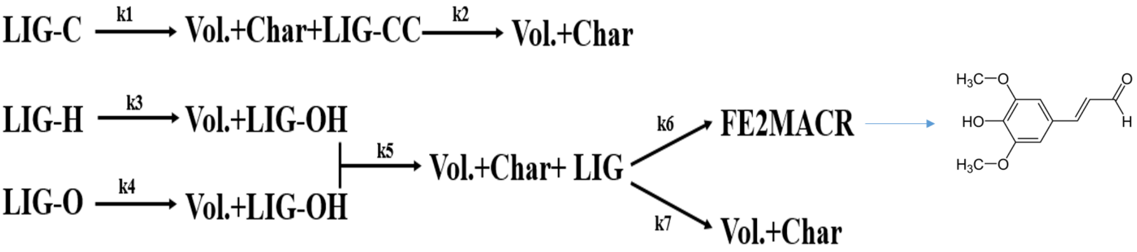

Figure 2.10 Lignin pyrolysis scheme with three kinds of lignin components [87]

Compared to the one-component kinetics, the multi-component includes more detailed reaction scenarios and considers specific chemical constituents, presenting as an important improvement. However, the sub-model inside multi-component kinetic mostly consists of three major components (i.e. hemicellulos, cellulose and lignin) and is essentially a one-component kinetic. Drawbacks of one-component scheme are possible to occur in multiple-component scheme as well. Notably, the prediction ability at different heating conditions is still unsatisfactory [75]. Even though the numerical complexity is never simple in multi-component kinetic, more reaction schemes must be further included to improve model's prediction capacity [89].

2.2 Distributed activation energy model (DAEM)

2.2.1 Formulation of DAEM

DAEM was firstly proposed by Vand [90] to analyse coal pyrolysis. Soon after, it was widely applied to various complex feedstocks including oil shale [91], sewage sludge [92], and biomass [93]. The model primarily calculates devolatilization reactions as a series of independent, parallel and first order or *n*th-order reactions with different activation energies. Every reaction group produces volatile ($V_i(t)$) at time *t* and follows the pseudo-*n*th-order rate equations as [93]:

$$\frac{dV_i(t)}{dt} = k_i\big(V_i^{\infty} - V_i(t)\big)^n \tag{2-1}$$

Where V_i^{∞} is maximum volatile production from reaction i, and n the reaction order (normally defined as natural number). The reaction rate constant, k_i, obeys an Arrhenius equation with pre-exponential factor (A_i) and activation energy (E_i):

$$k_i = A_i exp\left(-\frac{E_i}{RT(t)}\right) \tag{2-2}$$

Where R is the universal gas constant, R = 8.314 $\mathrm{J/(mol \cdot K)}$, and $T(t)$ is the absolute temperature at time t. A_i is assumed to be constant ($A_i = A$) for all reactions. The continuous function $f(E)$ defines the distribution of activation energies, which embeds the distribution of atomic interactions caused by the variability of macromolecules [94]. Chemical components with activation energy between E and E+dE have the reaction probability: $\int_E^{E+dE} f(E)dE$. The total integral of $f(E)$ equals 1 to keep normality:

$$\int_0^{+\infty} f(E)dE = 1 \tag{2-3}$$

So the integral form of conversion degree $X(t)$ is:

$$X(t)=\frac{V(t)}{V^{\infty}}=\begin{cases}1-\int_{0}^{\infty}\left[1-(1-n)\int_{t_0}^{t}Aexp\left(-\frac{E}{RT}\right)dt\right]^{1/(1-n)}f(E)dE & n\neq 1\\ 1-\int_{0}^{\infty}exp\left[-\int_{t_0}^{t}Aexp\left(-\frac{E}{RT}\right)dt\right]f(E)dE & n=1\end{cases} \tag{2-4}$$

2.2.2 Multi-distribution DAEM

Biomass is a complex mixture of chemical fractions and the published works proved that it is not possible to correctly represent the volatile production with one single distribution. Instead, the biomass is represented by several components with a continuous distribution for each of them [95].

Therefore, multiple-parallel DAEM distributions have been proposed to represent biomass [96]. Concepts of pseudo-components have also been proposed to correspond chemical components to the reaction clusters. The common formulation of multiple-parallel DAEM expresses as:

$$X(t)=\frac{V(t)}{V^{\infty}}=\begin{cases}1-\sum_{j=1}^{N_d}V_{max}(j)\int_{0}^{\infty}\left[1-(1-n)A_j\int_{t_0}^{t}exp\left(-\frac{E_j}{RT}\right)dt\right]^{\frac{1}{1-n}}f_j(E)dE & n\neq 1\\ 1-\sum_{j=1}^{N_d}V_{max}(j)\int_{0}^{\infty}exp\left[-A_j\int_{t_0}^{t}exp\left(-\frac{E_j}{RT}\right)dt\right]f_j(E)dE & n=1\end{cases} \tag{2-5}$$

Where N_d is the distribution number and $V_{max}(j)$ the weighting factor of its corresponding distribution $f_j(E)$.

Table 2.1 reviews several DAEM with different distribution number, ranging from 1 to 5, their degrees of freedom that relate to numerical complexities are also listed. Among them, multi-Gaussian DAEM still attracts the most attention. Moreover, comprehensive model consisting of three parallel DAEM is further claimed as the most accurate and up-to-date approach [93]. Herein, values of degree of freedom (D_f) varies among different model types, attributing to the differences in, i) overall distribution number and, ii) independent parameter in each distribution.

The pyrolysis systems of different feedstocks could be described by different sets of distributions. The popular choices are symmetric distributions like Gaussian and logistic, meanwhile the actual reactivity distributions of certain materials tend to asymmetric [66], which requires the corresponding asymmetric distributions such as Weibull and Gamma. Chemical interpretations are usually attached with multiple-distributions. The two-distribution scheme is generally explained with double-stage pyrolysis [78]. In three-distribution DAEM, the pseudo-component with largest weighting factor is attributed to cellulose; and the pseudo-components with largest range of activation energy is linked with lignin. While the overlapped or multiple-stage decompositions explain the schemes of four- and five-distribution DAEM [97].

Table 2.1- DAEM with different distribution numbers

Distribution number	Distribution type	D_f	Independent D_f in each distribution	Feedstock	Literature
1	logistic	4	4	Cellulose/xylan	[2]
1	Gaussian/Gamma/Logistic /Rayleigh/Weibull/log-normal	4-5	4-5	Chlorella pyrenoidosa	[98]
1	Gaussian	3	3	peanut shell	[99]
2	Gaussian	5	2	olive residue	[100]
2	Gaussian	8	4	wheat, barley, oat, straw	[78]
2	Gamma and Rayleigh	11	5	pine needles	[101]
2	logistic	6	3	5 lignocellulosic biomasses	[102]
3	Gaussian	8	2	coal, coal char	[103]
3	Gaussian	12	4	13 lignocellulosic biomasses	[104, 105]
3	Gaussian	15	5	tobacco stem	[106]
3	Weibull	9	3	Epoxy-Hexahydrophthalic Anhydride	[107]
4	Gaussian	8	2	lignin	[108]
5	Gaussian	10	2	hemicellulose	
5	Gaussian	16	3	bagasse/ sewage sludge	[109]

2.2.3 Mathematical shape of the function f(E)

Many trials have been done concerning the shape of the mathematical function, the most common ones are symmetric Gaussian and logistic distributions [110].Meanwhile, considering that actual forms of reaction activity is asymmetric especially during initial and final stage of pyrolysis [66], asymmetric distributions including Weibull, Gamma and Rayleigh distributions were also applied [111, 112]. Table 2.2 lists the mathematical formulas of probability density function (PDF), mean value and standard derivation of several applied distributions.

Table 2.2- Mathematical distributions used in the research of DAEM

Distributions name	PDF	Mean	Standard derivation
Gaussian	$\mathrm{f(E)} = \frac{1}{\sigma\sqrt{2\pi}} exp\left[-\frac{(E-E_0)^2}{2\sigma^2}\right]$	E_0	σ
Logistic	$\mathrm{f(E)} = \frac{\pi}{\sqrt{3}\sigma} \frac{exp\left[-\frac{\pi(E-E_0)}{\sqrt{3}\sigma}\right]}{\left\{1+exp\left[-\frac{\pi(E-E_0)}{\sqrt{3}\sigma}\right]\right\}^2}$	E_0	σ
Weibull	$\mathrm{f(E)} = \frac{\beta}{\eta}\left(\frac{E-\gamma}{\eta}\right)^{\beta-1} exp\left[-\left(\frac{E-\gamma}{\eta}\right)^{\beta}\right]$	$\gamma + \eta\Gamma(1+\frac{1}{\beta})$	$\sqrt{\eta^2\Gamma^2\left(\frac{2}{\beta}+1\right) - \eta^2\Gamma^2\left(\frac{1}{\beta}+1\right)}$
Gamma	$\mathrm{f(E)} = \frac{\beta^{\alpha}\left(\frac{E-E_{min}}{E_{min}}\right)^{\alpha-1} exp\left(-\beta\frac{E-E_{min}}{E_{min}}\right)}{\Gamma(\alpha)}$	$\left(\frac{\alpha}{\beta}+1\right)E_{min}$	$\frac{\sqrt{\alpha}}{\beta}$
Rayleigh	$\mathrm{f(E)} = \frac{E-E_0}{\sigma^2} exp\left[-\frac{(E-E_0)^2}{2\sigma^2}\right]$	$E_0 + \sigma\sqrt{\frac{\pi}{2}}$	$\sigma\sqrt{\frac{4-\pi}{2}}$

2.2.4 Frequency factor A and compensation effect

(1) Frequency factor A

During the parameter determinations, the frequency factor (or pre-exponential factor) A_i of every reaction remains controversy among different models. Three strategies have been adopted so far. The first practice (also the most common method) is to set a fixed value in advance for all reactions, in other words, pre-setting A_i before parameter identification process. For instance, three fixed values ($10^{14.13}$, $10^{13.71}$, $10^{13.90}$) had been assigned to three-distribution DAEM [113], or all distributions shared the same value of frequency factor (5×10^{11}) [103, 114]. The second practice is to correlate frequency factor with temperature (eq. 2-6). Here A_0 is a constant value and the exponent m ranges between -1.5 to 2.5 [115]. It sets specific values for all reactions, but these beforehand values are still independent from parameter identifications.

$$A = A_0 T(t)^m \tag{2-6}$$

The third practice is to introduce a correlation (eq. 2-7) when proceeding identification process.

$$lnA = a + bE \tag{2-7}$$

It is also known as “compensation effect”, this relation reflects that the change of E can be compensated by the proper change of A [116]. Even though the correlation simplifies identification by reducing one degree of freedom, it could still harm the accuracy with multiple sets of equal-fit parameters. This effect will be discussed in detail hereafter.

(2) Compensation effect

The linear relationship ($lnA\ vs. E$ in eq.2-7) for a series of related reactions is referred as “compensation effect”. It can be also written as the linearized form of Arrhenius equation as:

$$lnA = lnk_{iso} + \frac{1}{RT_{iso}}E \tag{2-8}$$

Where the k_{iso} is the isokinetic rate constant, T_{iso} is isokinetic temperature. They are treated as constants at a specific isokinetic condition [117]. It was first reported in the catalysis study, and was further found in the pyrolysis kinetics of biomass [118, 119] or its compositional material (cellulose, hemicellulose and lignin) [120, 121]. Possible causes of compensation effects had been concluded as: thermal lag [122], tunnel effect of electrons ions, or trivial errors in experimental data [123].

On one hand, compensation effects are useful in identifying reaction mechanism, checking reaction parameters, and characterizing similar decomposition groups [118]. On the other hand, during numerical simulation especially for the kinetic fitting in DAEM, the compensation effect causes several equally well-fit A and E values, this lack of uniqueness in kinetic parameters could greatly harm model accuracy and robustness. That’s why this functional form was not encouraged during DAEM identification process [124, 125].

2.2.5 Parameter determination and estimation

Inverse analysis of the model, which performs minimization of the gap between experimental and calculated data, is a classical way to determine the model parameters in DAEM modelling. Besides, the distribution-free method is an experiment-oriented tool for kinetic determination, which is also applied for comparing and estimating DAEM kinetics. Both methods will be presented hereafter.

2.2.5.1 Inverse analysis

Inverse analysis consists in a computational solution of the model and on an optimization algorithm to determine kinetic parameters. The predefined configurations include:

(1) The choice of the objective function (OF), likely to measure the gap between model simulation and experiment. It is usually defined as the residual sum of squares (RSS) between experimental and calculated conversion rates, over the number of experimental points N_{exp}:

$$OF = \sum_{a=1}^{N_{exp}} \left(X_{exp}(t) - X(t)\right)^2 \tag{2-9}$$

(2) The choice of the shape and number of the distribution function f(E).

(3) Some additional assumptions likely to facilitate the optimization. For instance, constant value of A, no interactions between pseudo-components, etc.

A logic flow chart of optimization algorithm is illustrated in figure 2.11 (parameter identification process). Reasonable parameters are initially provided, optimization loop subsequently calculates OF and alters model parameters to minimize the objective function. Many practical optimization algorithms have been applied in the model identification, which includes grid search, genetic algorithm [126], Nelder-Mead simplex algorithm [127], direct search [128], pattern search [99], simulated annealing method [129], and multistate algorithm [130]. Sufficient iterations ensured successful identification by ending with no difference between the penultimate and final optimization values. And finally, the process produces suitable set of kinetic parameters after the optimization.

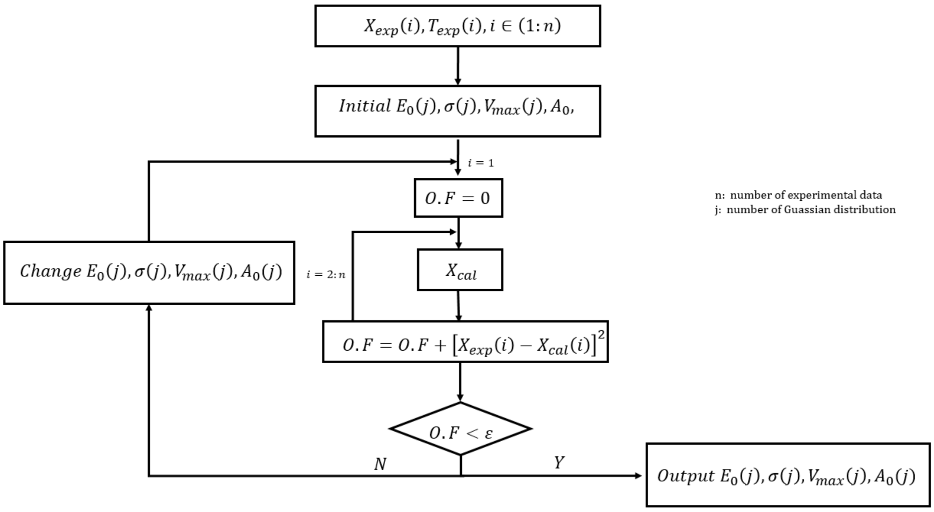

Figure 2.11- Calculation process diagram for model parameters' identification

2.2.5.2 Distribution-free method

Distribution-free methods can determine kinetic parameters without previous assumptions, they solely rely on several sets of experimental data obtained at different heating rates. They can therefore provide reliable initial kinetic parameters for modelling sections, and act as a simple and direct comparison references for DAEM parameters.

(1) Miura-Maki method

Miura and Maki first proposed a simple method to estimate values of $f(E)$ and A [131]. In their theory, the integrated form of Arrhenius equation at a constant heating rate α is approximated as:

$$ln\left(\frac{\alpha}{T^2}\right) = -\frac{E}{R}\frac{1}{T} + ln\left(\frac{AR}{E}\right) - ln\left\{-ln\left(1 - \frac{\Delta V}{\Delta V^*}\right)\right\} \tag{2-10}$$

Where ΔV and ΔV^* are evolved volatile and total effective volatile respectively. Further approximation simplifies the equation into:

$$ln\left(\frac{\alpha}{T^2}\right) = -\frac{E}{R}\frac{1}{T} + ln\left(\frac{AR}{E}\right) + 0.6075 \tag{2-11}$$

Figure 2.12 illustrates an example of Miura-Maki method. The linear correlation between $\frac{\alpha}{T^2}$ vs. $\frac{1}{T}$, at a specific conversion level of different heating rates, can determine E and A values by the slop and intercept respectively.

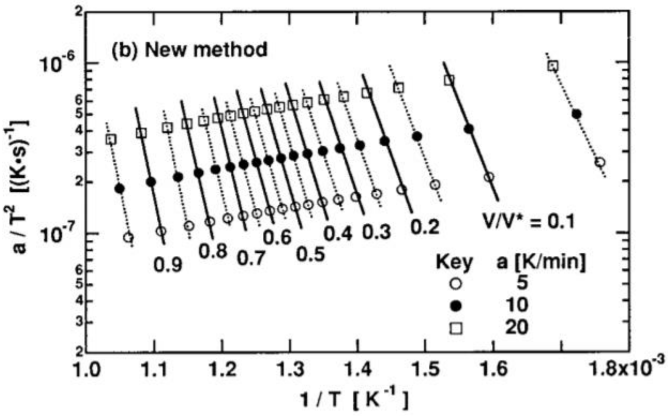

Figure 2.12- Linear plots of Miura-Maki method, $\frac{\alpha}{T^2}$ vs. $\frac{1}{T}$ at selected conversion rates of three heating rates [131]

(2) Ozawa method

Ozawa method also makes approximation during the integration of Arrhenius equation, presenting a linear-regression formulation as [132]:

$$ln\alpha = -0.4567\frac{E}{R}\frac{1}{T} + ln\left(\frac{EA}{R}\right) - ln\left[-\int_{x_0}^{x}\frac{dx}{f(x)}\right] - 2.315 \tag{2-12}$$

Here x is the conversion rate and $f(x)$ the conversion function that depends on reaction order. When reaction compound reaches a specific conversion degree, the linear fitting of $ln\alpha$ vs. $\frac{1}{T}$ gives the values of activation energy (E) and corresponding frequency factor A (example in figure 2.13).

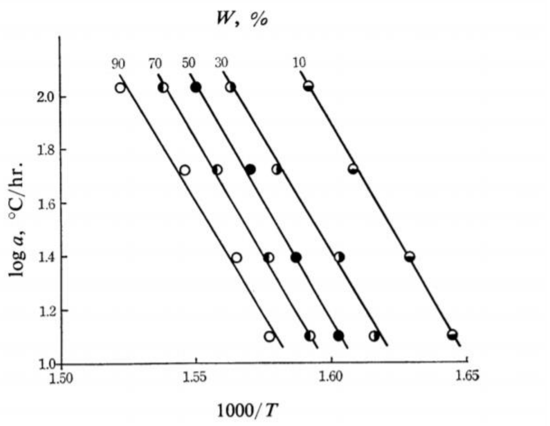

Figure 2.13- Linear plots of Ozawa method, $loga$ vs. $\frac{1}{T}$ at selected conversion rates at four heating rates [132]

(3) Kissinger method

Kissinger method is also known as peak-displacement method in quantitative thermal analysis [133]. The method involves presentative temperatures (T_p) corresponding to maximum reaction rate (peaks) at different heating conditions. Since the derivative form at the peak maxima should equal to 0 [134], it leads to a rearranged form:

$$ln\frac{\alpha}{T_p^2} = ln\left(\frac{AR}{E}\right) - \frac{E}{R}\frac{1}{T_p} \qquad (2\text{-}13)$$

Where α is the heating rate. A and E are the frequency factor and activation energy corresponding to the peak temperature. The slope ($-\frac{E}{R}$) and intercept ($ln\left(\frac{AR}{E}\right)$) from linear fitting can result in the values of A and E. Kissinger method is also an iso-conventional method based on empirical regression, the data inputs come from recognizable points in TG or DSC plots.

In comparison between the two methods, the distribution-free methods are iso-conversional with empirical linear regressions, their kinetic parameters are substantially affected by the chosen temperature regions that correspond to different heating rates. The accuracy is much depended on the measurement precision and test number, and the determined values have the average implications of all biomass components. They can estimate kinetic parameter in reasonable accuracy, being a good comparison references, or checking tool in DAEM. In the case of the inverse method, the identification of parameters responsible for global mass-loss kinetics and accuracy could benefit from multiple heating rates, therefore being more powerful [135]. When associated with a computational solution, this method can also take advantage of any time-temperature profiles. The objective function can also cumulate the RSS of several experimental tests to propose a global optimization.

2.3 Factors affecting biomass pyrolysis

2.3.1 Temperature and residence time

The temperature level basically provides necessary activation for fragmentations and secondary reactions during biomass pyrolysis, and residence time decides the reaction extents [136]. These two factors jointly affect pyrolysis kinetics, making their matching relations quite important. For instance, at the proper temperature levels between 400-550 °C, short residence time favoured bio-oil production, while long residence time would promote extra char formation and gaseous production [137-139]. residence time also matters at high temperature levels: no soot formed at 900-1500 °C with a short residence time (0.2s), yet the soot had significant production at >1000 °C when increasing residence time to 2s [140].

Relevant works also indicated their joint effects on product composition distributions. Phenols, as the major components in oil products, had an increased proportion at higher temperatures (600-900 °C) and longer solid residence times (6 min) [141]. With a long residence time (>15s) at 600 °C, the formation of polynuclear aromatic tars appeared to occur via gas phase molecular weight growth reactions [142]. Yields of PAHs (polycyclic-aromatic hydrocarbons) in bio-oil was found generally increase as the residence time increased from 90ms to 1400ms at 800°C [143]. The H/C ratio in char was found to decrease when increasing residence time from 0.3s to 1s at 800 °C [144].

Essentially, at the same residence time, pyrolysis can be divided into three stages according to different temperature ranges. The first stage below 127 °C corresponds to the removal of liquid and bound water; the second stage between 127 °C to 300-400°C has the dominant mass loss (80%-90%), attributing to the decomposition of hemicellulose and cellulose. The third section with temperature higher than 450 °C is responsible for lignin decomposition and secondary charring [145]. Temperature range between 400-550 °C and short residence time can result in the highest bio-oil yield. While further increase temperature to 600 °C, volatiles start to crack and promotes the gas yield [146]. The content of polycyclic aromatic hydrocarbons (PAHs) in bio-oil increases when temperature is higher than 700 °C. Generally, higher gas yield is obtained above 500 °C, and higher yields of H_2 and CO are found at high temperatures due to secondary cracking [147]. The increase of temperature from 400 °C to 700 °C can further degrade semi-coke when residence time is short [148].

In the single-particle level, inner-mass transfer efficiency decides the volatiles residence time. Short residence time at low temperature can avoid unnecessary secondary reactions. Relatively, long residence time increases volatiles contact with high-temperature solid and the possibilities of secondary reactions [149]. In the industrial plant, long residence time inside reactor and exportation system could cause serious product loss and blockages [150]. Fluidized-bed process usually releases produces quickly and achieves high bio-oil yield at high temperatures. While the long residence time and low temperature in the batch-operated fixed-bed tend to produce more bio-char. On the other hand, incomplete decomposition happens if the residence time is too short, which usually produces oxygenate bio-oil that requires further upgrading [151].

2.3.2 Heating rate

Heating rate distinguishes pyrolysis types (usually characterize as slow, fast, and flash pyrolysis) by reflecting different time-temperature profiles. This is a mean to act on the residence time. Slow pyrolysis is conducted under long residence time (>1h) at a temperature less than 500 °C [152]. Fast pyrolysis usually occurs at high heating rate (up to 800 °C/min) with very short residence time (<10s) [153]. Flash pyrolysis is characterized by much higher heating rates, e.g. 1000 °C/min and a very short residence time (<2 s), resulting in high oil yields up to 75–80% [153, 154].

A fast heating rate favours major fragmentation of organic functional groups, bio-oil yield is enhanced by fast release and minor secondary reactions like tar cracking and repolymerization [155]. By immediate volatile cooling and short residence time, an increase of 23.4% in oil yield was observed when increasing heating rate from 5 °C/min to 700 °C/min [156]. The thermal hysteresis in different heating rate conditions also result in different characteristic temperatures, for instance, the optimum temperature of maximum oil yield will shift to high values when the heating rate is high [157]. Meanwhile, oxygen-containing species (CO_2 or CO) have higher contents in the gaseous products at high heating rates, which suggests the promotion of C-O breakages during volatile cracking in the high heating rate conditions.

2.3.4 Particle size

Particle size could directly affect pyrolysis kinetics in terms of reaction rate, products yield and chemical properties. Understanding of the effect of particle size can help minimize heat/mass transfer problem, and optimize residence times for better product yields [156]. Figure 2.14 shows the mechanisms affected by particle size. When pyrolytic volatiles are generated in cell walls and subsequently diffuse into hollow lumen structures, the geometry-related mechanism can profoundly affect reactions in gaseous/condensed phase, mass transfer (volatile diffusion, convention), and thermal transfers. With an increase in particle size, the added cellular- and tissue-scale barriers cause more hermetic spaces and channels, which can obstruct internal devolatilizations. Thermal profile requires more time to develop uniformly inside large particles, and the centripetal temperature gradients lead to low-temperature core where re-condensation usually occurs. On the other hand, complex transfer tunnels prolong residence time and cause more chances for secondary reactions. The long transfer pathway also provides more catalytic surface and slower cooling for volatile, leading gas phases to re-polymerize by both homogeneous and heterogeneous reactions.

Even though unexpected higher yield of liquids are possible in larger biomass particles due to different biomass types [155] and reaction temperature up to 1000 °C [158], the general trends in small particles still promote bio-oil productions. Usually when matching with short residence time and fast cooling, higher bio-oil yield in small particle can be realized, attributing to the higher heating rate inside particle [159], less physical trapping [160] and less heat transfer limitations [161].

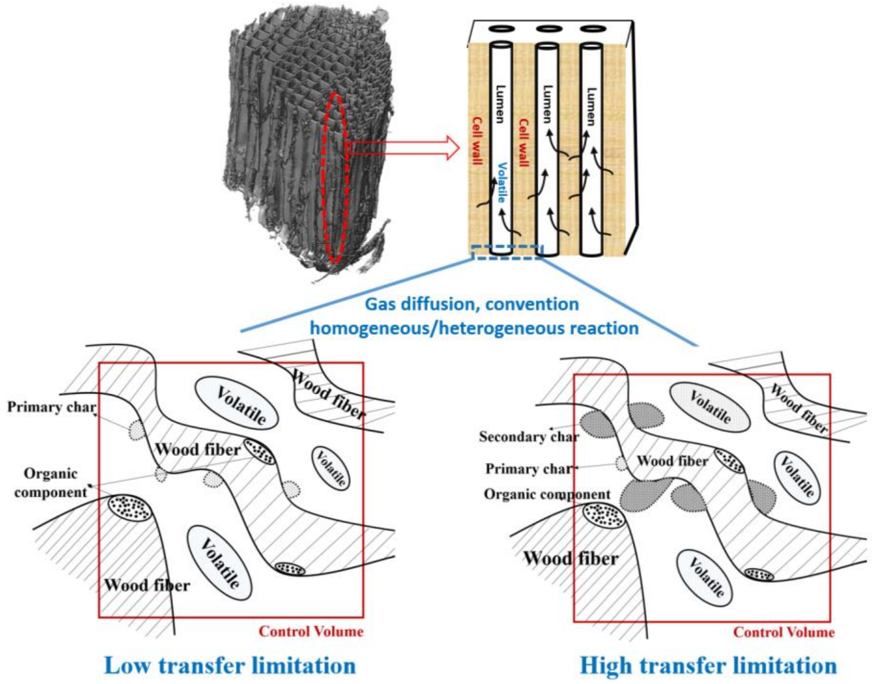

Figure 2.14- Affecting mechanism of particle size during biomass pyrolysis

2.4 Enthalpies in biomass pyrolysis

2.4.1 Reaction enthalpy

Reaction enthalpy in pyrolysis is defined as the energy required to drive all decomposition reactions. It is included inside the enthalpy balance [162] as:

$$-\dot{Q} = m_c \frac{dh_c}{dt} + m_s \frac{dh_s}{dt} + \dot{S} + \frac{dm}{dt}(h_v - h_s) \tag{2-14}$$

Where h are the specific enthalpies, $\dot{Q}$ the heat flux provieded to system, $\dot{S}$ the source term due to chemical reactions and dm the quantity of volatiles formed during the time interval dt. Indices c, s and v stand for crucible, sample and volatiles respectively. The therm $(h_v - h_s)$ is the enthalpy of volatilisation[163, 164], together with $\dot{S}$, they make up the pyrolysis enthalpy. The values of pyrolysis enthalpy are usually measured by a calorimeter [165], and they have large variability in literatures that range from endothermicity to exothermicity under different reaction conditions. Process conditions (small particle size, short residence time and high flow rate) favour quick release of volatile and avoid heterogeneous secondary reactions, overall endothermic heat is therefore promoted. Hence, fluidized bed (780-3300 kJ/kg) [166, 167] turns to have higher endothermic heat compared to fix bed (185-536 kJ/kg) [168] or screw reactor (1100-1600 kJ/kg) [169].

High operation pressure was found to enhance exothermic pyrolysis due to the low specific volume of the high reactive volatile [170]. Inorganic components favoured char formation which caused exothermic heat. This explains why washing pre-treatments could increase endothermicity [171]. The primary devolatilizations with chemical bond cleavages are endothermic, yet the secondary reactions of volatiles (both homogeneous and heterogeneous), including charring, partial oxidation, re-polymerization, cross-linking and condensation are exothermic [170, 172]. The char formations were estimated as exothermic between 2000-3600 kJ/kg [170, 173]. Many researches attributed exothermic heat to the enhanced char formations at the conditions of high temperature and hindered mass/heat transfer (lidded crucible, large particle, high material layer) [170, 171, 174, 175].

Reaction heat is clearly related to the decomposition of individual constituents (hemicellulose, cellulose, and lignin) with consecutive exothermic or endothermic stages. Overall thermal decomposition of hemicellulose is assigned as exothermic due to the presence of glucuronic acid units [145, 176], where decarboxylation of carboxylic acids groups produces carbon dioxide and releases heat. Initial melting period of cellulose is endothermic with enthalpy values between 200-710 kJ/kg [88, 177, 178], which reflect the latent heat requirement for vaporizing primary tar [88], including depolymerization of 1,4-glycosidic bond and ring breakage of light oxygenated components [179]. The further thermal evolution of pyrolytic cellulose at higher temperatures will exhibits exothermicity in spite of no obvious mass loss, which is due to : (1) carbonization through aldol condensation, cross-linking and aromatic condensations [180] ; (2) cracking of functional groups in residue [145]. Thermal decomposition of lignin between 150 to 800 °C is tested as exothermic. The primary degradation involves the breakage of β-O-4 linkage [181], its exothermicity at low temperature (<280 °C) is assigned to the release of energy stored in the lignocellulosic matrix. When further increasing temperature to 450 °C, the complete release of accumulated heat will overlap with the important exothermicity of cross-linking reactions (cross-linked aromatic residues) [182, 183]. Lignin exothermic degradation is responsible for temperature attainment and overshoot in large wood cylinders and spheres [184].

2.4.2 Specific enthalpy

The specific enthalpy (the h terms in eq.2-14) is the required energy for raising sample temperature to a specific value [185], It can be expressed as:

$$dh = mC_p \frac{dT}{dt} \tag{2-15}$$

Where m is sample mass and T is sample temperaure. C_p is the specific heat capacity, it is the energy required by one unit of mass to increase in one unit of temperature, its SI (international system of units) is J/(K kg).

Regarding the C_p values of biomass and remaining char during pyrolysis, their measurements are usually carried in adiabatic calorimeter [186], the values vary widely based on different biomass types with limited reliability and confidence intervals [187]. Noteworthily, for biomass, heat capacity can be only measured below 150 °C as thermal decomposition starts when the temperature goes higher. Similarly, the linear regressions of char are only validated at low temperatures below 400 °C, since heat reactivities at high temperatures are much complicated for distinguishments. And due to the complicated mixture situation of unreacted biomass and bio-char, the measurements of specific heat and heat capacity that subject to conversion rates are still very rare. Up to date, we only found a computer-aided thermal analysis (CATA technique [188]) which was capable of estimating specific heat during biomass pyrolysis up to 600 °C. The technique was based on the minimisations of the errors between measured and calculated temperatures, and subsequently determined the heat capacities during the whole conversion process of biomass to charcoal.

To deal with the complexity of specific heat capacity during modelling, its value is either settled as constants or estimated as a linear function of temperature [189, 190]. Specific heat capacity of wood char could be assumed as that of graphite [191] (curve a in figure 2-15) , or similar linear correlations (curve b and c) [171, 192].

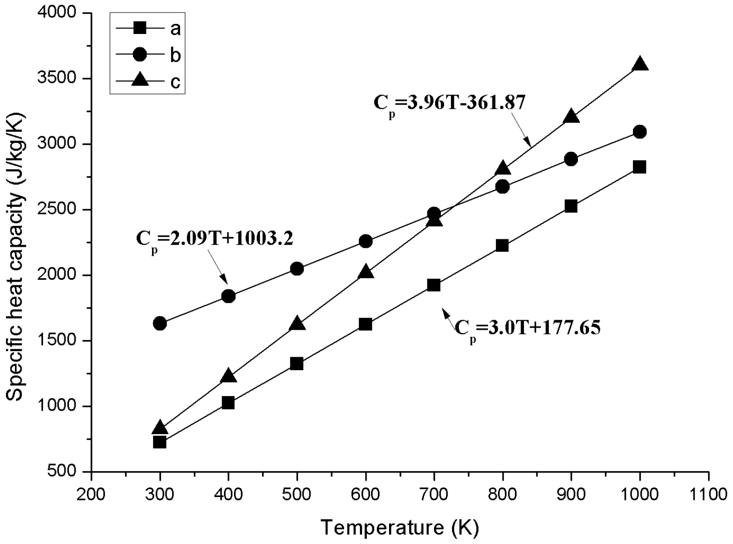

Figure 2.15- Specific heat capacity of biomass char (a cited from [191], b cited from [192], c cited from [171])

The choices for the values of biomass follow similar principles, which could be determined by DSC measurement as ca. 1.0 $\text{kJ}\cdot\text{kg}^{-1}\cdot\text{K}^{-1}$ [190]. Literatures [174, 193] also used linear correlations for C_p of dry wood particle as: $C_p = 1.11 + 4.8567(T - 273.15)(\text{kJ}\cdot\ \text{kg}^{-1}\cdot\text{K}^{-1})$, and similar correlations of plenty biomass types and three main constituents were also measured [171, 190, 194].

2.5 Conclusion

This chapter mainly reviews in following aspects: (1) kinetics schemes of biomass pyrolysis including one-component, multi-component; (2) formulation of DAEM and relevant concepts; (3) affecting factors in pyrolysis; (4) reaction enthalpy and specific enthalpy.

The broad range of kinetic models proposed in literatures, from one-component to multi-distribution DAEM, give the general views in choosing suitable models depending on the intended uses. One-component mechanism has concise formulation but less accuracy; the subsequent multi-component mechanism shows improvement by involving more sequential/parallel reactions, and sub-kinetics of three main chemical constituents also make this scheme more accurate. The DAEM approach is an excellent solution to include most reaction kinetics, further multi-distribution DAEM contributes to the most comprehensive kinetic. Both symmetric and asymmetric distributions endow different kinetic profiles. Parameter estimation methods (distribution free/ distribution fitting) help identify model parameters. The joint effects of temperature and residence time clearly influence products yields and corresponding composition distributions. Heating rate presents a synthetic driver from both temperature and residence time. High heating rate, which couples with proper temperature and short residence time, could promotes fragmentations for a high bio-oil yield. Particle size causes different transfer profiles of heat and mass, hermetic and long transfer tunnels in large particle essentially cause long residence time and uneven temperature profile, which leads to more re-condensation and char formations. Reaction heat is affected by both reaction conditions and the chemical nature of major components. On the other hand, specific heat is hard to determine due to the complex mixture of char/biomass that change at different reaction extent, hence, several correlations have been applied to ease relevant modelling work.

.

Chapter 3 Materials and methods

This chapter will focus on the general experimental protocols, and the characterization methods. The strategy of experimental part is illustrated in figure 3.1, first the intrinsic kinetics will be determined on powders of two wood species (spruce and poplar), their thermogravimetric (TG) and differential scanning calorimeter (DSC) data will be further applied in modelling part for kinetic parameter identifications. Different particle size samples are prepared in the follow-up works, this second dataset will serve as input experimental data for interpretation and modelling of the effect of particle size.

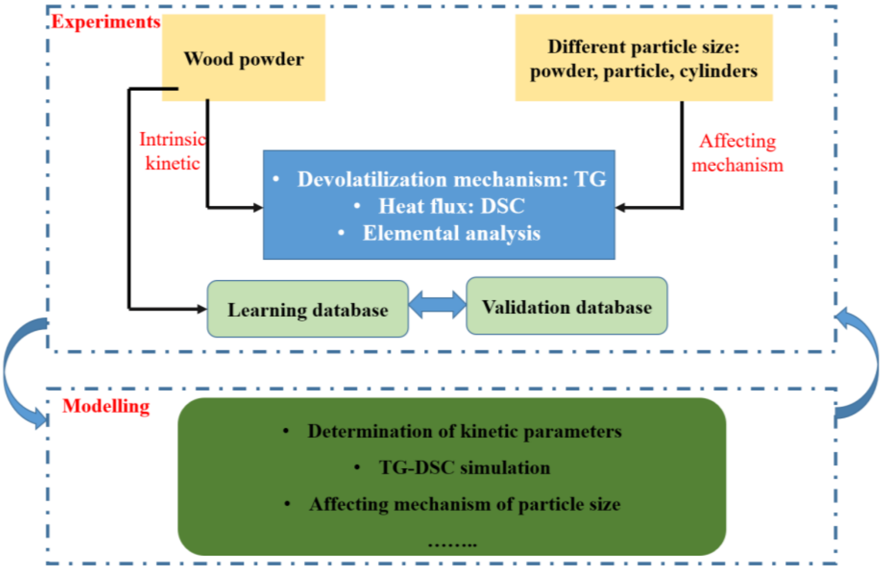

Figure 3.1- Experimental strategy adopted in the PhD work

3.1 Wood sample

Two wood species are chosen in this work based on their different biological origin: softwood (spruce) and hardwood (poplar). These two types of wood have different densities and resilience to heat treatment. Softwood originates from gymnosperm trees that have needles and cones, and it presents medullary and tracheid micro-structure. Hardwood originates from angiosperm trees that are broad-leaved. Their anatomical structure contains fibres, vessels, and ray cells.

Spruce wood (*Picea abies*) used in this research comes from a 73-year-old tree from *Auverge* region, France, it has a density of 450 kg/m^3 when its moisture content is 33%. Poplar wood (*Populus euro-americana* ‘koster’) comes from a 25-year-old tree in the forest

Suippe, la Marne, France, its density is 364 kg/m^3 at a moisture content of 12%. This work will use five types of particle sizes for each wood samples, their morphological descriptions are listed in table 3.1. The protocols of manufacturing wood samples will be explained in detail in the afterward chapters.

Table 3.1- Morphological descriptions of wood samples used in the research

Particle type	Powder	Particle	Cylinder-1mm	Cylinder-2mm	Cylinder-4mm
Dimension Size	0.063-0.08 mm	0.63-0.8 mm	diameter:5 mm height:1 mm	diameter:5 mm height:2 mm	diameter:5 mm height:4 mm

The basic chemical information of two wood samples is listed in table 3.2, the ultimate and approximate analyses are conducted in Thermo Fisher Scientific FLASH 2000 organic elementary analyser and Nabertherm LV/9/11 furnace by the standards of ASTM E1755, E872. The chemical composition analysis is based on a standard method of NREL (National Renewable Energy Laboratory, U.S. Department of Energy).

Table 3.2- Properties of spruce and poplar on dry basis

Analysis name	Composition	Spruce	Poplar
Proximate analysis (wt.%)	Volatile	84.93	86.29
	Ash	0.29	0.37
	Fix carbon	14.77	13.34
Ultimate analysis (wt.%)	C	47.07	48.06
	H	5.97	5.95
	O	43.65	43.76
Chemical composition (wt.%)	Cellulose	42.49	44.68
	Hemicellulose	14.89	13.02
	Lignin	31.59	24.44

3.2 Pyrolysis experiment

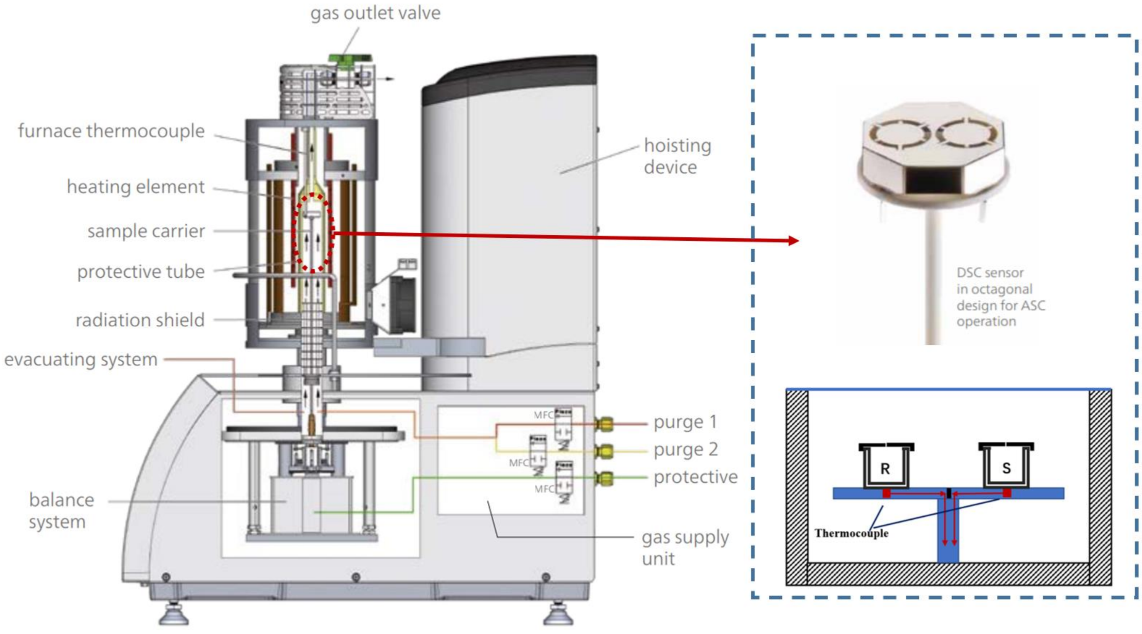

Thermal Gravimetric Analyzer (TGA) **Sample carrier**

Figure 3.2- Thermal gravimetric Analyser used in the present work: STA 449 F3 Jupiter, NETZSCH. (partial figures are taken from the website of the instrument manufacturers [195])

Thermogravimetric (TG) and differential scanning calorimetry (DSC) are detected simultaneously in the TGA (STA 449 F3 Jupiter, NETZSCH). As shown in figure 3.2, it mainly consists of a furnace, a sample carrier, a gas system, and a balance system. The mass resolution is 0.1μg and the heat flux resolution is 1μW. The high-performance furnace (steel furnace, -150 °C to 1000 °C, heating rates up to 1000 °C /min) is designed to impose an accurate time-temperature profiles to the sample. Under the plateau of the sample carrier, two thermocouples allow both the temperature control and the acquisition of the DSC signal. The gas system comprises three gas inlets for the furnace and the balance system: the protective gas (N_2, 99.999%) is devoted to protect the balance from temperature and volatiles, inlets 1 and 2 control the gas flow rate in the furnace and allows the reaction atmosphere to be chosen and modified during the experiment. Before any test, the calibrations of both TG and DSC are mandatory. They are realized by standard materials that are homogenous and stable with accurate certified values. Detection signals of experimental conditions are matched with quantifications of standard materials as closely as possible. A series of standard material (NETZSCH calibration set) will be tested covering the full temperature range of measurement protocol, including indium, tin, bismuth, zinc, aluminium, and silver. Also, blank test will be conducted before every experiment with the same crucible to exclude buoyancy effects and thermal drift.

Two types of temperature programs will be applied: static and dynamic. Their profiles are shown in figure 3.3. All test starts with a drying period at 100°C for 30 minutes. Then, the static program raises the temperature at 10 °C/min up to the plateau temperature, and maintains the isothermal stage for two hours. A series of tests are performed from 250 °C to 500 °C by 50 °C increments (250, 300, 350, 400, 450, 500 °C).

After the drying stage, the dynamic program raises the temperature to 800 °C at a constant heating rate. Four different rates were used here (1 °C/min, 2 °C/min, 5 °C/min and 10 °C/min).

To conduct the parameter estimations based on fitting methods, the data sources are therefore very demanding to cover multiple kinetic scenarios. The multiple heating rates and high final temperature in dynamic tests cover a wide range of temperature/residence time pathways, these dominant coverages on pyrolysis kinetics could serve as solid learning database for parameters identification [196]. On the other hand, the temperature levels from 250 °C to 500 °C represent different pyrolysis degrees from initial to complete. Together with the unique long isothermal stages, they constitute a demanding database for validation purposes.

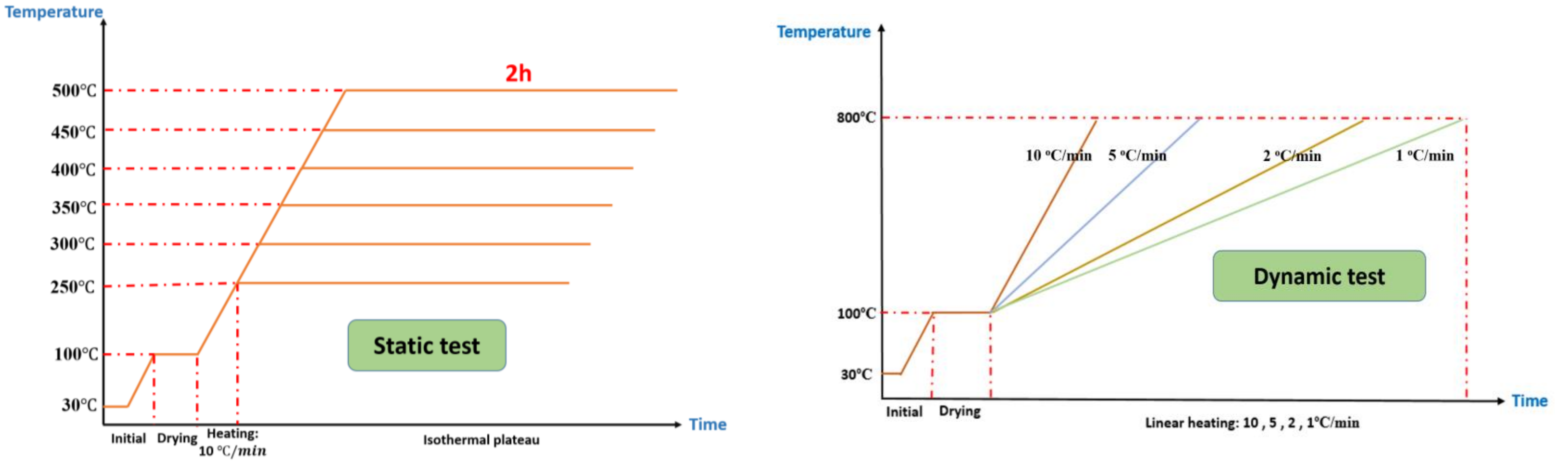

Figure 3.3- Temperature profiles for static (left) and dynamic (right) tests

Chapter 4 Optimal strategy to choose the number and shape of DAEM distributions

This chapter proposes a rigorous strategy to propose a good trade-off of number and shape of DAEM distributions. Rigorous identification/validation processes were quantified and further plotted as a function of the number of degrees of freedom, which allowed comprehensive comparisons in terms of prediction ability and numerical complexity. The best trade-offs in both distribution number and shape were therefore obtained hereafter. The strategy of two Gaussian + one exponential was proved to be the best compromise. It is therefore recommended for further studies and, consistently, applied to the rest of this PhD work.

- This work is published in **Energy Conversion and Management** [197].

Multiple-distribution DAEM modelling of spruce pyrolysis: an investigation of the best trade-off regarding the number and shape of distributions

Yong TIAN[a,*], Patrick Perré[a,b]

[a] LGPM, CentraleSupélec, Université Paris-Saclay, 3 Rue Joliot Curie, 91190 Gif-sur-Yvette, France

[b] LGPM, Centre Européen de Biotechnologie et de Bioéconomie (CEBB), 3 Rue des Rouges Terres, 51110, Pomacle, France

[*]Corresponding author.

E-mail address: Yong.Tian@centralesupelec.fr (Yong TIAN), patrick.perre@centralesupelec.fr (Patrick Perré)

Abstract

The distributed activation energy model (DAEM) is a widely used, accurate and robust method to model biomass pyrolysis. However, the appropriate numerical strategy in terms of distribution number and shape has not been systematically determined. This study analysed spruce powder pyrolysis under different scenarios of multiple-distribution DAEMs with symmetric/asymmetric distributions (Gaussian, logistic and exponential) and different distribution numbers. Dynamic tests at four heating rates (1, 2, 5 and 10 °C/min up to 800 °C) provided solid numerical learning database, and the optimization of residues between numerical calculation and database enabled identification of model parameters. Subsequently, validation was performed with static tests (250 to 500 °C with an interval of 50 °C and 2h-isothermal stages), and their corresponding residue analysis provided a fundamental basis to assess the model's true prediction ability. The trade-off between the model's prediction ability and degrees of freedom was robustly investigated with regard to the number and shape of the distribution. As stated by the quality of validations, a series of Gaussian-DAEMs (distribution number ranged from one to five) allowed for the determination of the best trade-off when the distribution number was three. Finally, the two-Gaussian plus one exponential distribution exhibited the best overall prediction capacity among different multiple-distribution DAEMs, and was confirmed as the best strategy with regard to both distribution shape and number. A DTG simulation investigated each model's simulation effects with three assigned variation sections and justified the correspondence between pseudo-components and biomass constituents. Finally, the DAEM's capability to distinguish the effects of heating rate was demonstrated.

Keywords: Pyrolysis, DAEM, Exponential distribution, Gaussian distribution, Trade-off

1. Introduction

Biomass pyrolysis receives substantial attention as a key thermal conversion technology in bio-refineries [198] in the production of high value-added chemicals (bio-oil, char and biogas). It also acts as the main initial process for gasification and combustion. The ability to predict constituent kinetics and thermal behaviours during pyrolysis are therefore of great importance, namely for reactor design and industrial scale-up. Thermogravimetric analysis (TGA) is an advanced technology used to study the pyrolysis mechanism relating to devolatilization, which also provides sufficient data for kinetic modelling [199].

Pyrolysis is a rather complicated process with numerous chemical reactions, traditional methods of global first- and second-order kinetics are not applicable to biomass pyrolysis [66], which encourages the development of more effective models. Among them, a lumped-kinetic model accounting for more than 30 species has been developed [26], and competitive multi-step models have helped include primary devolatilizations and homogeneous secondary reactions in biomass components [75]. The distributed activation energy model (DAEM) has been proposed to manage the complexity of chemical reactions [93]. In this approach, pyrolysis is assumed to proceed as independently parallel reactions with different activation energies, which are further described by distribution functions.

The DAEM has been proposed to be the most comprehensive model to represent the pyrolysis of various complex feedstocks including coal [200], oil shale [91], sewage sludge [92], and biomass [93]. Its prediction kinetics are believed capable of working as sub-models in further industrial simulations [201]. Multiple-distribution DAEM is able to represent major chemical constituents [202] or multiple reaction stages [75], contributing to precise simulations of kinetics. Three-distribution models are widely applied due to its comprehensiveness and excellent correspondence with hemicellulose, cellulose and lignin [79]. Meanwhile the choices of two [78], four [203] and five [108] distributions are also proposed.

Concerning the mathematical forms of distribution, continuous statistic distributions are normally applied [108]. Meanwhile finite discrete distribution is also employed, which introduces relations between activation energy and pre-exponential factor either with [204] or without functional forms [131]. Yet differences between these two distribution types could be basically limited, since continuous distributions are necessarily discretized for computational implementations.

While symmetric distributions such as Gaussian and logistic have been widely applied in DAEMs [2], asymmetric distributions have also attracted attentions, as partial reactivity distribution in pyrolysis tends to be asymmetric, notably during the final stages [93]. Asymmetric distributions, including Weibull and gamma, have been assessed in several studies. Lakshmanan [111] first employed a Weibull DAEM to describe the thermal-chemical kinetics of multiple types of biomass. Recently, Li [112] found the Weibull outperformed other distributions in a study of two- and three-distribution DAEMs in polymer pyrolysis testing of both symmetric and asymmetric distributions. Xu [3] compared single-distribution DAEMs to asymmetric gamma, Rayleigh and Weibull distributions, and found that kinetic parameters relied heavily on distribution form. Alok [205] used asymptotic expansion for gamma distribution’s numerical integral in a DAEM, yet the simulation effect was poor. Gamma distribution offers a wide range of shapes that are capable to fit various kinetic profiles. In the decomposition context, its rate parameter measures the average life-time of active component [206], while its shape parameter endows multiple forms. Exponential distribution, as the degeneracy of gamma, shows particular features in lifetime distribution, stochastic process in general [207] and reliability analysis [208]. However, to the best of our knowledge, it has never been employed in multiple-distribution DAEM.

The application of multiple-distribution DAEMs has usually focused on the corresponding distribution number with equal pseudo-components or multiple-stage processes [100, 109], yet the effects of distribution number on prediction ability and numerical complexity have received little attention. Indeed, the increase of the distribution number in DAEMs could improve accuracy [108], as more subtle details might be captured in addition to the reaction kinetics. However, the simultaneous growth in numerical complexity could substantially endanger model robustness. Furthermore, the determination of parameters would face local minima or even be meaningless after model identification [209]. On the other hand, single- distribution DAEM shows insufficiency for biomass pyrolysis. In particular, single-Gaussian was found inappropriate to reproduce DTG data [108], and more than one logistic distribution was required for kinetic description [102]. Therefore, regarding the choice of distribution number, a trade-off between a model's prediction capacity and degrees of freedom should be seriously considered.

In previous studies, kinetic parameters have generally been determined by single non-isothermal experiments, which introduce the risks of local minima or compensation effects [2]. In this context, multiple experimental data have been proposed to reduce parameter uncertainties, especially those of activation energy and pre-exponential factors [125]. Pyrolysis profiles with two or more heating rates have been proved effective to distinguish between kinetic models [66], and they could mitigate the compensation effect and more closely resemble operations in a genuine industrial system.

Generally, identification of model parameters has been based on the principle of minimizing residues between numerical calculations and the learning database, during which advanced optimization algorithms are applied such as the pattern search method [99], differential evolution algorithm [210] and genetic algorithm [211]. Beyond the pursuit of high accuracy and efficiency during model identification, the more important model validations should be emphasized to assess the model's true fit qualities under different reaction conditions. Várhegyi [113] evaluated prediction ability at 40 °C/min with model determined at 4 °C/min. Scott [212] extrapolated kinetic parameters that were identified at 20 °C/min and 30 °C/min to the theoretical curve at 10000 °C/min. Lin [213] performed predictions for 15 °C/min and 25 °C/min with the model that was identified at 20 °C/min. Nonetheless, solid validations with quantifiable uncertainties were relatively rare. Only recently, Ahmad [214] applied artificial neural network (ANN) for validating DAEM accuracy with histogram error distribution. And error analyses, in forms of absolute percentage error (MAPE) and root mean square error (RMSE), were employed in predicting mass loss at different heating rate [215] and biomass type [216] for validation purposes. On the other hand, the kinetic triplets (activation energy, pre-exponential factor and reaction rate) are barely verified since the multiple temperature profiles of parameter determinations couldn't be identical for prediction tests [217]. However, to assess the true model applicability in pyrolysis kinetics, it is logical and necessary to test the fitted parameters against reaction conditions that are different from those used for identification. Therefore, validation with additional temperature profiles should be conducted.

This work aims to assess the applicability of the multiple-distribution DAEM considering distribution shape (symmetry/asymmetry), and distribution number using a rigorous approach. To that purpose, a set of dynamic tests were used as learning database and a completely different dataset, consisting of static tests over a wide range of plateau temperatures, was used as a validation database. The best trade-offs between the number of degrees of freedom and the prediction quality will be determined by using up to five-Gaussian distributions. The choice of distribution shape will be tested with two extra DAEMs (three-logistic and two Gaussian + one exponential). Performance of the distributions and its correspondence with biomass constituents will be studied in the subsequent DTG simulations. Finally, DAEM's performance in distinguishing the effect of the heating rate will be analysed.

2. Material and methods

2.1 Material

The biomass used in this study is European spruce (*Picea abies*), a softwood species. A 73-year-old tree was originally cut from the Auvergne region, France and subsequently processed to samples. A tree log 40–50 cm in diameter, 2 m in length was cut 2 m above the bottom. It was cut axially into 2.5-cm thick boards, and a portion 10 cm from the centre was taken to make samples for pyrolysis analysis. A rectangular column 2.5×2.5×5 cm^3 was cut from the healthy sapwood part of the board, where wood properties were relatively uniform. It was first sliced and ground in a cutting mill (RETSCH SM300) with a bottom sieve of 1 mm trapezoidal holes, followed by additional grinding with a universal mill (M20-IKA). A sieve stack of 0.063 mm and 0.08 mm opening sizes was used for sieving wood powder in a vibratory sieve shaker (RETSCH AS 200) at an amplitude of 90 % for 30 min. The sieved wood powder between 0.063–0.08 mm was dried at 105 °C for 24 h and stored in a desiccator.

Table 1 lists the basic chemical information of sprue sample. The ultimate and proximate analyses of the wood sample (density 450 kg/m^3) on a dry basis were conducted using a Thermo Fisher Scientific FLASH 2000 organic elementary analyser and Nabertherm LV/9/11 furnace, respectively, following the ASTM E1755 and E872 standards. The chemical composition analysis was based on the standard method of NREL (National Renewable Energy Laboratory, U.S. Department of Energy).

Table 1. Results of proximate, ultimate and chemical composition analyses of European spruce powder on a dry basis

Proximate analysis (wt.%)			Ultimate analysis (wt.%)			Chemical composition (wt.%)		
Volatile	Ash	FC	C	H	O	Cellulose	Hemicellulose	Lignin
84.93	0.29	14.78	47.1	6.0	43.7	42.49	14.89	31.59

2.2 Experimental method

Pyrolysis of spruce powder was performed in a thermogravimetric analyser (TGA, STA 449 F3 Jupiter, NETZSCH). TG signals were detected at data acquisition intervals of 0.1 min. For each test, a ca. 10-mg sample was evenly spread in an alumina crucible. Measurements were conducted under a pure nitrogen (99.999%) purge and protective gases at 50 ml/min and 20 ml/min, respectively.

Dynamic tests consisted of four different heating rates (1 °C/min, 2 °C/min, 5 °C/min and 10 °C/min) during the pyrolysis stages. The entire temperature program started by increasing the temperature from 30 °C to 100 °C at 10 °C/min, then maintaining it for 30 min to eliminate the residual bound water present in sample. The temperature was linearly increased to 800 °C at the four aforementioned heating rates, then cooled to room temperature under the nitrogen purge. The thermogravimetric data from dynamic tests were set as a learning database for the subsequent model identification process.

Static tests served as a model validation database. Similar to the dynamic tests above, the wood sample was heated from 30 °C to 100 °C at 10 °C/min and held for 30 min. Then the temperature was raised to the plateau at 10 °C/min, and an isothermal period maintained at this value for 2 h. A series of tests were performed from 250 °C to 500 °C in 50 °C increments (250, 300, 350, 400, 450, 500 °C).

Temperature and sensitivity calibrations were performed in advance with standard materials specific to crucible type, temperature rate and gas type. The certified standards (NETZSCH calibration set) include indium, tin, bismuth, zinc, aluminium and silver. A blank was analysed before every test with the same crucible to exclude buoyancy effects and thermal drift. Dimensionless residual mass (DRM) and conversion rate (X_{exp}) were used to manage TG signals as:

$$DRM(t) = \frac{m_t}{m_0} \times 100\% \,, \qquad X_{exp}(t) = 1 - DRM(t) \tag{1}$$

in which m_t is the remaining mass at time t, and m_0 the dry mass, determined as the mass after the 30-minute plateau at 100 °C.

All dynamic and static tests were repeated twice to ensure accuracy. Standard deviations (SD) of all DRM data between two duplicate tests were calculated for verifications, herein table 2 lists two indexes: mean and maximum values of SD. The mean values got very limited range between 0.12% to 0.48%, and the maximum values that represented severe situation, was ranged between 0.30% to 1.81%. They both provided solid proofs of small errors between two duplicates and ensured the repeatability of experimental data.

Table 2. Mean and maximum values of standard deviations (SD) of DRM values in duplicate tests

Values of SD	Static test						Dynamic test			
	250 °C	300 °C	350 °C	400 °C	450 °C	500 °C	1 °C/min	2 °C/min	5 °C/min	10 °C/min
Mean (%)	0.46	0.13	0.12	0.47	0.48	0.29	0.33	0.26	0.41	0.32
Maximum (%)	0.88	0.30	1.61	1.12	0.73	0.44	1.30	0.98	1.32	1.81

3. Model formulation

3.1 DAEM formulation

The distributed activation energy model (DAEM) treats biomass pyrolysis as numerous parallel and irreversible first-order reactions, among them, decomposition rate of reaction i is：

$$\frac{dV_i(t)}{dt} = k_i\big(V_i^{\infty} - V_i(t)\big) \tag{2}$$

in which V_i^{∞} represents maximum volatile production from reaction i, and $V_i(t)$ is the generated volatile at time t. Reaction rate constant k_i is defined by the Arrhenius equation with the pre-exponential factor (A_i) and activation energy (E_i):

$$k_i = A_i exp\left(-\frac{E_i}{RT(t)}\right) \tag{3}$$

in which R is a universal gas constant and $T(t)$ is the temperature at time t. A_i is assumed as constant (A) for all reactions, $V(t)$ is the total volatile production at time t, and statistical distribution $f(E)$ describes the activation energy, resulting in the integral form of conversion degree $X(t)$:

$$X(t) = \frac{V(t)}{V^\infty} = 1 - \int_0^\infty exp\left(-\int_{t_0}^{t} Ae^{-E/RT(t)}dt\right) f(E)dE \tag{4}$$

Wood is treated as the sum of multiple pseudo-components without any interactions during pyrolysis. Distributions $f_j(E)$ with a different weighting factor $V_{max}(j)$ are assigned to the pseudo-component j in wood ($j \in [1{:}N_d]$), N_d is the total number of distributions. Superposition of their volatile productions provides the final formulation of biomass conversion degree as:

$$X(t) = 1 - \sum_{j=1}^{N_d} V_{max}(j) \int_0^\infty exp\left(-A\int_0^t e^{-E/RT(t)}dt\right) f_j(E)dE \tag{5}$$

3.2 Distribution functions and mathematical implementation

Two common symmetric distributions, Gaussian and logistic distributions, and one asymmetric distribution, gamma distribution, were used in this study. These distributions in DAEM could represent physically the atomic interactions caused by the variability of macromolecules and their interaction in the cell wall [94]. Table 3 summarizes their mathematical formulas of probability density function (PDF), mean value and standard deviation. Their representative curves are depicted in Figure 1. Gaussian distribution, also known as normal distribution, is formulated by its mean value (E_0) and standard deviation value (σ). Its PDF curve is symmetrical and bell-shaped. Logistic distribution is another important symmetric probability distribution. It resembles Gaussian distribution but has heavier tails (larger kurtosis value) and thinner peaks around the mean value. The gamma distribution is defined by the shape parameter α and the rate parameter β. A minimum activation energy (E_{min}) must be added to obtain sufficient degrees of freedom to define the kinetics. The factor $\frac{E-E_{min}}{E_{min}}$ therefore scales the gamma distribution. The flexibility of the gamma distribution can produce different curve shapes by suitable combinations of its two parameters. For instance, when $\alpha = 1$, the gamma distribution becomes an exponential distribution; when $\alpha = \frac{k}{2}$ (k is nature number) and $\beta = 0.5$, it becomes a Chi-squared distribution.

Table 3. Three types of distribution used in the research

Distributions	PDF	Mean	Standard deviation
Gaussian	$\mathrm{f(E)} = \frac{1}{\sigma\sqrt{2\pi}} exp\left[-\frac{(E-E_0)^2}{2\sigma^2}\right]$	E_0	σ
Logistic	$\mathrm{f(E)} = \frac{\pi}{\sqrt{3}\sigma} \frac{exp\left[-\frac{\pi(E-E_0)}{\sqrt{3}\sigma}\right]}{\left\{1+exp\left[-\frac{\pi(E-E_0)}{\sqrt{3}\sigma}\right]\right\}^2}$	E_0	σ
Gamma	$\mathrm{f(E)} = \frac{\beta^\alpha \left(\frac{E-E_{min}}{E_{min}}\right)^{\alpha-1} exp\left(-\beta\frac{E-E_{min}}{E_{min}}\right)}{\Gamma(\alpha)}$	$\left(\frac{\alpha}{\beta}+1\right)E_{min}$	$\frac{\sqrt{\alpha}}{\beta}$

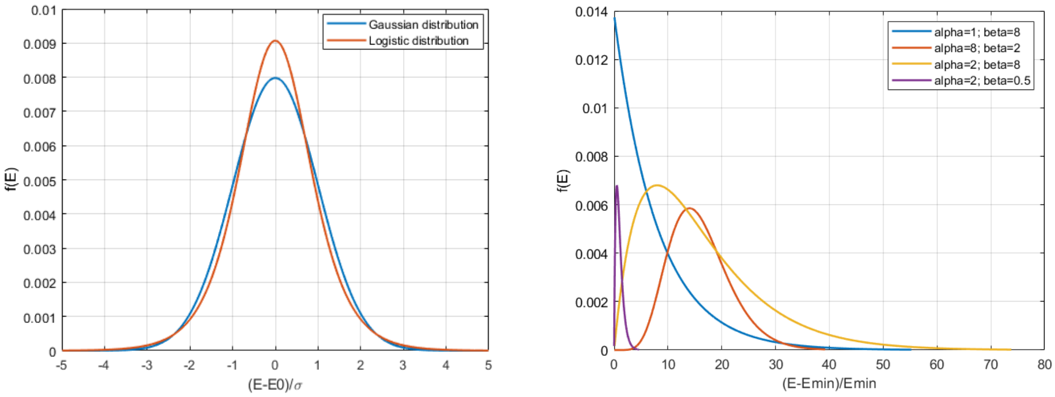

Figure 1. Examples of Gaussian, logistic distributions (left) and gamma distributions (right) with different parameters

Applying the aforementioned distributions into DAEM, the double integration (over time and energy) and the lack of an exact analytical solution required multiple precautions. Mathematical implementations were realized using the in-house MATLAB codes, including numerical discretization and integral approximation. The detailed formulation is shown hereafter.

(a) Gaussian distribution

In the discretization of Gaussian distribution, the domain $(-\infty, +\infty)$ changed to finite intervals as $[E_0 - n\sigma, E_0 + n\sigma]$, in which $n = 3$ to ensure 99.9% area coverage (figure 1). Each interval length σ was evenly divided by m to generate fine increments: $dE = \frac{\sigma}{m}$. Prior trials had determined the proper choice of increment number since it might cause solution oscillation with small values and long calculation time with large values [218]. $m = 10$ was found as good compromise for both correct representation of continuous function and concision in algorithm, the discretized activation energy for reaction i became:

$$E_i = E_0 - n\sigma + (i - 0.5)dE, \qquad i = [1, 2mn] \tag{6}$$

The discrete form of Gaussian distribution was therefore presented as:

$$f(E_i) = \frac{1}{\sigma\sqrt{2\pi}} \exp\left(-\frac{(E_i - E_0)^2}{2\sigma^2}\right) \tag{7}$$

(b) Logistic distribution

As in symmetrical distribution, finite intervals $[E_0 - 3\sigma, E_0 + 3\sigma]$ were enough for logistic distribution to ensure 99.9% area coverage. The discretization strategy of activation energy E_i was the same as equation 6, and its discretized function was expressed as

$$f(E_i) = \frac{\pi}{\sqrt{3}\sigma} \frac{exp\left[-\frac{\pi(E_i - E_0)}{\sqrt{3}\sigma}\right]}{\left\{1 + exp\left[-\frac{\pi(E_i - E_0)}{\sqrt{3}\sigma}\right]\right\}^2} \tag{8}$$

(c) Gamma distribution

Compared to common symmetric distribution, asymmetric gamma distribution had more complicated numerical implementations. The concepts of minimum (E_{min}) and maximum values (E_{max}) described the discretized activation energy. They formed a finite function domain to avoid extremely large energies which were impossible to appear in decomposition reactions.

$$E_{max} = E_{min} \cdot \left(1 + \frac{n\alpha}{\beta}\right) \tag{9}$$

Here $n = 5$ was set to ensure a distribution function with good representation and extended in reasonable ranges. Equal partitioning of the whole interval by n_g produced fine increments dE:

$$dE = \frac{(E_{max} - E_{min})}{n_g} \tag{10}$$

in which the fine interval number n_g was set as 100 to ensure accuracy as well as short solution time. Then gamma distribution discrete normalization form was obtained:

$$f(E_i) = \frac{\beta^{\alpha}\left(\frac{E_i - E_{min}}{E_{min}}\right)^{\alpha-1} exp\left(-\beta\frac{E_i - E_{min}}{E_{min}}\right)}{\Gamma(\alpha)} \tag{11}$$

The term $\left(\frac{E_i - E_{min}}{E_{min}}\right)^{\alpha-1}$ in gamma distribution demanded preliminary determinations of discrete strategy, for instance, sudden mutations occurred when α becomes less to the unit, which produces infinite value at zero ($E_i = E_{min}$), and invalidates the numerical value at the zero point. Careful prerequisite determinations had been performed which indicated the optimal choice of the exponential distribution, a degeneracy of gamma, to facilitate model implementation. The detailed determination process could be found in supporting materials. Finally, numerical discretization in exponential distribution can be decided as:

$$E_i = E_{min} + (i - 0.5)dE, \qquad i = [1, n_g] \tag{12}$$

$$f(E_i) = \beta exp\left(-\beta\frac{E_i - E_{min}}{E_{min}}\right) \tag{13}$$

For every distribution, the characteristic time-constant of the distribution reduced with the increasing temperature level. For the smallest values of the activation energies, a simple first-order derivative might fail [219]. To avoid the difficult problem of checking the time-step for all activation energy values, the effective increment of chemical reaction dV_i was computed using the exact exponential form [220, 221]:

$$dV = \sum_{j=1}^{N_d}\sum_{i=1}^{N_p}\left[1 - exp\left(-k_i^j dt\right)\right](V_i^{j,\infty} - V_i^j(t)) \tag{14}$$

$$k_i^j = A\exp\left(-\frac{E_i^j}{RT(t)}\right);\qquad V_i^{j,\infty} = V_{max}(j)\cdot m_0\cdot f_j\left(E_i^j\right);\quad V_i^j(t=0)=0 \tag{15}$$

in which N_d is the number of distributions, N_p is the number of increment points in each distribution. E_i^j is the ith activation energy in distribution j. $f_j\left(E_i^j\right)$ were determined only once according to the numerical implementations of every distribution at the initialization stage of the simulation. During the time-increment, the values of $V_i^j(t)$ were updated and stored in the calculation loop within the numerical domain. The updated conversion rate $X(t)$ at time t was finally obtained as follows:

$$X(t) = 1 - \frac{\sum_{j=1}^{N_d}\sum_{i=1}^{N_p}\left\{\left[1-exp\left(-k_i^j dt\right)\right](V_i^{j,\infty} - V_i^j(t))\right\}}{m_0} \tag{16}$$

Parameter identification was based on the optimization of the objective function, *OF*, which was the residual sum of squares (RSS) between experimental and calculated conversion rates of all data points alongside the entire reaction history:

$$OF = \sum_{a=1}^{N_{exp}}\sum_{t=0}^{t_f}\left(X_{exp}(t) - X(t)\right)^2 \tag{17}$$

in which N_{exp} is the total number of experimental data and t_f is the final reaction time. Here four dynamic tests were analysed simultaneously as a learning database. This wide range of temperature-time pathways together with the large temperature range ensured quasi-complete pyrolysis was likely to provide an accurate and robust parameter determination. Regarding the different number and shape of distributions, their initial parameters were reasonably derived from the relevant literature [93, 94, 96, 100, 222] to avoid local minima in the optimization algorithm. A derivative-free method of the simplex searching algorithm was adopted, and sufficient iterations ensured successful identification by ending with no difference between the penultimate and final optimization values. The whole protocol therefore consists of the following steps: i) choosing a set of reasonable initial parameters, ii) automatic minimization algorithm, iii) perturbation of model parameters to check the robustness of the solution. If a better solution is found at stage iii), steps ii) and iii) are repeated until a stable solution is found.

To assess the effect of distribution number, a series of Gaussian-DAEMs was proposed with the distribution number ranging from one to five. Concerning the shape of distributions, three-logistic DAEM and two-Gaussian + one exponential DAEM were further proposed. Herein, only one asymmetric exponential distribution was introduced since it was enough to focus on the performances of high-temperature reactions and provided sufficient flexibility in the model [66].

To measure the discrepancy between experimental data and model simulations, two evaluation indexes were applied: root mean square error (RMSE) and the maximum deviations (D_m). They had the same meaning to DRM, aiming to provide comprehensive views on the average and maximum errors in both model identification and validation phases.

$$RMSE = \frac{\sqrt{\sum_{a=1}^{N_{exp}} \sum_{t=0}^{t_f} \left(X_{exp}(t) - X(t)\right)^2}}{N_{exp}} \tag{18}$$

$$D_m = Max\left|X_{exp}(t) - X(t)\right|, \ \ \forall t \in \left[0, t_f\right] \tag{19}$$

For the assessment in DTG simulations, dimensionless DTG was defined as the ratio between real-time DTG signal ($\frac{dm}{dt}$) and initial anhydrous mass (m_0):

$$DTG(t) = \frac{1}{m_0} \frac{dm_t}{dt} \tag{20}$$

Its local residue $\left(R_L(t)\right)$ was defined by the differences between calculated ($DTG_{cal}(t)$) and experimental values $DTG_{exp}(t)$:

$$R_L(t) = DTG_{cal}(t) - DTG_{exp}(t) \tag{21}$$

With its standard deviation of residue as:

$$\sigma_R = \sqrt{\frac{1}{t_f - 1} \sum_{t=0}^{t_f} (R_L(t) - \overline{R_L})^2} \tag{22}$$

4. Results and discussions

4.1 Determination of distribution number

Figure 2 shows the effects of Gaussian distribution number on both identification and validation stages. Initial sections of DRM curves in identifications were magnified here for comparison among five models; usually, they were challenging to describe numerically because of their very slow kinetics and absence of asymptotic behaviour [223]. In terms of identification stages, one-Gaussian presented very poor overlaps due to its limitations in describing the nature of multiple clusters of reactions [202]. Two-Gaussian demonstrated a slight improvement, yet several noticeable errors still occurred, and the initial stages were poorly produced. For the distribution number from three to five, simulations exhibited quasi-perfect agreements with all experimental data, where most overlaps indicated successful identification. The increase in distribution number represented the increase of pseudo-components, an advanced description strategy of thermal features in multi-step reactions [108]. This was further evidenced by the improved simulation accuracy in initial sections, in which error reduction could be observed by increasing distribution number, and almost complete overlap could be realized by five-Gaussian DAEM.

For the validation stages, one-Gaussian showed poor predictive ability at all temperature levels, and two-Gaussian also performed unsatisfactorily, with obvious errors from 250 to 350 °C. The three-, four- and five-Gaussian showed similarly good predictive abilities, demonstrating excellent overlap during heating periods and only slight deviations in the isothermal plateaus. Major deviations occurred on the curves of 300 °C and 350 °C, while at the other temperatures, the models showed very good predictive abilities throughout the experiments.

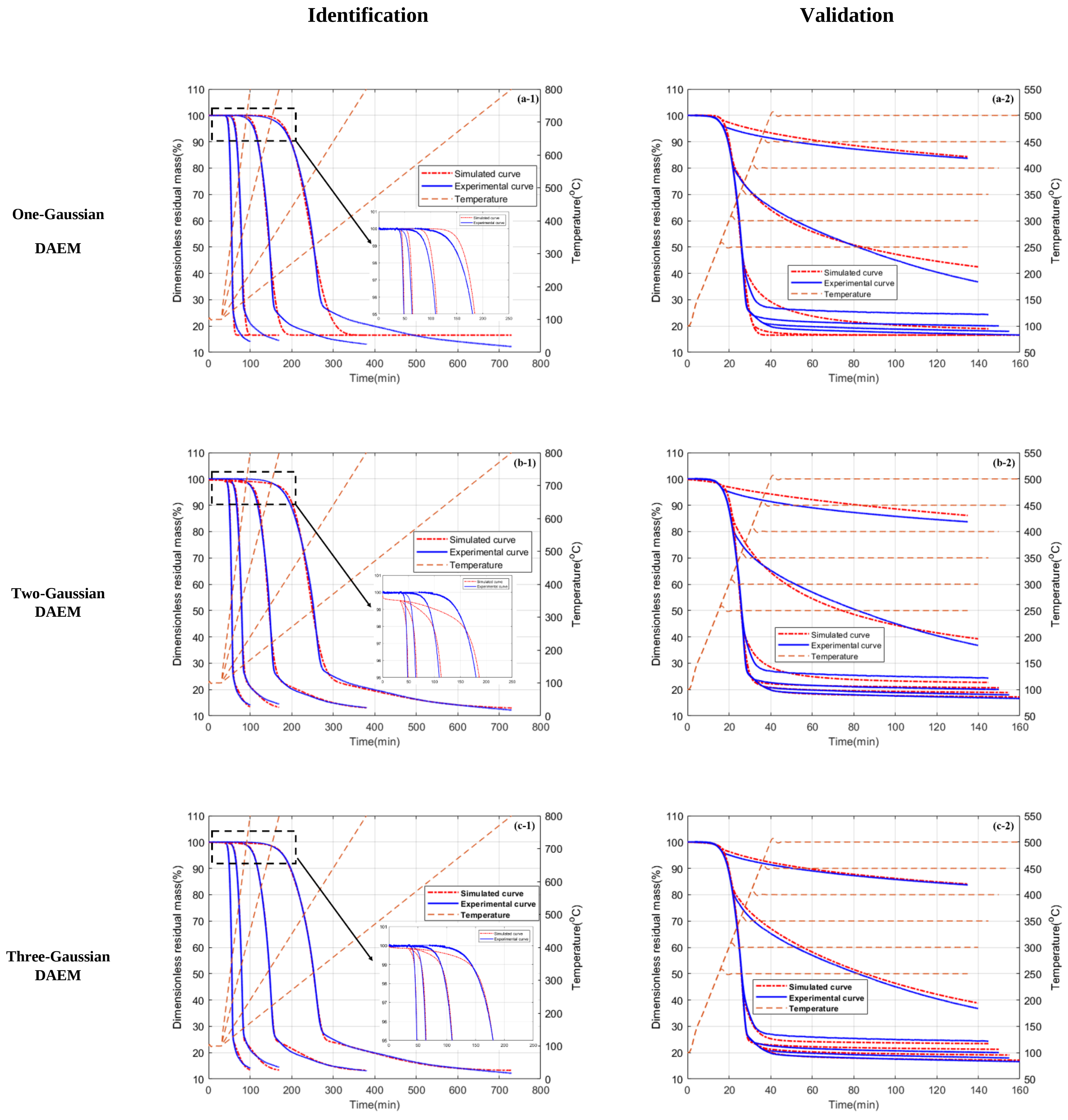
Identification
Validation
One-Gaussian
DAEM
Two-Gaussian
DAEM
Three-Gaussian
DAEM
(a-1)
(a-2)
(b-1)
(b-2)
(c-1)
(c-2)
Simulated curve
Experimental curve
Temperature
Dimensionless residual mass(%)
Temperature(°C)
Time(min)
110
100
90
80
70
60
50
40
30
20
10
0
200
300
400
500
600
700
800
550
450
350
250
150
120
140
160

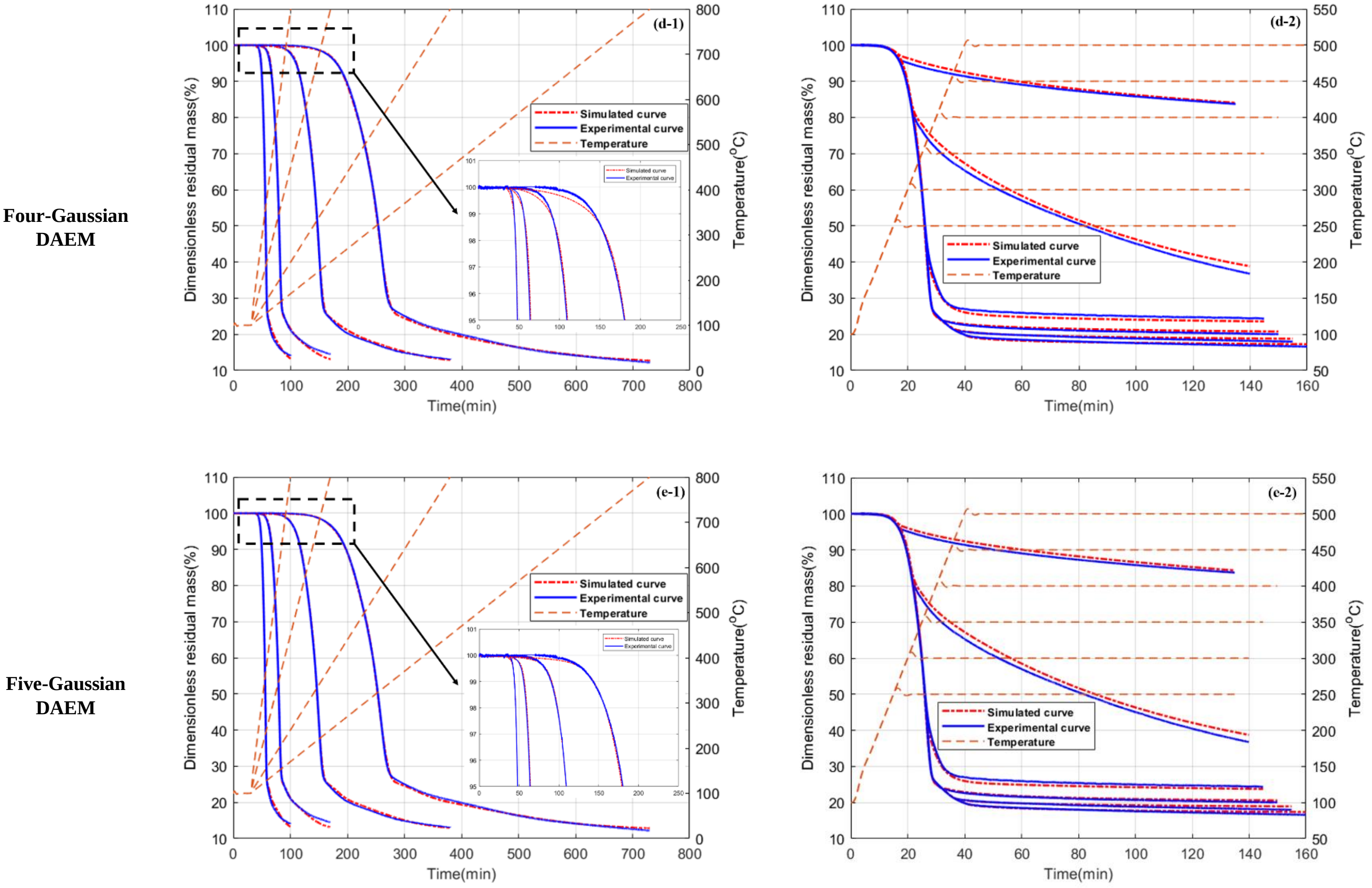

Figure 2. DRM curves of identification and validation stages and corresponding simulation curves based on identified parameters in multiple Gaussian DAEMs

(a) one-Gaussian DAEM, (b) two-Gaussian DAEM, (c) three-Gaussian DAEM, (d) four-Gaussian DAEM and (e) five-Gaussian DAEM

Identified parameters of five types of Gaussian DAEMs are listed in Table 4. The sum of weighting factors in each model ranged from 0.8345 to 0.8769, which reflected the total content of decomposable species in wood. For one-Gaussian DAEM, its coverage of activation energy was obviously incomplete due to the limitation of distribution number. The two-Gaussian DAEM introduced two distinct distributions that functioned in both low and high activation energy zones. The further increase of distribution number in three-, four- and five-Gaussian DAEM achieved more precise ranges of activation energy. Furthermore, complicated repartitions and interactions emerged among multiple distributions. For example, third and fourth Gaussian distributions were partially overlapped in four-Gaussian DAEM, and the first and second distributions interacted in five-Gaussian DAEM.

Table 4. Identified model parameters of five multiple-Gaussian DAEMs

DAEM type	Distributions	V_{max}	$A(\times 10^{13} s^{-1})$	E_0 (kJ/mol)	σ (kJ/mol)
One-Gaussian	1st Gaussian	0.8345	1.56	183.78	10.59
Two-Gaussian	1st Gaussian	0.7153	0.36	175.70	6.74
	2nd Gaussian	0.1574		215.68	54.00
Three-Gaussian	1st Gaussian	0.2125	1.37	170.82	5.77
	2nd Gaussian	0.5001		185.28	1.31×10^{-9}
	3rd Gaussian	0.1553		224.67	45.80
Four-Gaussian	1st Gaussian	0.1660	1.75	170.90	4.21
	2nd Gaussian	0.4954		186.02	6.99×10^{-7}
	3rd Gaussian	0.1205		190.40	25.91
	4th Gaussian	0.0950		259.17	49.18
Five-Gaussian	1st Gaussian	0.0583	1.70	162.40	6.05
	2nd Gaussian	0.1347		172.05	5.74×10^{-3}
	3rd Gaussian	0.5284		185.87	4.01×10^{-4}
	4th Gaussian	0.0347		208.19	6.64
	5th Gaussian	0.1182		244.74	49.57

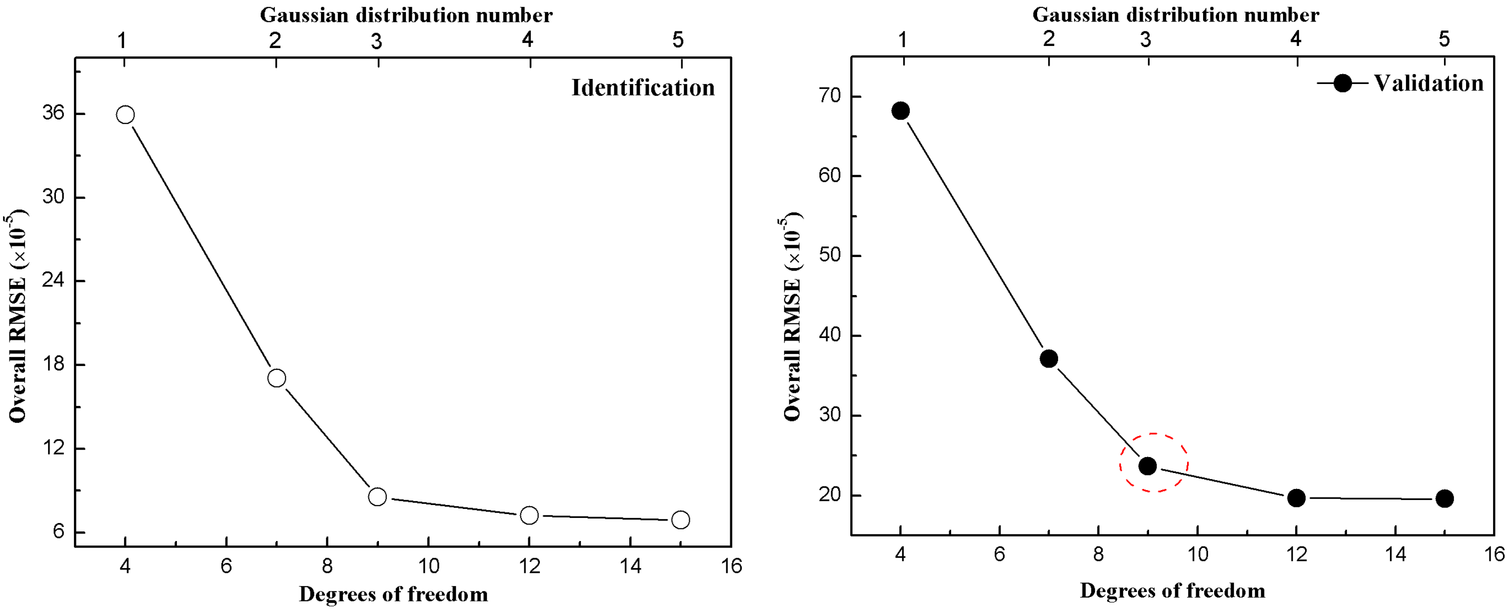

Figure 3. Relationships between the model's degrees of freedom and overall RMSE in identification and validation of multiple-Gaussian-DAEM

Figure 3 shows the correlations between multiple-Gaussian DAEM's degrees of freedom (D_f) and overall values of RMSE in both identification and validation stages. Followed by the increase of the degrees of freedom, the overall RMSE initially decreased rapidly and then was stable, indicating that prediction ability was effectively improved by increasing the distribution number to three. Increasing the distribution number to four and five introduced limited improvements. A high value of D_f inevitably aggravated the numerical complexity, and a trade-off was, therefore, necessary with respect to the model's prediction ability and complexity. Using the one-Gaussian DAEM as a reference, the decrease ratios of overall residue were 45.59%, 65.40%, 71.20% and 71.36%, respectively, for two-, three-, four- and five-Gaussian DAEMs during the validation stage. Using the three-Gaussian model, the 'inflexion point' (as highlighted with a red circle) was where a significant improvement in prediction ability was gained with a relatively small increase in D_f. Even though further increasing distribution number could still promote prediction potential, the disadvantage was that one extra distribution introduced three more kinetic parameters. It was doubtless unnecessary to pursue very limited improvements at the expense of large complexity, or perhaps even worse, a decline in the model's robustness with complicated compensation effects [224]. In this context, the strategy of three Gaussian distributions was the best trade-off between model's complexity and prediction capability.

As for the identification process, proposed models showed similar matching relationships between D_f and RMSE, which also demonstrated the good trade-off of the three-Gaussian DAEM. Considering most studies have applied three-distribution DAEMs because they can correlate with main chemical constituents [75, 104], the trade-off strategy herein provides new support for using three distributions in a model.

4.2 Determination of distribution shapes

4.2.1 Three-distribution DAEMs

As a three-Gaussian model was determined to be the optimal choice among multiple-Gaussian DAEMs, its counterpart models, three-logistic and two Gaussian + one exponential DAEM, were analysed to determine the shape of the distribution (symmetry/asymmetry).

Identification and validation effects of all three-distribution DAEMs are compared in Figure 4. In the general view of identification stages for three models, as expected, simulations exhibited perfect agreements with all experimental data. Three-Gaussian and three-logistic DAEMs had similar negative deviations during the initial stages of simulations, and the two Gaussian + one exponential DAEM modified these plateaus with fewer errors. In the validation stage, the two Gaussian + one exponential DAEM showed noticeable improvements at 400, 450 and 500 °C compared to those of three-Gaussian and three-logistic DAEMs.

Identified parameters of three models are listed in Table 5. Combinations of distribution shapes made distinctive impacts on model parameters. Compared to the three-Gaussian DAEM, the three-logistic DAEM cut back its second and third weighting factors to compensate on the first. While in the two Gaussian + one exponential DAEM, the second distribution reduced its weighting factor to account for increased first and third distributions. This evident alteration was mainly caused by the third exponential distribution, which spread uniquely in the high activation energy zone due to its asymmetry, and required more weighting factors to more accurately represent chemical reactions at high temperatures. Moreover, all three models maintained their second distribution with the largest weighting factor and narrowest range; this pseudo-component could be correlated to the high content and crystalline nature of cellulose [225].

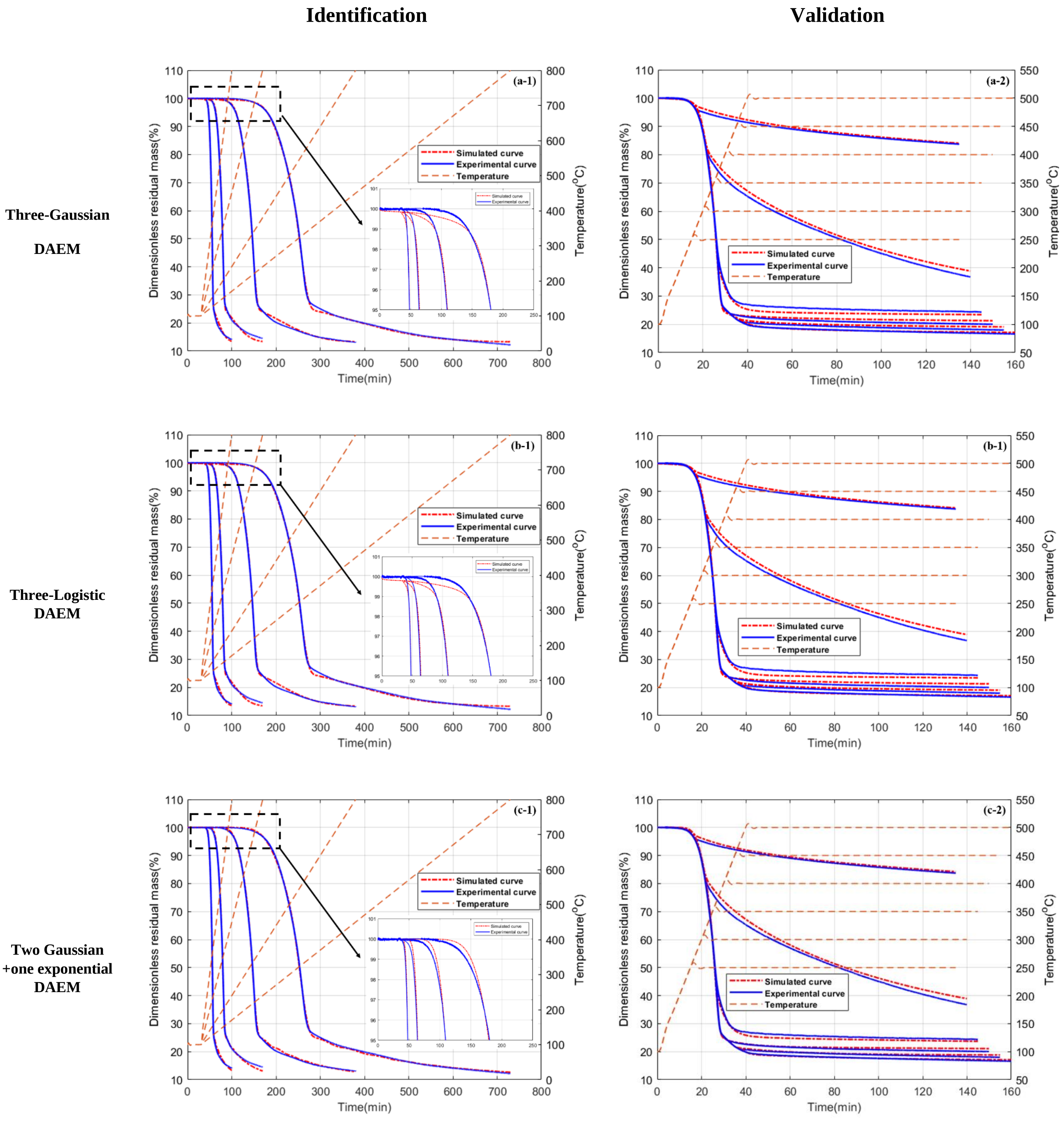

Figure 4. DRM curves of identification and validation stages and corresponding simulation curves of three types of DAEM

(a) three-Gaussian DAEM, (b) three-logistic DAEM and (c) two Gaussian+ one exponential DAEM

Cai [93] reviewed three-distribution DAEM in eight types of biomass, where parameter features were quite consistent with corresponding values herein. For instance, $E_{0,1}$ ranged between 169.71 kJ/mol to 186.77 kJ/mol which included our values; the narrowest ranging nature of second pseudo-component and the widest of the third were also confirmed here. Várhegyi [113] tested four biomasses with the three-parallel DEAM, showing similar kinetic parameters as presented in table 5, especially that $E_{0,2}$ (185 kJ/mol) almost equalled our identified parameters.

Table 5. Identified model parameters of three-distribution DAEM

DAEM type	Distributions	V_{max}	$A(\times 10^{13} s^{-1})$	E_0 or E_{min} (kJ/mol)	σ (kJ/mol)
Three-Gaussian	1st Gaussian	0.2125	1.37	170.82	5.77
	2nd Gaussian	0.5001		185.28	1.31×10^{-9}
	3rd Gaussian	0.1553		224.67	45.80
Three-Logistic	1st Logistic	0.2233	1.43	171.25	6.63
	2nd Logistic	0.4959		185.50	2.51×10^{-6}
	3rd Logistic	0.1496		227.80	48.87
Two Gaussian + one exponential	1st Gaussian	0.2816	1.67	173.19	8.79
	2nd Gaussian	0.4199		186.15	1.66×10^{-7}
	Exponential	0.1940		175.96	α=1, β=0.43

4.2.2 Overall model trade-offs

Table 6 and 7 list the values of RMSE and D_m among all proposed models during identification and validation stages, respectively. Herein, the individual and overall values of RMSE were distinguished by their different data number according to eq. 18. Since the one-Gaussian and two-Gaussian DAEMs had poor prediction abilities, they will not be discussed in detail hereafter. The hybrid model type (one Gaussian+ one logistic+ one exponential) was previously tested, but the numerical complexity and unobvious improvements in simulation quality didn't encourage us to make further investigations. But still we list its corresponding data in both table 6 and 7. The main comparisons will be made among the three-distribution

DAEMs (three-Gaussian, three-logistic, and two-Gaussian + one exponential), and four- and five-Gaussian DAEM.

For these models, their identification stages exhibited overall RMSE less than 9×10^{-5} and the maximum deviations were reasonably small (from 1.02 to 2.74%), acting as solid proof of successful identification. Fit qualities generally increased with a decrease in heating rates and the smallest D_m always appeared at 1 °C/min, possibly caused by the low fluctuation and stable temperature profiles at low heating rates, when thermal overshoot was less obvious [226]. The overall identification ability was in the order five-Gaussian > four-Gaussian > two Gaussian + one exponential > three-Gaussian > three-logistic. Among the three-distribution DAEMs, asymmetric exponential distribution improved identification accuracy, attributing to its capability of describing the unique behaviour at high temperatures.

Table 6: Parameter identification qualities in the dynamic tests with an average residual sum of squares and maximum deviations under each heating rate

DAEM type	RMSE ($\times 10^{-5}$)					D_m (%)			
	1°C/min	2°C/min	5°C/min	10°C/min	Overall	1°C/min	2°C/min	5°C/min	10°C/min
One-Gaussian	31.5	35.5	47.2	50.4	35.9	6.50	6.82	6.17	5.26
Two-Gaussian	12.2	17.1	27.9	33.6	17.0	4.16	4.86	4.66	4.29
Three-Gaussian	5.0	8.0	16.6	22.4	8.5	1.68	1.42	1.34	2.71
Four-Gaussian	4.0	6.6	14.4	20.7	7.2	1.21	1.56	1.44	2.59
Five-Gaussian	3.7	6.2	14.2	20.4	6.9	1.02	1.36	1.41	2.49
Three-Logistic	5.2	8.2	16.6	22.5	8.7	1.71	1.46	1.30	2.74
Gaussian + logistic + exponential	4.2	7.1	14.8	21.5	7.6	1.32	1.56	1.43	3.23
Two-Gaussian + one exponential	4.2	7.2	14.8	20.9	7.5	1.27	1.57	1.43	2.54

Table 7: Validation qualities in the static tests with an average residual sum of squares and maximum deviations under each heating rate

DAEM type	RMSE ($\times 10^{-4}$)							D_m (%)					
	250°C	300°C	350°C	400°C	450°C	500°C	Overall	250°C	300°C	350°C	400°C	450°C	500°C
One-Gaussian	3.9	6.5	9.7	9.9	6.5	4.3	6.8	2.22	5.71	5.45	5.06	5.09	5.14
Two-Gaussian	7.1	4.7	4.3	2.3	2.3	2.1	3.7	3.12	4.20	3.91	4.00	4.09	4.03
Three-Gaussian	1.8	3.9	3.4	2.3	1.9	1.0	2.4	1.29	2.20	1.99	1.46	1.54	1.51
Four-Gaussian	2.0	3.8	2.5	1.4	1.3	1.1	2.0	1.32	2.24	1.77	1.59	1.53	1.54
Five-Gaussian	2.3	3.9	2.2	1.1	1.4	1.1	2.0	1.12	2.05	1.76	1.50	1.47	1.44
Three-Logistic	1.8	3.9	3.4	2.3	1.9	1.0	2.3	1.22	2.17	2.01	1.42	1.51	1.48
Gaussian + logistic + exponential	1.6	4.1	2.4	1.7	1.3	1.1	2.0	1.22	2.34	1.84	1.73	1.68	1.69
Two-Gaussian + one exponential	1.5	3.8	2.4	1.7	1.3	1.0	1.9	1.22	2.36	1.67	1.60	1.70	1.67

In the validation of static tests, the models' true prediction potentials were therefore comparable and quantifiable at different temperature levels. The overall RMSE of five compared models ranged between 1.9×10^{-4} to 2.4×10^{-4}, which were plausibly low considering that model parameters originated from dynamic tests without any further identification. Maximum deviations were satisfactorily small in every validation stage of all models. The smallest value appeared at 250 °C (1.12% for five-Gaussian DAEM), and the largest value was at 300°C (2.36% for two Gaussian+ one exponential DAEM); such low values were considered good signs of prediction precision [79, 113]. The accuracy benefits from the comprehensive identification database and numerical training: these two indexes reflected excellent prediction potential for the five DAEM models.

Generally, the largest errors occurred at 300 °C and 350 °C among all validation phases, yet good fits were found at the other temperature levels. Because parameters were identified over the full pyrolysis condition up to 800 °C, they faced some difficulties in describing incomplete pyrolysis, even though the prediction remained rather good, and was in agreement with the literature [227] in which higher simulation errors tended to appear at low temperatures. The mass loss under mild pyrolysis at 250 °C was slow and, in addition, quite well predicted by the DAEM model. These two reasons explain the relatively small errors found for this test.

Among these models, overall prediction ability proceeded in the order of two Gaussian + one exponential > five-Gaussian > four-Gaussian > three-Gaussian > three-logistic.

Notably, the asymmetric exponential distribution exhibited excellent potential in predicting pyrolysis kinetics with plausible complexity: it provided the lowest RMSE values at 250, 300 and 500 °C, and most importantly, the lowest overall RMSE. Due to its asymmetry, exponential distribution expanded uniquely on the side of high activation energy, which only focused its accuracies in high-temperature reactions. In contrast, Gaussian and logistic distributions expanded symmetrically. When they intended to describe large ranges of high activation energies, the symmetry forced distribution to cover the same portion of low values. It conflicted with the distribution that originally represented low activation energy; thus, overall prediction potential was not effectively elevated even with additional symmetric distributions. Beyond that, the increase in distribution number ameliorated identification accuracy in the cases of four- and five-Gaussian DAEMs, yet their overall prediction potentials were not necessarily the best. It was, therefore, indispensable to conduct model identification and validation separately, to obtain correct and comprehensive assessments of the model.

The two Gaussian + one exponential DAEM demonstrated its best performances in validation stages, proving a superior strategy for the distribution's shape. This performance was further verified in Figure 5, which depicted the match relationships between qualities in both identifications and validations (overall RMSE) and model's degrees of freedom (D_f). As noticed, even though four- and five-Gaussian had lower RMSE values during model identifications, their prediction abilities were inferior to two Gaussian+ one exponential DAEM. On the other hand, three-Gaussian and three-logistic DAEM had identically small D_f as two Gaussian + one exponential DAEM, yet they both demonstrated worse prediction potentials. Two Gaussian and one exponential successfully located both its RMSE and D_f in the low 'optimal zone' (highlighted with the red circle), which ensured accurate prediction ability while avoiding excessive numerical complexity. In this sense, two-Gaussian and one exponential provided the best trade-off between prediction ability and degrees of freedom.

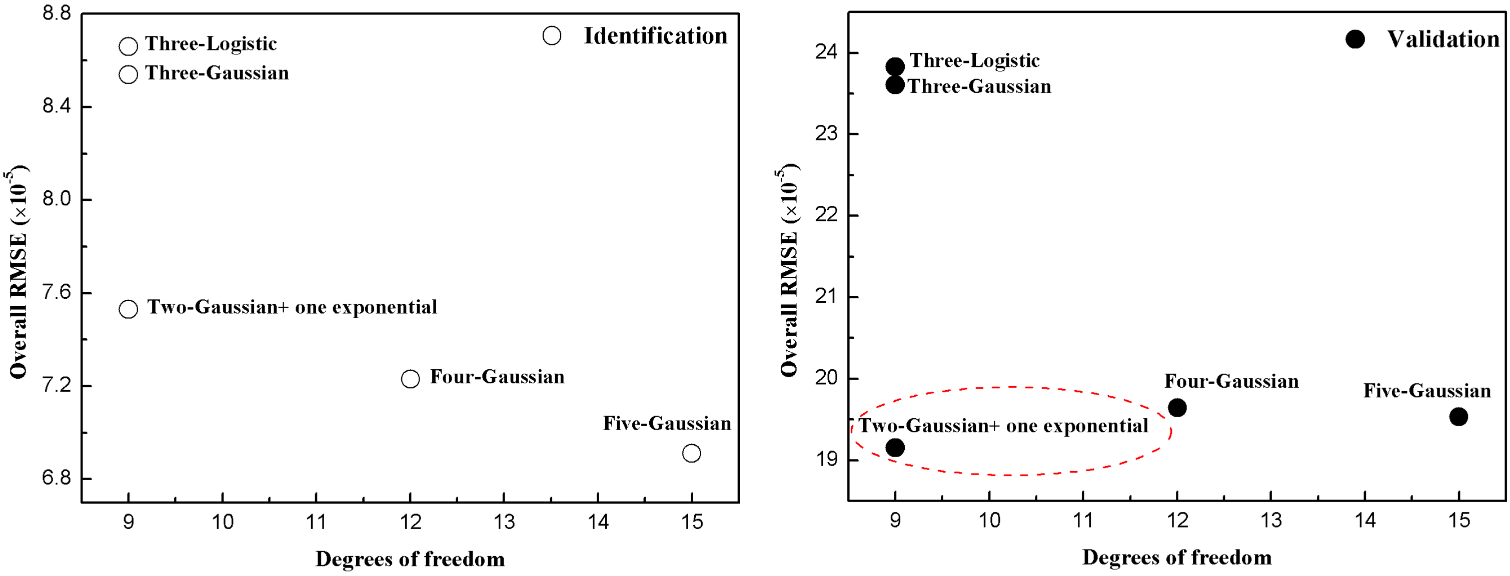

Figure 5. Degrees of freedom and overall RMSE in both identification and validation of five types of DAEM

Independent and global first-order reaction mechanism was additionally considered herein for comparison purpose. This kinetic method often worked for simple approximation that treated biomass as single or multiple pseudo-components [228, 229], in which each set of kinetic equation (Arrhenius equation) required at least two independent parameters, i.e. pre-exponential factor and global activation energy. Becidan [230] claimed 7 to 8 partial reactions were required for acceptable fit, in other words, it needed 8 to 9 independent parameters with assumption that they shared same pre-exponential factor, which was still too complicated. Its limited reaction types were unlikely appropriate descriptions of the infinite number in real pyrolysis. Worse still, the mechanism faced poor applicability in fitting multiple temperature profiles [217, 230]. Yet in two-Gaussian + one exponential DAEM, 10 parameters were sufficient to capture essences of massive reactions, being adequately concise and meantime powerful. From this perspective, the proposed two-Gaussian + one exponential again presented as excellent model choice for kinetic determinations.

To further confirm the superiority of two-Gaussian + one exponential DAEM, three-n*th*-order mechanism was also applied for comparison [231]. Herein, pre-exponential factor (A) was assumed identical in three reactions, and each scheme had its activation energy (E) and reaction order (n). The superposition of three n*th*-order reaction schemes was subsequently fitted in both dynamic and static tests for parameter identification and verification (table 8). Regarding the overall RMSE in identification, 7.6×10^{-5} of two-Gaussian + one exponential DAEM was much smaller than that in three-n*th*-order model, revealing better fitting quality. More importantly, this three-n*th*-order mechanism had worse prediction capacity compared to two-Gaussian + one exponential DAEM (RMSE=2.0×10^{-4} in validation), yet its numerical complexity was hardly simplified ($D_f = 10$), which again support the better performances of proposed DAEM.

Table 8. Identified parameters of three-n*th*-order model and overall RMSE in identification and validation stages

Pseudo-component	V_{max}	A (s^{-1})	E (kJ/mol)	n	Overall RMSE in identification	Overall RMSE in validation
First	0.3234	2.98×10^{11}	152.88	0.83	1.9×10^{-4}	4.5×10^{-4}
Second	0.4728		165.53	1.10		
Third	0.2931		227.95	0.69		

4.3 DTG simulation

DTG simulations were conducted to assess the performance of different distributions in the five comparable DAEMs. Figure 6 illustrated DTG simulations by the overall model and individual distributions at 5 °C/min. The heating rate was chosen due to its moderate baseline fluctuations; DTG simulations at other heating rates are within the supplementary material. It was obvious that the overall DTG simulations of five models overlapped substantially with experimental data, and the only visible deviations occurred near the DTG peak. For analysis, the main variations of local residue $\left(R_L(t)\right)$ were manually divided into three noticeable sections here, ranging between 100–300, 300–400 and 400–800 °C, respectively. The first and third sections moderately fluctuated, and hemicellulose decomposition was mainly attributed to the first. Meanwhile, lignin decomposition and secondary reactions were responsible for the third section [145]. The second section showed the most severe fluctuations with two obvious peaks; they were believed to originate from the mixed pyrolysis of hemicellulose and cellulose [4]. Cellulose decomposed rapidly within a very narrow temperature range after its crystallites melted [232] and it partially merged with hemicellulose. Inevitably more detectable errors emerged in this section during simulations.

Overall DTG with local residues

Separate and overall DTG

Three-Gaussian

DAEM

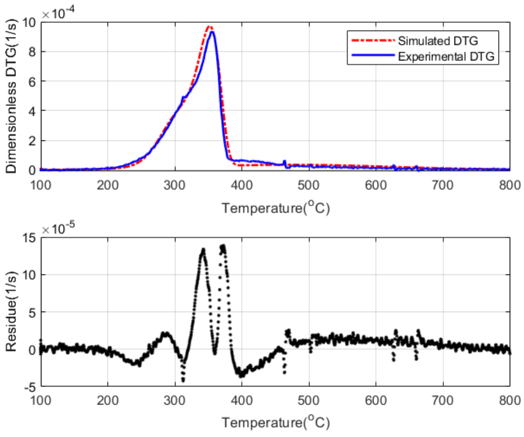

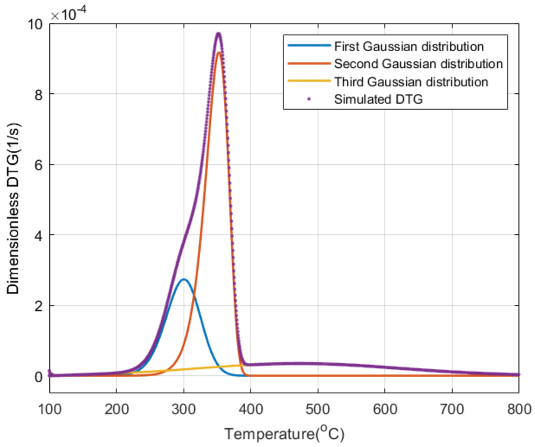

Three-Logistic
DAEM

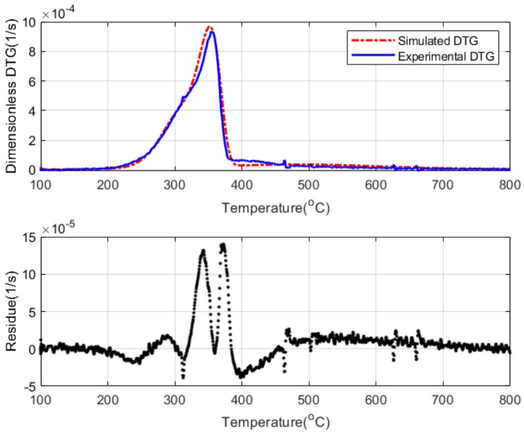

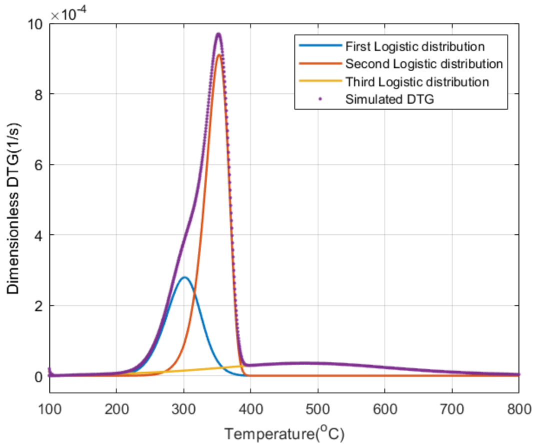

Two Gaussian
+one exponential
DAEM

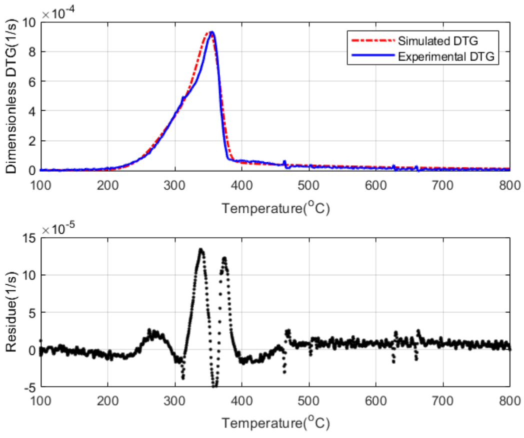

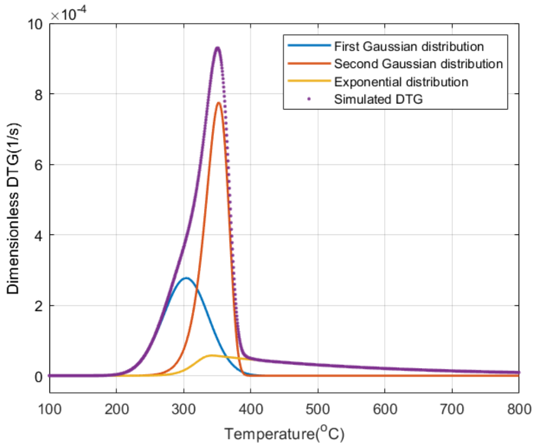

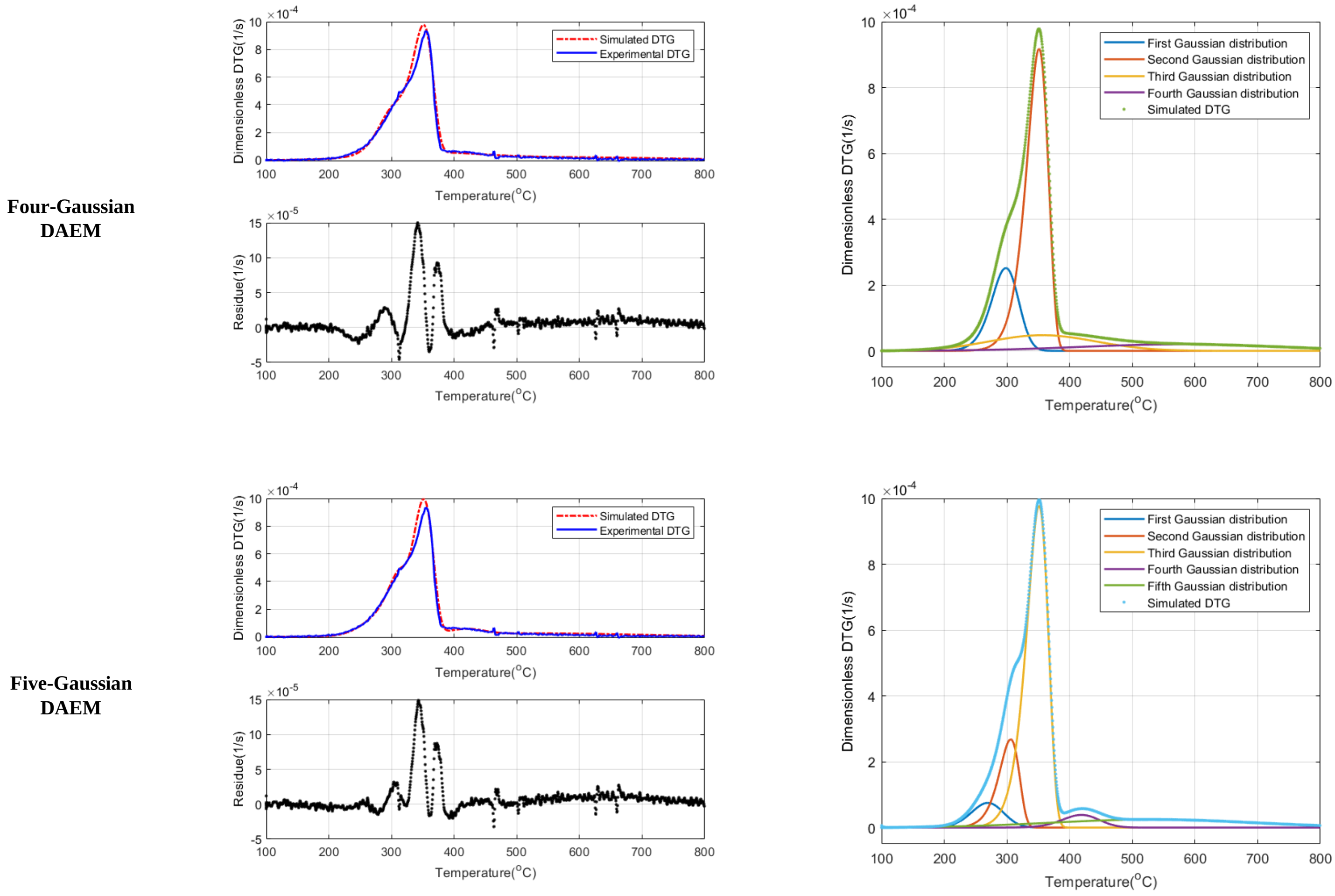

Figure 6. Experimental, simulated DTG curves and corresponding local residues (left), separate and overall DTG simulations (right) of five DAEM at the heating rate of 5 °C/min

Standard deviations (σ_R) of sectional simulations were compared in Table 9. Among the DAEMs with three distributions, two Gaussian + one exponential DAEM exhibited the best simulation improvements, especially in the third section wherein the asymmetric exponential uniquely functioned. Further compared to two Gaussian + one exponential DAEM, four-Gaussian DAEM showed only slight improvements in first and second sections, and five-Gaussian DAEM improved in all three sections. However, as previously emphasized, it was not practical nor feasible to increase numerical complexity for limited error improvement. Using the two Gaussian + one exponential DAEM as a reference, the error reduction ratios in three sections realized by four-Gaussian DAEM were 4.34 %, 1.60 %, 0 %, respectively, and 42.03 %, 10.49 %, 8.33 %, respectively, by five-Gaussian DAEM. The five-Gaussian DAEM provided the only notable improvement in the first section, which represented a very small part of pyrolysis kinetics. So, here the asymmetric exponential distribution again presented a good trade-off strategy to improve accuracy and maintain numerical concision.

Table 9. The sectional standard deviation of DTG residue at the heating rate of 5°C/min of five models

Temperature section (°C)	σ_R ($\times 10^{-6}$)				
	Three-Gaussian	Three-Logistic	Two Gaussian+one exponential	Four-Gaussian	Five-Gaussian
100–300	7.2	7.4	6.9	6.3	4.0
300–400	57.3	57.3	56.2	55.3	49.5
400–800	11.9	12.2	7.2	7.2	6.6

Separate DTG simulation further depicted each pseudo component's contribution to the overall decomposition rate (right row of Figure 6). The three-Gaussian and three-logistic DAEMs had same decomposition ranges of three pseudo-components: 200–375 °C (first pseudo-component), 250–400 °C (second pseudo-component) and 100–800 °C (third pseudo-component). Compared to these two models, two Gaussian + one exponential DAEM altered the decomposition range of first pseudo-component (200–400 °C), induced no change for second pseudo-component (250–400 °C), and increased initial decomposition temperature of the third pseudo-component (270–800 °C). For the four-Gaussian DAEM, four pseudo-components decomposed in the temperature ranges as 220–360, 250–400, 160–550 and 100–800 °C respectively. Finally, the decomposition temperature ranges of five-Gaussian DAEM's pseudo-components were: 165–375, 200–350, 240–400, 280–520 and 100–800 °C, respectively.

It was always worthwhile to identify pseudo-components as the signatures of major chemical components. The totality of specific species could be described by one unique distribution, and further assist in understanding the multi-component mechanism of biomass pyrolysis. In this vein, Table 10 shows relevant thermogravimetric decomposition temperatures of the three main constituents in biomass. Generally, hemicellulose consists of polysaccharides that are heterogeneously branched and are non-covalently bonded to the surface of cellulose microfibril [22]. The less stable chemical structures make hemicellulose more reactive with lower temperature ranges of decomposition. Cellulose is a saturated linear polysaccharide with high polymerization and degree of crystallinity and decomposes in very narrow temperature ranges [23]. Lignin is a set of irregular phenolic polymers consisting of more than four substituted phenyl propane, which endow lignin with large decomposition ranges during the entire pyrolysis process [233]. Many published values provided reliable references for featuring pseudo-components. By comparing chemical constituents' decomposition temperatures with model calculations, it was, therefore, feasible to correspond the three pseudo-components to hemicellulose, cellulose and lignin respectively in the three-Gaussian, three-logistic and two Gaussian + one exponential DAEM, which were well-accepted strategies [93, 113, 234]. For the four-Gaussian DAEM, first and second pseudo-components were linked with hemicellulose and cellulose, while the third and fourth pseudo-components possibly presented the two-stage decomposition scheme of lignin [97]. In the five -Gaussian DAEM, the first and second pseudo-components together represent hemicellulose, then the third pseudo-component was assigned to cellulose. The fourth and fifth components were attributed to two overlapped partial reactions, the scission of oxygen functional groups and rearrangement of the carbon skeleton were believed responsible for these two distributions, respectively [223].

Table 10. Summary of individual biomass component's decomposition temperature range

Heating rate (°C/min)	Decomposition temperature range (°C)			Reference
	Hemicellulose	Cellulose	lignin	
10	220–315	315–400	>400	[235]
10	200–320	280–360	140–600	[236]
20	200–350	260–430	200–500	[237]
20	253–308	319–368	259–482	[238]
20	244–324	294–371	197–653	[239]
50	250–350	350–500	>500	[240]
60	200–327	327–450	200–550	[199]
<5	225–325	324–375	250–500	[241]

Peak temperatures observed in both experimental and simulated DTG at different heating rates are listed in Table 11. The peak temperatures corresponded to the extreme reaction stage of cellulose decomposition, and they followed a decreasing trend with an increase of heating rate, which was caused by the altered pyrolysis kinetics relating to inter-particle heat transfer [178]. In general, five models reproduced the peak temperatures accordingly at four heating rate conditions, with considerably small errors less than 5 °C. It was clear that multiple-distribution DAEMs were capable of distinguishing the effects of heating rates, which has rarely been observed in relevant researches. Peak values were usually applied in Kissinger procedure for determining activation energy [242], as a direct and easy method. However, its limitations arose in merely staying at observation stage based on existing experimental data. By comparison, multiple-distribution DAEMs herein presented a precise description of peak temperatures and confirmed the prediction abilities already proved on mass loss. Therefore, it would be safe to conclude that the proposed models could advance one step further as prediction tools in isoconversional kinetics. DAEM may be applied for the accurate description of global pyrolysis kinetics under different reaction conditions.

Table 11. Peak decomposition temperature from experiments and model simulations

Heating rate (°C/min)	Experimental	Three-Gaussian	Three-Logistic	Two Gaussian+ one exponential	Four-Gaussian	Five-Gaussian
1	366.58	363.58	363.58	362.59	362.59	362.59
2	354.73	351.73	352.23	350.73	350.73	351.23
5	339.06	337.08	337.08	335.88	336.08	336.48
10	329.44	326.64	326.64	325.13	325.43	325.83

Conclusion

A rigorous strategy of both identification and validation was applied in the DAEM for analysing the effects of distribution number and shape. First, in a series of Gaussian-DAEMs with distribution number ranging from one to five, three-distribution was determined as the best trade-off between prediction ability and degrees of freedom. Logistic and exponential distributions were proposed to account for distribution shapes. Exponential distribution allowed good simulations for high-temperature reactions, and together with two Gaussian distribution, they exhibited as the best strategy in terms of both prediction capacity and numerical concision. The overall DTG simulation at 5 °C/min was analysed within three major variation sections, where two-Gaussian + one exponential DAEM achieved obvious error reduction with plausible numerical concision. Degradation temperature ranges by separate DTG simulations evidenced the correspondences between pseudo-components and chemical components, and DAEM’s was able to distinguish the effect of heating rate on the peak decomposition temperature.

Supporting material

1. Choice of exponential distribution

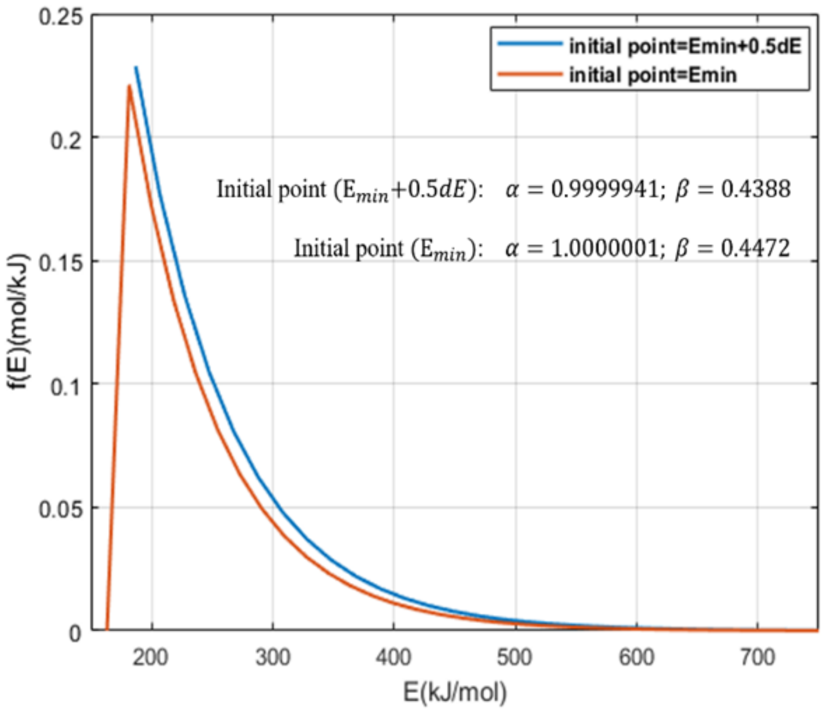

Supplementary Figure 1. Identified gamma distributions with two initial calculation points

Supplementary figure 1 shows the gamma distribution curves after model identification using two scenarios of initial calculation points. When the initial discretion point was set to E_{min}, to obtain suitable coverage, the curve peak of the gamma distribution was pushed toward E_{min} where it manifested as an almost vertical line. In this case, α was obligated to remain larger than 1 to avoid an invalid value (NaN), and the optimization algorithm manipulated it to infinitely approach but never equal to 1. In contrast, when setting the initial point as $(E_{min} + 0.5dE)$, the gamma formulation faced no risk of becoming an invalid value, it crossed over the critical point and identified $\alpha < 1$, but still, the optimization process manipulated it to infinitely approach 1. Both strategies coincidentally demonstrated best performances when the distribution was in the exponential shape, revealing that exponential distribution ($\alpha = 1$) was the optimal strategy to best represent gamma distribution during model identification. Therefore, $\alpha = 1$ will be manually set in corresponding DAEMs, and the initial point will be set to $E_{min} + 0.5dE$ to better realize numerical integration and avoid invalid values.

2. DTG simulations

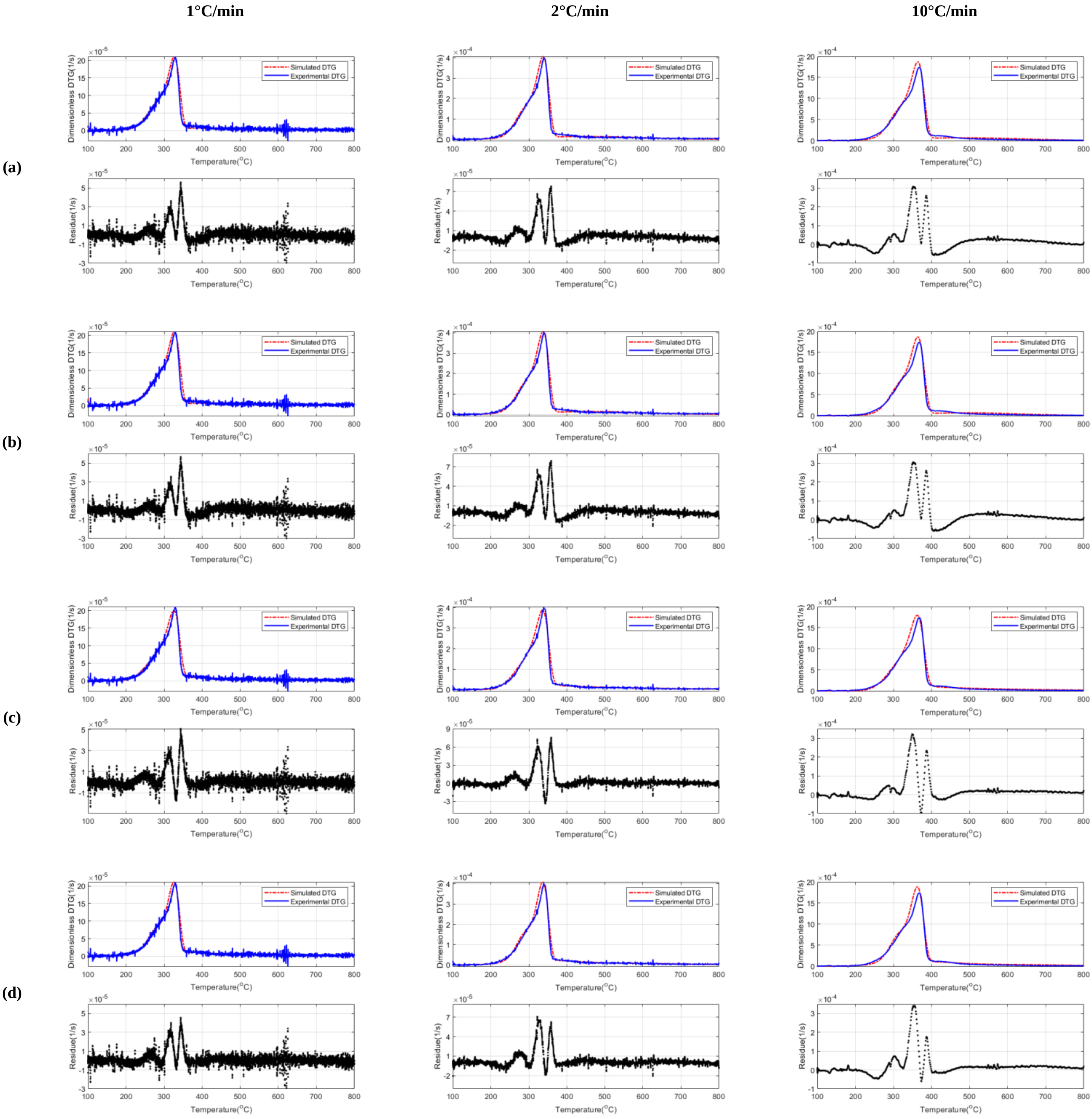

(e)

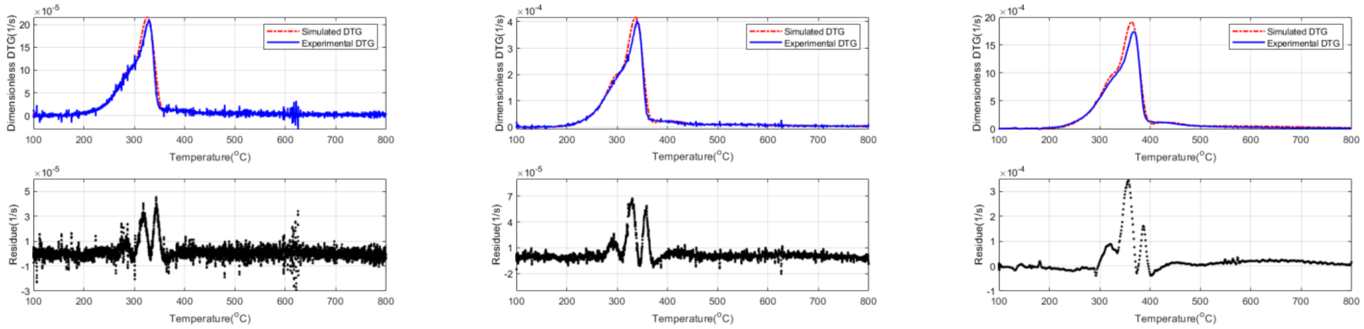

Supplementary Figure 2. Experimental, simulated DTG curves and corresponding local residue at 1 °C/min, 2 °C/min and 10 °C/min. (a) three-Gaussian DAEM, (b) three-logistic DAEM, (c) two Gaussian+ one exponential DAEM, (d) four-Gaussian DAEM and (e) five-Gaussian DAEM

3. Trade-off in test number

The preliminary tests have been conducted to determine the test number in identification database. Up to now, seven heating rates have been adopted, meantime the validation database keeps unchanged (six static tests varied from 250 °C to 500 °C).

First, model parameters of two-Gaussian+ Exponential DAEM are identified in various single dynamic test, and further validated with static tests (Supplementary table 1). Overall RMSE values in identification generally increase with the increase of heating rate, attributing to the larger fluctuations at high heating rate. This is in accordance with literature findings that the uncertainties increased with heating rate [125]. Accordingly, the validations exhibit generally increased RMSE and deviations. What's worse, the predication effects are apparently not desirable with notable errors in simulated TG curves, putting forward the necessity of multi-tests as identification database.

Supplementary table1- Fit qualities in both identification and validation when applying single test during parameter identifications

Heating rate (°C/min)	Identification		Validation	
	Overall RMSE (10^{-5})	D_m (%)	Overall RMSE (10^{-4})	D_m (%)
1	2.72	0.94	3.79	7.59
2	3.69	0.77	5.49	9.8
5	5.25	1.02	5.24	11.14
10	6.22	0.7	8.24	19.83
15	7.55	0.95	10.51	17.69
20	6.91	0.88	8.99	18.73
30	6.94	0.85	12.95	22.42

Subsequently, the choice of multi-test follows the low-to-high sequence of heating rates, for instance, two-test is based on 1 and 2 °C/min, three-test is based on 1, 2 and 5 °C/min, high-heating rate will be subsequently added when increasing the test number. Supplementary table 2 compares the qualities in both identifications and validations among different test number, and one-test of 1 °C/min is chosen because of the best validation quality among its counterparts.

For identification, overall RMSE increases with the increase of test number, attributing to the accumulations of simulation errors. And obvious increase of RMSE is introduced by the tests at high heating rate (> 15 °C/min). Moreover, it warns that identification errors are not solid proves for model’s fitting quality, otherwise single test would be the best choice because of its lowest error in identification. That’s why the more important prediction capacity is encouraged for solid verifications [113, 116]. Herein, the prediction ability is evidently improved by increasing test number from one to four, yet the further increase of test number brings oppositely worse prediction effects. The minimum RMSE in four-test indicates the optimal strategy between identification test number and prediction capacities. Accuracy is improved at limited extent by the increase of test number, and it will be undermined when further employing high-heating rate test.

Supplementary table 2- Fit qualities in both identification and validation when applying multi-tests during parameter identifications

Test number	Heating rate (°C/min)	Identification		Validation	
		Overall RMSE (10^{-5})	D_m (%)	Overall RMSE (10^{-4})	D_m (%)
one-test	1	2.72	0.94	3.79	7.59
two-test	1+2	4.87	1.51	2.67	4.53
three-test	1+2+5	6.38	2.09	1.99	2.36
four-test	1+2+5+10	7.53	2.54	1.91	2.36
five-test	1+2+5+10+15	12.18	5.45	2.33	2.45
six-test	1+2+5+10+15+20	13.42	5.41	2.34	2.48
seven-test	1+2+5+10+15+20+30	15.22	5.38	2.37	2.54

The correlations between overall RMSE of identification and validation is further presented in supplementary figure 3, and the calculation number in one loop (N_c) is also displayed to represent the numerical complexity during parameter identifications. The non-monotonic relation here clearly indicates the optimal position of four-test, which achieves the best trade-off between predication ability and identification errors. The obvious decrease of validation errors at initial stage (from one-test to four-test) is associated with test numbers, the increase of which gradually leads to the complete coverage of whole pyrolysis mechanism, and validation quality is guaranteed at the expense of acceptable error increase during identifications. However, the following stage (from four-test to seven-test) indicates that predication ability is no longer elevated by the increase of test number, in contrast, it brings more errors and numerical complexities. It’s very possible that four-test is sufficient to cover most kinetic features, the effects of adding test number will merely express as error increase, being unnecessary and redundant.

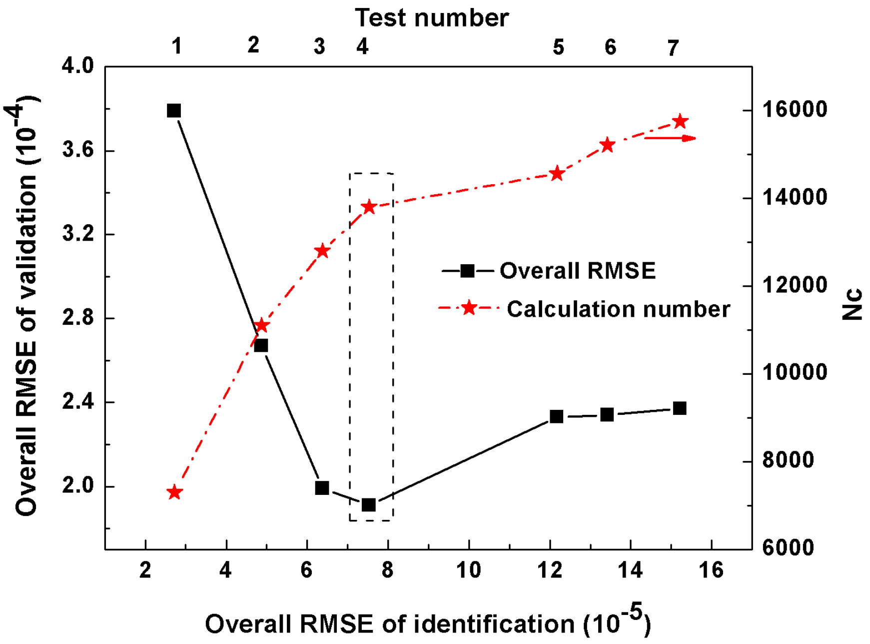

Supplementary figure 3. Relations of overall RMSE of identification and validation with different test number and corresponding calculation numbers

Chapter 5 Intrinsic kinetic modelling of spruce and poplar powder

This chapter will further apply the two-Gaussian+ exponential DAEM into the intrinsic kinetic study of both spruce and poplar powder. Reliable kinetic parameters will be obtained by identifications of dynamic tests and further validated by static tests. Reaction enthalpy was first coupled with the comprehensive model and present satisfactory simulation effects. Two applications were further applied concerning: (1) prediction in a correlation between atomic ratio and mass loss; (2) description of temperature/heat flux evolution.

- This work is published in **FUEL [162]**.

A robust and frugal model of biomass pyrolysis in the range 100-800 °C: inverse analysis of DAEM parameters, validation on static tests and determination of heats of reaction

Patrick Perré[a,b,*], Yong TIAN[b], Pin Lu[a], Barbara Malinowska[b], Jamila El Bekri[b], Julien Colin[a,b]

[a] LGPM, Centre Européen de Biotechnologie et de Bioéconomie (CEBB), 3 Rue des Rouges Terres, 51110, Pomacle, France

[b] LGPM, CentraleSupélec, Université Paris-Saclay, 3 Rue Joliot Curie, 91190 Gif-sur-Yvette, France

E-mail address: patrick.perre@centralesupelec.fr (Patrick Perré)

Abstract:

This paper presents a robust and frugal Distributed Activation Energy Model to simulate pyrolysis of lignocellulosic biomass (spruce and poplar) over a wide range of temperature and residence time. The learning database consists of dynamic TGA-DSC experiments performed up to 800 °C at four heating rates (1, 2, 5 and 10 °C /min). By employing one non-symmetrical distribution, three distributions and only 9 independent parameters were needed to correctly fit the experimental data: a Gaussian distribution for hemicelluloses, a Gaussian function degenerated into a Dirac function for cellulose and a gamma function degenerated into an exponential function for lignin.

The robustness of the model was successfully validated with 2-hours isothermal tests (250 °C to 500 °C with increments of 50 °C). The heats of reaction were determined using the heat flux measured under fast dynamic conditions, thus reducing the crucial problem of baseline drift. The prediction potential of the model is highlighted by two examples: pathway in the Van Krevelen's diagram and control of the temperature rise to limit the heat source due to reactions.

The model equations, the discretization and computational implementation, as well as the complete set of model parameters are presented in great detail, so that the reader can use them for process modelling, including the crucial concern of thermal runaway occurring in large particles or packed beds.

Keywords: computational modelling, identification, poplar, prediction, spruce, validation

1. Introduction

Biofuel derived from biomass is a source of renewable energy for transportation [243]. Technologies based on thermal processes are part of the conversion route from biomass to biofuel and energy source, among which pyrolysis is often the first step before combustion, gasification or grinding. During this process, biomass decomposes under inert atmosphere in the form of gas, bio-oil, and char.

Thermogravimetric analysis (TGA) is the most common analytical method for experimental investigation of biomass decomposition [244-246]. TGA detects online the evolution of mass loss, a good indicator of the alterations of biomass properties [247]. The earliest kinetics works were performed at isothermal conditions and the decomposition rates were formulated over a certain range of temperature and pre-heating conditions [76, 248, 249]. Dynamic tests are, however, more widely-used for their ability to investigate a wide range of temperature and to use analytical solutions for kinetics determination. On the contrary, when analysed using analytical solutions, isothermal kinetics suffered from the noticeable weight loss during warm-up time [250-252].

The earliest kinetics works have formulated the degradation kinetics of lignocellulosic biomass or their components (cellulose, hemicelluloses, and lignin) as a set of competitive and/or consecutive reactions [228, 253-258].

Currently, Distributed Activation Energy Model (DAEM) became the standard modelling tools for thermal degradation of biomass. This concept was developed by to model pyrolysis of coal and was later applied to lignocellulosic biomass [79, 135, 259]. This model represents the decomposition process as a continuous series of independent and parallel reactions with different activation energies which were further described by continuous distribution functions. Analytical method was first derived to extract the distribution functions from experimental data [131]. In the case of biomass, the actual decomposition process involved complicated steps with different activation energy distributions. As multi-distribution models are required, the common practice is to use a computational solution to solve a full set of distributions of any shape.

This kind of model is among the most comprehensive models for describing pyrolysis kinetics of lignocellulosic biomass and its components [2, 93] and already proved its prediction potential for tests that were not include in the learning database [94]. Recent DAEM developments include a whole set of works using multiple normal distributed activation energy model. Depending on the experimental database, and probably also on the authors' expectations, two [100], three[104, 234] or even five[109] normal distributions are proposed to get a good fit with the experimental data.

Many works were devoted to the refinement of the pre-exponential factor A (also called the frequency factor). Some authors proposed this factor to depend on temperature: $A = A_0 T^n$ [260]. Sfakiotakis and Vamvuka [261] proposed this factor to depend on the heating rate (HR). A linear relationship between the logarithm of the pre-exponential factor A and the mean value of the activation energy distribution was also introduced [2, 262]. In all proposals, the authors claimed, and proved, that this allows the quality of the fit to be improved. This is not so surprising as any additional degree of freedom in the inverse procedure necessarily reduces the residues. Other improvements concerned the shape of the distribution functions. As Gaussian distributions are still widely used, other shapes, such as Logistic, Uniform and Weibull function have been proposed [93, 112].

However, the complexity of this approach, namely the number of degrees of freedom, together with the well-known compensation effect make it difficult to propose an unambiguous set of model parameters [125, 263]. Thus, any kinetics model based on inverse analysis should include two steps: i) Parameters identification on a learning database and ii) Model validation using alternating time-temperature pathways.

Yet, to the best of our knowledge, we found only two works that includes the validation step. Lin et al [112] used experimental data performed at 20 K/min as learning database and used the identified parameters to successfully predict tests performed at 15 K/min and 25 K/min. In [112], the same team used the identified model to predict the distribution of activation energies.

Besides, the heats of reaction are of utmost importance to properly simulate the intricate heat and mass coupling occurring during the thermo-chemical process, either inside particles large enough for the fields to be non-uniform [219]or in a bed of particles [94, 264]. Unfortunately, the literature remains sparse regarding the heats of reaction, even though this information is of crucial importance to consider the thermal runaway that is likely to appear in industrial processes. Former studies on the determination of reaction enthalpies encountered difficulties like large errors in pyrolysis calculation [265], uncertainty, and unknown accuracies [167]. The lack of precision is often attributed to the experimental conditions, which includes the sample size, the nature of the atmosphere, and the presence of impurities.

To gain accuracy, differential scanning calorimetry (DSC) could to be an effective way [174]. Note however that, in this case, it is difficult to rely the heat flux to the mass loss evolution, hence to determine reaction enthalpies. The published reaction enthalpies range from -3800 to 418 kJ/kg for wood [174, 253, 266, 267], from -510 to 322 kJ/kg for cellulose, from -455 to 79 kJ/kg for lignin and from -700 to 42 kJ/kg for hemicelluloses [268]. Such large variations, ranging from endothermic to exothermic, point out the real difficulty to determine these heats of reaction [75, 174]. A value of -850 kJ/kg was determined by inverse analysis for the degradation of hemicelluloses in [219]. This value was tuned to predict the correct thermal runaway in a coupled heat and mass transfer computational code. However, one must keep in mind that this value is strongly tied to the kinetics model implemented in the code. Anyway, the temperature overshot measured inside the macro-particle [219] or in a packed-bed [94, 256] proves that pyrolysis involves exothermic reactions, which is in contradiction with other published works [222, 269].

In the present paper, we propose a robust DAEM model to simulate pyrolysis of two types of lignocellulosic products (spruce and poplar) over a wide range of temperature levels and treatment durations. The inspiration for this work is i) to find best compromise between the sobriety of the number of parameters to be identified and the robustness of the model validated on very distinct experimental data and ii) to use to the DSC signal to identify heats of reaction. The whole procedure is explained in detail to allow the reader to implement the modelling strategy for its own needs. The full dataset is supplied for poplar and spruce (kinetics parameters and reaction enthalpies), which can be used for the simulation of biomass pyrolysis, including thermal runaway likely to occur in large particle or packed beds of particles.

2. Material and methods

Poplar (*Populus euramerican* cv. I-214) was selected from a 17-year-old tree (cottonwood native black poplar in the Po Valley, female). The spruce tree (*Picea abies*) was about 31-year-old and selected from the Brin forest, Champenoux, France. The choice of these species was motivated by two objectives: i) The selection of potential species for biofuel production due to their availability ii) the scientific interest of comparing hardwoods and softwoods in regard to their pyrolysis behaviour. Healthy trees with no apparent injury were used. Stem disks were cut from each tree at 6 m above the ground. Small blocks were selected from these disks avoiding the sapwood and the pith regions. All samples were milled by using a grinder (IKA M20

Universal mill) and subsequently sieved. The particle size fraction from 0.063 to 0.08 mm was selected in order to neglect internal heat and mass transfer limitations during pyrolysis. The ultimate analysis was conducted in elementary analyzer (FLASH 2000 CHNS/O, Thermo Fisher Scientific) and proximate analysis was based on standard methods of ASTM E1755 and E872, they were all calculated on a dry basis. For both wood species, all tests were preformed in triplicate and the mean values were taken to ensure results accuracy and repeatability.

The experimental TGA apparatus was a thermogravimetric analyzer (STA 449 F3 Jupiter, NETZSCH) with a weighting sensitivity of 0.025 μg and a balance drift lower than 2 μg/hour. The TGA-DCS sample carrier was mounted for simultaneous measurement of mass loss and heat flux. All measurements were carried out under a nitrogen flow of 50 mL/min and a protective gas flow of 20 mL/min. Dynamic tests started by heating the sample up to 100 °C for a 30-minute plateau at this temperature to eliminate the residual water, then the temperature increased to 800 °C with a constant heating rate (10, 5, 2 and 1 K/min). Static tests started by the same plateau at 100 C, then followed by a heating phase at 10 K/min to the desired temperature (250 °C, 300 °C, 350 °C, 400 °C, 450 °C and 500 °C) for a 2-hour plateau.

Blank experiments were conducted for all experimental protocols and each experiments was repeated three times. In order to exclude buoyancy effects and effect of crucible mass on heat capacity, each final result is the raw data calibrated by subtracting a blank test performed with the same protocol and the same crucible. The mass recorded at the end of 100 °C plateau was considered as oven-dry mass (m_0) for the determination of mass loss. In equation 1, the dimensionless residual mass (DRM) is defined as the ratio of the instantaneous sample mass (m_s) over the oven-dry mass:

$$\mathrm{DRM}(t) = \frac{m_s(t)}{m_0} \tag{1}$$

The dimensionless mass loss (DML, equ. 2) is simply the complement to the unity:

$$\mathrm{DML} = 1 - \mathrm{DRM} \tag{2}$$

3. Modelling

3.1 DAEM formulation

The DAEM formulation (equ. 3) [90] assumes that the product degrades through a large number of independent, parallel and irreversible first-order reactions i:

$$\frac{dV_i}{dt} = k_i(V_i^{\infty} - V_i) \tag{3}$$

$$k_i = A_i \exp(-\frac{E_i}{RT}) \tag{4}$$

In these equations, V_i represents the quantity of volatiles generated during reaction i, V_i^{∞} is the total quantity likely to be produced by this reaction. k_i is the kinetic constant for reaction i. Its thermal activation is assumed to obey an Arrhenius law (equ. 4), defined by an activation energy E_i and a pre-exponential factor A_i (kinetics constant at infinite temperature).

A time integration of equation (3) allows the time evolution of V_i to be derived as:

$$V_i^{\infty} - V_i(t) = V_i^{\infty} \exp\left(-\int_{t_0}^{t} k_i(T(t))dt\right) \tag{5}$$

In practice, a continuous function is used instead of equation (5) to represent a large number of reactions. This function $F(E)$ represents the fraction of volatiles produced by all reactions which have an activation energy smaller than E. The derivative of function F over the activation energy is a distribution function $f(E)$ which represents the potential of volatile production related to each energy value E:

$$dV^{\infty} = V^{\infty} f(E) dE \tag{6}$$

Assuming the pre-exponential factor to be the same for all reactions ($A_i = A\ \forall i$), a combination of equations (5) and (6) yields equation (7):

$$1 - \frac{V(t)}{V^{\infty}} = \int_{-\infty}^{\infty} exp\left(-\int_{t_0}^{t} Ae^{-E/RT(t)} dt\right) f(E) dE \tag{7}$$

Obviously, the whole set (continuous or discrete) of reactions should represent the entire product. Hence the integration over the entire range of activation energy gives the total potential of volatiles (equ. 8) that can be produced by the product:

$$\sum_{i=-\infty}^{+\infty} V_i^{\infty} = V^{\infty} \qquad or \qquad \int_{-\infty}^{+\infty} dV^{\infty} = V^{\infty} \tag{8}$$

The norm of function f therefore equals the unit (equ. 9):

$$\int_{-\infty}^{+\infty} f(E) dE = 1 \tag{9}$$

3.2 Gaussian distributions

A common practice is to adopt a Gaussian function for this distribution (or a combination of Gaussian functions). Function f is then defined by the average energy E_0 and its standard deviation σ (equ. 10) . The factor $\frac{1}{\sigma\sqrt{2\pi}}$ ensures the unit norm:

$$f(E) = \frac{1}{\sigma\sqrt{2\pi}} \exp\left(-\frac{(E-E_0)^2}{2\sigma^2}\right) \tag{10}$$

In order to use such a function in a computational code, the domain of this function, defined from $-\infty$ to $+\infty$, has to be restricted to a finite interval and, inside this interval, the continuous function should be approximated by a set of discrete values. As a Gaussian function is well defined by its standard deviation σ, it is reasonable to limit its domain over a certain number k of σ : $[E_0 - k\sigma, E_0 + k\sigma]$ and, inside each interval of length σ, approximate the function by m increments dE of equal length, as expressed in equation:

$$\begin{gathered} E_i = E_0 - n\sigma + (i - 0.5)dE, \quad i = 1,2km \\ with \qquad dE = \sigma/m \end{gathered} \tag{11}$$

Equation (12) depicts the corresponding discrete weighting factors of the Gaussian distribution:

$$f_i = f(E_i) = \frac{1}{\sigma\sqrt{2\pi}} \exp(-\frac{(E_i - E_0)^2}{2\sigma^2}) \tag{12}$$

For the discretized function to correctly represent the continuous function, k has to be equal or greater than 3 (with $k = 3$, the area under the curve is 99.7% of the total area, against 95.4% for $k = 2$). Preliminary simulations have shown that a typical m value of 10 allows a precise restitution of the kinetics (Fig. 1).

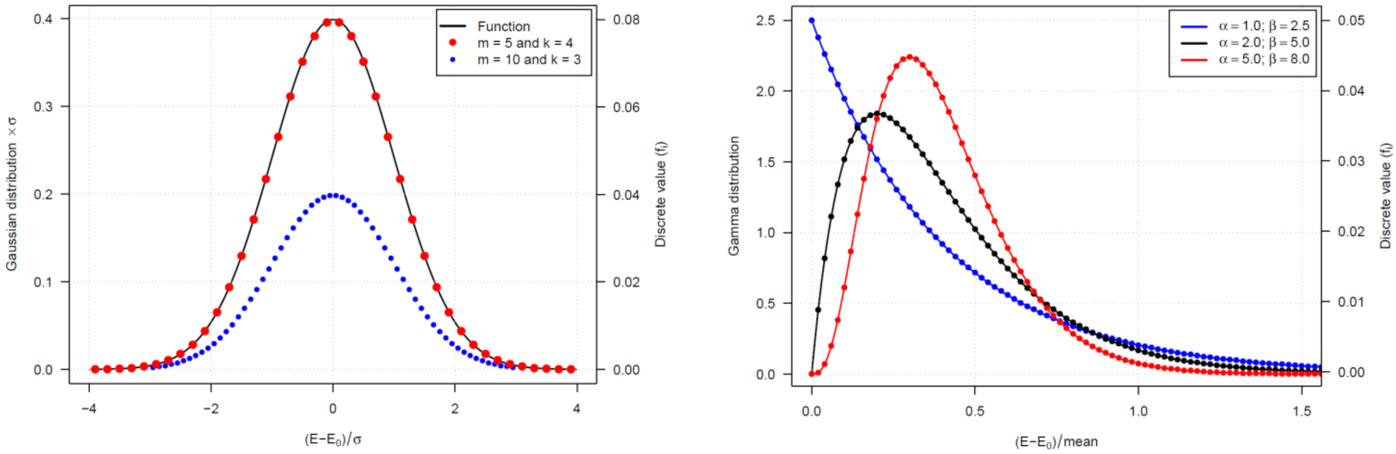

Figure 1. a) Sampling the Gaussian curve to get the discrete values f_i of function f. These values are proportional to the number of points i within each segment of length σ), b) The diversity of shapes that could be obtained with gamma distributions and its sampling obtained using 100 points over the interval $[E_{min}, E_{min}(1 + n\alpha/\beta)]$.

3.3 Gamma distributions

In the present work, we used gamma distributions as non-symmetrical distributions. The function f is defined by a minimum energy value E_{min} and two independent parameters, for example, the shape parameter α and the rate parameter β:

$$f(E) = Gamma\left(\frac{E - E_{min}}{E_{min}}, \alpha, \beta\right)$$

$$where \qquad Gamma(x, \alpha, \beta) = \frac{\beta^{\alpha} x^{\alpha-1} e^{-x\beta}}{\Gamma(\alpha)} \tag{13}$$

Where Γ is the gamma function defined as $\Gamma(z) = \int_0^\infty x^{z-1} e^{-x} dx, \quad (z > 0)$. To sample equation (13) for modeling purposes, the domain of the gamma distribution is restricted to a finite interval $[0, x_{max}]$, where x_{max} is n times the expected value (α/β). Function f is therefore approached on the interval $[E_{min}, E_{max}]$, with $E_{max} = E_{min}(1 + n\alpha/\beta)$. Inside this interval, the function f is discretized in m increments dE of equal length (equ. 14):

$$E_i = E_{min} + (i - 0.5)dE, \quad i = 1, m$$

$$with \qquad dE = (E_{max} - E_{min})/m \tag{14}$$

In this work, the gamma distributions were sampled with $n = 5$ and $m = 100$, which insures an accurate representation of the continuous function.

3.4 Computational implementation

Thanks to this discrete approximation, the kinetics of volatiles production is easily deduced from equation (3). Equations (15) and (16) summarise the set of equation to be computed:

$$\frac{dV}{dt} = \sum_{i=1}^{2km} \frac{dV_i}{dt} = \sum_{i=1}^{2km} k_i(V_i^{\infty} - V_i(t)) \tag{15}$$

$$k_i = A\exp(-\frac{E_i}{RT(t)}); \quad V_i^{\infty} = f_i V^{\infty} \quad ; \quad V_i(t = 0) = 0 \tag{16}$$

In the simulation code, the values of E_i and f_i are computed just once during the initialization procedure. On the contrary, all values of V_i have to be stored and updated along the simulation. Last refinement, the increments update along the time step of the kinetics defined by equation (15) is a first order approximation. However, due to thermal activation, former works [219, 258] told us that the combination of high temperature level and wide range of activation energy in DAEM might result in very small characteristic times (the factor τ in the time function $exp(-t/\tau)$, i.e. the inverse of k_i in equation 5). To ensure accuracy, an exact formulation of the increment of the chemical reactions during time step dt has been implemented (equ. 17) . This involves an exponential factor in the time increment expression:

$$dV_i = (1 - exp(-k_i dt))(V_i^{\infty} - V_i(t)) \tag{17}$$

As several distributions are often required to correctly represent the kinetics (we will use three distributions in the present work), equation (15) should be summed over all distributions. As each distribution n has its own sampling, the discrete coefficients should be indexed by the distribution number (f_i^n). Similarly, the total volatile substances likely to be produced by the distribution n is called $V^{n,\infty}$.

The final formulation for a computational solution of the DAEM model with three distributions is summarized as the change dV^n of total volatiles produced over the time step n, which represents the time interval $[t^n, t^{n+1}]$ with $t^{n+1} = t^n + dt$:

$$dV^n = \sum_{n=1}^{N} \sum_{i=1}^{2km} dV_i^n = \sum_{n}^{N} \sum_{i}^{2km} (1 - exp(-k_i^n dt))(V_i^{n,\infty} - V_i^n(t)) \tag{18}$$

$$k_i^n = A^n \exp\left(-\frac{E_i^n}{RT(t)}\right); \quad V_i^{n,\infty} = f_i^n V^{n,\infty} \quad ; \quad V_i^n(t=0) = 0 \tag{19}$$

$$\begin{gathered} DML(t^N) = \sum_{n=0}^{N-1} dV^n \\ DRM(t^N) = 1 - DML(t^N) \end{gathered} \tag{20}$$

The incremental DAEM formulation (equ. 18-20) allows any pathway time-temperature to be simulated. In the following, all simulations will be performed with the actual temperature, as recorded for each test by the TGA device.

3.5 Identification

The distribution parameters were determined by inverse analysis. The identification process minimises the objective function based on the difference between the experimental and calculated DRM values, computed in the sense of the mean-square error over a time interval ranging from the end of the drying plateau (time indice i_{ini}) to the end of the experiment (time indice i_{fin}). Moreover, in order to benefit from all the experimental information, this objective function F_{obj} is computed over several tests simultaneously (the 4 dynamic tests simultaneously in the present work):

$$F_{obj} = \frac{1}{N_{tests}} \sum_{\ell=1}^{N_{tests}} \left[\frac{1}{(i_{fin} - i_{ini} + 1)} \sum_{i=i_{ini}}^{i_{fin}} (\mathrm{DRM}_i^{\ell,exp} - \mathrm{DRM}_i^{\ell,cal})^2 \right] \tag{21}$$

In equation (21), the experimental dimensionless residual mass $DRM_i^{\ell,exp}$ is obtained by equation (1) and the calculated dimensionless residual mass is tied to the DEAM model (equ. 18) through to total, dimensionless, mass of volatiles produced at time t ($\mathrm{DRM}_i^{\ell,cal} = 1 - V^\ell(t_i)$).

The kinetic model is solved using an in-house software written in Fortran 95 by Patrick Perré. This code solves equation (18) with the actual furnace temperature of each test, as collected by the TGA device, for each time t_i. The objective function is minimized using the Nelder-Mead algorithm. As all experiments are treated simultaneously, all experimental conditions are computed for each increment of the Nelder-Mead algorithm [127], using the current set of parameters, to evaluate the objective function. The computational engine is embedded in a graphical library *Winteracter* to create a Windows application, with fields for parameter input/output and curve plot for visual check. It can be used either to simulate desired configurations or to identified parameters values from a set of experimental data.

It is important to notice that the identification procedure is not straightforward as many local minima exist: the initial parameter guess is therefore important for the algorithm to converge towards the global minimum. The in-house graphical application allows the free parameters, the experimental tests under interest and the active time interval of each test to be chosen. In order to tune the initial guess, we usually proceed stepwise: the first distributions are optimized over a reduced range of temperatures (namely by selecting a subset of the experimental times) and additional distributions are added along with additional experimental information. Finally, all tests are optimized with the full set of parameters to refine the solution. This is restarted several times with a large initial simplex, to check that the solution is the global minimum. The graphical output of the application and the display of residues greatly ease the procedure.

3.6 Enthalpy of reaction

The enthalpies of reaction are of utmost importance at the industrial scale to control thermal runaway and to evaluate the energetic yield over the whole transformation chain of biomass. Consequently, these values need to be included in the enthalpy balance to compute the source/sink terms due to degradation reactions. This is crucial to predict the temperature field, hence the kinetic activation at the scale of one macroscopic particle or at a level of bed of particles [219, 264]. Yet, the literature is still sparse in values of reaction enthalpies.

A first sight, the best way to measure enthalpies of reaction is to use isothermal tests, during which the heat capacity of sample and crucible is not involved. However, as pyrolysis reactions are quite slow, the total reaction enthalpies spread over long duration and produce in a very low signal. In such conditions (small heat flux and large durations) the drift of the heat flux baseline turns out to be larger than the signal. Instead, in the present work, we used dynamic tests, together with the robust, validated, DAEM model, to get a quite good accuracy of the identified reactions enthalpies, using the whole piece of information available with a ATG-DSC device : heat flux, temperature and mass loss. It is important to note that such an analysis would not have been possible with a simple DSC which is not able to give the mass evolution, in spite of the much better accuracy of such devices regarding heat flux.

To that purpose, the energy balance should to be properly formulated (equ. 22). In particular, the change of mass over time needs to be considered to evaluate the heat required to change the sample temperature. As the transformation occurs at constant pressure, we write the enthalpy conservation of the system (sample + crucible) between time t and time $t + dt$.

$$\underbrace{m_c h_s + m_s h_s}_{\text{Time}t} = \underbrace{\dot{Q}dt + \dot{S}dt + m_c(h_s + dh_c) + (m_s - dm)(h_s + dh_s) + dmh_v}_{\text{Time}t+dt} \tag{22}$$

Where h are the specific enthalpies, $\dot{Q}$ the heat flux provided to the system, $\dot{S}$ the source term due to chemical reactions and dm the quantity of volatiles formed during the time interval dt. Indices c, s and v stand for crucible, sample and volatiles respectively.

Rearranging equation (22) in terms of derivatives truncated at the first order yields equation (23):

$$-\dot{Q} = m_c \frac{dh_c}{dt} + m_s \frac{dh_s}{dt} + \dot{S} + \frac{dm}{dt}(h_v - h_s) \tag{23}$$

The fourth term of the right-hand side of equation (23) represents the enthalpy of volatilisation [163, 164]. In the following, the two last terms of the right-hand side are considered lumped together to form the production of pyrolysis enthalpy $\dot{H}_{pyro}$. As the blank tests are performed with the same crucible, the thermal inertia of the crucible is canceled after blank correction. The final equation for the blank corrected test is obtained by introducing the heat capacity of the sample (equ. 24):

$$-\dot{Q} = m_s(t)c_{p,s}\frac{dT}{dt} + \dot{H}_{pyro} \tag{24}$$

In the result section, the pyrolysis enthalpy $\dot{H}_{pyro}$ will be identified for the predicted heat flux (right-hand side of equation 24 : sum of enthalpy production and sensible heat) to match the heat flux measured by the TGA-DSC device ($-\dot{Q}$). In this calculation, we will assume that the reaction enthalpy, ΔH^n, is the same for all reactions involved in a given distribution n. This is a quite strong assumption, but was required for the identification to be realistic. The enthalpy production (equ. 25) reads then as follows:

$$\dot{H}_{pyro} = \sum_{n=1}^{N} \sum_{i=1}^{2km} \Delta H^n \frac{dV_i^n}{dt} \tag{25}$$

Keeping in mind that $V(t)$ is the dimensionless production of enthalpy, the final equation (equ. 26) used in the identification becomes:

$$-\dot{Q} = m_0(1 - V(t))c_{p,s}\frac{dT}{dt} + \sum_{n=1}^{N} \Delta H^n \left(\sum_{i=1}^{2km} k_i^n (V_i^{n,\infty} - V_i^n(t)) \right) \tag{26}$$

4. Identification and validation

4.1 Identification of DAEM parameters

Dynamic experiments were used to identify the parameters of the DAEM model. It is important to remind here that the four dynamic tests were used simultaneously (equ. 21) for each species. The importance of this feature was reported in [125]. Note however that our learning database includes a wider range of heating rates (from 1 to 10 K/min) than in this reference. For a Gaussian distribution, E_0 is the mean activation energy, which informs on the global resilience to decomposition: pseudo-components with smaller value of E_0 are prone to decompose more easily than those with high E_0. The standard deviation of the Gaussian distribution σ quantifies the width of activation energy values around the mean value. A distribution with a large standard deviation means that the corresponding pseudo-component decomposes over a large temperature range (or a large range of characteristic times) around the average value. The pre-exponential factor A controls the overall reaction rates. The weighting factor $V^{n,\infty}$ represents the total proportion of the initial biomass that can produce volatiles.

During the identification procedure, several distributions were required to correctly represent the evolution of DRM over the whole range of experimental conditions. As our strategy was to limit the number of degrees of freedom, we tried to limit the number of distributions. Two Gaussian distributions were able to capture the behaviors for moderate temperature levels. However, the symmetry of Gaussian functions is a strong constraint regarding the behaviour of thermo-activation: with a symmetrical distribution, it is not possible to spread the kinetics over high temperature levels without spreading also the kinetics over low temperatures. This fact was already observed and led scientists to use non-symmetrical distributions [93, 112]. The third distribution, devoted to the behavior up to 800 °C, was therefore set as a gamma distribution. This choice was crucial to obtain a good representation with three distributions. During the optimisation procedure, the need of asymmetry for this third distribution was so strong that the minimum value of residues was obtained with a value of α less than one, with induces an infinite value at zero. Such a function becomes very tricky to represent by discrete values : the parameters values depend on the sampling density, which is very difficult to reproduce. To avoid this side effect, we added the constraint $\alpha \geqslant 1$. The inverse procedure eventually gives $\alpha = 1$, which limits the gamma distribution to the subset of exponential functions and reduced by one the degrees of freedom.

As the learning database includes the asymptotic behavior (temperature level and duration enough to approach equilibrium), the sum of the weighting factors of all distributions is smaller than the unit. The complement of this sum to the unity therefore represents the asymptotic value of Dimensionless Residual Mass at infinite time.

In spite of slight differences, the parameters values identified for spruce and poplar depict the same trends (Table 1). In both cases, the second distribution has the largest weighting factor, indicating the largest portion of pseudo-components described by this distribution. For both species, the standard deviation of the second distribution is very small. No kinetics difference was observed for $\sigma \to 0$. This results in a unique activation energy, 183.3 kJ/mol for spruce and 181.4 kJ/mol for poplar, in good agreement with the value 185 kJ/mol obtained in [270]. The second distribution is basically reduced to a simple first-order reaction (a Dirac distribution), which decreases the number of degrees of freedom by one. This is explained by the sudden and large mass loss arising at around 300 °C. Finally, the third distribution acts after the second one in terms of temperature level and its action lasts over a large range of high temperatures. Finally, the proposed DAEM model comprises three different distributions:

- a Gaussian distribution for hemicelluloses,
- a Gaussian function degenerated into a Dirac function for cellulose,
- a gamma function degenerated into an exponential function for lignins.

Table 1: DAEM parameters of spruce and poplar identified on dynamic pyrolysis experiments. Parameters in red represent meaningless parameters related to the degeneration of distribution functions (Gaussian to Dirac and gamma to exponential).

Biomass	Distribution	V_{max}	$E_0 (kJ \cdot mol^{-1})$	$\sigma, \alpha \; or \; \beta (kJ \cdot mol^{-1})$	$A \; (s^{-1})$
Spruce	1 (Gaussian)	0.2344	168.5	$\sigma = 7.51$	9.67×10^{12}
	2 (Gaussian)	0.4927	183.3	$\sigma = 0.089$	
	3 (gamma)	0.1563	182.8	$\beta = 2.812; \alpha = 1$	
Poplar	1 (Gaussian)	0.2584	163.6	$\sigma = 6.62$	7.03×10^{12}
	2 (Gaussian)	0.4928	181.4	$\sigma = 0.128$	
	3 (gamma)	0.1630	181.3	$\beta = 2.205; \alpha = 1$	

For both species, the 3-distribution DAEM model is in excellent agreement with the experimental results (Fig. 2). This proves the ability of model to describe the pyrolysis behavior over a large range of temperatures and heating rates although we were frugal in the number of independent parameters. This qualitative assessment is confirmed by objective criteria (Table 2). The standard deviation is around or less than 0.5% and the maximum deviation, a very severe criterion, is around 1 to 1.5 %, except for spruce at 10 °C per minute, for which a slightly larger difference (2.27%) is observed at the end of the test. This difference is not obvious on the graph as the maximum deviation is obtained during the rapid mass decrease, where the curve slopes are very large. These excellent results are obtained by assuming a constant pre-exponential factor A, identical for all distributions ($\forall n, A^n = A$). This is in contradiction with the latest published works in which authors propose the pre-exponential factor to be a function of temperature, heating rate or average activation energy [2, 260-262, 270]. Even with our experimental datasets that include a large range of temperature levels and residence times, it was not necessary to use such functions, neither to obtain a small residues nor to successfully validate the mode against distinct time-temperature pathways. We can therefore affirm that a constant value of A is perfectly able to reproduce the kinetics behavior over a wide range of temperature levels and heating rates. We owe this success to the strategy to identify one single set of parameters simultaneously on the entire series of tests, together with the highly asymmetrical shape of the third distribution.

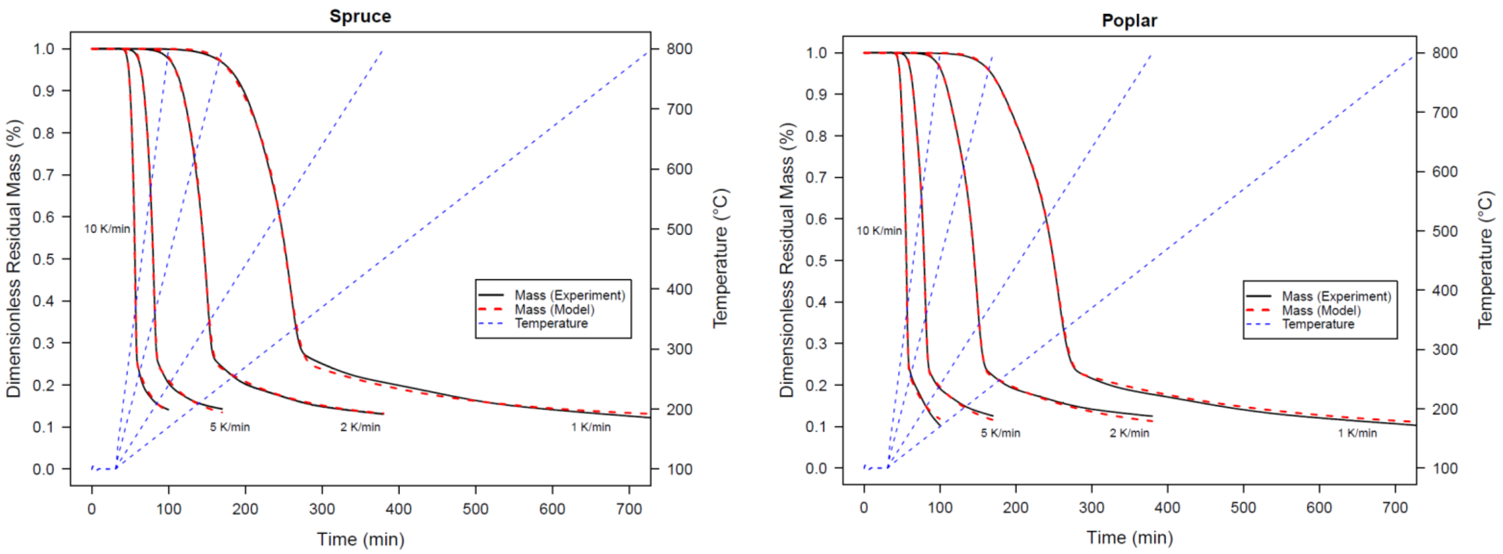

Figure 2. TG curves for dynamic experiments at different heating rates (10 °C /min, 5 °C /min, 2 °C /min and 1 °C /min) and corresponding DAEM curves based on identified parameters and temperature evolutions. Time origin is at the end of the 30-minute 100 °C plateau.

The temperature response of the three distributions together with these respective weighting factors confirm well-accepted trends in the pyrolysis behavior of lignocelluloses [104, 271]. The first distribution accounts for the degradation of hemicelluloses, the most prone to thermal degradation. Hemicelluloses are linear branched polymers made by different types of monosaccharide units [272] and it decomposes in the range 225-325 °C. Poplar hemicelluloses are mainly composed of xylan, whereas spruce hemicellulose are mainly composed of glucomannan [59]. In agreement with published results [273, 274], this explains that spruce is more thermally stable than poplar at moderate temperatures: E_0 of the first distribution is smaller for poplar than for spruce.

As can be seen from the V_{max} values, the second distribution affects roughly half of the production of volatile substances with rapid degradation above 300 °C. This is undoubtedly the signature of cellulose, which represents ca. 50% of the total mass and is very resilient to degradation in crystalline state, but with a rapid thermal decomposition once melt [275]. Cellulose has macromolecular structures which are constructed by semi-crystalline array of β-1,4 glucan chains and it decomposes at 325-385 °C [241, 276]. For Gaussian distributions 1 and 2, the present results depict similar trends as those proposed by [234]. However, our third distribution is very different from the very wide Gaussian distribution proposed in [234]: the gamma distribution captures nicely the degradation of the most reluctant part of the biomass, which can be attributed mostly to lignins [277]. Lignins present a highly branched three-dimensional phenolic structure made of C_6C_3 units, namely, p-hydroxyphenyl (H), guaiacyl (G), and syringyl (S) units, in various proportions depending on the species. Lignins present a large range of decomposition temperature from 250 °C to over 500 °C. Hardwood lignins are composed of S and G units, together with trace amounts of H units. Softwood lignins consist mainly of G units and low levels of H units [278, 279]. Consequently, spruce lignins contain fewer β-O-4 bonds and more 5-5 branching structures than poplar lignins. As β-O-4 bonds are the main targets of thermal degradation [280, 281], it is not surprising to obtain a minimum activation energy E_0 for the gamma distribution slightly smaller for poplar.

As a summary, hemicelluloses are the first components to be altered by temperature, cellulose, ca. half the cell wall mass, is very resilient before melting, but depicts a rapid degradation after melting (with a melting temperature around 300 °C) and lignins is the part of the cell wall the most resilient to degrade. This simple correspondence between the distributions and the components of the cell wall is certainly related to the absence of significant interaction between these components during pysolysis [274, 282].

Table 2: Learning procedure on dynamic tests : quality of the model with the best fit of parameters for each temperature level assessed as the standard deviation and the maximum error.

	Heating rate (°C/min)	Standard deviation (% DRM)	Maximum deviation (% DRM)
Spruce	10	0.45	2.27
	5	0.43	1.22
	2	0.35	1.57
	1	0.58	1.56
Poplar	10	0.53	1.43
	5	0.43	1.09
	2	0.55	1.31
	1	0.50	1.00

4.2 Validation on static experiments

So far, we proved the ability of the kinetic model to represent a quite large pyrolysis database with a moderate number of identified parameters. In this section, the model will be tested on a completely different experimental database, the set of static tests. The experimental and predicted DRM curves are depicted in figure 3. It is worth mentioning that this is a true validation test : the parameters used in the model are the parameters derived from the dynamic tests of Table 2, without any further identification.

Overall, the predictions are in very good agreement, even with the static tests at moderate temperature (250 °C, 300 °C). These tests are severe due to their slow kinetics, without asymptotic behavior. Such good predictions obtained for this demanding validation confirm the resilience of the DAEM formulation in comparison with a set of simple chemical reactions occurring simultaneously or in cascade [94, 258]. The good agreement is confirmed by the computed residues (Table 5). This is an additional proof regarding the assumption of constant and common value for the pre-exponential factor A.

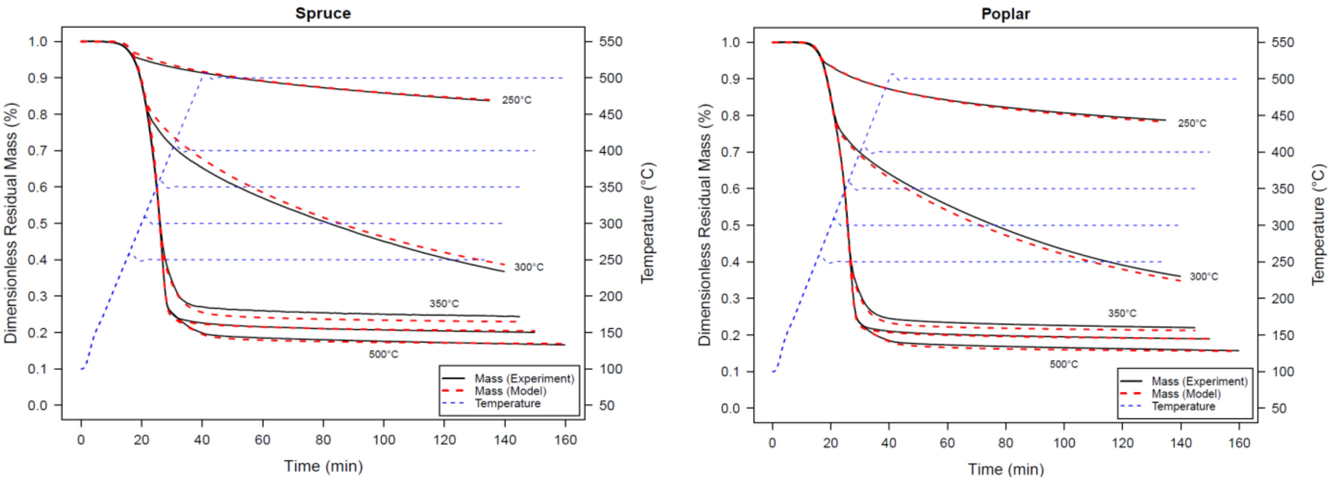

Figure 3. Model validation using a set of static experiments at different plateau temperatures (250 °C, 300 °C, 350 °C, 400 °C and 500 °C).

Table 3: Validation step on static tests : quality of prediction with the parameters fitted on the learning database for each plateau temperature assessed as the standard deviation and the maximum error.

	Temperature (°C)	Standard deviation (% DRM)	Maximum deviation (% DRM)
Spruce	250	0.39	1.22
	300	1.62	2.87
	350	1.48	1.92
	400	0.42	2.14
	450	0.44	2.18
	500	0.51	2.17
Poplar	250	0.32	0.53
	300	1.21	1.64
	350	0.96	1.33
	400	0.33	1.66
	450	0.83	1.93
	500	0.55	1.49

The rate of decomposition, the first derivative of the differential thermogravimetry (DTG) curves, depicts more detail during the decomposition process as it is more affected by slight changes during the reactions. Comparing experiment and model prediction in terms of derivative is very challenging as it is likely to reveal any differences between the curves. For the sake of example, the results obtained for poplar are shown in figure 4. One might observe that the experimental derivative is noisy, which is a classical effect when deriving an experimental curve. Yet, the DAEM model perfectly predicts the degradation rate, both in terms of position and intensity, over the wide range of temperatures of these static tests. This is an additional and convincing proof of validation. The test at 250 °C depicts a very small DTG peak at 20 hours, due to the partial degradation of hemicelluloses occurring at this temperature level. The peak significantly increases at 300 °C and spreads over slightly longer times. For tests at 350 °C, the shape clearly depicts a double peak by its shoulder on the left side due to the degradation of hemicelluloses followed, at around 350 °C, by the deep and narrow peak formed by the sudden degradation of cellulose. As the degradation of these two components is almost complete at 350 °C, the shape and maximum amplitude are no longer affected at higher temperature values.

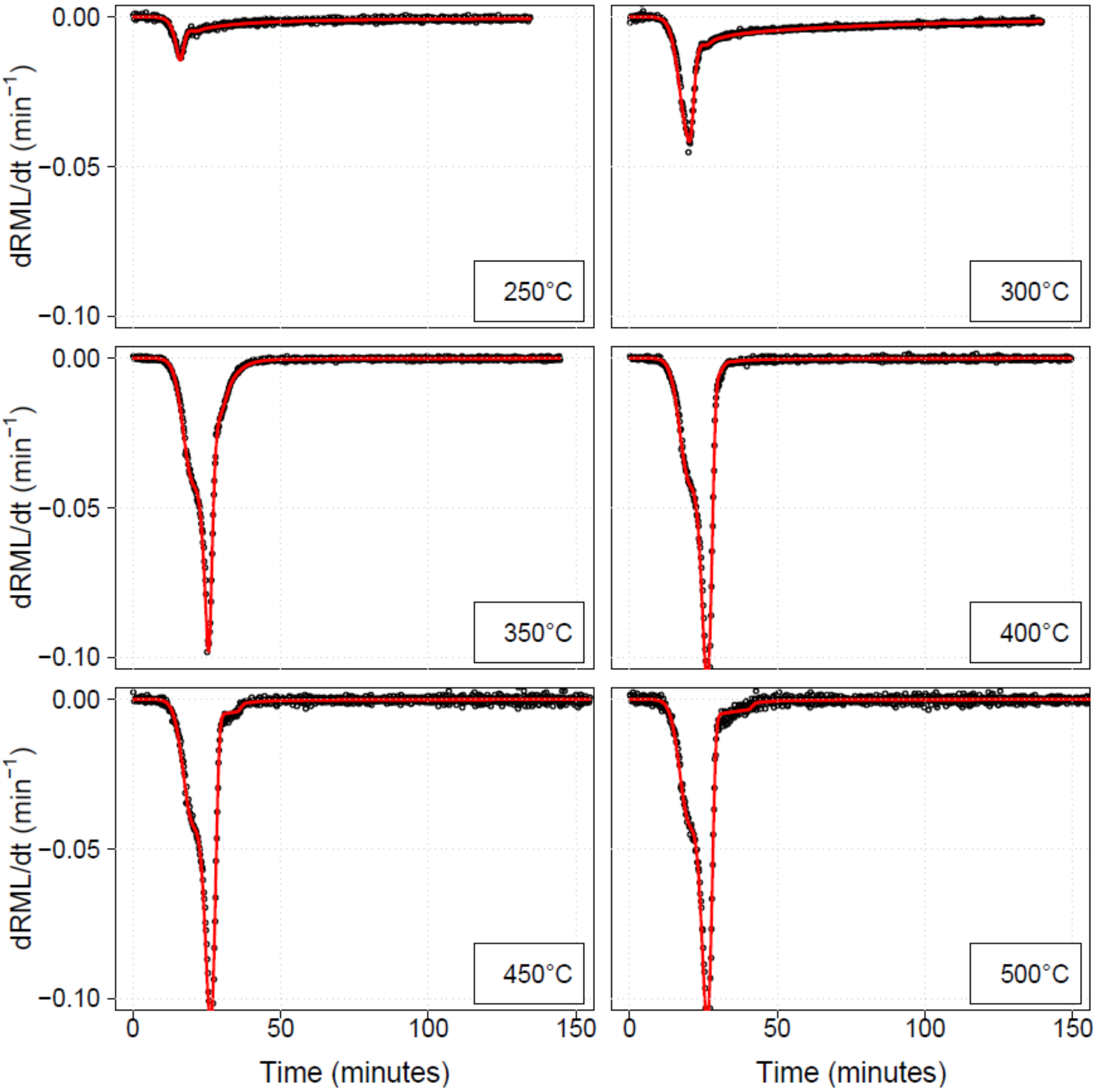

Figure 4. Model validation : experimental (black circles) and corresponding simulation (red lines) of the derivative of DML for the set of static tests Case of poplar.

4.3 Reaction enthalpies

The DSC signal of two types of wood have been analysed to determine the reaction enthalpies. In order to reduce the problem of baseline drift and thanks to the confidence in the DAEM model provided by the validation step, the dynamic tests at 5 °C/min were used to identified the reaction enthalpies using the formulation presented in section 3.4 (equ. 26). The test at 10 °C/min was likely to present an even lower baseline shift, but has been discarded due to its noise level.

Figure 5 shows the experimental DSC signal for spruce and poplar as red lines. The model prediction, as computed using equation (26) and after parameter indetification, appears in these figures as blue dashed lines. Note that positive DSC values represent an exothermic behavior (heat removed from the sample) and negative values an endothermic behavior (heat provided to the sample).

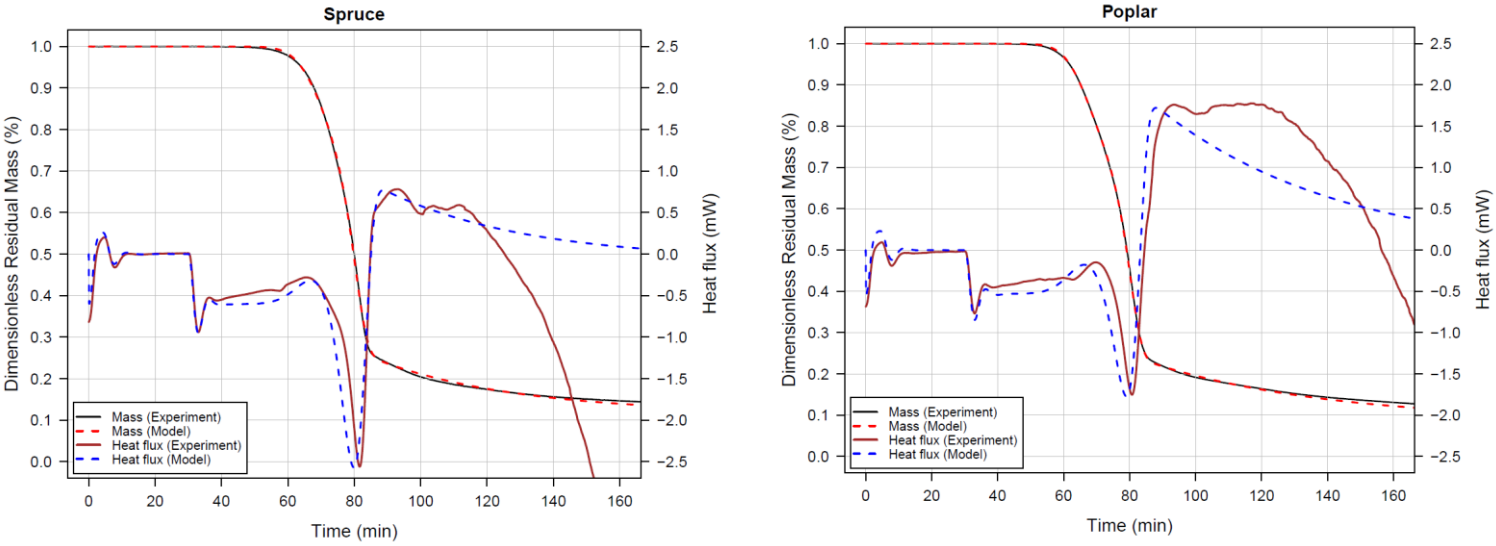

Figure 5. DSC curves to determine reaction enthalpies of spruce and poplar using the dynamic experiments at 5 °C/min.

During the drying period (plateau at 100 °C), the heat flux needed to water evaporation appears on the experimental curve. This is not present in the model as evaporation is not included in equation 26. At the end of this plateau, the temperature is constant and evaporation stops : consistently, the experimental and simulated heat fluxes are equal to zero. After this plateau, the temperature increases linearly in time, which required the sensible heat to be supplied to the sample. The experimental overshoot is due to the control of the furnace temperature. It can be nicely reproduced by the model as the actual furnace temperature is included in equation 26. While the temperature remains low, no thermal degradations occur : this range is suitable for the determination of the heat capacity. A first exothermic effect can be observed for both species between 60 and 70 minutes (which correspond to the temperature range 250 °C to 300 °C). This peak can be captured by the reaction enthalpy of the first distribution. It is probably due to the charing reaction of hemicellulose, as solid char forms during the primary decomposition at 200-400 °C [4, 235]. At 80 minutes (ca. 350 °C) an important endothermic peak is evidenced. This corresponds to the rapid and important mass loss observed during this period. This large endothermic peak is tied to the decomposition of cellulose, which has the highest percentage in biomass and has endothermic pyrolysis characteristic, at this temperature most portion of cellulose decomposes. Afterward, the decomposition of lignin together with secondary reactions including charring and aromatization result in the last and important exothermic peak of the DSC curves [182, 283]. To some extent, the decomposition and phase transformations of inorganic matters in ash might also be involved [284, 285].

The difference peaks and troughs of the DSC curves found in our measurements are in good agreement with the analysis performed on the different components of wood [286]. The enthalpy values determined for both spruce and poplar are summarised in table 4. The identified heat capacity is similar for spruce and poplar. These values are a bit low compared to published values [287]. Prior to the tests, the device was calibrated using sapphire as reference material and, up to 873 K, the values were in a $\pm 5\%$ agreement with published data [288]. A slight production of heat by thermal degradation is likely to explain the obtained values.

The heats of reaction related to the first Gaussian distribution are slightly exothermic. They allows the first heat flux increase at the beginning of mass loss to be obtained (-140 and -120 kJ/kg for spruce and poplar, respectively). The values obtained for the second Gaussian distribution are definitely endothermic (+339 and +338 kJ/kg for spruce and poplar, respectively). These values were needed to explain the deep decrease of the heat flux during the phase of rapid mass loss, tied to the degradation of cellulose. Finally, very large exothermic values are needed for the third distribution to explain the spectacular increase of heat flux just after the trough of the curve. This heat production should be obtained with a very limited additional mass loss, which explains the high value as the unit for the enthalpy of reaction is in kJ per kg. Note that these values are in agreement with the values obtained by [174] in the reaction branch producing char and gas. Contrary to all other data that were similar for spruce and poplar, this third reaction enthalpy has a much higher absolute value for poplar (-4300 kJ/kg to be compared to -1900 kJ/kg for spruce). This is consistent with the peak of the heat flux values, much larger for poplar than for spruce. The same trends were observed for all tests, whatever the heating rate (not show here).

At the highest temperature levels, the predicted curves differs from the experimental curves. This is likely to be due to the change of radiative properties between the empty crucible and the crucible with the degraded sample [174]. To address this problem, we performed tests with a lid, but, as the presence of a lid changes the mass loss, the DAEM model was not valid any more.

Table 4: Enthalpy for decomposition reactions obtained for spruce and poplar by adjustment on the 5 °C/min dynamic tests. Positive value indicates endothermic reaction, and negative value exothermic reaction.

Biomass	$C_p (J/(kg \cdot K))$	$\Delta H^1 (kJ/kg)$	$\Delta H^2 (kJ/kg)$	$\Delta H^3 (kJ/kg)$
Spruce	720	-140	+339	-1900
Poplar	650	-120	+308	-4300

5. Use of model

In the previous section, the DAEM parameters has been identified on the learning database. The proposed choice of distributions required only 9 independent parameters : 3 activation energy $E_0(n)$, 3 weighting factor $V^{n,\infty}$, 1 standard deviation $\sigma(1)$, β and the pre-exponential factor A. The DAEM model was then successfully validated using very different temperature-time routes. Thanks to this success, the model was be further used to determine the enthalpies of reaction. In this section, the model is used for prediction purposes: prediction of the pathway in the Van Krevelen's diagram and the control of the temperature rise to limit the released energy.

5.1 Elemental analysis

The results of ultimate and proximate analysis for untreated spruce and poplar are summarized in table 5. The nitrogen content was lower than 0.1% for native samples and lower than 0.3% for treated samples. Sulphur was not detected in any sample. These values are, at best, of the order of the experimental accuracy and were therefore not reported in this table.

Table 5: Ultimate and proximate analysis of native spruce and poplar.

Biomass type	Proximate analysis (wt.%)			Ultimate analysis (wt.%)		
	VM	Ash	FC	C	H	O
Spruce	84.93	0.29	14.77	47.07	5.97	43.65
Poplar	86.29	0.37	13.34	48.06	5.95	43.76

The remaining biomass char of each static test has been collected to determine char yield and to perform elemental analysis (Table 6). For both spruce and poplar the H/C and O/C ratios decrease simultaneously, indicating a pathway towards pure carbon. This is a classical finding in heat treatment of biomass : H and O contents decrease due to the volatilization of organic components into gas with low molecular mass.

Table 6: Char yield and ultimate analysis of pyrolysis char from spruce and poplar powder in static tests.

	Temperature (°C)	C(wt.%)	H(wt.%)	O(wt.%)	Char yield (wt.%)
Spruce	250	50.77	5.7	39.69	76.67
	300	65.26	4.27	24.53	27.87
	350	71.01	3.09	19.19	24.70
	400	74.28	3.05	15.24	21.54
	450	79.22	3.11	12.42	19.45
	500	82.67	2.88	9.49	17.42
Poplar	250	50.30	5.65	40.10	76.55
	300	62.28	4.75	28.32	32.94
	350	70.90	3.23	19.99	21.57
	400	74.44	2.86	16.44	18.94
	450	77.11	2.87	13.21	16.91
	500	81.50	2.63	9.62	15.73

Figure 6 plots the O/C and H/C ratios found for the different plateau temperatures in a Van Krevelen's diagram [22]. At increasing temperature levels, the positions of char in this diagram move towards the down-left corner which represents highly carbonized material. The difference between spruce and poplar observed at low temperature is not visible on this diagram. On the contrary, char from poplar stands beneath that of spruce for the most severe conditions, indicating that poplar has more prone to charring than spruce for severe pyrolysis.

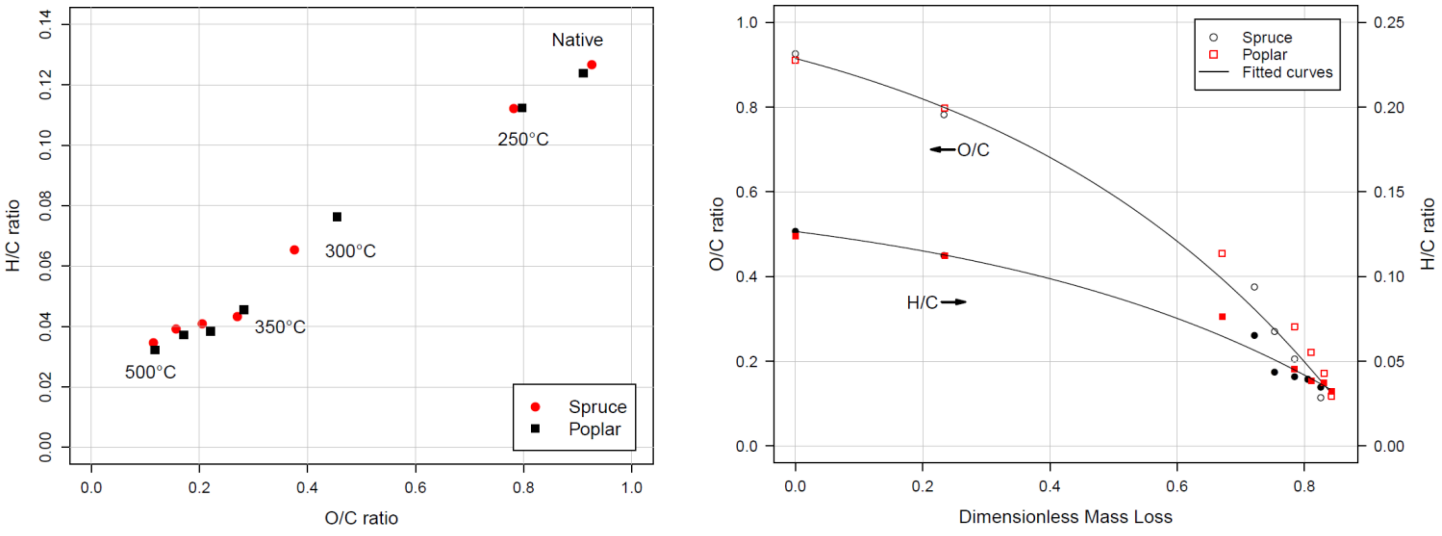

Figure 6. a) O/C and H/C ratios from char of spruce powder and poplar powder and corresponding biomass, b) O/C (open markers) and H/C (plain markers) ratios as a function of dimensionless mass loss (DML). Experimental data and fitted curves.

The difference between the two species is however quite low when plotted as a function of Dimensionless Mass Loss (DML). This allowed us to propose a single set of equations fitted to predict the O/C and H/C ratios as a function of DML:

$$\begin{aligned} O/C &= 1.134 - 0.219 \times \exp(1.815DML) \\ H/C &= 0.1534 - 0.0268 \times \exp(1.783DML) \end{aligned} \qquad (27)$$

Obviously, for prediction purpose, the DML value can be predicted by the validated DAEM model for any time-temperature pathway using equations 18-20.

5.2 Process control

All the kinetic parameters as well as the reaction enthalpies confer a predictive potential to the code. Its eventual purpose is to be implemented in a multi-scale macroscopic particle model, able to deal with the non-uniform variable fields within the particle [219] or with a packed-bed [264, 289]. Such a work is in progress in our team. Even at the micro-particle scale, the prediction potential of the model can be tested. For example, limiting the heat flux due to reactions might be important to minimize the temperature perturbation during ATG tests. Figure 7 compared two different temperature pathway :

(1) A linear temperature increase from 100 °C to 650 °C in 200 minutes

(2) An optimised control : the temperature increase is controlled to limit the heat flux in the range [-0.5 mW, +0.5 mW] for a sample of 10 mg as initial mass.

For case 2), a simple PD (proportional, derivative) control was implemented, which explains the small oscillations. However, it is obvious that the obtained temperature increase allows the same temperature range to be investigated over the experiment duration (200 minutes), while avoiding the heat flux peaks. One can see that the constraint reduces the temperature increase when the kinetics produces high values of heat flux. In order to give an in-depth view of the DAEM model, we plotted the evolution of the three distribution in the case of the optimised control (Fig. 7). The first Gaussian distribution is wide with low activation energy. Consequently, this is the first one to be affected by heat. It gradually disappears, starting to the left-hand side, which represents the lowest activation energies. This peak completely disappears after ca; 50 minutes. The second peak is very narrow and no difference of kinetics may be observed over the, very small, distribution energy. Following the rapid mass loss depicted by all the previous curves, its degradation lasts over a short time interval and disappears completely very soon after the first distribution. Finally, the last distribution is non-symmetrical and depicts a very wide range of activation energies. Again, the kinetics affects the left-hand side of the distribution. After 200 minutes, most of the large values from the left-hand sides disappeared (one has to remember that the initial shape is an exponential curve). However, the right-hand side, which contains very large values of activation energy (above 200 kJ/mol) are not degraded yet. This is consistent with the lignin behaviour, whose degradation spreads over a very large temperature range.

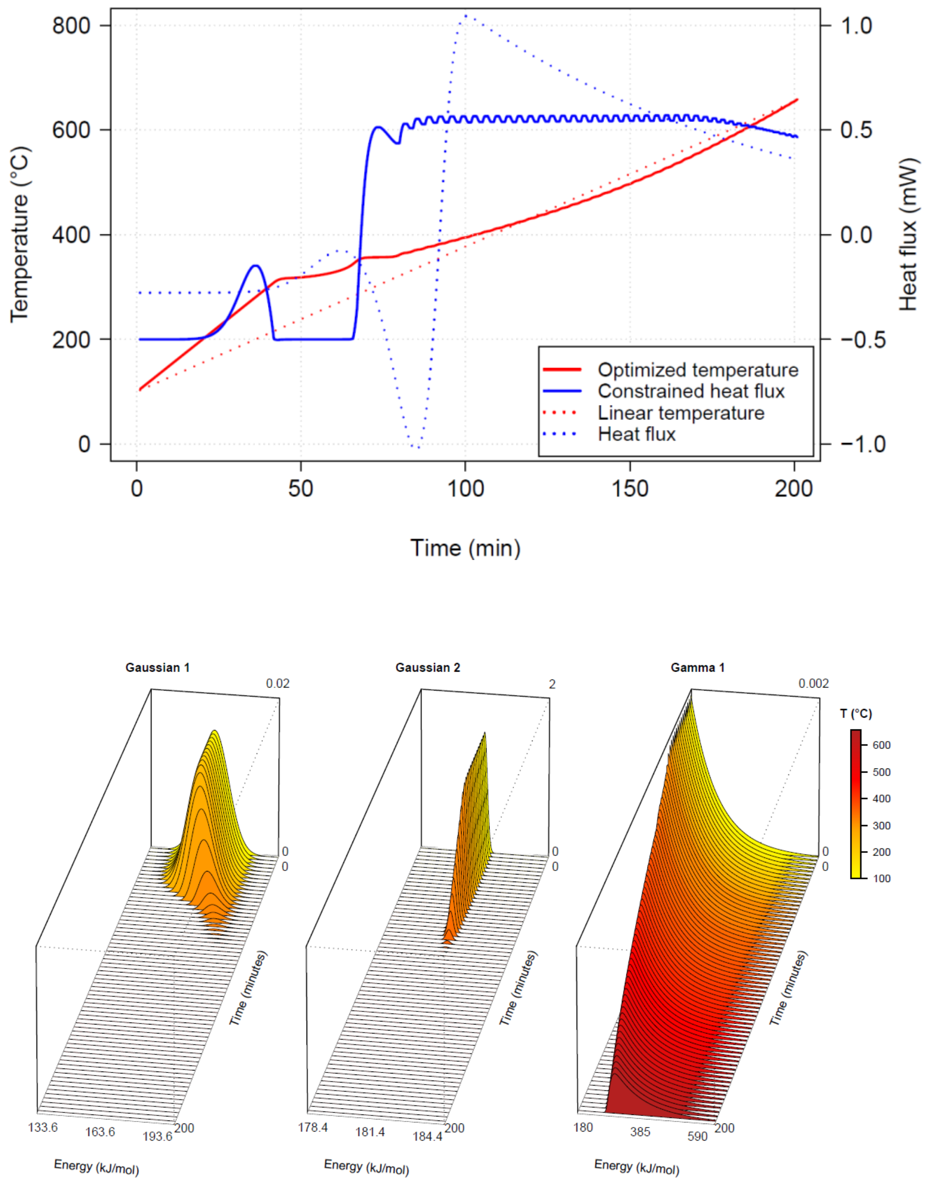

Figure 7. Top), Temperature and heat flux evolution for a constant heating rate and for an optimised temperature profile. Bottom) Evolution of the residual parts of each distribution for the optimised temperature profile.

6. Conclusion

A robust three-distribution DAEM model was derived to simulate two types of lignocellulosic products over a wide range of treatment time and temperatures. The comprehensive approach includes i) parameters identification using a learning database (dynamic tests with different heating rates), validation with static tests ranging from 250 °C to

500 °C and iii) the use of the measured heat flux to determine the heats of reaction. The potential of the model has been highlighted by two application examples : the prediction of the biomass pathway in the Van Krevelen's diagram and the use of the heats of reaction to control the process at the micro-particle level.

The main outcomes of this work are as follows :

(1) The kinetics and heat flux formulation are presented in detail, as well as the computational strategy to correctly solve these equations, which is intended to serve as a guide for the reader,

(2) To use of a gamma distribution allows the model to include only 9 independent parameters,

(3) In spite of its sparcity, the model perfectly predicts the kinetics over a large range of temperature and duration, for dynamic and static tests

(4) Heats of reactions were determined using the experimental DSC signal

(5) The model has a great prediction potential, including as local model to be included in a multiscale approach

In the near future, this reaction model will be embedded in a comprehensive heat and mass transfer computational code to model the process at the level of a large particle or of a packed-bed of particles. One specific point to be addressed is the crucial question of thermal runaway. Such simulations will be compared to experimental results to check whether or not the heats of reaction identified on powders, with or without lid, remain pertinent for large particles. To the best of our knowledge, this is still an open question that deserves consideration.

Acknowledgement

Financial supports from Grand Reims, the Marne department and the Grand Est region are gratefully acknowledged. Yong Tian acknowledges the financial support by the China Scholarship Council (CSC) for the opportunity to study in France.

Chapter 6 Thermogravimetric experiment and multi-distribution DEAM for various particle sizes.

This chapter is mainly devoted to the study of the effect of particle size on the pyrolysis kinetics. The mechanisms will be closely studied by both experimental and numerical methods. Five different particle shapes of two wood species allowed a comprehensive investigation on kinetic variations, and the proposed two-Gaussian+ exponential DAEM was used to reveal the changes of kinetic parameters when particle size changed. More importantly, model’s prediction ability was validated by additional experiments performed at multiple static temperature levels, and being further extended to predict char compositions among different of particle sizes.

- This work is submitted to **FUEL.**

Effects of particle size on the pyrolysis of spruce and poplar: thermogravimetric analyses, DAEM modelling, validation, and prediction of secondary charring

Yong TIAN[a*], Patrick PERRÉ[a,b]

[a] LGPM, CentraleSupélec, Université Paris-Saclay, 3 Rue Joliot Curie, 91190 Gif-sur-Yvette, France

[b] LGPM, Centre Européen de Biotechnologie et de Bioéconomie (CEBB), 3 Rue des Rouges Terres, 51110, Pomacle, France

[*]Corresponding author.

E-mail address: Yong.Tian@centralesupelec.fr (Yong TIAN), patrick.perre@centralesupelec.fr (Patrick Perré)

Abstract:

Particle size plays a crucial role in biomass pyrolysis mechanisms and their subsequent industrial uses. However, an applicable kinetic method that combines thermogravimetric data with distributed activation energy model (DAEM) adapted to the sample size is still missing. This work investigated pyrolysis kinetics of two wood species (spruce and poplar) with five particle shapes (powder, particle, 5-mm diameter cylinders with heights of 1 mm, 2 mm, and 4 mm) and one additional reaction condition (powder with lid). The experimental data were numerically simulated by a two Gaussian + one exponential DAEM distributions. Thermogravimetric results evidenced a significant effect of particle geometry on char yields, which increased by 81% and 66%, from powder to 4-mm high cylinders, for spruce and poplar respectively. The increase in particle size and use of a crucible lid led to an increase of exothermic heat. Elemental analysis demonstrated a contradictory relation between carbonization and mass loss, which was explained by secondary charring. Synthetic indexes built from the kinetics parameters of the DAEM model clearly depicts the effect of particle sizes. The prediction ability of the model was checked by further experiments performed at different time-temperature patterns with several particle sizes. Finally, correlations between dimensionless residual mass (DRM) and element compositions allowed us to determine the composition of secondary charring, which consists mainly of carbon. The elemental composition of char can therefore be predicted using the difference of DAEM kinetics between fine powder and a given particle size.

Keywords: Biomass; Elemental analysis; Particle size; Pseudo-component; Wood.

1. Introduction

Lignocellulosic biomass is an important renewable energy source for the worldwide energy supply. Its large deposits and carbon neutrality offer an enormous potential to meet future energy demands and reduce environmental pollution [290]. Pyrolysis is part of the thermochemical route to convert biomass into high value-added chemical products: bio-oil, charcoal, and gaseous fuels. It is the initial step before further thermochemical technologies such as combustion and liquification, making pyrolysis a key link in the BtL (biomass to liquid) industrial chain and subsequent exploitation. Process factors including temperature, heating rate, particle size, and residence time could effectively alter product categories and yields [4, 147, 196]. Among them, the particle size specifically affects the pyrolysis mechanism in relation to volatile interaction, mass, and heat transport, which imposes strict requirements on industrial reactors [291]. Therefore, both experimental and theoretical kinetic works are necessary to determine and predict the effect of particle size.

A considerable number of studies have been conducted to test the effect of particle size on biomass pyrolysis. Mass and heat transfer were severely affected in large particles (>1.5mm) during both pyrolysis experiments and modeling [292]. Di Blasi [293] calculated that, in terms of thermal transfer, particle size affects the internal heating rate in fast pyrolysis, which decreased from 760 °C /s to 23 °C /s when the particle diameter was increased from 0.1 mm to 1 mm. Okekunle [294] found the intra-particle temperature gradient increased with particle size and aspect ratio, which promoted intra-particle char formation. Perré and co-workers [219, 264] developed comprehensive computational models that emphasized the effect of particle size or particle beds on the evolution of the temperature profiles, with opposite effects in the heating period and during the reaction period due to exothermic reactions. A model developed by Anshu [295] claimed more devolatilization delay occurred in larger biomass samples because of intra-particle transfer retardation. Suriapparao [296] and Acma [297] found higher apparent activation energy with increasing particle size due to mass transfer limitation and the intra-particle thermal gradient.

It was concluded that increasingly non-isothermal processes in large particles led to low oil and high char yields [298, 299]. Shen [159] postulated that a decreased heating rate in large particles was primarily responsible for lower bio-oil yield, and the fiber destruction in small particles favored high oil yield. Ayhan [300] observed an elevated char yield when particle size increased, while a high heating rate led to char yield reduction in small particles. Zhou [160] proved that physical trapping of thermally ejected oligomers occurred as a function of particle size, from milled particles (0.3–0.55 mm) to cylinders (3–14 mm). Westerhof [161] argued that physical retainment of vapors or aerosols caused excessive volatile condensation in large particles and cylinders.

With an increase in particle size, the added cellular- and tissue-scale barriers have an increasing impact on pyrolysis [301]. More specifically, the effects due to size have two origins: (1) different degrees of destruction of fiber structures in milled particles; and (2) different dimensions in an integral cylinder or chip. In the first origin scenario, milled samples lose most typical wood channel structures. Small particles usually impose less resistance on both heat and mass transfer profiles due to their microstructures; tissue expansion and lumina cell wall stretch are therefore less restricted [301], leading to easier volatile release. For the second origin scenario, geometry differences in cylinders cause hermetic spaces and anisotropic channels that can obstruct internal volatilization to varying degrees, and the vapor outflow pattern is largely affected by internal heat transfer limitations [161]. The increase of particle size, in this case, delays volatile’s escape inside the material matrix and offers additional possibilities for secondary charring. Moreover, axial conductivity values have been found to be three times larger for thermal transfer and fifteen times larger for mass transfer than the radial conductivity values [302], larger anisotropic degree in the large cylinder leads to significant temperature gradients and flow gradients, generally causing volatile blockage and char generation [303].

Secondary reactions in biomass pyrolysis usually occur in two competitive pathways: charring and cracking, leading to carbon deposition and gas production, respectively. As long residence times of volatiles in hot zones favor polymerization and carbonization, the reduction of heating rate inhibits complete vaporization [304], and high pressure stimulates carbonization by concentrating the vapor phase [305]. All these process parameters help secondary charring prevail over cracking. Meanwhile, other factors such as chemical compositions, density, and the presence of inorganics (alkali metals) also influence secondary charring [306, 307]. In contrast, cracking converts volatiles into small molecular gases normally accompanied by short residence times, high heating rates, or dilute vapor phases [308].

Regarding the main constituents of biomass, hemicellulose undergoes charring through rearrangement reactions of polysaccharides and further demethylation [86]; cellulose undergoes secondary charring by the depolymerization of levoglucosan [309]; lignin is a fine charring precursor due to its original high aromatic ring content, whose short substitutes cleaves increase the aromaticity and reticulation in the residue over the temperature range of 500–800 °C [86].

It is worthwhile to investigate the effect of particle size using a kinetics model that can be used in complicated multi-scale simulations and operational controls in industrial processes [310]. The DAEM is an efficient and robust approach to represent the kinetics of complex decomposition reactions [90], and at present, is widely used to model the pyrolysis of biomass [108, 215]. The model assumes that biomass pyrolysis occurs as a series of independent and parallel reactions with continuous activation energy distributions, representing the variability of interactions due to complex macromolecular structures and their interactions in the cell wall [94]. Three-parallel-distribution DAEM presents an even more accurate approach to the description of the pyrolysis kinetics of various lignocellulosic biomasses [93, 106, 234], and the interpretation of pseudo-components as chemical constituents (hemicellulose, cellulose, and lignin) is justified as a useful method in kinetic research [252, 311]. The kinetic additivity of the three main constituents provides universal applicability for various biomass species [312], being crucial for single-particle reaction kinetics as well as large-scale process implementations. However, the nature of devolatilization theory in the DAEM formulation makes it difficult to account for recondensation and secondary charring reactions among different particle sizes. DAEM has rarely been applied to distinguish the effects of particle size; furthermore, the three-distribution DAEM has never been employed to distinguish the kinetics of different particle sizes. The two Gaussian + one exponential DAEM was recently proved to be very efficient in handling multiple temperature profiles and complex heat fluxes, including at the validation stage [162]. Hence, this model was applied in the present work to analyze the pyrolysis kinetics of different particle sizes.

This study aims to investigate the effects of particle size by coupling thermogravimetric kinetics and numerical methods. Thermogravimetry (TG) and differential scanning calorimetry (DSC) will be performed at two heating rates for a wide range of particle sizes. Elemental analyses will demonstrate that the relation between carbonization and mass loss is directly linked to the particle size. Further, Synthetic indexes will be built from the kinetics parameters of the DAEM model to clearly depict the effect of particle sizes. Importantly, the prediction ability of the model will be validated using an additional set of experiments performed with different temperature pathways: a linear increase of temperature followed by a plateau at constant temperature (different temperature levels will be performed). Finally, correlations between mass loss (ML) and element compositions will allow us to determine the composition of secondary charring. This composition will be used to predict the elemental composition of char for a given particle size.

2. Material and methods

2.1 Material

One gymnosperm and one angiosperm species were used in this study: European spruce (*Picea abies*, softwood, 450 kg/m^3, cut from a 73-year-old tree grown in the forest in the Auvergne region, France) and poplar (*Populus euroamericana* ‘Koster’, hardwood, 364 kg/m^3, cut from a 25-year-old tree grown in the forest in La Suippe Valley in la Marne, France). The complete sample preparation protocol is depicted in Figure 1. Second-bottom tree logs (2 m long, cut at 2 m high above the ground) of 40–50 cm diameter were used. They were cut evenly into 2.5 cm-thick boards, and the one 10 cm from the pith was taken for the present study. Rectangular sticks of 2.5 cm × 2.5 cm × 20 cm (length × width × height) were cut from a healthy sapwood part of the board to ensure uniform properties. The stick was further processed into cylinders with a diameter of 5 mm and a length of 3 cm by a lathe (PROMAC 961V), then cut into small cylinders by a precision cut-off machine (Struers, Secotom-15) with two successive sequences of 1 mm, 2 mm, and 4 mm. The rest of the stick was ground with an M20-IKA universal mill, then put into sieve stacks of 0.063 mm, 0.08 mm, 0.63 mm, and 0.8 mm opening sizes on a vibratory sieve shaker (RETSCH AS 200) at 90% amplitude for 30 minutes. The sieving cut between 0.063–0.08 mm was taken as wood powder, and the cut between 0.63–0.8 mm was taken as wood particles. The strict protocol defined here is intended to limit any difference in composition between all types of samples and to constrain the size of the small particles. Therefore, it is reasonable to assume that differences in pyrolysis behavior were derived exclusively from the particle geometry. After the preparations, all samples were dried at 105 °C in an oven for 24 h and stored in a desiccator.

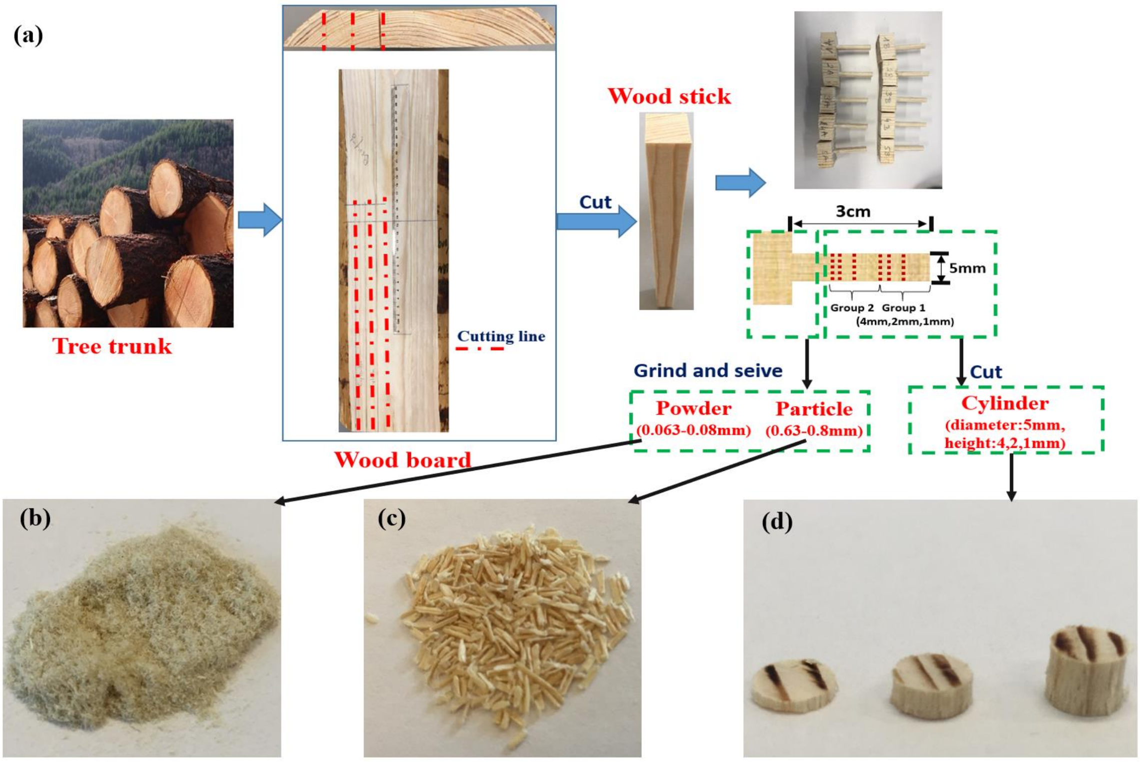

Figure 1. (a) Flow chart of the preparation protocol of the wood samples; and pictures of three scales of samples (using spruce as an example): (b) powder, (c) particles, and (d) cylinders.

Ultimate and proximate analyses were conducted in a Thermo Fisher Scientific FLASH 2000 organic elementary analyzer and a Nabertherm LV/9/11 furnace, respectively, by the standards ASTM E1755 and E872. The basic chemical properties of two types of wood on a dry basis are shown in Table 1.

Table 1. Proximate and ultimate analysis of spruce and poplar

Biomass type	Proximate analysis (wt.%)			Ultimate analysis (wt.%)		
	Volatile	Ash	FC	C	H	O
Spruce	84.93	0.29	14.78	47.07	5.97	43.65
Poplar	86.29	0.37	13.34	48.06	5.95	43.76

The microstructures of the samples are shown in Figure 2. Powder and particles were analyzed by environmental scanning electron microscopy (ESEM, FEI Quanta electron microscope), and cylinders were examined using 3D X-ray tomography (RX Solutions EasyTom XL Ultra 150-160). For both spruce and poplar, the differences in microstructure between the different particle sizes were obvious. The powder presented broken, fragmented pieces, with damaged lumens and inner cell wall structures were largely exposed. Particle samples preserved the cellular structure of wood: cells retained partial intact structures and exposed lumens at the edges. As expected, wood cylinders maintained the original anatomical structure of wood. Spruce, despite obvious annual rings, had a uniform anatomical pattern that consisted mainly of tracheids. As a diffuse ring-porous hardwood, poplar presented two contrasting sizes of pore: vessels and fibers.

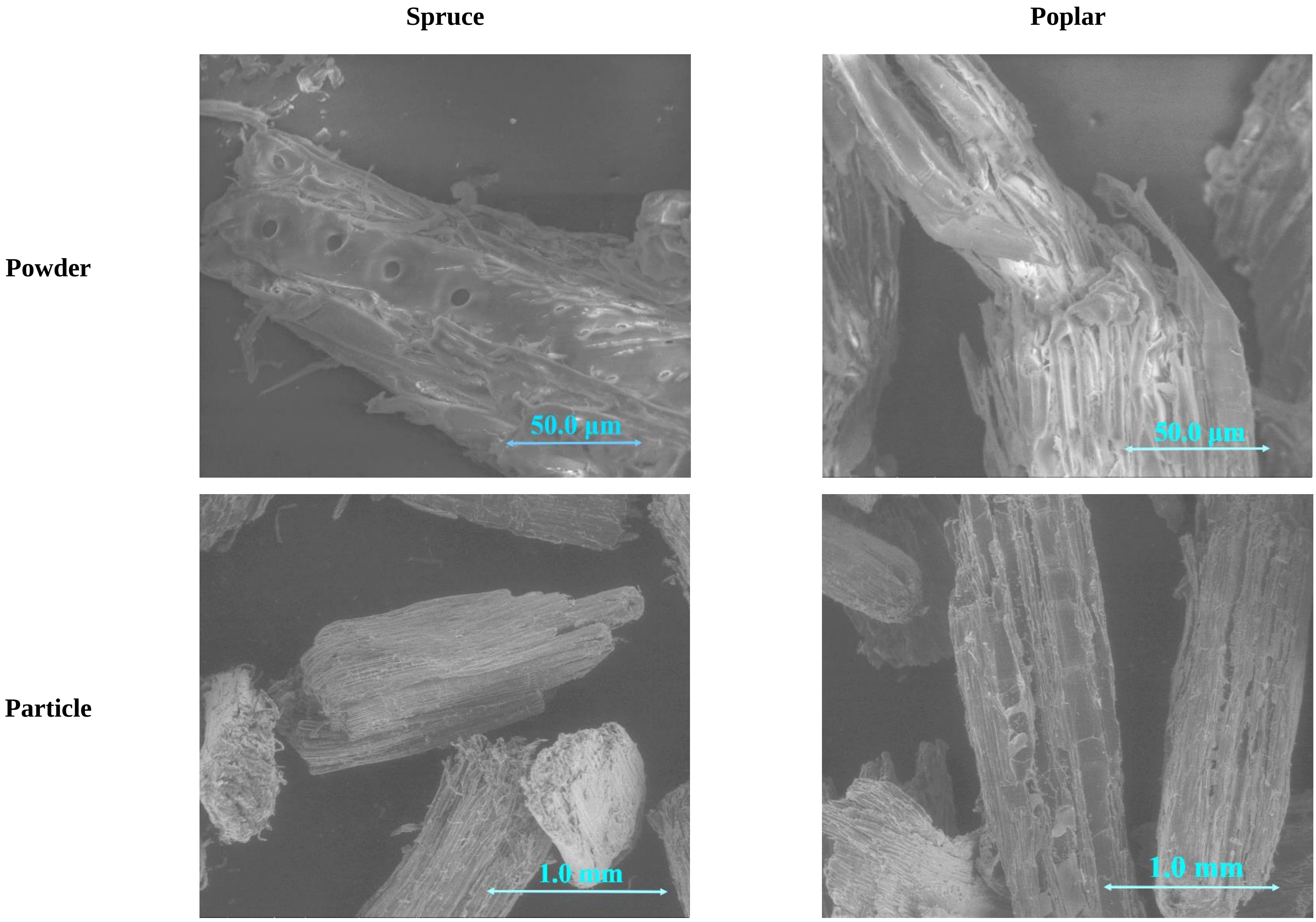

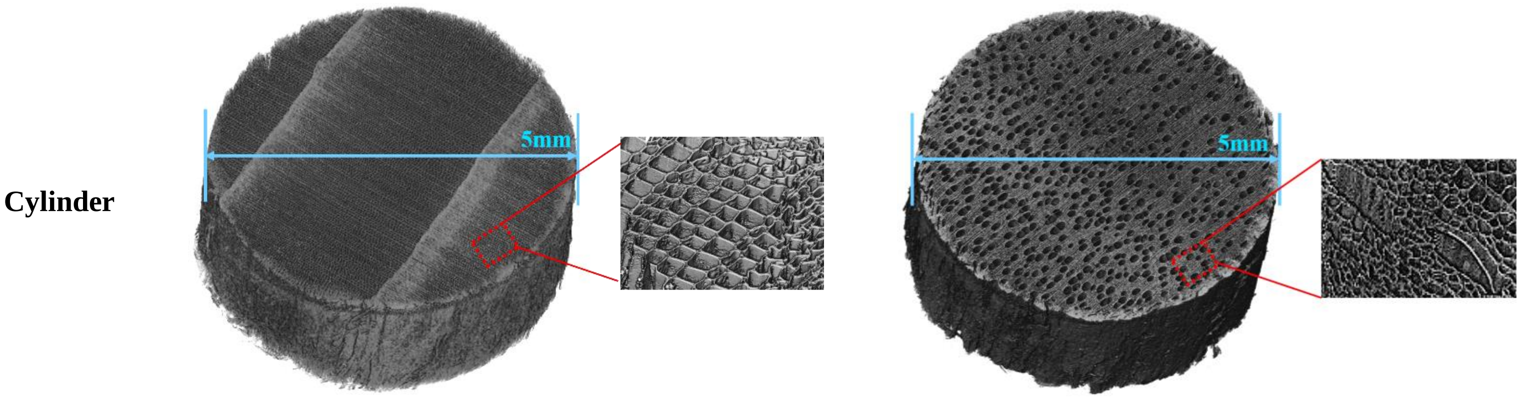

Figure 2. SEM images of biomass powder and particles, tomographic images of cylinders (spatial resolution: 3μm) of spruce (first column) and poplar (second column)

2.2 Experimental method

Wood pyrolysis was carried out in a thermogravimetric analyzer (STA 449 F3 Jupiter, NETZSCH). Thermal gravimetric (TG) and differential scanning calorimetry (DSC) signals were simultaneously acquired at a time interval of 0.1 min. Measurements were conducted under a nitrogen purge (99.999%) of 50 ml/min and a protective gas flow of 20 ml/min. Dynamic tests at two heating rates (1 °C/min and 10 °C/min) were applied for all wood samples. The program began by heating the sample from 30 °C to 100 °C at 10 °C/min and was held for 30 minutes to eliminate the residual water in sample. Then the temperature was increased from 100 °C to 800 °C at the aforementioned heating rates. Finally, the temperature dropped to 30 °C with unchanged nitrogen sweeping. Additional tests with a pierced lid (central hole of 0.5 mm) were also performed with biomass powder. Therefore, three particle geometries: powder, particles, and cylinders (heights: 1 mm, 2 mm, and 4 mm) together with another type of reactor (crucible with lid) resulted in six sample configurations performed for spruce and poplar at two heating rates. In addition, static tests were performed for validation purposes. Their temperature programs began with the same sequence, heating powder samples from 30 °C to 100 °C at 10 °C/min and holding for 30 minutes. Then the temperature was raised at a rate of 10 °C/min to the plateau temperature (from 250 °C to 500 °C by an increment of 50 °C plus one test at 800 °C). The plateau temperature was maintained for 2 h, followed by cooling to 30 °C with unchanged nitrogen sweeping.

Temperature and sensitivity calibrations were performed specific to crucible type, temperature rate, and gas type. The certified standards (NETZSCH calibration set) include indium, tin, bismuth, zinc, aluminum, and silver. The accuracy of the DSC signal was also checked with sapphire, according to the NETZSCH handbook. Blank tests were conducted before every sample test with the same crucible to keep the same buoyancy effects and ensure the same heat capacity. Dimensionless residual mass (DRM) and conversion rate (X_{exp}) were used to process TG signals:

$$DRM(t) = \frac{m_t}{m_0} \times 100\%, \quad X_{exp}(t) = 1 - DRM(t) \tag{1}$$

where m_t is the remaining mass at time t, and m_0 is the anhydrous mass after the 30 minute plateau at 100 °C.

2.3 DAEM formulation

DAEM calculates the volatile contributions from parallel and irreversible first-order reactions. The integral form of conversion degree, $X(t)$, could be expressed as:

$$X(t) = \frac{V(t)}{V^{\infty}} = 1 - \int_0^{\infty} exp\left(-\int_{t_0}^{t} A_0 e^{-E/RT(t)} dt\right) f(E) dE \tag{2}$$

where V^{∞} is the theoretical total volatile amount, $V(t)$ is the volatile production at time t, E is the activation energy. The important assumption of keeping pre-exponential factors of all reactions as a constant, A_0, has been justified for accurate identification and model concision [162, 197]. R is the universal gas constant and $T(t)$ is the temperature at time t. $f(E)$ is the statistical function for describing the activation energy distribution.

Wood is treated as an aggregate of three pseudo-components based on the assumptions that no interactions exist during pyrolysis, and they correspond to three distributions ($f_j(E)$) with different weighting factors $V_{max}(j), (j = 1{,}2{,}3)$. The final formulation of biomass conversion degree is therefore expressed as:

$$X(t) = 1 - \sum_{j=1}^{3} V_{max}(j) \int_0^{\infty} exp\left(-A_0 \int_0^{t} e^{-E/RT(t)} dt\right) f_j(E) dE \tag{3}$$

In this work, two Gaussian and one exponential distributions are chosen for the excellent trade-off between accuracy and model conciseness [197]. Two Gaussian distributions are used to represent the first and second pseudo-components. They are formulated using the mean activation energy E_0 and standard deviation σ as:

$$f(E) = \frac{1}{\sigma\sqrt{2\pi}} \exp\,(-\frac{(E - E_0)^2}{2\sigma^2}) \tag{4}$$

The third pseudo-component is represented by an exponential distribution, one degeneracy form of the gamma distribution:

$$f(E) = \beta exp\left(-\beta \frac{E - E_{min}}{E_{min}}\right) \tag{5}$$

where β is the rate parameter and E_{min} is the minimum activation energy. The integral term of equation 3 demands further numerical discretization for each type of distribution, which has been presented in detail in our recent works [162, 197]. For better accuracy, the effective increment of chemical reaction dV_i over the time step is expressed in its original exponential form [220, 221]:

$$dV_i = [1 - exp(-k_i dt)](V_i^{\infty} - V_i(t)) \tag{6}$$

$$k_i = A_0 \exp\left(-\frac{E_i}{RT(t)}\right); \quad V_i^{\infty} = f(E_i) \cdot V^{\infty}; \quad V_i(t = 0) = 0 \tag{7}$$

which gives the final form of the conversion rate $X_{cal}(t)$ at experimental points $a(t_a)$:

$$X_{cal}(t) = 1 - \frac{1}{m_0} \sum_{t=0}^{t=t_a} \sum_{j=1}^{3} \sum_{i=1}^{2mn} [1 - exp\left(-k_i^j dt\right)](V_i^{j,\infty} - V_i^j(t)) \tag{8}$$

Finally, kinetic parameters in the three distributions are identified by optimizing the objective function *F*, which is the residual sum of squares (RSS) between the experimental conversion rate $X_{exp}(t)$ and the calculated conversion rate $X_{cal}(t)$. Here, N_{exp} is the total number of experimental values:

$$F(parameters) = \sum_{a=1}^{N_{exp}} \sum_{t=0}^{t_a} \left(X_{\exp}(t) - X_{cal}(t)\right)^2 \tag{9}$$

The numerical discretization was combined with in-house MATLAB code, and the derivative-free Nelder–Mead simplex algorithm [127] was used to minimize the objective function. Herein, an entire set of data from two dynamic tests was used to compute the objective function. In order to avoid local minima, the initial set of parameters was derived from the solution values obtained in our previous study [162]. In addition, intentional perturbations were applied after identification to restart the procedure and check the stability of the solution. To evaluate the discrepancy between experiments and model, two criteria, root mean square error (RMSE) and maximum deviation (D_m), were used:

$$RMSE = \frac{\sqrt{\sum_{a=1}^{N_{exp}} \sum_{t=0}^{t_a} \left(X_{exp}(t) - X_{cal}(t)\right)^2}}{N_{exp}} \tag{10}$$

$$D_m = Max\left|X_{exp}(t) - X_{cal}(t)\right|, \ \ \forall t \in [0, t_a] \tag{11}$$

3. Results and discussions

3.1 Thermogravimetric results

Figure 3 depicts the DRM curves of spruce and poplar at two different heating rates. Three distinct sections could be identified for both species. In the first temperature region, the DRM was stable from 100 °C to 200 °C. At this temperature, hemicelluloses melt into the liquid form [313], but the production of volatiles was very limited. The second region, from 250 °C to 400 °C, exhibited the most important release of volatiles due to the decomposition of hemicelluloses and cellulose. Within this region, random fragmentation of glycosidic bonds in cellulose and hemicellulose generated volatiles with high oxygen contents and left carbonaceous residues [314]. Lignin pyrolysis and secondary charring of volatiles mainly corresponded to the last region, from 400°C to 800 °C, where the main charring process occurred in the form of re-organization of benzene rings into polycyclic structures [86].

Mass transfer limitations occurring in large particles or the crucible with lid promoted final char yields, and major differences emerged in the last temperature regions, which clearly indicated different pyrolysis mechanisms. These deviations began around 330 °C at 1 °C/min and 370 °C at 10 °C/min for both spruce and poplar. The effect of particle sizes enlarged differences at high temperatures, where the mass loss was mainly associated with the rearrangement of residue in the charring process [315], including the important conversion of aromatic structures through demethoxylation [316], dehydration, cross-linking, and re-polymerization [308].

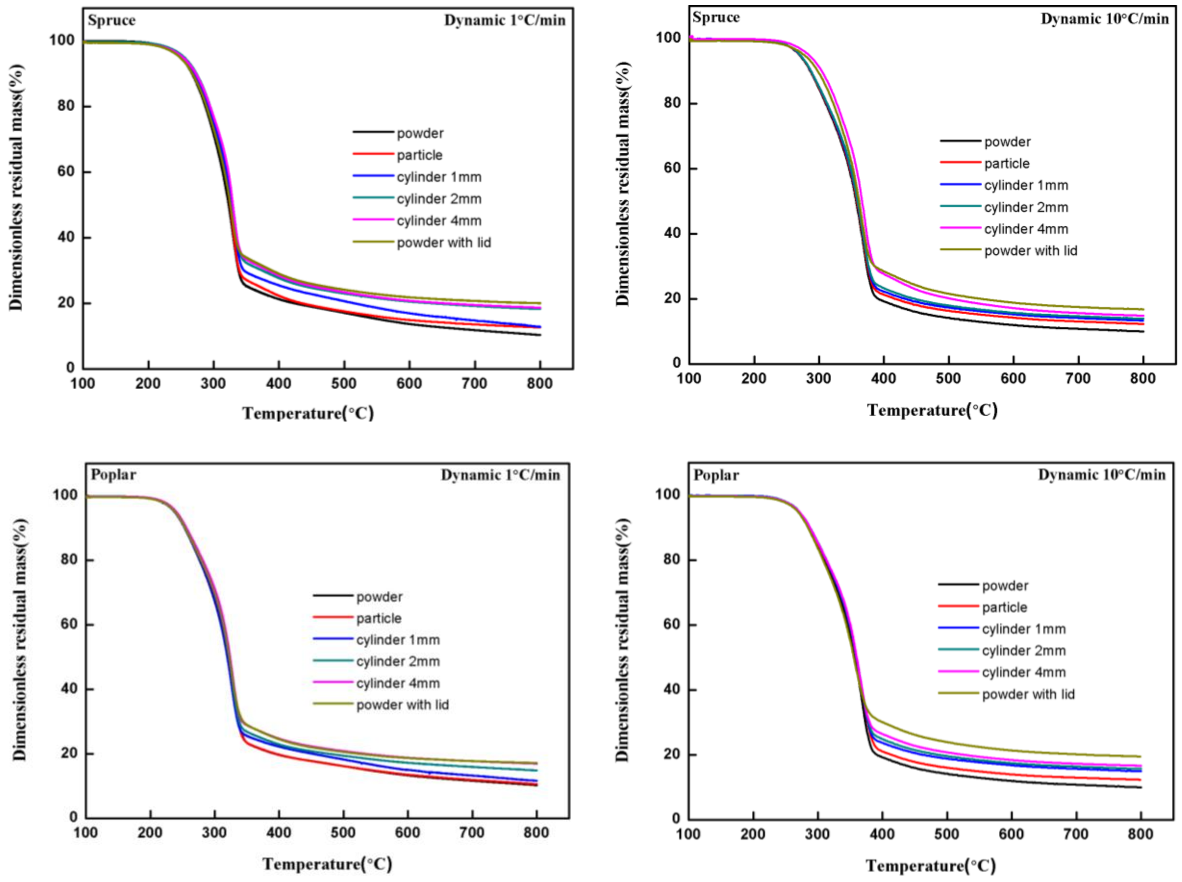

Figure 3. Pyrolysis DRM curves of spruce and poplar samples at two heating rates.

Table 2 lists the final DRM values (final char yields) of all particle types under all conditions. Owing to the open microstructure and fast release of volatiles, powder presented the lowest DRM values in all cases. Yet, together with the particle size enlargement from powder to the 4 mm-cylinder, kinetic differences turned into noticeable char yield increases. Spruce had an increase in DRM from 10.3 wt.% to 18.7 wt.% at 1 ºC/min and from 10.0 wt.% to 14.8 wt.% at 10 ºC/min, and poplar rose from 10.3 wt.% to 16.9 wt.% at 1 ºC/min and from 10.0 wt.% to 16.7 wt.% at 10 ºC/min. Therefore, setting the wood powder as a reference, the increase of particle size promoted char yields by 81% (1 ºC/min) and 48% (10 ºC/min) for spruce, and 65% (1 ºC/min) and 66% (10 ºC/min) for poplar. In contrast, the powder with a lid exhibited the maximum increase for all cases, confirming the charring nature of the gaseous phase in lidded crucibles [317]. Obstruction of the mass transfer efficiency decisively promotes charring in the sample matrix [306], either by increasing the residence time or promoting secondary reactions within the solid matrix. Therefore, increased char formation by both intra- and extra-particle mass transfer limitations caused different thermogravimetric behaviors.

Table 2. Final DRM values (wt.%) of all sample types of spruce and poplar at 1 ºC/min and 10 ºC/min

Sample type	Spruce		Poplar	
	1 ºC/min	10 ºC/min	1 ºC/min	10 ºC/min
powder	10.31	10.00	10.27	10.01
particle	12.64	12.30	10.59	12.33
cylinder, 1 mm	12.82	13.35	11.61	14.93
cylinder, 2 mm	18.24	13.91	14.80	15.66
cylinder, 4 mm	18.67	14.82	16.92	16.66
powder with lid	20.03	16.78	17.10	19.50

In light of the shift of DSC baseline over long times and the fluctuation of derivative thermogravimetry (DTG) baseline for 1 °C/min tests, DSC and DTG curves at 10 °C/min were selected here to further analyze the kinetic differences (Figure 4). The DTG and DSC signals were divided by the initial anhydrous mass of the samples. DTG curves exhibited similar trends between samples, but with noticeable differences between 300 °C and 400 °C in spruce, while more differences appeared between 270 °C and 415 °C in poplar. Major peaks appeared around the same temperatures: 370 ºC for spruce and 365.5 ºC for poplar, attributed to the rapid decomposition of cellulose. Plot shoulders at lower temperatures, 320–350 ºC, belonged to hemicellulose decomposition, which flattened and shifted towards higher temperatures at increasing particle sizes, indicating the delayed decomposition of hemicellulose. Meanwhile, the peak temperatures for the powder sample with lid shifted from 370 ºC to 365.5 ºC for spruce and from 365.5 ºC to 358.5 ºC for poplar, attributed to the condensation of highly reactive tarry volatiles inside the lidded crucibles [318].

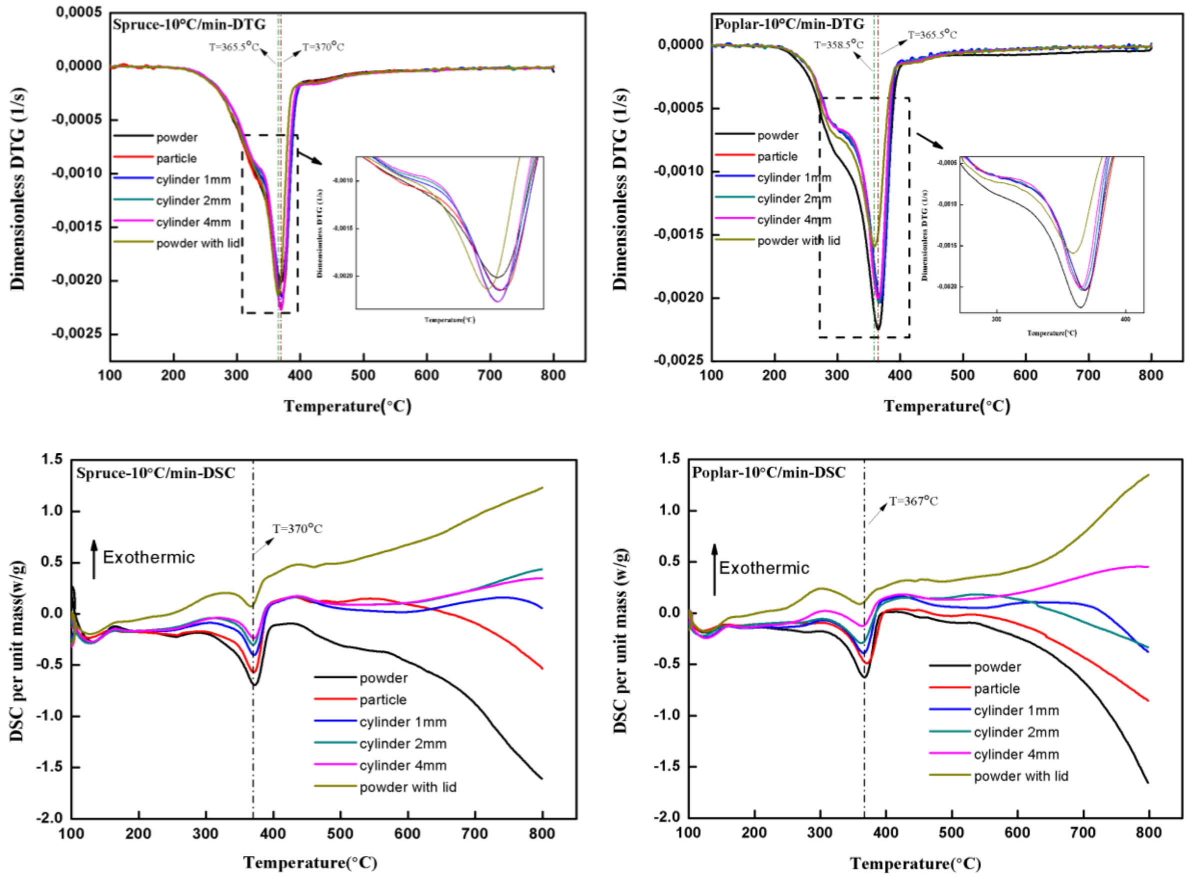

Figure 4. DTG (first row) and DSC (second row) signals normalized to the mass of spruce and poplar at 10°C/min.

The analysis of DSC data would be focused on the temperature range of 250–600 ºC. The signal was very small below this range and, as seen on the curves in Figure 4, the heat flux signal was seriously affected by radiation at higher temperatures [319]. From powder to cylinders, endothermic DSC peaks (around 370 ºC for spruce and 367 ºC for poplar) were in good accordance with the DTG peaks of cellulose decomposition. This major endothermicity corresponded to the depolymerization of the 1,4-glycosidic bond and ring breakage of light oxygenates [179]. The transition from endothermic to exothermic in large particles was possibly caused by cellulosic char formation due to the presence of alkyl furans, benzenoid aromatics, and condensed aromatics [180, 320]. An obvious tendency of heat release was observed as the particle size increased for both wood species. Important exothermicity was assigned to carbonization including re-polymerization and cross-linking in aromatic residues [183], in which exothermic heat had been proven to be proportional to char yield [170]. The alteration of thermal profile therefore indicated the enhancement of exothermic charring in large particles. In contrast, for the powder sample with lid, its largest exothermicity was attributed to the hindered volatile escape that enhanced condensation and charring [171]. Detained volatiles went through severe secondary carbonizations both homogeneously and heterogeneously, evidenced by the experimental observations of carbon depositions on the inner walls of the crucible, and the lid.

The O/C and H/C ratios of residual char were indicators for carbonization degree [321], they were therefore coupled with the dimensionless mass loss (DML) of different particle sizes for analysis purposes (Table 3). For both wood species at both heating rates, DML decreased consistently due to secondary charring. Meanwhile, the decreasing trends of H/C and O/C ratios indicated that char became more carbonaceous [322] because of dehydration and demethylation. Dehydration drove the oxidation of saturated hydrocarbons to form aromatic structures, serving as the precursor for biochar [323]. And the methyl removal in demethylation decreased the H/C ratio for C enrichment in the char product [324].

Table 3. Atomic O/C, H/C ratios and corresponding DML values in dynamic tests with different particle sizes of spruce and poplar

Wood type	Particle condition	1 °C /min			10 °C /min		
		O/C	H/C	DML(%)	O/C	H/C	DML(%)
Spruce	powder	0.032	0.20	89.69	0.032	0.24	90.00
	particle	0.027	0.15	87.36	0.029	0.18	87.70
	cylinder, 1mm	0.026	0.16	87.18	0.028	0.15	86.65
	cylinder, 2mm	0.026	0.12	81.76	0.027	0.14	86.09
	cylinder, 4mm	0.025	0.12	81.33	0.023	0.15	85.18
	powder with lid	0.023	0.11	79.97	0.019	0.12	83.22
Poplar	powder	0.037	0.16	89.73	0.037	0.17	89.99
	particle	0.034	0.15	89.41	0.035	0.18	87.67
	cylinder, 1mm	0.033	0.15	88.39	0.034	0.17	85.07
	cylinder, 2mm	0.033	0.15	85.20	0.032	0.15	84.34
	cylinder, 4mm	0.029	0.13	83.08	0.032	0.14	83.34
	powder with lid	0.027	0.13	82.90	0.031	0.13	80.50

Data at 10 °C/min, chosen as reference, were further compared with those of wood powder obtained in the isothermal tests in Figure 5 (detailed data from the static tests can be found in the supporting material). Two opposite relations were identified: dynamic tests had increasing DML values that matched with decreasing carbonization degree (increases in O/C and H/C), while static tests showed the opposite relation between DML and carbonization. The low temperatures of static tests (<500 °C) and powder shapes mostly triggered the decomposition of non-aromatic carbon bonds and a small amount of the aromatic groups in lignin [325], and devolatilization reactions were dominantly responsible for the changes in the DML. However, different thermochemical pathways in the dynamic tests indicated interceptions of primary volatiles that interacted with recondensation products, contributing directly to decreased DML in large particles. And the simultaneous polymerization and secondary charring reactions caused higher degrees of carbonization. These different relationships between DML and carbonization indicated the traces of enhanced charring when particle sizes increased.

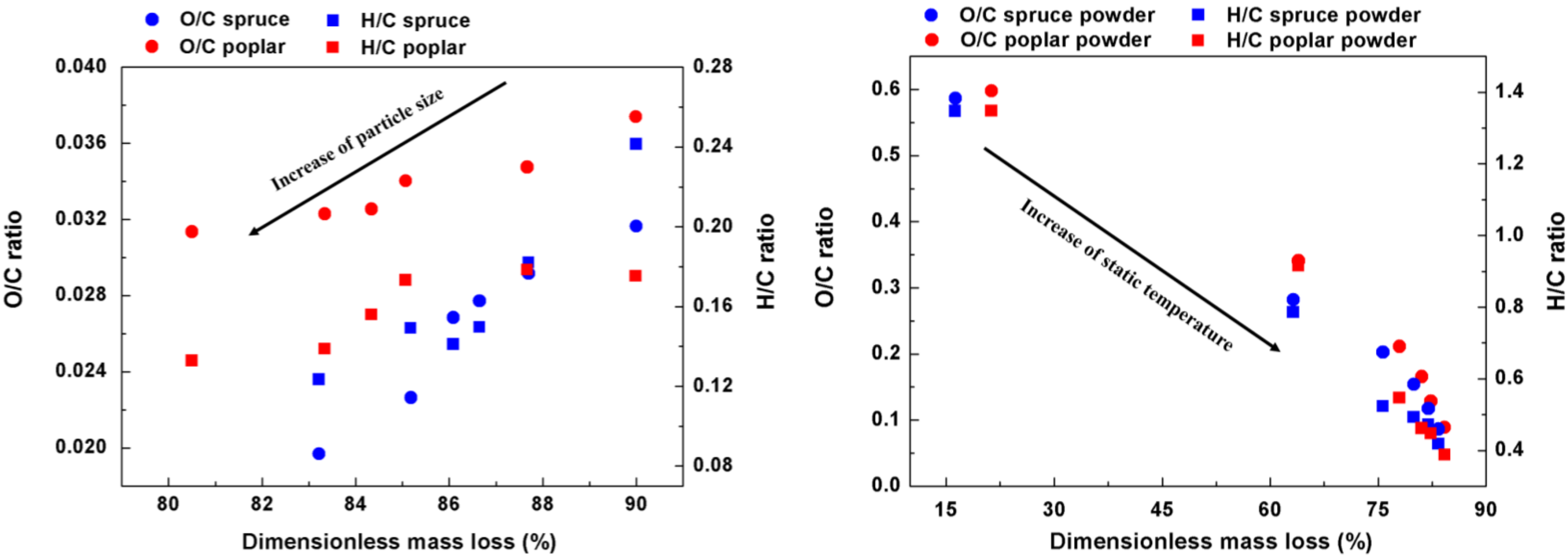

Figure 5. Atomic O/C, H/C ratios vs. DML in dynamic tests with different particle sizes of spruce and poplar (left); in static tests of spruce and poplar powder (right)

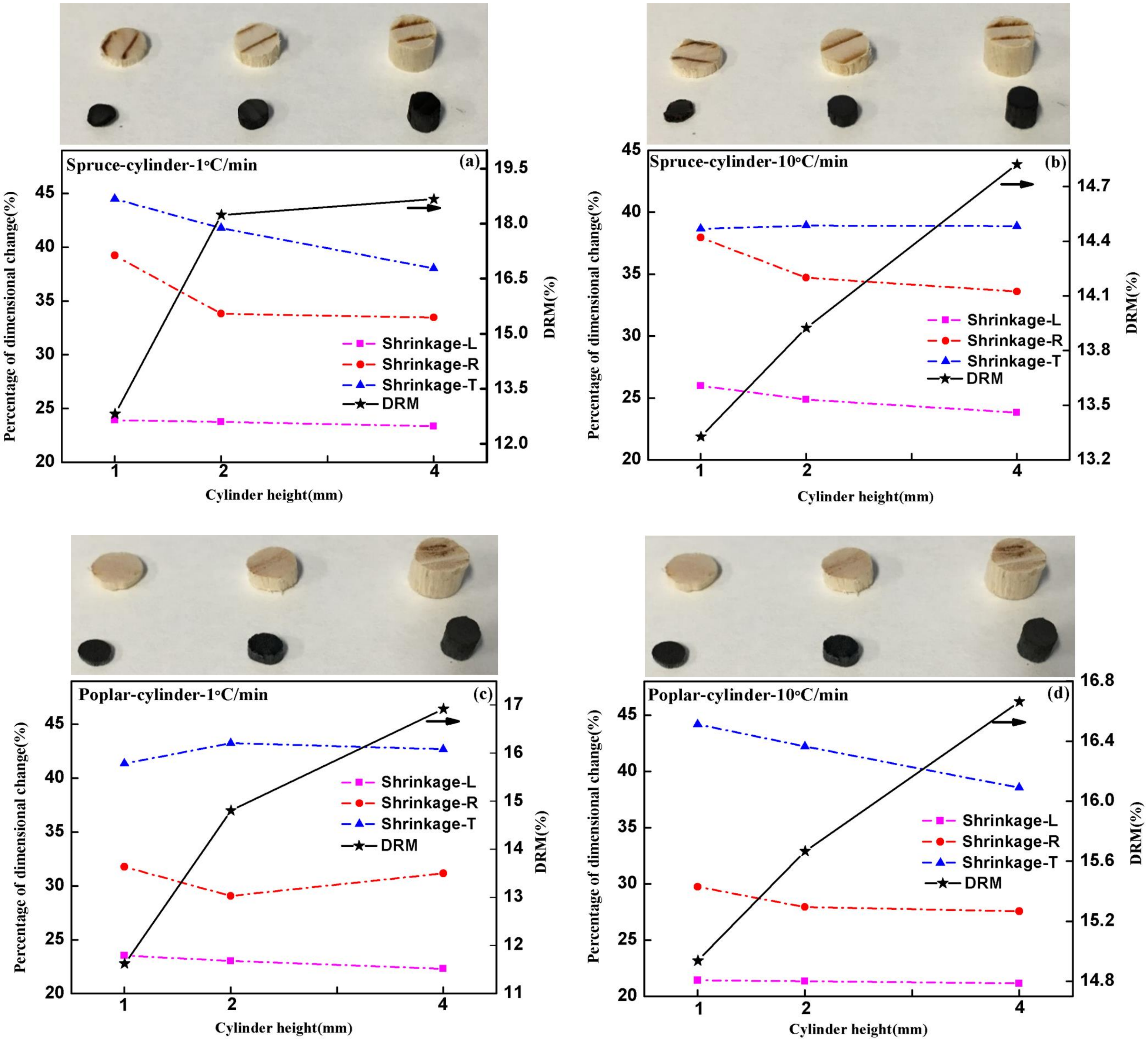

Figure 6. Comparison of dimensional shrinkages (in longitudinal, radial, and tangential directions) and corresponding DRM values in different cylinders of spruce and poplar at heating rates of 1 and 10 ºC/min

Cylinder shrinkages in three directions were calculated as the ratio of dimensional reduction over the initial dimensions (Figure 6). The orders of shrinkages (tangential> radial> longitudinal) for both species followed the general trend of hydric shrinkage found in wood

[326]. Instead of bound water removal, devolatilizations occurring in the cell wall was here the driving force of macroscopic shrinkage [327]. However, compared to torrefaction (mild pyrolysis), where intact microfibrils of cellulose imposed a negligible longitudinal shrinkage [328], the longitudinal shrinkage (between 20% to 27%) became significant for the intense carbonization which occurred. This indicated severe destruction of cellulose crystallites, in accordance with the previous finding that cellulose crystallinity index decreased largely (by 35%) during flash pyrolysis at 500 °C [329]. Overall, the three shrinkage values tended to decrease with the cylinder height, being consistent with the concomitant reduction of volatilization (i.e., increase in DRM).

3.2 DAEM modeling

3.2.1 Model identification

Kinetic parameters fitted to the two Gaussian distributions and one exponential distribution in DAEM are listed in Table 4 for all samples. The corresponding full sets of experimental and simulated DRM curves could be found in the supporting material. The root mean square error (RMSE) and maximum deviation (D_m) for each particle condition assessed the quality of identification. The reasonably low ranges of RMSE values: 0.98×10^{-4} –1.64×10^{-4} for spruce and 0.47×10^{-4} –0.84×10^{-4} for poplar indicated very small deviations in general, which confirmed the relevance of number and shapes of the distributions [79]. Furthermore, the maximum deviation D_m presented in acceptable ranges: 2.77% –4.08% for spruce and 1.87% –3.34% for poplar. Usually, this error was not visually obvious in the curves because it tended to appear fast decomposition regions (250 °C to 350 °C), where the curve slopes were very large. Therefore, these two indexes exhibited reasonably small deviations and ensured simulation accuracies.

The general characteristics of the parameters in three distributions were consistent with previous work [93, 230], namely the lowest content of the first Gaussian, the largest content and narrowest range of the second Gaussian, and the exponential exhibited partial overlap with the other two distributions. Herein, $V_{max}1$, the weighting factor of the first distribution, generally decreased when particle size increased from powder to 4-mm cylinder for both wood species, indicating that secondary charring could undermine the volatile contributions of the first pseudo-component (hemicellulose) in large particles. $V_{max}1$ was less affected for powder with lid, which was possibly due to the heterogeneous gaseous reactions outside particles that led to devolatilization [330]. The other two weighting factors followed complicated variation trends that will be further investigated in the subsequent section. Nonetheless, the comprehensive data of various particle sizes might be a good resource for other kinetic researches.

An advantage of the robust DAEM model was that devolatilization in the three pseudo-components can be analyzed independently. The inverse reconstruction of devolatilization profiles for each pseudo-component allows the effects of particle size to be further analyzed. For the sake of example, the plot of three extreme sample sizes : powder, 4-mm cylinder and powder with lid are inclided as supporting material.

Table 4. Identified two Gaussian + one exponential DAEM parameters for different particle sizes of spruce and poplar

Biomass	Spruce						Poplar					
Size condition	Powder	Particle	Cylinder 1 mm	Cylinder 2 mm	Cylinder 4 mm	Powder with lid	Powder	Particle	Cylinder 1 mm	Cylinder 2 mm	Cylinder 4 mm	Powder with lid
$V_{max}1$	0.1670	0.1130	0.1115	0.1140	0.1070	0.1520	0.1704	0.1402	0.1316	0.1183	0.0951	0.1620
$V_{max}2$	0.4704	0.4683	0.4801	0.4248	0.4149	0.3643	0.4902	0.5258	0.5136	0.4960	0.4622	0.4179
$V_{max}3$	0.2913	0.3168	0.3129	0.2540	0.2862	0.2866	0.2556	0.2461	0.2713	0.2452	0.2777	0.2496
A_0(s^{-1})	8.19×10^{15}	3.60×10^{16}	1.55×10^{14}	1.90×10^{15}	1.07×10^{15}	4.66×10^{14}	1.94×10^{13}	3.75×10^{12}	1.03×10^{12}	8.03×10^{12}	7.30×10^{13}	8.24×10^{13}
E_0_1(kJ/mol)	201.30	209.56	182.40	191.18	187.12	184.69	169.05	160.52	154.10	163.75	174.11	171.86
E_0_2(kJ/mol)	216.58	224.08	197.38	209.95	206.80	201.21	186.39	178.31	171.15	181.73	192.72	193.10
E_{min}(kJ/mol)	176.10	185.94	160.88	188.35	184.00	180.32	150.29	143.99	137.76	148.15	158.54	169.37
Ơ$_1$(kJ/mol)	3.86	2.12	1.20	10.23	12.53	12.55	4.43	2.75	1.47	1.84	1.34	7.51
Ơ$_2$(kJ/mol)	9.82×10^{-7}	7.21×10^{-3}	5.93×10^{-8}	7.37×10^{-7}	1.27×10^{-6}	4.98×10^{-6}	2.84×10^{-7}	2.83×10^{-6}	4.79×10^{-7}	1.61×10^{-7}	2.45×10^{-7}	5.76×10^{-9}
β	0.49	0.31	0.56	0.27	0.26	0.24	0.51	0.51	0.63	0.40	0.32	0.26
RMSE ($\times10^{-4}$)	1.11	0.98	1.07	1.64	1.58	1.34	0.84	0.47	0.60	0.48	0.58	0.81
D_m(%)	3.46	4.08	2.92	3.78	3.74	2.77	3.34	1.87	2.26	2.12	2.22	2.79

Since kinetic parameters in each group interacted with dependences, their direct analysis might suffer from complicated interactions and unclear mechanism. Instead, synthetic indexes were built: $T_p(j)$ and $V_p(j)$, $j \epsilon [1:3]$ were the temperature and dimensionless volatile quantities corresponding to the maximum devolatilization rate for the three pseudo-components (Table 5).

$T_p(1)$ generally decreased in spruce when particle size increased but was stable in poplar, possibly due to the difference in hemicellulose structure. Namely, spruce contains monosaccharide units while poplar contains glucomannan units, and the former are more easily decomposed [59, 272]. The decreasing trend of $V_p(1)$ for both species indicated that the first pseudo-component reduced its devolatilization contributions in large particles. $T_p(2)$ underwent limited changes while particle size increased in both species. This can be explained by the cellulose crystalline structure that decomposed rapidly once reaching the melting point [251]. This stable temperature-dependent nature indicated that the $T_p(2)$ value was more related to chemical alteration than to particle size [88]. Furthermore, the devolatilization amount of spruce second pseudo-component was more affected by the particle size, as revealed by more decrease trend of $V_p(2)$ in spruce compared to that in poplar. A general increase of $T_p(3)$ in spruce indicated that the decomposition of the third pseudo-component was shifted towards higher temperatures in large particles, possibly caused by the increased activation energy of charring [331].

Table 5. Synthetic values of three pseudo-components in spruce and poplar in dynamic tests at 10°C/min.

Pseudo-component	Peak values	Spruce						Poplar					
		Powder	Particle	Cylinder, 1mm	Cylinder, 2mm	Cylinder, 4mm	Powder With lid	Powder	Particle	Cylinder, 1mm	Cylinder, 2mm	Cylinder, 4mm	Powder with lid
First	Tp(1)	283.75	288.94	282.94	270.74	265.84	269.34	267.45	264.74	263.33	265.33	268.05	254.84
	Vp(1)	3.85	3.14	2.68	1.79	1.22	1.54	3.26	3.08	3.12	2.87	2.51	2.37
Second	Tp(2)	327.65	328.34	328.06	329.04	328.14	323.55	325.24	324.93	321.84	324.14	325.05	324.35
	Vp(2)	12.77	12.81	12.42	11.38	10.98	9.54	11.86	12.21	11.59	11.76	11.56	10.49
Third	Tp(3)	234.46	242.55	238.36	284.54	279.54	279.63	231.24	232.34	229.95	234.84	237.74	269.55
	Vp(3)	1.13	1.85	1.06	1.56	1.84	1.99	0.96	0.91	0.83	1.12	1.57	1.59

*$T_p(j)$: Peak temperature, °C.

$V_p(j)$: Dimensionless volatile, 10^{-4}.

j: Pseudo-component, $j\epsilon[1:3]$.

3.2.2 Model validation

Prediction of mass loss

The model parameters commented previously were identified from the learning database, which consisted of dynamic tests performed at 1 and 10 °C/min. To further assess the prediction potential of the model, these identified parameters were used to simulate static tests (Figure 7). The final DRM (Dimensionless Residual Mass) values (DRM = 1-DML) were calculated for all samples. Three temperature levels (300, 500, and 800 °C) were chosen to represent the three typical pyrolytic phases, which were located in three reaction zones: initial decomposition, major pyrolysis, and secondary reaction stages [155, 290].

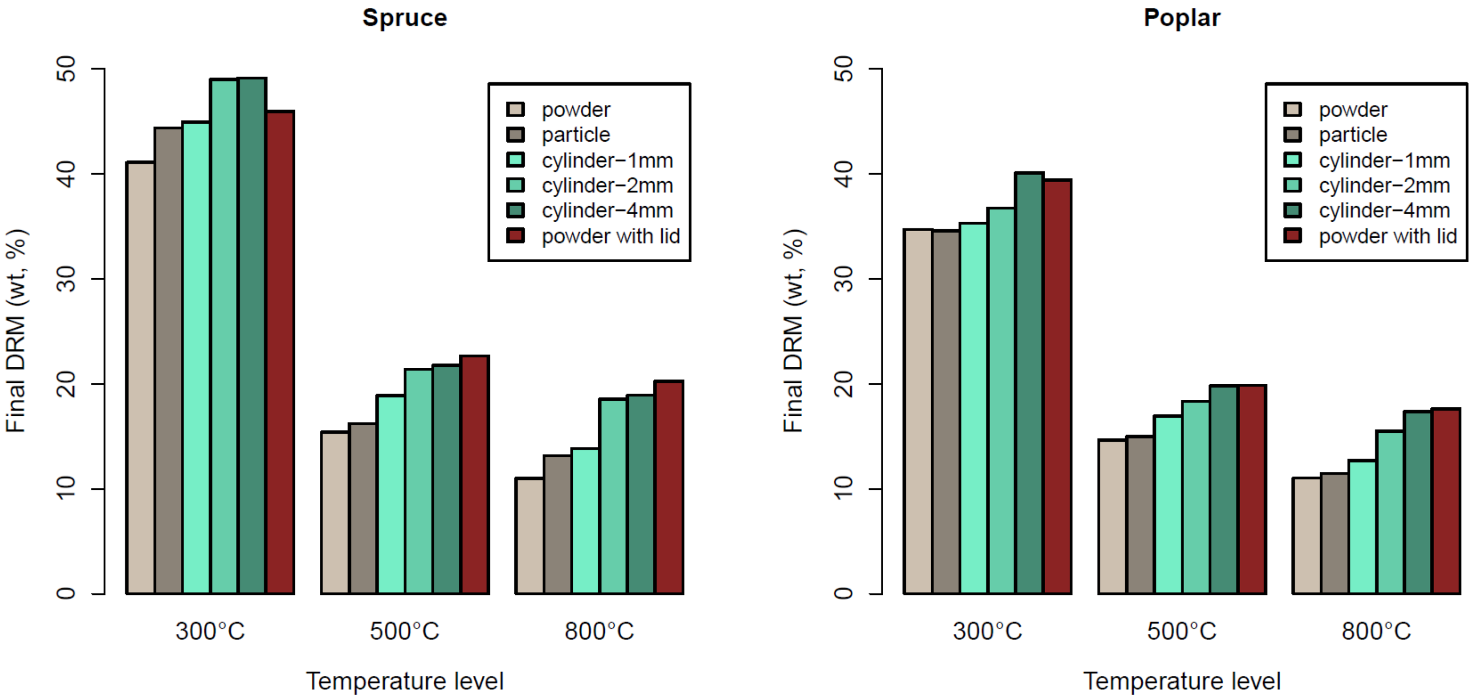

Figure 7. Predictions of final DRM values of spruce and poplar samples in three static tests (temperature levels of 300, 500, and 800 °C)

For both spruce and poplar, the predicted DRM values at all three temperature levels simultaneously increased when increasing the particle size from powder to the 4-mm cylinder, as direct effect of particle size. Since the promotion of char formation by intra-particle mass transfer limitations is well-admitted [306] and included in the learning database, these numerical predictions were logical and reasonable. Regarding the effect of temperature level, it was understandable that further devolatilization caused generally lower DRM values at 500 °C compared to those of 300 °C, and the final high-temperature decomposition of lignin and partial secondary cracking reactions caused the lowest DRM values at 800 °C. Meanwhile, the powder with lid exhibited the largest char yield at 500 and 800 °C levels for both species, corresponding to the experimental findings of the most severe charring in powder with lid. Note however that the DRM of powder with lid found at 300°C is smaller than the two longer cylinders.

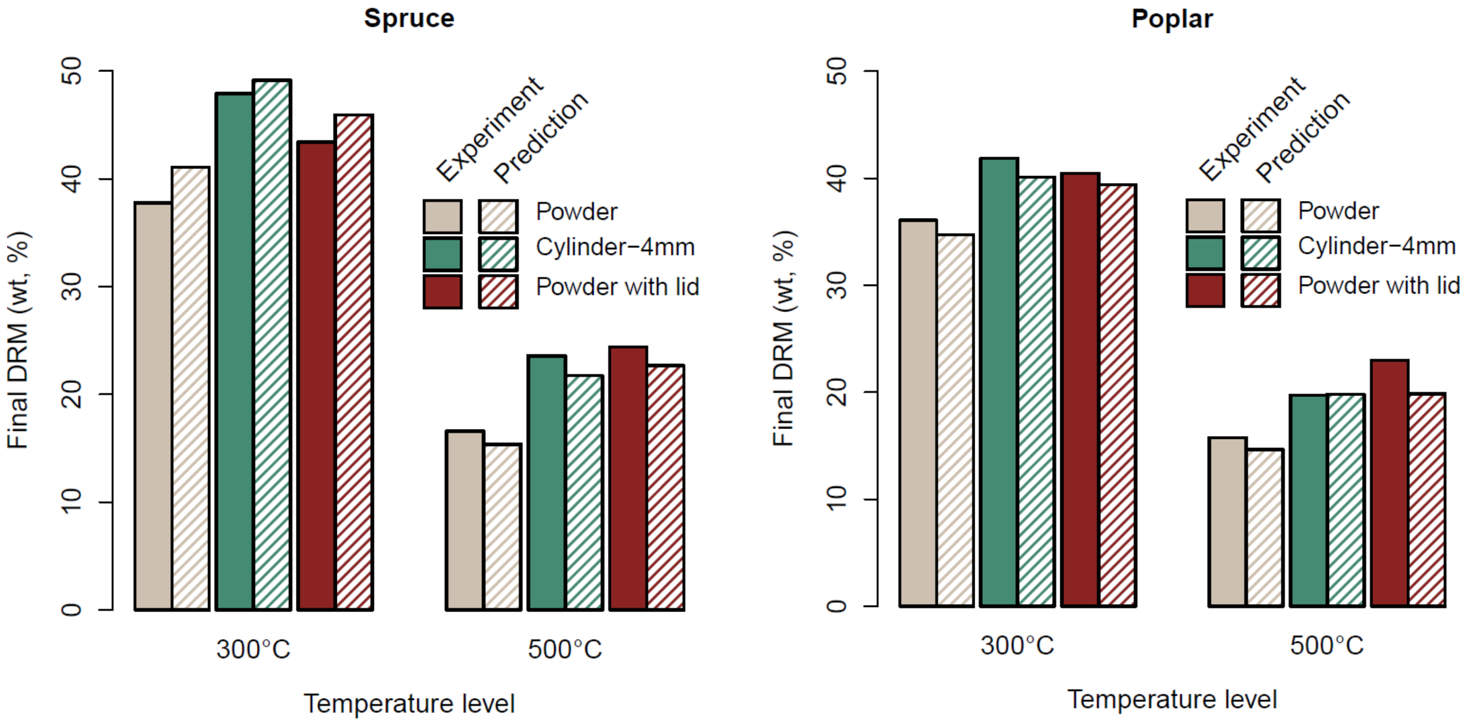

Figure 8. Experiment validations of residual mass for powder, 4mm cylinder and powder with lid for static tests at in 300°C, 500 °C, left) spruce and right) poplar

Static tests at 300 °C and 500 °C were performed for the purpose of validation (Figure 8). The static test at 300 °C was a particularly demanding validation test as the kinetics was very slow at this temperature, resulting in very partial volatilization at the end of the experiment, likely to introduce prediction errors. Herein, due to the strict sampling protocol that largely limited the sample amount, only representative sample types (powder, 4-mm cylinder, powder with lid) were tested. The comparison between experiment and prediction depicted excellent trends with limited errors for all conditions. The error ranges, 1.20–3.31% for spruce and 1.09–3.12% for poplar, were acceptable compared to previously published works proposing predictions [113]. And it was remarkable to observe that the smaller DRM of powder with lid predicted by the model at 300 °C was confirmed by the experiment.

To conclude, kinetic differences originated from intra-particle limitations were nicely predicted by the model despite the very different time–temperature pathways of the validation database compared to the learning database. Therefore, this last section demonstrated the ability of the multi-distribution DEAM parameters to predict volatilization for contrasted pyrolysis conditions.

Prediction of char composition

As commented in the experimental section, the relation between char composition and DML revealed the presence of secondary charring when changing particle size. Assuming the elemental composition of char resulting from secondary charring is not affected by the particle size, the elemental composition can be deduced as a weighted average between primary reactions and secondary charring. Herein, wood powder is used as reference for primary reactions. This weighted average therefore allows the element contents of char (c_1 to c_4) to be predicted from the elemental contents of powder and secondary charring, the DRM of powder and the change of DRM with the considered particle:

$$c_i = \frac{\left(DRM_{powder}\right) \cdot \alpha_i + \Delta DRM \cdot \beta_i}{DRM_{powder} + \Delta DRM}, \quad i \in [1:4] \tag{12}$$

Where DRM_{powder} is the dimensionless residual mass of wood powder, ΔDRM the additional residual mass of the particle compared to powder, α_i are the contents in the char of wood powder, and β_i, the element contents in char produced by secondary charring. Indices *i* stands for carbon, hydrogen, oxygen, and ash. It is assumed that char from secondary charring contains no ash:

$$\beta_C + \beta_H + \beta_O = 1; \qquad \beta_{ash} = 0 \tag{13}$$

An identification process was conducted for minimizing the RMSE between c_i and actual experimental values at 10 °C/min, to obtain β_i for both wood species (Table 6). To be noted, the highly dominant content of carbon (β_C) confirms that carbonization is the major effect of secondary reactions.

Table 6. Identified element content parameters in two wood species at 10 °C/min

Wood Species	β_C	β_H	β_O
Spruce	0.9885	4.4712×10^{-10}	0.01149
Poplar	0.9582	9.1484×10^{-3}	0.03265

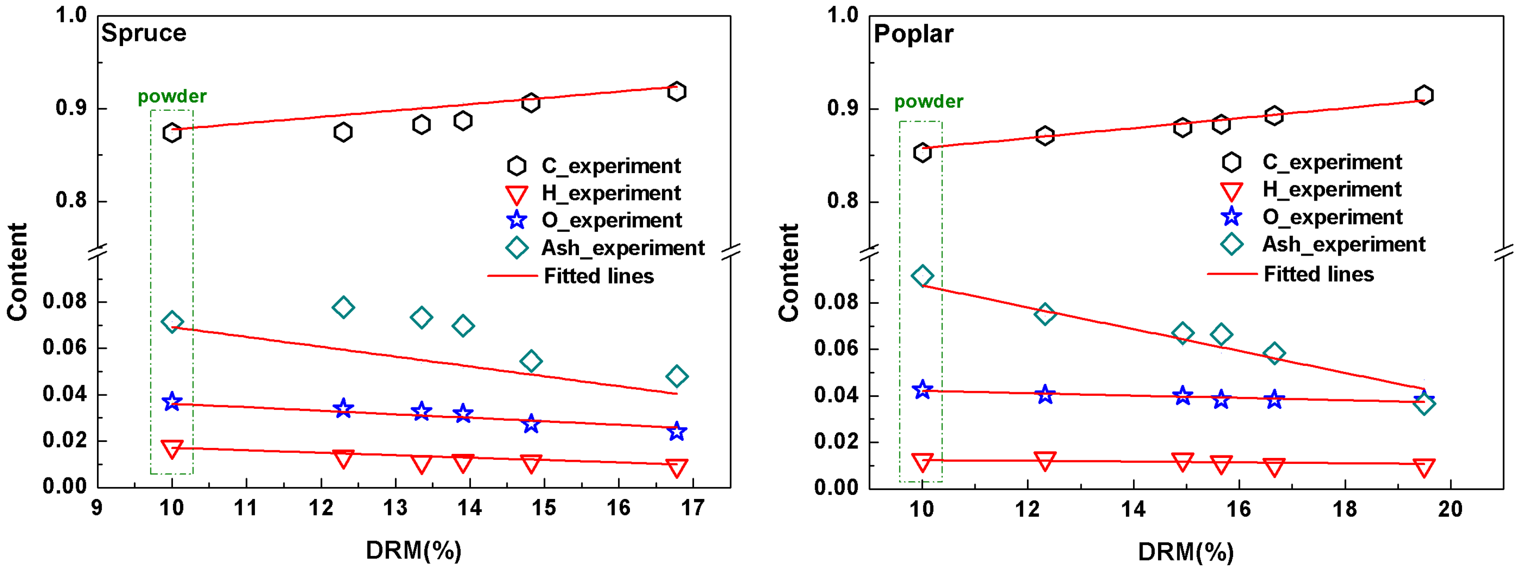

Figure 9. Elementary contents *vs*. dimensionless residual mass (DRM) of samples with different particle sizes in the 10 °C/min dynamic tests, and corresponding fitted curves

The predictions using equation (12) together with the composition of secondary charring (Table 6) were plotted for both species (Figure 9), which depicts an excellent correlation between the change of composition and the change of DRM. The good correlation obtained for ash is consistent with the assumption on the absence of ash in secondary reactions. In practice, this observation allows a clear conclusion to be drawn. As the kinetic prediction of the DAEM model is already validated, the change of DRM between a certain particle size and powder can be predicted for any time-temperature profile. Hence, equation (8) supplied with the data of table 6, can be used to predict the elemental analysis of char whatever the conditions underwent by the particle. To that purpose, the elemental analysis of char from powder could be predicted as a function of the Dimesnsionless Residual Mass (DRM) thanks to the correlation proposed in [162]:

$$\begin{aligned}\frac{O}{C} &= 1.134 - 0.219 \times \exp(1.815 - 1.815DRM)\\ \frac{H}{C} &= 0.1534 - 0.0268 \times \exp(1.783 - 1.783DRM)\end{aligned} \tag{14}$$

This opens new possibilities in process design and control, as this method can be applied to any industrial process, provided one knows the history of conditions imposed to the particles. This could be applied, for example, to the prediction of elemental composition along the reactor height for the pyrolysis of a packed bed [94].

4. Conclusions

This study is devoted to the effect of particle size on the pyrolysis of two wood species: spruce and poplar. Various sample geometries treated in TG/DSC allowed comprehensive analyses of the mass and heat limitations from intra-particle (powder to cylinder) and reactor type (crucible with and without lid). A negative mass loss/carbonization pathway confirmed additional charring at increasing particle size. Exothermicity from char formation was promoted by particle size (or extra-particle limitations).

From this learning database, a robust DAEM model, with two Gaussian and one exponential DAEM distributions, was derived. The DAEM model was used to simulate and predict mass loss for different time-temperature profiles. These predictions were successfully validated by additional experiments. The composition of char produced by secondary charring was determined from the linear relation found between elemental analyses and residual masses. This allows the elemental composition of char to be predicted for a given particle size for any time-temperature pathway. This prediction involves the kinetic differences between powder and a given particle, as predicted by the DAEM model.

In conclusion, this paper addresses the important question of the effect of particle size on biomass pyrolysis and proposes simulation tools to predict the kinetics and the elemental composition of char. These tools are intended for use in the design and control of industrial processes.

Acknowledgements

The authors are grateful for the financial support of the Conseil Général de la Marne, Grand Reims and the Région Grand Est, France. The support from the China Scholarship Council (CSC) is also gratefully acknowledged.

Supporting material

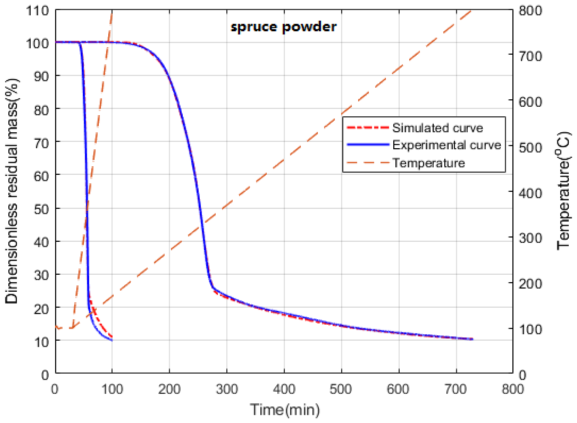

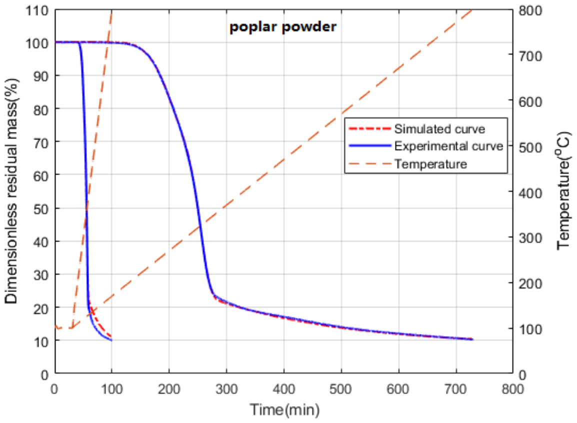

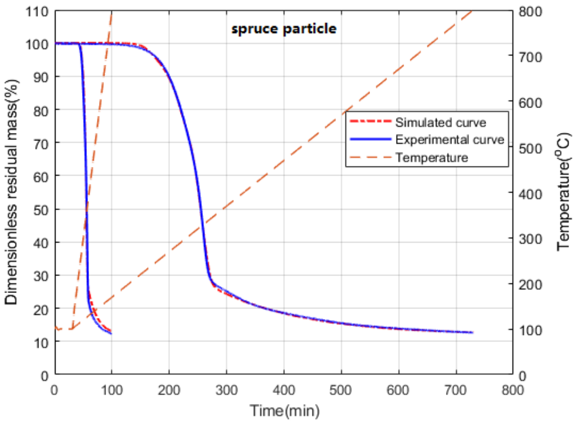

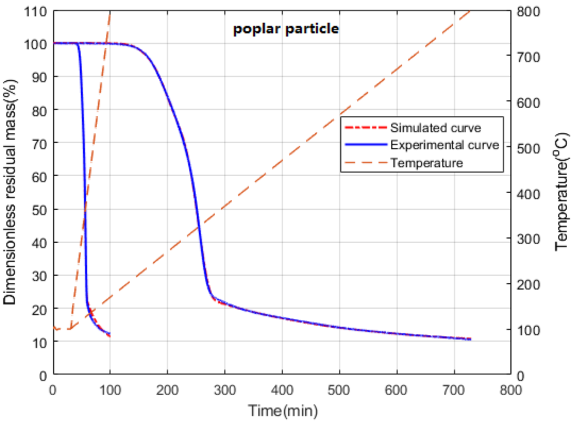

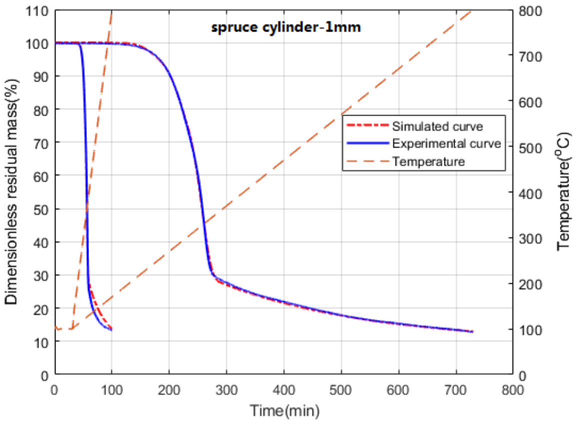

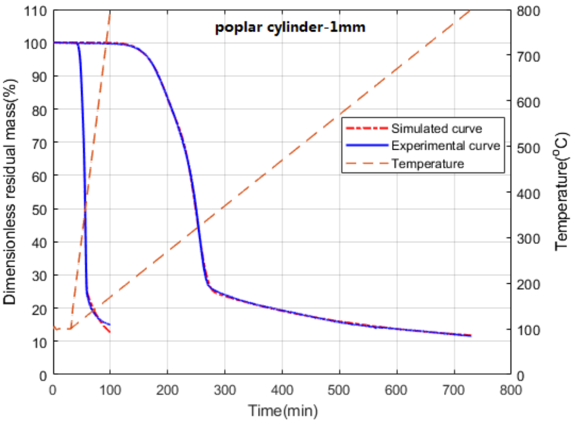

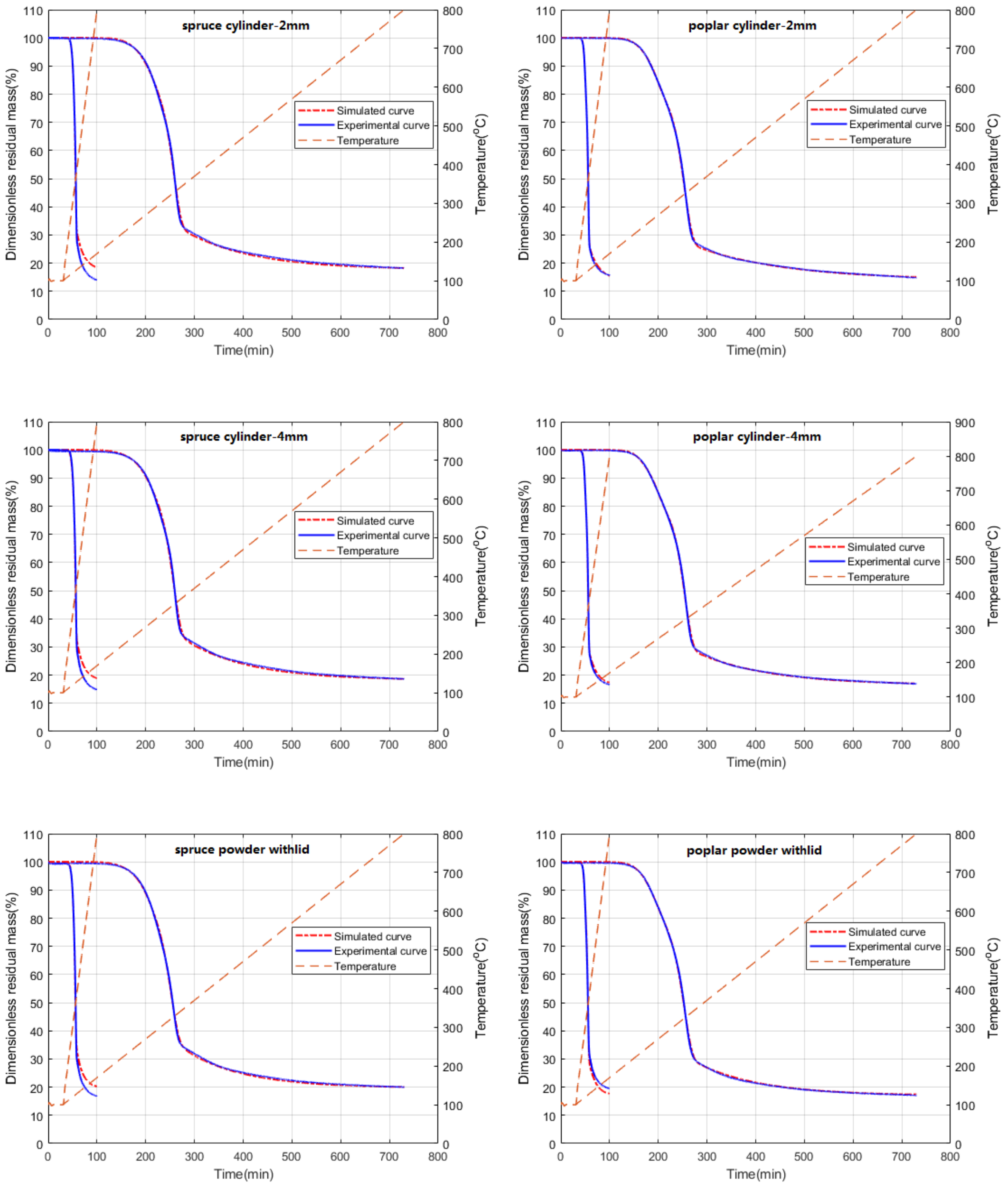

Supplementary Figure 1. Thermogravimetric DRM curves of experiments and model simulations at different sample conditions of spruce (left column) and poplar (right column)

Pseudo-component	**Spruce**	**Poplar**
First	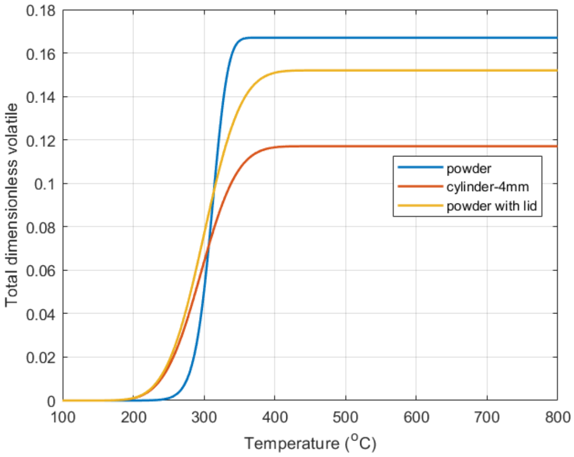	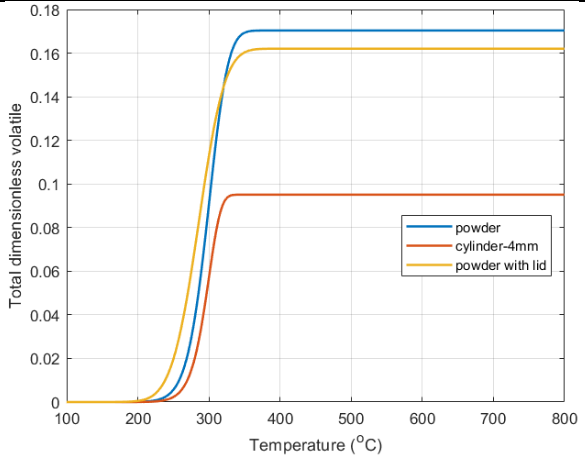
Second	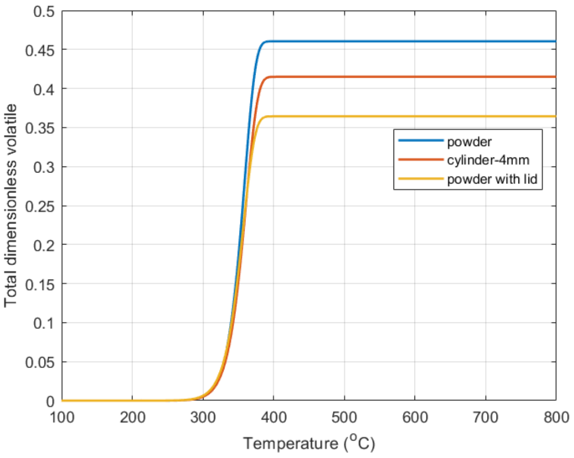	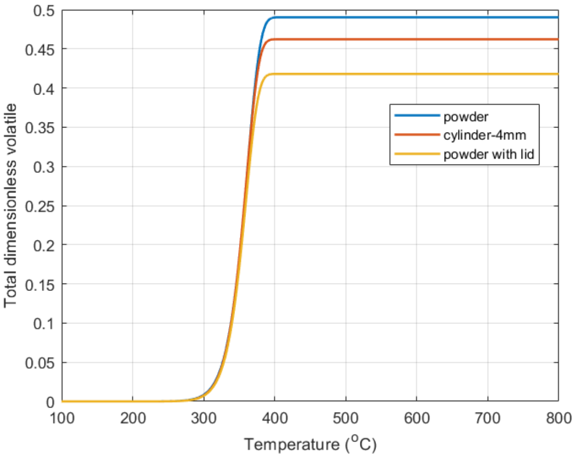
Third	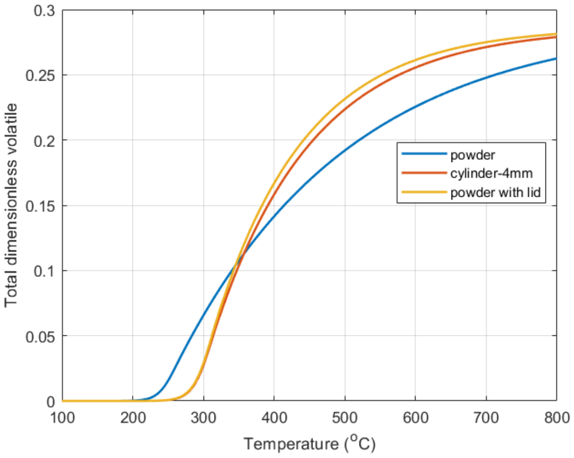	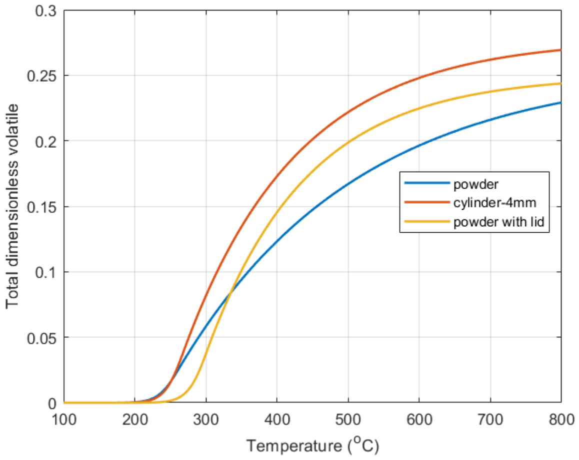

Supplementary Figure 2. Devolatilization profiles of three pseudo-components in 10 °C /min tests of powder, 4-mm cylinder, and powder with lid, computed from the identified model parameters for spruce and poplar

Devolatilization of the first pseudo-component generally occurred between 163–355 °C; it corresponded to the hemicelluloses that were more reactive at lower temperatures [22], in agreement with similar temperatures reported in the literatures [236, 237]. The narrow pyrolytic range and high volatile yield of the second pseudo-component closely matched cellulose, which made up the largest portion of the wood and decomposed at a specific narrow temperature range around 320 °C [233, 241, 275]. The temperature of the third pseudo-component had the largest range, from 180 to 800 °C, which was consistent with lignin decomposition characteristics, in which irregular phenolic polymers endowed extended decomposition ranges [332].

Among the three sample types, major differences caused by secondary charring were clearly distinguished by the devolatilization profiles of the pseudo-components. Accompanied by the enlargement of particle size and the use of lid, the first and second pseudo-components reduced their volatile formation rates and final yields, possibly due to the volatile interceptions in hemicellulose and cellulose fractions. On the other hand, the higher volatile content in the third pseudo-component of cylinder-4mm and powder with lid, could be caused by the predominance of lignin devolatilization at high temperatures that raised gas formation rate [75]

Supplementary Table 1. Elemental analyses of char in static tests of wood powder

	spruce powder						poplar powder					
Temperature (°C)	250	300	350	400	450	500	250	300	350	400	450	500
C (wt.%)	50.77	65.26	71.01	74.28	79.22	82.67	50.30	62.28	70.90	74.44	77.11	81.50
H (wt.%)	5.70	4.27	3.09	3.05	3.11	2.88	5.65	4.75	3.23	2.86	2.87	2.63
O (wt.%)	39.69	24.53	19.19	15.24	12.42	9.49	40.10	28.32	19.99	16.44	13.21	9.62

Chapter 7 Conclusions and perspective

Experimental and modelling tools had been applied for two wood species: spruce and poplar, allowing a comprehensive kinetic study that covered numerical strategy, intrinsic mechanism, complicated heat/mass transfer phenomenon and chemical compositions. This works comprised successive and complementary sections as: (1) model determination by the trade-off strategy; (2) intrinsic kinetic determination from wood powder pyrolysis; (3) effects of particle size and corresponding model predictions. Their main conclusions will be summarized hereafter.

7.1 Model determination

Both the dynamic and static databases, that covered wide range of treatment time and temperature levels, had been employed to ensure comprehensive model assessments during identification and validation. The trade-off strategy was conducted between root mean square error (RMSE) and degrees of freedom (D_f), which presented prediction ability and numerical complexity respectively. Three-distribution DAEM exhibited the best trade-off among a series of multi-Gaussian-DAEMs that ranged distribution number from one to five. Further the two-Gaussian+ exponential DAEM presented the best prediction ability and numerical conciseness, which also showed superiority over first-order and *n*th-order models, being determined as the final strategy regarding distribution number and shape. The subsequent DTG simulation well verified model's advantages in reducing error with considerable numerical concision, and established correspondences between pseudo-components and chemical constituents. Also, the model had shown its good capacity in distinguishing the effects of heating rates.

7.2 Intrinsic kinetic

Wood powder of spruce and poplar had been pyrolyzed with both dynamic and static temperature programs. The sufficient dynamic tests acted as learning database for determining intrinsic parameters in two-Gaussian + exponential DAEM. Subsequently the solid validations with static databased verified model's prediction capacities.

As benefits of the robust model strategy, intrinsic kinetic parameters were presented in detail for both wood species, which could serve as fundamental guidance for relevant researchers. The work also realised, for the first time, the heat flux determination and the extraction of reaction enthalpy factors based on DSC signals. Correlations were established between char compositions and dimensionless residual mass (DRM) of wood powder, allowing char contents to be predicted by DAEM. Finally, model showed a control strategy in temperature raise.

7.3 Effect of particle size

Both experimental observations and numerical simulations among varied particle shapes had been presented in this chapter. Five types of multi-scale samples (powder, particle, 5-mm diameter cylinders with heights of 1 mm, 2 mm, and 4 mm) plus one extra reactor (powder with lid) were employed, aiming to analyse the effects of particle size and extra-particle limitations. Thermogravimetry analyses depicted a reduction in kinetics and a gain in carbonization when the particle size increased. DSC showed the important exothermic heat that was promoted in large particle and powder with lid. The negative match relation between carbonization and mass loss in elemental analyses evidenced the charring enhancements in large particle sizes.

Kinetics parameters fitted with two Gaussian and one exponential DAEM distributions ensured accurate descriptions in mechanism, potentially serving as resources for further kinetic researches, such as upscaling approaches. Synthetic indexes of the maximum devolatilizations in each pseudo-component depicted comprehensively the variation trends due to particle size.

A set of successful validation tests was proposed based of time-temperature profiles different from the learning database, highlighting model’s predicting ability among different particle sizes. Subsequent correlation between residual mass and element content revealed the main composition of carbon in secondary charring, endowing DAEM to predict kinetic differences compared to fine powder, hence elemental compositions for different particle sizes as a function of pyrolysis conditions.

7.4 Prospective

The comprehensiveness of our model will confer great potentials for several investigations fields, herein two pathways are presented that we consider valuable in the future researches:

(1) Trade-off strategy concerning the number of identification/validation tests

In order to guarantee the calculation accuracy and limit numerical complexity at the same time, the test number should also be investigated by a trade-off strategy. As widely acknowledged, multiple test number could improve parameter accuracy and verification effects. Yet the multiple heating rates/temperature levels in experiments were quite complex and time-demanding, and it didn’t necessarily demand as many tests as possible. In contrast, a “turning-point” was very possible that ensured identification/validation quality at the expense of suitable tests. This trade-off has already been determined concerning verification database in chapter 4. To further apply the trade-off strategy in verification database, it required more temperature levels to be conducted in static tests in the future.

(2) Coupling between DAEM and transfer models

An extended application of DAEM is to couple with transfer models, which will be applicable in more complicated situations. A 3-D model that combines DAEM with heat/mass transfer formulations can provide a more comprehensive and universal method to deal with multiple sample sizes, thermal conditions, and even large-scale process controls. Investigations at macroscopic scale is therefore worthwhile for a better process strategy. Early works [219, 220] had established a 3-D model that included primary and secondary reactions of three components, but the kinetic parameters (weighting factor, pre-exponential factor and activation energy) still needed to cite from literature values. Thanks to the accurate kinetics described by the DAEM, it could provide parameters in the scheme (figure 7.1) and further couple into a 3-D model.

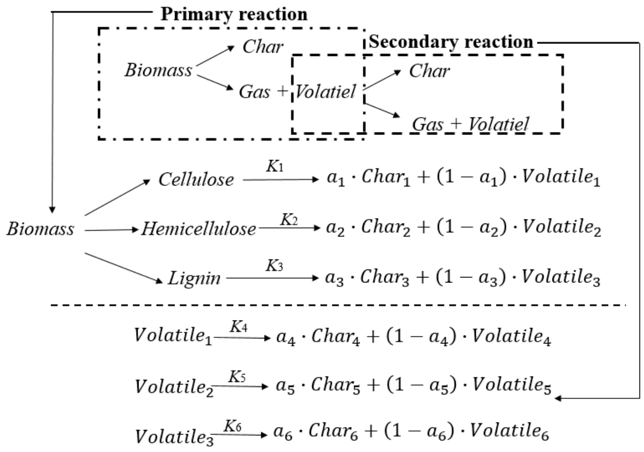

Figure 7.1. Possible biomass pyrolysis scheme coupling first-order primary and secondary reactions

The biomass solid follows conservations in the primary reactions as:

$$\overline{\rho_s^s}\frac{\partial \varepsilon_s}{\partial t} + \nabla \cdot \left(\overline{\rho_s \mathbf{v}_s}\right) = -\frac{1}{V_s}\sum_{i=1}^{3}(K_i m_i) \tag{7-1}$$

$$m_1 = m_{Cellulose} = c_1 \cdot m_{wood} \tag{7-2}$$

$$m_2 = m_{Hemicellulose} = c_2 \cdot m_{wood} \tag{7-3}$$

$$m_3 = m_{Lignin} = c_3 \cdot m_{wood} \tag{7-4}$$

Take cellulose for example, the derivation of volumetric mass rate is as follows:

$$[Cellulose] = [A], [Volatile_1] = [B], [Volatile_4] = [C] \tag{7-5}$$

$$[A] = [A]_0 e^{-K_1 t}, \frac{d[B]}{dt} = K_1[A] - K_4[B], \frac{d[C]}{dt} = (1-a_4)K_4[B] \tag{7-6}$$

$$[B] = [A]_0 \frac{K_1}{K_4 - K_1}\left(e^{-K_1 t} - e^{-K_4 t}\right) \tag{7-7}$$

$$[C] = \frac{(1-a_4)[A]_0}{K_4 - K_1}\left(\left(K_1 e^{-K_4 t} - K_4 e^{-K_1 t}\right) - (K_1 - K_4)\right) \tag{7-8}$$

The total volatile:

$$[B] + [C] = [A]_0\left(\left(1 - a_4 - e^{-K_1 t}\right) - \frac{a_4}{K_4 - K_1}\left(K_1 e^{-K_4 t} - K_4 e^{-K_1 t}\right)\right) \tag{7-9}$$

Therefore, volumetric mass rate of volatile production from three components can express as:

$$\langle \dot{m}_V \rangle = \frac{1}{V_G}\sum_{i=1}^{3} M_i\Big((1 - a_{i+3} - e^{-\mathrm{K}_i t}) - \frac{a_{i+3}}{\mathrm{K}_{i+3} - K_i}(K_i e^{-K_{i+3} t} - K_{i+3} e^{-K_i t})\Big) \tag{7-10}$$

where $\overline{\rho_s^s}$, ε_s and V_s are average density, fraction volume and total volume of solid phase, $\mathbf{v}_s$ is the velocity. c_1, c_2, c_3 are the contents of three components and they are identified from DAEM model (intrinsic parameters). The mass terms here will be determined by DAEM, and then coupled into mass conservation and the atomic conservation for determining secondary reactions. Subsequently, these terms will be coupled into mass conservations (solid conservation, volatile conservation) and energy conservations.

Appendix

1. Introduction générale

La consommation de combustibles fossiles dans le monde a considérablement augmenté au cours des dernières décennies, ce qui entraîne plusieurs problèmes environnementaux, notamment les émissions de gaz à effet de serre et la détérioration de la qualité de l'air. Dans ce contexte, la bioénergie est promue à l'échelle mondiale en raison de ses mérites d'être renouvelable, neutre en carbone et respectueuse de l'environnement. La biomasse est une matière biologique issue d'organismes vivants ou récemment vivants, produite directement ou indirectement par photosynthèse, le plus souvent des plantes ou des matières d'origine végétale. La pyrolyse est une voie de décomposition thermique sous une atmosphère sans oxygène. Elle a reçu une attention considérable en tant que technologie clé de conversion thermique dans les bio-raffineries et dans la production de produits chimiques à haute valeur ajoutée (bio-huile, charbon de bois et biogaz). Il agit également comme le principal processus initial de gazéification et de combustion.

La pyrolyse de la biomasse est un phénomène sophistiqué concernant à la fois les processus chimiques (réactions) et physiques (transfert de chaleur et de masse). Et sa modélisation est tout à fait essentielle tant pour les analyses cinétiques que pour l'optimisation des processus industriels. Le modèle de multidistribuée d'énergie d'activation (DAEM) est un outil robuste de modélisation de la cinétique de pyrolyse. Il suppose que la pyrolyse de la biomasse se produit comme une série de réactions indépendantes et parallèles avec des énergies d'activation continues, qui expliquent la non-uniformité inhérente des liaisons chimiques. Les énergies d'activation sont soumises à des distributions statistiques uniques ou multiples, parmi lesquelles le multi-distribution DAEM se tourne pour fournir des descriptions plus précises. Et les concepts de pseudo composants à l'intérieur de multi-distributions DAEM correspondent bien aux significations chimiques des constituants de la biomasse (c'est-à-dire l'hémicellulose, la cellulose et la lignine).

La stratégie optimale concernant le nombre et la forme des distributions reste une question ouverte. Les formes de distribution de DAEM représentent divers comportements cinétiques. Les distributions symétriques comme gaussienne et logistique ont été largement utilisées. Entre-temps, en raison du comportement asymétrique au cours des étapes initiales et finales de la décomposition thermique, les distributions asymétriques attirent une attention croissante, y compris les distributions de Weibull et Gamma. Le nombre de distribution décide également de la précision de la simulation et de la complexité numérique. C'est un facteur clé qui affecte profondément les implémentations informatiques.

La mise en œuvre du modèle implique toujours les identifications cinétiques, dans lesquelles de multiples profils de température réduisent efficacement les incertitudes des paramètres. C'est un point-clé de la stratégie de modélisation: la qualité réelle du modèle doit être évaluée sur une base de données de validation, qui doit être différente de la base de données d'apprentissage. Cependant, cette étape cruciale de validation est à peine menée dans les recherches pertinentes.

La taille des particules modifie le couplage entre le transfert de chaleur et de masse, la réaction thermo activée, les réactions hétérogènes entre les volatiles et la phase solide, et le transfert d'enthalpie par changement de phase. Celles-ci encouragent grandement les recherches cinétiques pertinentes avec des modèles complets.

Cette thèse est motivée par les avantages du DAEM dans la détermination cinétique de la pyrolyse, y compris l'analyse du flux thermique et de la taille des particules. Les enquêtes porteront sur les aspects suivants:

(1) Stratégie optimale entre le nombre et la forme des distributions dans le multi-distribution DAEM.

(2) Détermination du mécanisme intrinsèque par DAEM (deux gaussiennes + une exponentielle), y compris l'analyse du flux thermique pour extraire les enthalpies de réaction.

(3) Effet de la taille des particules dans les analyses TG et les simulations DAEM correspondantes.

(4) Prédiction de la perte de masse et de la composition du charbon pour différentes tailles de particules.

Pour atteindre ces objectifs de recherche, cette thèse appliquera deux approches de recherche mutuellement soutenues. Ce sont des appareils thermogravimétriques, ainsi que les développements de DAEM à distribution multiple. Les travaux expérimentaux sont réalisés par des appareils thermogravimétriques (TG / DSC) et des méthodes de caractérisation (analyse élémentaire, SEM et imagerie tomographique). Entre-temps, la stratégie du modèle est déterminée dans le cadre d'un vaste processus des optimisations. Les bases de données d'apprentissage et de validation garantissent une stratégie d'identification / vérification fiable pour les DAEMs. Cela fournit des prédictions et des simulations précises de la cinétique de pyrolyse dans diverses conditions. Plus tard, la stratégie de modèle optimale est appliquée pour la détermination cinétique et les prédictions.

2. Principaux résultats et conclusions

Les principales réalisations de ce travail ont été conclues dans trois articles de revues. La première partie concerne la stratégie optimale de DAEM, les comparaisons de la capacité de prédiction et des degrés de liberté du modèle ont été rigoureusement étudiées sur le nombre et la forme de la distribution. Il a été prouvé que trois distributions gaussiennes assurent une bonne prédiction avec une concision appropriée. Plus tard, la combinaison de deux distributions gaussiennes et d'une distribution exponentielle a montré la meilleure capacité de prédiction, qui a été confirmée comme la meilleure stratégie en ce qui concerne la forme et le nombre de distribution. De plus, ils sont plus efficaces que les schémas classiques du premier et du n-ième ordre.

La deuxième partie a appliqué le modèle optimal pour déterminer les paramètres cinétiques intrinsèques dans la pyrolyse de la poudre de bois, qui sont validés avec précision. L'enthalpie de réaction a été couplée au modèle complet et présente des effets de simulation satisfaisants. Deux applications ont ensuite été appliquées concernantes :i) la prédiction d'une corrélation entre le rapport atomique et la perte de masse ; ii) description de l'évolution température/flux thermique.

La troisième partie a principalement étudié les mécanismes par des méthodes expérimentales et numériques. Cinq formes de particules différentes ont permis une enquête approfondie sur les variations cinétiques, et le DAEM a été utilisé pour révéler les changements de paramètres cinétiques lorsque la taille des particules changeait. Plus tard, la capacité de prédiction du modèle a été validée par des expériences supplémentaires réalisées à plusieurs niveaux de température statique et étendues pour prédire les compositions de char parmi différentes tailles de particules.

References

[1] S. Bucksch, K.-E. Egebäck, The Swedish program for investigations concerning biofuels, Science of the total environment 235(1-3) (1999) 293-303.
[2] D. Xu, M. Chai, Z. Dong, M.M. Rahman, X. Yu, J. Cai, Kinetic compensation effect in logistic distributed activation energy model for lignocellulosic biomass pyrolysis, Bioresource technology 265 (2018) 139-145.
[3] T. Xu, F. Xu, Z. Hu, Z. Chen, B. Xiao, Non-isothermal kinetics of biomass-pyrolysis-derived-tar (BPDT) thermal decomposition via thermogravimetric analysis, Energy Conversion and Management 138 (2017) 452-460.
[4] T. Kan, V. Strezov, T.J. Evans, Lignocellulosic biomass pyrolysis: A review of product properties and effects of pyrolysis parameters, Renewable and Sustainable Energy Reviews 57 (2016) 1126-1140.
[5] R. Houghton, Biomass, (2008).
[6] R. Saxena, D. Adhikari, H. Goyal, Biomass-based energy fuel through biochemical routes: A review, Renewable and sustainable energy reviews 13(1) (2009) 167-178.
[7] R. Saidur, E. Abdelaziz, A. Demirbas, M. Hossain, S. Mekhilef, A review on biomass as a fuel for boilers, Renewable and sustainable energy reviews 15(5) (2011) 2262-2289.
[8] M. Parikka, Global biomass fuel resources, Biomass and bioenergy 27(6) (2004) 613-620.
[9] A. Demirbas, Biofuels securing the planet's future energy needs, Energy Conversion and Management 50(9) (2009) 2239-2249.
[10] https://www.iea.org/statistics/renewables/.
[11] R.E. Sims, W. Mabee, J.N. Saddler, M. Taylor, An overview of second generation biofuel technologies, Bioresource technology 101(6) (2010) 1570-1580.
[12] S. Wang, X. Jiang, N. Wang, L. Yu, Z. Li, P. He, Research on pyrolysis characteristics of seaweed, Energy & Fuels 21(6) (2007) 3723-3729.
[13] A. Holma, K. Koponen, R. Antikainen, L. Lardon, P. Leskinen, P. Roux, Current limits of life cycle assessment framework in evaluating environmental sustainability–case of two evolving biofuel technologies, Journal of cleaner production 54 (2013) 215-228.
[14] L. Mishnaevsky Jr, H. Qing, Micromechanical modelling of mechanical behaviour and strength of wood: state-of-the-art review, Computational Materials Science 44(2) (2008) 363-370.
[15] F.F. Kollmann, E.W. Kuenzi, A.J. Stamm, Principles of Wood Science and Technology: II Wood Based Materials, Springer Science & Business Media2012.
[16] A. Panshin, C. De Zeeuw, Textbook of wood technology. Part 1. Formation, anatomy, and properties of wood, McGraw-Hill, New York, USA, 1980.
[17] C. Plomion, G. Leprovost, A. Stokes, Wood formation in trees, Plant physiology 127(4) (2001) 1513-1523.
[18] T.E. Timell, Compression wood in gymnosperms. V. 1: Bibliography, historical background, determination, structure, chemistry, topochemistry, physical properties, origin and formation of compression wood. V. 2: Occurrence of stem, branch and root compression woods, factors causing formation of compression wood, physiology of compression wood formation, inheritance of compression, wood. V. 3: Ecology of compression wood formation, silviculture and compression wood, mechanism of compression wood action, compression wood in the lumber and pulp and paper industries, compression wood induced by the balsam woolly aphid, opposite wood, Springer1986.
[19] D. Fengel, M. Stoll, Variation in cell cross sectional area, cell wall thickness and wall layer of spruce tracheids within an annual ring, Holzforschung 27 (1973) 1-7.
[20] P. Perre, Coupled heat and mass transfer in porous media: insight and perspective of multiscale modelling, 2017.
[21] R. Thomas, Wood: Structure and chemical composition, ACS Publications1977.
[22] P. McKendry, Energy production from biomass (part 1): overview of biomass, Bioresource technology 83(1) (2002) 37-46.
[23] S. Prasad, A. Singh, H. Joshi, Ethanol as an alternative fuel from agricultural, industrial and urban residues, Resources, Conservation and Recycling 50(1) (2007) 1-39.

[24] S.V. Vassilev, D. Baxter, L.K. Andersen, C.G. Vassileva, T.J. Morgan, An overview of the organic and inorganic phase composition of biomass, Fuel 94 (2012) 1-33.
[25] R. Rowell, The chemistry of solid wood, The chemistry of solid wood. (1984).
[26] A. Anca-Couce, Reaction mechanisms and multi-scale modelling of lignocellulosic biomass pyrolysis, Progress in Energy and Combustion Science 53 (2016) 41-79.
[27] M. Dereca Watkins, M.H. Nuruddin, T.-N. Alfred, Extraction and characterization of lignin from different biomass resources, (2014).
[28] E. Adler, Lignin chemistry—past, present and future, Wood science and technology 11(3) (1977) 169-218.
[29] H. Kawamoto, Lignin pyrolysis reactions, Journal of Wood Science 63(2) (2017) 117-132.
[30] C. Lapierre, Application of new methods for the investigation of lignin structure, Forage cell wall structure and digestibility (1993) 133-166.
[31] K. Pandey, A study of chemical structure of soft and hardwood and wood polymers by FTIR spectroscopy, Journal of Applied Polymer Science 71(12) (1999) 1969-1975.
[32] J. Deng, T. Xiong, H. Wang, A. Zheng, Y. Wang, Effects of cellulose, hemicellulose, and lignin on the structure and morphology of porous carbons, ACS Sustainable Chemistry & Engineering 4(7) (2016) 3750-3756.
[33] V. Dhyani, T. Bhaskar, A comprehensive review on the pyrolysis of lignocellulosic biomass, Renewable Energy 129 (2018) 695-716.
[34] S. Sharma, R. Meena, A. Sharma, P. Goyal, Biomass conversion technologies for renewable energy and fuels: A review note, IOSR J. Mech. Civ. Eng 11(2) (2014) 28-35.
[35] P. Adams, T. Bridgwater, A. Lea-Langton, A. Ross, I. Watson, Biomass conversion technologies, Greenhouse Gas Balances of Bioenergy Systems, Elsevier2018, pp. 107-139.
[36] R. Nandi, S. Sengupta, Microbial production of hydrogen: an overview, Critical reviews in microbiology 24(1) (1998) 61-84.
[37] I. Ntaikou, G. Antonopoulou, G. Lyberatos, Biohydrogen production from biomass and wastes via dark fermentation: a review, Waste and Biomass Valorization 1(1) (2010) 21-39.
[38] E. Gnansounou, A. Dauriat, Ethanol fuel from biomass: A review, (2005).
[39] A. Singh, S.I. Olsen, A critical review of biochemical conversion, sustainability and life cycle assessment of algal biofuels, Applied Energy 88(10) (2011) 3548-3555.
[40] P.C. Hallenbeck, J.R. Benemann, Biological hydrogen production; fundamentals and limiting processes, International journal of hydrogen energy 27(11-12) (2002) 1185-1193.
[41] S.S. Tan, L. Zou, E. Hu, Photosynthesis of hydrogen and methane as key components for clean energy system, Science and Technology of Advanced Materials 8(1-2) (2007) 89.
[42] M. Balat, Biomass energy and biochemical conversion processing for fuels and chemicals, Energy Sources, Part A 28(6) (2006) 517-525.
[43] A. Demirbas, Biomass resources for energy and chemical industry, Energy Edu. Sci. Technol 5(1) (2000) 21-45.
[44] https://www.eesi.org/papers/view/fact-sheet-biogasconverting-waste-to-energy.
[45] J. Koppejan, S. Van Loo, The handbook of biomass combustion and co-firing, Routledge2012.
[46] P. McKendry, Energy production from biomass (part 2): conversion technologies, Bioresource technology 83(1) (2002) 47-54.
[47] https://www.afconsult.com/en/do-business/references/international/renewable-energy/edinburg-waste-to-energy-plant/.
[48] J. Akhtar, N.A.S. Amin, A review on process conditions for optimum bio-oil yield in hydrothermal liquefaction of biomass, Renewable and Sustainable Energy Reviews 15(3) (2011) 1615-1624.
[49] A. Gollakota, N. Kishore, S. Gu, A review on hydrothermal liquefaction of biomass, Renewable and Sustainable Energy Reviews 81 (2018) 1378-1392.
[50] P. Biller, A. Ross, Production of biofuels via hydrothermal conversion, Handbook of biofuels production, Elsevier2016, pp. 509-547.
[51] L. Garcia Alba, C. Torri, C. Samorì, J. van der Spek, D. Fabbri, S.R. Kersten, D.W. Brilman, Hydrothermal treatment (HTT) of microalgae: evaluation of the process as conversion method in an algae biorefinery concept, Energy & fuels 26(1) (2012) 642-657.

[52] P. Basu, Biomass gasification, pyrolysis and torrefaction: practical design and theory, Academic press2018.
[53] J.A. Ruiz, M. Juárez, M. Morales, P. Muñoz, M. Mendívil, Biomass gasification for electricity generation: Review of current technology barriers, Renewable and Sustainable Energy Reviews 18 (2013) 174-183.
[54] T. Chmielniak, M. Sciazko, Co-gasification of biomass and coal for methanol synthesis, Applied energy 74(3-4) (2003) 393-403.
[55] S.C. Bhattacharya, P.A. Salam, A review of selected biomass energy technologies: gasification, combustion, carbonization and densification, Regional Energy Resources Information Centre, Asian Institute of Technology2006.
[56] M. Van de Velden, J. Baeyens, A. Brems, B. Janssens, R. Dewil, Fundamentals, kinetics and endothermicity of the biomass pyrolysis reaction, Renewable energy 35(1) (2010) 232-242.
[57] H.L. Chum, Biomass Pyrolysis to Hydrocarbon Fuels in the Petroleum Refining Context: Cooperative Research and Development Final Report, CRADA Number CRD-12-500, National Renewable Energy Lab.(NREL), Golden, CO (United States), 2018.
[58] R.J. Evans, T.A. Milne, Molecular characterization of the pyrolysis of biomass, Energy & Fuels 1(2) (1987) 123-137.
[59] S. Wang, G. Dai, H. Yang, Z. Luo, Lignocellulosic biomass pyrolysis mechanism: a state-of-the-art review, Progress in Energy and Combustion Science 62 (2017) 33-86.
[60] A.V. Bridgwater, Review of fast pyrolysis of biomass and product upgrading, Biomass and bioenergy 38 (2012) 68-94.
[61] W.-J. Liu, W.-W. Li, H. Jiang, H.-Q. Yu, Fates of chemical elements in biomass during its pyrolysis, Chemical Reviews 117(9) (2017) 6367-6398.
[62] J. Corella, J.M. Toledo, G. Molina, A review on dual fluidized-bed biomass gasifiers, Industrial & Engineering Chemistry Research 46(21) (2007) 6831-6839.
[63] S. Beis, Ö. Onay, Ö. Koçkar, Fixed-bed pyrolysis of safflower seed: influence of pyrolysis parameters on product yields and compositions, Renewable energy 26(1) (2002) 21-32.
[64] A. Dutta, J.A. Schaidle, D. Humbird, F.G. Baddour, A. Sahir, Conceptual process design and techno-economic assessment of ex situ catalytic fast pyrolysis of biomass: A fixed bed reactor implementation scenario for future feasibility, Topics in Catalysis 59(1) (2016) 2-18.
[65] E. Ranzi, A. Cuoci, T. Faravelli, A. Frassoldati, G. Migliavacca, S. Pierucci, S. Sommariva, Chemical kinetics of biomass pyrolysis, Energy & Fuels 22(6) (2008) 4292-4300.
[66] A.K. Burnham, R.L. Braun, Global kinetic analysis of complex materials, Energy & Fuels 13(1) (1999) 1-22.
[67] F. Shafizadeh, P.P. Chin, Thermal deterioration of wood, ACS Symposium Series American Chemical Society, 1977.
[68] C. Di Blasi, C. Branca, A. Santoro, E.G. Hernandez, R.A.P. Bermudez, Dynamics and products of wood pyrolysis, Progress in thermochemical biomass conversion (2001) 1143-1157.
[69] C. Di Blasi, Analysis of convection and secondary reaction effects within porous solid fuels undergoing pyrolysis, Combustion Science and Technology 90(5-6) (1993) 315-340.
[70] C. Di Blasi, Heat, momentum and mass transport through a shrinking biomass particle exposed to thermal radiation, Chemical engineering science 51(7) (1996) 1121-1132.
[71] M.J. Antal, A review of the vapor phase pyrolysis of biomass derived volatile matter, Fundamentals of thermochemical biomass conversion, Springer1985, pp. 511-537.
[72] M.J. Antal Jr, Effects of reactor severity on the gas-phase pyrolysis of cellulose-and kraft lignin-derived volatile matter, Industrial & Engineering Chemistry Product Research and Development 22(2) (1983) 366-375.
[73] M.J. Antal, Biomass pyrolysis: a review of the literature part 1—carbohydrate pyrolysis, Advances in solar energy, Springer1983, pp. 61-111.
[74] M.L. Boroson, J.B. Howard, J.P. Longwell, W.A. Peters, Product yields and kinetics from the vapor phase cracking of wood pyrolysis tars, AIChE Journal 35(1) (1989) 120-128.
[75] C. Di Blasi, Modeling chemical and physical processes of wood and biomass pyrolysis, Progress in energy and combustion science 34(1) (2008) 47-90.
[76] B. Wagenaar, W. Prins, W.P.M. van Swaaij, Flash pyrolysis kinetics of pine wood, Fuel processing technology 36(1-3) (1993) 291-298.

[77] K.R.G. Burra, A.K. Gupta, Modeling of biomass pyrolysis kinetics using sequential multi-step reaction model, Fuel 237 (2019) 1057-1067.
[78] G. Várhegyi, H. Chen, S. Godoy, Thermal decomposition of wheat, oat, barley, and Brassica carinata straws. A kinetic study, Energy & fuels 23(2) (2009) 646-652.
[79] J. Cai, W. Wu, R. Liu, Sensitivity analysis of three-parallel-DAEM-reaction model for describing rice straw pyrolysis, Bioresource technology 132 (2013) 423-426.
[80] R.S. Miller, J. Bellan, A generalized biomass pyrolysis model based on superimposed cellulose, hemicelluloseand liqnin kinetics, Combustion science and technology 126(1-6) (1997) 97-137.
[81] J.P. Diebold, A unified, global model for the pyrolysis of cellulose, Biomass and Bioenergy 7(1-6) (1994) 75-85.
[82] G.N. Richards, Glycolaldehyde from pyrolysis of cellulose, Journal of Analytical and Applied Pyrolysis 10(3) (1987) 251-255.
[83] J.L. Banyasz, S. Li, J.L. Lyons-Hart, K.H. Shafer, Cellulose pyrolysis: the kinetics of hydroxyacetaldehyde evolution, Journal of Analytical and Applied Pyrolysis 57(2) (2001) 223-248.
[84] A. Anca-Couce, I. Obernberger, Application of a detailed biomass pyrolysis kinetic scheme to hardwood and softwood torrefaction, Fuel 167 (2016) 158-167.
[85] A. Anca-Couce, P. Sommersacher, R. Scharler, Online experiments and modelling with a detailed reaction scheme of single particle biomass pyrolysis, Journal of analytical and applied pyrolysis 127 (2017) 411-425.
[86] F.-X. Collard, J. Blin, A review on pyrolysis of biomass constituents: Mechanisms and composition of the products obtained from the conversion of cellulose, hemicelluloses and lignin, Renewable and Sustainable Energy Reviews 38 (2014) 594-608.
[87] G. Gauthier, T. Melkior, S. Salvador, M. Corbetta, A. Frassoldati, S. Pierucci, E. Ranzi, H. Bennadji, E. Fisher, Pyrolysis of thick biomass particles: experimental and kinetic modelling, Chemical Engineering Transactions 32 (2013).
[88] I. Milosavljevic, V. Oja, E.M. Suuberg, Thermal effects in cellulose pyrolysis: relationship to char formation processes, Industrial & Engineering Chemistry Research 35(3) (1996) 653-662.
[89] E. Mészáros, G. Várhegyi, E. Jakab, B. Marosvölgyi, Thermogravimetric and reaction kinetic analysis of biomass samples from an energy plantation, Energy & Fuels 18(2) (2004) 497-507.
[90] V. Vand, A theory of the irreversible electrical resistance changes of metallic films evaporated in vacuum, Proceedings of the Physical Society 55(3) (1943) 222.
[91] J.L. Hillier, T.H. Fletcher, Pyrolysis kinetics of a Green River oil shale using a pressurized TGA, Energy & fuels 25(1) (2011) 232-239.
[92] A. Soria-Verdugo, N. Garcia-Hernando, L. Garcia-Gutierrez, U. Ruiz-Rivas, Analysis of biomass and sewage sludge devolatilization using the distributed activation energy model, Energy Conversion and Management 65 (2013) 239-244.
[93] J. Cai, W. Wu, R. Liu, An overview of distributed activation energy model and its application in the pyrolysis of lignocellulosic biomass, Renewable and Sustainable Energy Reviews 36 (2014) 236-246.
[94] S. Cavagnol, J.F. Roesler, E. Sanz, W. Nastoll, P. Lu, P. Perré, Exothermicity in wood torrefaction and its impact on product mass yields: From micro to pilot scale, The Canadian Journal of Chemical Engineering 93(2) (2015) 331-339.
[95] J. Bailey, Lumping analysis of reactions in continuous mixtures, The Chemical Engineering Journal 3 (1972) 52-61.
[96] J. Zhang, T. Chen, J. Wu, J. Wu, A novel Gaussian-DAEM-reaction model for the pyrolysis of cellulose, hemicellulose and lignin, Rsc Advances 4(34) (2014) 17513-17520.
[97] H. Chen, N. Liu, W. Fan, Two-step consecutive reaction model and kinetic parameters relevant to the decomposition of Chinese forest fuels, Journal of Applied Polymer Science 102(1) (2006) 571-576.
[98] Z. Chen, J. Lei, Y. Li, X. Su, Z. Hu, D. Guo, Studies on thermokinetic of Chlorella pyrenoidosa devolatilization via different models, Bioresource technology 244 (2017) 320-327.
[99] J. Cai, L. Ji, Pattern search method for determination of DAEM kinetic parameters from nonisothermal TGA data of biomass, Journal of Mathematical Chemistry 42(3) (2007) 547-553.

[100] B. de Caprariis, M.L. Santarelli, M. Scarsella, C. Herce, N. Verdone, P. De Filippis, Kinetic analysis of biomass pyrolysis using a double distributed activation energy model, Journal of Thermal Analysis and Calorimetry 121(3) (2015) 1403-1410.
[101] A. Dhaundiyal, S.B. Singh, M.M. Hanon, Study of distributed activation energy model using bivariate distribution function, f (E1, E2), Thermal Science and Engineering Progress 5 (2018) 388-404.
[102] Z. Dong, Y. Yang, W. Cai, Y. He, M. Chai, B. Liu, X. Yu, S.W. Banks, X. Zhang, A.V. Bridgwater, Theoretical analysis of double Logistic distributed activation energy model for thermal decomposition kinetics of solid fuels, Industrial & Engineering Chemistry Research 57(23) (2018) 7817-7825.
[103] H. Wang, S. Ti, Triple-Gaussian distributed activation energy model for the thermal degradation of coal and coal chars under a CO2 atmosphere, Asia-Pacific Journal of Chemical Engineering 15(3) (2020) e2443.
[104] Z. Chen, M. Hu, X. Zhu, D. Guo, S. Liu, Z. Hu, B. Xiao, J. Wang, M. Laghari, Characteristics and kinetic study on pyrolysis of five lignocellulosic biomass via thermogravimetric analysis, Bioresource Technology 192 (2015) 441-450.
[105] W. Wu, Y. Mei, L. Zhang, R. Liu, J. Cai, Effective activation energies of lignocellulosic biomass pyrolysis, Energy & fuels 28(6) (2014) 3916-3923.
[106] C. Wang, L. Li, Z. Zeng, X. Xu, X. Ma, R. Chen, C. Su, Catalytic performance of potassium in lignocellulosic biomass pyrolysis based on an optimized three-parallel distributed activation energy model, Bioresource technology 281 (2019) 412-420.
[107] J. Cai, R. Liu, Weibull mixture model for modeling nonisothermal kinetics of thermally stimulated solid-state reactions: application to simulated and real kinetic conversion data, The Journal of Physical Chemistry B 111(36) (2007) 10681-10686.
[108] J. Zhang, T. Chen, J. Wu, J. Wu, Multi-Gaussian-DAEM-reaction model for thermal decompositions of cellulose, hemicellulose and lignin: Comparison of N2 and CO2 atmosphere, Bioresource technology 166 (2014) 87-95.
[109] Y. Lin, Z. Chen, M. Dai, S. Fang, Y. Liao, Z. Yu, X. Ma, Co-pyrolysis kinetics of sewage sludge and bagasse using multiple normal distributed activation energy model (M-DAEM), Bioresource technology 259 (2018) 173-180.
[110] J. Cai, C. Jin, S. Yang, Y. Chen, Logistic distributed activation energy model–Part 1: Derivation and numerical parametric study, Bioresource technology 102(2) (2011) 1556-1561.
[111] C.C. Lakshmanan, N. White, A new distributed activation energy model using Weibull distribution for the representation of complex kinetics, Energy & fuels 8(6) (1994) 1158-1167.
[112] M. Li, L. Liu, L. Jiang, F.-H. Gou, J.-H. Sun, Application of distributed activation energy models to polymer pyrolysis: Effects of distributed model selection, characteristics, validation, and sensitivity analysis, Fuel 254 (2019) 115594.
[113] G. Várhegyi, B. Bobály, E. Jakab, H. Chen, Thermogravimetric study of biomass pyrolysis kinetics. A distributed activation energy model with prediction tests, Energy & Fuels 25(1) (2011) 24-32.
[114] B. De Caprariis, P. De Filippis, C. Herce, N. Verdone, Double-Gaussian distributed activation energy model for coal devolatilization, Energy & Fuels 26(10) (2012) 6153-6159.
[115] T. Wanjun, L. Yuwen, Y. Xil, W. Zhiyong, W. Cunxin, Approximate formulae for calculation of the integral ò T 0 T m exp (-E/RT) dT, Journal of thermal analysis and calorimetry 81(2) (2005) 347-349.
[116] G. Várhegyi, Z. Czégény, E. Jakab, K. McAdam, C. Liu, Tobacco pyrolysis. Kinetic evaluation of thermogravimetric–mass spectrometric experiments, Journal of Analytical and Applied Pyrolysis 86(2) (2009) 310-322.
[117] R.K. Agrawal, On the compensation effect, Journal of thermal analysis 31(1) (1986) 73-86.
[118] E. Chornet, C. Roy, Compensation effect in the thermal decomposition of cellulosic materials, Thermochimica Acta 35(3) (1980) 389-393.
[119] D. Xu, M. Chai, Z. Dong, M.M. Rahman, X. Yu, J. Cai, Kinetic Compensation Effect in Logistic Distributed Activation Energy Model for Lignocellulosic Biomass Pyrolysis, Bioresource technology (2018).

[120] E.L. Mui, W. Cheung, V.K. Lee, G. McKay, Compensation effect during the pyrolysis of tyres and bamboo, Waste management 30(5) (2010) 821-830.
[121] R.K. Agrawal, Compensation effect in the pyrolysis of cellulosic materials, Thermochimica acta 90 (1985) 347-351.
[122] R. Narayan, M.J. Antal, Thermal lag, fusion, and the compensation effect during biomass pyrolysis, Industrial & engineering chemistry research 35(5) (1996) 1711-1721.
[123] E. Cremer, The compensation effect in heterogeneous catalysis, Adv. Catal 7 (1955) 75-91.
[124] K. Miura, T. Maki, A simple method for estimating f (E) and k 0 (E) in the distributed activation energy model, Energy & Fuels 12(5) (1998) 864-869.
[125] A. Soria-Verdugo, E. Goos, N. García-Hernando, Effect of the number of TGA curves employed on the biomass pyrolysis kinetics results obtained using the Distributed Activation Energy Model, Fuel Processing Technology 134 (2015) 360-371.
[126] Y.-f. SUN, H. GAO, T.-z. WANG, Application of Genetic Algorithm in Distributed Activation Eenrgy Model of Biomass Pyrolysis, Journal of Shenyang Ligong University 3 (2010).
[127] J.A. Nelder, R. Mead, A simplex method for function minimization, The computer journal 7(4) (1965) 308-313.
[128] M. Güneş, S. Güneş, A direct search method for determination of DAEM kinetic parameters from nonisothermal TGA data (note), Applied Mathematics and Computation 130(2-3) (2002) 619-628.
[129] T. Mani, P. Murugan, N. Mahinpey, Determination of distributed activation energy model kinetic parameters using simulated annealing optimization method for nonisothermal pyrolysis of lignin, Industrial & Engineering Chemistry Research 48(3) (2009) 1464-1467.
[130] K. Kirtania, S. Bhattacharya, Application of the distributed activation energy model to the kinetic study of pyrolysis of the fresh water algae Chlorococcum humicola, Bioresource technology 107 (2012) 476-481.
[131] K. Miura, A new and simple method to estimate f (E) and k0 (E) in the distributed activation energy model from three sets of experimental data, Energy & Fuels 9(2) (1995) 302-307.
[132] T. Ozawa, A new method of analyzing thermogravimetric data, Bulletin of the chemical society of Japan 38(11) (1965) 1881-1886.
[133] P. Boswell, On the calculation of activation energies using a modified Kissinger method, Journal of Thermal Analysis and Calorimetry 18(2) (1980) 353-358.
[134] D. Chen, X. Gao, D. Dollimore, A generalized form of the Kissinger equation, Thermochimica acta 215 (1993) 109-117.
[135] D. Shen, S. Gu, B. Jin, M. Fang, Thermal degradation mechanisms of wood under inert and oxidative environments using DAEM methods, Bioresource technology 102(2) (2011) 2047-2052.
[136] J. Solar, I. De Marco, B. Caballero, A. Lopez-Urionabarrenechea, N. Rodriguez, I. Agirre, A. Adrados, Influence of temperature and residence time in the pyrolysis of woody biomass waste in a continuous screw reactor, Biomass and Bioenergy 95 (2016) 416-423.
[137] X. Miao, Q. Wu, High yield bio-oil production from fast pyrolysis by metabolic controlling of Chlorella protothecoides, Journal of biotechnology 110(1) (2004) 85-93.
[138] S. Xiu, A. Shahbazi, V. Shirley, D. Cheng, Hydrothermal pyrolysis of swine manure to bio-oil: effects of operating parameters on products yield and characterization of bio-oil, Journal of analytical and applied pyrolysis 88(1) (2010) 73-79.
[139] Q. Lu, X.-c. Yang, C.-q. Dong, Z.-f. Zhang, X.-m. Zhang, X.-f. Zhu, Influence of pyrolysis temperature and time on the cellulose fast pyrolysis products: Analytical Py-GC/MS study, Journal of Analytical and Applied Pyrolysis 92(2) (2011) 430-438.
[140] X. Wang, S. Bai, Q. Jin, S. Li, Y. Li, Y. Li, H. Tan, Soot formation during biomass pyrolysis: Effects of temperature, water-leaching, and gas-phase residence time, Journal of Analytical and Applied Pyrolysis 134 (2018) 484-494.
[141] G. Ningbo, L. Baoling, L. Aimin, L. Juanjuan, Continuous pyrolysis of pine sawdust at different pyrolysis temperatures and solid residence times, Journal of analytical and applied pyrolysis 114 (2015) 155-162.
[142] G. Newalkar, K. Iisa, A.D. D’Amico, C. Sievers, P. Agrawal, Effect of temperature, pressure, and residence time on pyrolysis of pine in an entrained flow reactor, Energy & Fuels 28(8) (2014) 5144-5157.

[143] T. McGrath, R. Sharma, M. Hajaligol, An experimental investigation into the formation of polycyclic-aromatic hydrocarbons (PAH) from pyrolysis of biomass materials, Fuel 80(12) (2001) 1787-1797.
[144] C. Dupont, J.-M. Commandre, P. Gauthier, G. Boissonnet, S. Salvador, D. Schweich, Biomass pyrolysis experiments in an analytical entrained flow reactor between 1073 K and 1273 K, Fuel 87(7) (2008) 1155-1164.
[145] H. Yang, R. Yan, H. Chen, D.H. Lee, C. Zheng, Characteristics of hemicellulose, cellulose and lignin pyrolysis, Fuel 86(12-13) (2007) 1781-1788.
[146] J. Li, R. Yan, B. Xiao, X. Wang, H. Yang, Influence of temperature on the formation of oil from pyrolyzing palm oil wastes in a fixed bed reactor, Energy & fuels 21(4) (2007) 2398-2407.
[147] M.N. Uddin, W.W. Daud, H.F. Abbas, Effects of pyrolysis parameters on hydrogen formations from biomass: a review, Rsc Advances 4(21) (2014) 10467-10490.
[148] B.B. Uzun, A.E. Pütün, E. Pütün, Fast pyrolysis of soybean cake: product yields and compositions, Bioresource technology 97(4) (2006) 569-576.
[149] X. Wang, S.R. Kersten, W. Prins, W.P. van Swaaij, Biomass pyrolysis in a fluidized bed reactor. Part 2: Experimental validation of model results, Industrial & engineering chemistry research 44(23) (2005) 8786-8795.
[150] Z. Luo, S. Wang, Y. Liao, J. Zhou, Y. Gu, K. Cen, Research on biomass fast pyrolysis for liquid fuel, Biomass and bioenergy 26(5) (2004) 455-462.
[151] A. Bridgwater, Principles and practice of biomass fast pyrolysis processes for liquids, Journal of analytical and applied pyrolysis 51(1-2) (1999) 3-22.
[152] P.T. Williams, S. Besler, The influence of temperature and heating rate on the slow pyrolysis of biomass, Renewable energy 7(3) (1996) 233-250.
[153] A. Magdziarz, M. Wilk, M. Wądrzyk, Pyrolysis of hydrochar derived from biomass–Experimental investigation, Fuel 267 (2020) 117246.
[154] M. Amutio, G. Lopez, R. Aguado, J. Bilbao, M. Olazar, Biomass oxidative flash pyrolysis: autothermal operation, yields and product properties, Energy & fuels 26(2) (2012) 1353-1362.
[155] J. Akhtar, N.S. Amin, A review on operating parameters for optimum liquid oil yield in biomass pyrolysis, Renewable and Sustainable Energy Reviews 16(7) (2012) 5101-5109.
[156] A.E. Pütün, N. Özbay, E. Apaydın Varol, B.B. Uzun, F. Ateş, Rapid and slow pyrolysis of pistachio shell: effect of pyrolysis conditions on the product yields and characterization of the liquid product, International journal of energy research 31(5) (2007) 506-514.
[157] A. Debdoubi, A. El Amarti, E. Colacio, M. Blesa, L. Hajjaj, The effect of heating rate on yields and compositions of oil products from esparto pyrolysis, International journal of energy research 30(15) (2006) 1243-1250.
[158] S. Septien, S. Valin, C. Dupont, M. Peyrot, S. Salvador, Effect of particle size and temperature on woody biomass fast pyrolysis at high temperature (1000–1400 C), Fuel 97 (2012) 202-210.
[159] J. Shen, X.-S. Wang, M. Garcia-Perez, D. Mourant, M.J. Rhodes, C.-Z. Li, Effects of particle size on the fast pyrolysis of oil mallee woody biomass, Fuel 88(10) (2009) 1810-1817.
[160] S. Zhou, M. Garcia-Perez, B. Pecha, A.G. McDonald, R.J. Westerhof, Effect of particle size on the composition of lignin derived oligomers obtained by fast pyrolysis of beech wood, Fuel 125 (2014) 15-19.
[161] R.J.M. Westerhof, H. Nygard, W.P.M. van Swaaij, S.R. Kersten, D.W.F. Brilman, Effect of particle geometry and microstructure on fast pyrolysis of beech wood, Energy & fuels 26(4) (2012) 2274-2280.
[162] P. Perré, Y. Tian, P. Lu, B. Malinowska, J. El Bekri, J. Colin, A robust and frugal model of biomass pyrolysis in the range 100–800° C: Inverse analysis of DAEM parameters, validation on static tests and determination of heats of reaction, Fuel (2020) 119692.
[163] W. Frederick Jr, C. Mentzer, Determination of heats of volatilization for polymers by differential scanning calorimetry, Journal of Applied Polymer Science 19(7) (1975) 1799-1804.
[164] J. Suwardie, R. Artiaga, The determination of heat of curing accompanied by reactant volatilization using simultaneous thermal analysis (STA), Thermochimica acta 357 (2000) 205-210.
[165] P. Buryan, M. Staff, Pyrolysis of the waste biomass, Journal of thermal analysis and calorimetry 93(2) (2008) 637-640.

[166] R. Xu, L. Ferrante, C. Briens, F. Berruti, Flash pyrolysis of grape residues into biofuel in a bubbling fluid bed, Journal of Analytical and Applied Pyrolysis 86(1) (2009) 58-65.
[167] D.E. Daugaard, R.C. Brown, Enthalpy for pyrolysis for several types of biomass, Energy & fuels 17(4) (2003) 934-939.
[168] J. Ábrego, M. Atienza-Martínez, F. Plou, J. Arauzo, Heat requirement for fixed bed pyrolysis of beechwood chips, Energy 178 (2019) 145-157.
[169] H. Yang, S. Kudo, H.-P. Kuo, K. Norinaga, A. Mori, O.e. Mašek, J.-i. Hayashi, Estimation of enthalpy of bio-oil vapor and heat required for pyrolysis of biomass, Energy & Fuels 27(5) (2013) 2675-2686.
[170] L. Basile, A. Tugnoli, C. Stramigioli, V. Cozzani, Thermal effects during biomass pyrolysis, Thermochimica acta 636 (2016) 63-70.
[171] Q. Chen, R. Yang, B. Zhao, Y. Li, S. Wang, H. Wu, Y. Zhuo, C. Chen, Investigation of heat of biomass pyrolysis and secondary reactions by simultaneous thermogravimetry and differential scanning calorimetry, Fuel 134 (2014) 467-476.
[172] C. Di Blasi, C. Branca, A. Galgano, P. D'Agostino, Thermal behavior of beech wood during sulfuric acid catalyzed pyrolysis, Energy & Fuels 29(10) (2015) 6476-6484.
[173] W.S.-L. Mok, M.J. Antal Jr, Effects of pressure on biomass pyrolysis. II. Heats of reaction of cellulose pyrolysis, Thermochimica Acta 68(2-3) (1983) 165-186.
[174] J. Rath, M. Wolfinger, G. Steiner, G. Krammer, F. Barontini, V. Cozzani, Heat of wood pyrolysis, Fuel 82(1) (2003) 81-91.
[175] W.C. Park, A. Atreya, H.R. Baum, Experimental and theoretical investigation of heat and mass transfer processes during wood pyrolysis, Combustion and Flame 157(3) (2010) 481-494.
[176] K. Werner, L. Pommer, M. Broström, Thermal decomposition of hemicelluloses, Journal of Analytical and Applied Pyrolysis 110 (2014) 130-137.
[177] F. Rogers, T. Ohlemiller, Cellulosic insulation material I. Overall degradation kinetics and reaction heats, Combustion Science and Technology 24(3-4) (1980) 129-137.
[178] M. Stenseng, A. Jensen, K. Dam-Johansen, Investigation of biomass pyrolysis by thermogravimetric analysis and differential scanning calorimetry, Journal of analytical and applied pyrolysis 58 (2001) 765-780.
[179] D.O. Usino, P. Ylitervo, A. Pettersson, T. Richards, Influence of temperature and time on initial pyrolysis of cellulose and xylan, Journal of Analytical and Applied Pyrolysis (2020) 104782.
[180] I. Pastorova, R.E. Botto, P.W. Arisz, J.J. Boon, Cellulose char structure: a combined analytical Py-GC-MS, FTIR, and NMR study, Carbohydrate research 262(1) (1994) 27-47.
[181] A. Galano, J. Aburto, J. Sadhukhan, E. Torres-García, A combined theoretical-experimental investigation on the mechanism of lignin pyrolysis: Role of heating rates and residence times, Journal of Analytical and Applied Pyrolysis 128 (2017) 208-216.
[182] F. Kifani-Sahban, A. Kifani, L. Belkbir, A. Belkbir, A. Zoulalian, J. Arauzo, T. Cardero, A physical approach in the understanding of the phenomena accompanying the thermal treatment of lignin, Thermochimica Acta 298(1-2) (1997) 199-204.
[183] B. Shrestha, Y. Le Brech, T. Ghislain, S. Leclerc, V. Carré, F. Aubriet, S. Hoppe, P. Marchal, S. Pontvianne, N. Brosse, A multitechnique characterization of lignin softening and pyrolysis, ACS Sustainable Chemistry & Engineering 5(8) (2017) 6940-6949.
[184] C. Di Blasi, C. Branca, A. Galgano, On the experimental evidence of exothermicity in wood and biomass pyrolysis, Energy Technology 5(1) (2017) 19-29.
[185] R. Nave, HyperPhysics, Georgia State University, Department of Physics and Astronomy2000.
[186] A.V. Blokhin, O.V. Voitkevich, G.J. Kabo, Y.U. Paulechka, M.V. Shishonok, A.G. Kabo, V.V. Simirsky, Thermodynamic properties of plant biomass components. Heat capacity, combustion energy, and gasification equilibria of cellulose, Journal of Chemical & Engineering Data 56(9) (2011) 3523-3531.
[187] J. Collazo, J.A. Pazó, E. Granada, Á. Saavedra, P. Eguía, Determination of the specific heat of biomass materials and the combustion energy of coke by DSC analysis, Energy 45(1) (2012) 746-752.
[188] V. Strezov, B. Moghtaderi, J.A. Lucas, Computational calorimetric investigation of the reactions during thermal conversion of wood biomass, Biomass and Bioenergy 27(5) (2004) 459-465.
[189] J. Comesaña, M. Nieströj, E. Granada, A. Szlek, TG-DSC analysis of biomass heat capacity during pyrolysis process, Journal of the Energy Institute 86(3) (2013) 153-159.

[190] C. Dupont, R. Chiriac, G. Gauthier, F. Toche, Heat capacity measurements of various biomass types and pyrolysis residues, Fuel 115 (2014) 644-651.
[191] S. Picard, D.T. Burns, P. Roger, Determination of the specific heat capacity of a graphite sample using absolute and differential methods, Metrologia 44(5) (2007) 294.
[192] C. Koufopanos, N. Papayannakos, G. Maschio, A. Lucchesi, Modelling of the pyrolysis of biomass particles. Studies on kinetics, thermal and heat transfer effects, The Canadian journal of chemical engineering 69(4) (1991) 907-915.
[193] C. Gomez, E. Velo, F. Barontini, V. Cozzani, Influence of secondary reactions on the heat of pyrolysis of biomass, Industrial & engineering chemistry research 48(23) (2009) 10222-10233.
[194] T. Hatakeyama, K. Nakamura, H. Hatakeyama, Studies on heat capacity of cellulose and lignin by differential scanning calorimetry, Polymer 23(12) (1982) 1801-1804.
[195] https://www.netzsch-thermal-analysis.com/en/products-solutions/simultaneous-thermogravimetry-differential-scanning-calorimetry/sta-449-f3-jupiter/.
[196] D. Chen, Y. Li, K. Cen, M. Luo, H. Li, B. Lu, Pyrolysis polygeneration of poplar wood: Effect of heating rate and pyrolysis temperature, Bioresource Technology 218 (2016) 780-788.
[197] Y. Tian, P. Perré, Multiple-distribution DAEM modelling of spruce pyrolysis: An investigation of the best trade-off regarding the number and shape of distributions, Energy Conversion and Management 229(0196-8904) (2021) 113756.
[198] M. Balat, M. Balat, E. Kırtay, H. Balat, Main routes for the thermo-conversion of biomass into fuels and chemicals. Part 1: Pyrolysis systems, Energy conversion and Management 50(12) (2009) 3147-3157.
[199] Q. Liu, Z. Zhong, S. Wang, Z. Luo, Interactions of biomass components during pyrolysis: A TG-FTIR study, Journal of Analytical and Applied Pyrolysis 90(2) (2011) 213-218.
[200] G. Pitt, The kinetic of the evolution of volatile products from coal, Fuel 41 (1962) 267-274.
[201] Q. Xiong, J. Zhang, F. Xu, G. Wiggins, C.S. Daw, Coupling DAEM and CFD for simulating biomass fast pyrolysis in fluidized beds, Journal of Analytical and Applied Pyrolysis 117 (2016) 176-181.
[202] H. Liu, M.S. Ahmad, H. Alhumade, A. Elkamel, R.J. Cattolica, Three pseudo-components kinetic modeling and nonlinear dynamic optimization of Rhus Typhina pyrolysis with the distributed activation energy model, Applied Thermal Engineering 157 (2019) 113633.
[203] J. Wu, Y. Liao, Y. Lin, Y. Tian, X. Ma, Study on thermal decomposition kinetics model of sewage sludge and wheat based on multi distributed activation energy, Energy 185 (2019) 795-803.
[204] A.K. Burnham, R.L. Braun, H.R. Gregg, A.M. Samoun, Comparison of methods for measuring kerogen pyrolysis rates and fitting kinetic parameters, Energy & Fuels 1(6) (1987) 452-458.
[205] A. Dhaundiyal, S.B. Singh, J.C. Salcedo-Reyes, Asymptotic approximations to the isothermal pyrolysis of deodara leaves using gamma distribution, Universitas Scientiarum 22(3) (2017) 263-284.
[206] B.P. Boudreau, B.R. Ruddick, On a reactive continuum representation of organic matter diagenesis, American Journal of Science 291(5) (1991) 507-538.
[207] K. Balakrishnan, Exponential distribution: theory, methods and applications, Routledge2018.
[208] S. Nadarajah, S. Kotz, The beta exponential distribution, Reliability engineering & system safety 91(6) (2006) 689-697.
[209] C. Chen, W. Miao, C. Zhou, H. Wu, Thermogravimetric pyrolysis kinetics of bamboo waste via Asymmetric Double Sigmoidal (Asym2sig) function deconvolution, Bioresource technology 225 (2017) 48-57.
[210] K. Santos, F. Lobato, T. Lira, V. Murata, M.A. Barrozo, Sensitivity analysis applied to independent parallel reaction model for pyrolysis of bagasse, Chemical Engineering Research and Design 90(11) (2012) 1989-1996.
[211] A.I. Ferreiro, M. Rabaçal, M. Costa, A combined genetic algorithm and least squares fitting procedure for the estimation of the kinetic parameters of the pyrolysis of agricultural residues, Energy Conversion and Management 125 (2016) 290-300.
[212] S. Scott, J. Dennis, J. Davidson, A. Hayhurst, An algorithm for determining the kinetics of devolatilisation of complex solid fuels from thermogravimetric experiments, Chemical engineering science 61(8) (2006) 2339-2348.

[213] Y. Lin, Y. Tian, Y. Xia, S. Fang, Y. Liao, Z. Yu, X. Ma, General distributed activation energy model (G-DAEM) on co-pyrolysis kinetics of bagasse and sewage sludge, Bioresource technology 273 (2019) 545-555.
[214] M.S. Ahmad, H. Liu, H. Alhumade, M.H. Tahir, G. Çakman, A. Yıldız, S. Ceylan, A. Elkamel, B. Shen, A modified DAEM: To study the bioenergy potential of invasive Staghorn Sumac through pyrolysis, ANN, TGA, kinetic modeling, FTIR and GC–MS analysis, Energy Conversion and Management 221 (2020) 113173.
[215] C.N. Arenas, M.V. Navarro, J.D. Martínez, Pyrolysis kinetics of biomass wastes using isoconversional methods and the distributed activation energy model, Bioresource technology 288 (2019) 121485.
[216] A. Soria-Verdugo, M. Rubio-Rubio, E. Goos, U. Riedel, Combining the lumped capacitance method and the simplified distributed activation energy model to describe the pyrolysis of thermally small biomass particles, Energy Conversion and Management 175 (2018) 164-172.
[217] S. Vyazovkin, A.K. Burnham, J.M. Criado, L.A. Pérez-Maqueda, C. Popescu, N. Sbirrazzuoli, ICTAC Kinetics Committee recommendations for performing kinetic computations on thermal analysis data, Thermochimica acta 520(1-2) (2011) 1-19.
[218] M. Güneş, S. Güneş, The influences of various parameters on the numerical solution of nonisothermal DAEM equation, Thermochimica acta 336(1-2) (1999) 93-96.
[219] I. Turner, P. Rousset, R. Rémond, P. Perré, An experimental and theoretical investigation of the thermal treatment of wood (Fagus sylvatica L.) in the range 200–260 C, International Journal of Heat and Mass Transfer 53(4) (2010) 715-725.
[220] P. Perré, I.W. Turner, A 3-D version of TransPore: a comprehensive heat and mass transfer computational model for simulating the drying of porous media, International Journal of heat and mass transfer 42(24) (1999) 4501-4521.
[221] R. Remond, I. Turner, P. Perre, Modeling the drying and heat treatment of lignocellulosic biomass: 2D effects due to the product anisotropy, Drying Technology 28(8) (2010) 1013-1022.
[222] R.K. Mishra, K. Mohanty, Pyrolysis kinetics and thermal behavior of waste sawdust biomass using thermogravimetric analysis, Bioresource technology 251 (2018) 63-74.
[223] G. Varhegyi, M.J. Antal Jr, E. Jakab, P. Szabó, Kinetic modeling of biomass pyrolysis, Journal of analytical and Applied Pyrolysis 42(1) (1997) 73-87.
[224] P.J. Barrie, The mathematical origins of the kinetic compensation effect: 1. The effect of random experimental errors, Physical Chemistry Chemical Physics 14(1) (2012) 318-326.
[225] L.-q. Jiang, A.-q. Zheng, J.-g. Meng, X.-b. Wang, Z.-l. Zhao, H.-b. Li, A comparative investigation of fast pyrolysis with enzymatic hydrolysis for fermentable sugars production from cellulose, Bioresource technology 274 (2019) 281-286.
[226] Z. Ma, J. Xie, N. Gao, C. Quan, Pyrolysis behaviors of oilfield sludge based on Py-GC/MS and DAEM kinetics analysis, Journal of the Energy Institute 92(4) (2019) 1053-1063.
[227] A. Soria-Verdugo, L. Garcia-Gutierrez, L. Blanco-Cano, N. Garcia-Hernando, U. Ruiz-Rivas, Evaluating the accuracy of the distributed activation energy model for biomass devolatilization curves obtained at high heating rates, Energy conversion and management 86 (2014) 1045-1049.
[228] G. Varhegyi, M.J. Antal Jr, T. Szekely, P. Szabo, Kinetics of the thermal decomposition of cellulose, hemicellulose, and sugarcane bagasse, Energy & fuels 3(3) (1989) 329-335.
[229] J.J. Manya, E. Velo, L. Puigjaner, Kinetics of biomass pyrolysis: a reformulated three-parallel-reactions model, Industrial & engineering chemistry research 42(3) (2003) 434-441.
[230] M. Becidan, G. Várhegyi, J.E. Hustad, Ø. Skreiberg, Thermal decomposition of biomass wastes. A kinetic study, Industrial & engineering chemistry research 46(8) (2007) 2428-2437.
[231] T.R. Rao, A. Sharma, Pyrolysis rates of biomass materials, Energy 23(11) (1998) 973-978.
[232] M. Weinstetn, A. Broido, Pyrolysis-crystallinity relationships in cellulose, Combustion Science and Technology 1(4) (1970) 287-292.
[233] D. Mohan, C.U. Pittman Jr, P.H. Steele, Pyrolysis of wood/biomass for bio-oil: a critical review, Energy & fuels 20(3) (2006) 848-889.
[234] T. Chen, J. Zhang, J. Wu, Kinetic and energy production analysis of pyrolysis of lignocellulosic biomass using a three-parallel Gaussian reaction model, Bioresource Technology 211 (2016) 502-508.

[235] H. Yang, R. Yan, H. Chen, C. Zheng, D.H. Lee, D.T. Liang, In-depth investigation of biomass pyrolysis based on three major components: hemicellulose, cellulose and lignin, Energy & Fuels 20(1) (2006) 388-393.
[236] S.D. Stefanidis, K.G. Kalogiannis, E.F. Iliopoulou, C.M. Michailof, P.A. Pilavachi, A.A. Lappas, A study of lignocellulosic biomass pyrolysis via the pyrolysis of cellulose, hemicellulose and lignin, Journal of analytical and applied pyrolysis 105 (2014) 143-150.
[237] S. Wang, X. Guo, K. Wang, Z. Luo, Influence of the interaction of components on the pyrolysis behavior of biomass, Journal of Analytical and Applied Pyrolysis 91(1) (2011) 183-189.
[238] E. Biagini, F. Barontini, L. Tognotti, Devolatilization of biomass fuels and biomass components studied by TG/FTIR technique, Industrial & Engineering Chemistry Research 45(13) (2006) 4486-4493.
[239] E. Biagini, L. Tognotti, A generalized procedure for the devolatilization of biomass fuels based on the chemical components, Energy & fuels 28(1) (2014) 614-623.
[240] K. Raveendran, A. Ganesh, K.C. Khilar, Pyrolysis characteristics of biomass and biomass components, Fuel 75(8) (1996) 987-998.
[241] F. Shafizadeh, Pyrolytic reactions and products of biomass, Fundamentals of thermochemical biomass conversion, Springer1985, pp. 183-217.
[242] H.E. Kissinger, Reaction kinetics in differential thermal analysis, Analytical chemistry 29(11) (1957) 1702-1706.
[243] A. Demirbas, Biofuels sources, biofuel policy, biofuel economy and global biofuel projections, Energy conversion and management 49(8) (2008) 2106-2116.
[244] M. Grønli, M.J. Antal, G. Varhegyi, A round-robin study of cellulose pyrolysis kinetics by thermogravimetry, Industrial & Engineering Chemistry Research 38(6) (1999) 2238-2244.
[245] M.J. Antal, G. Varhegyi, E. Jakab, Cellulose pyrolysis kinetics: revisited, Industrial & engineering chemistry research 37(4) (1998) 1267-1275.
[246] J.E. White, W.J. Catallo, B.L. Legendre, Biomass pyrolysis kinetics: a comparative critical review with relevant agricultural residue case studies, Journal of analytical and applied pyrolysis 91(1) (2011) 1-33.
[247] G. Almeida, J. Brito, P. Perré, Alterations in energy properties of eucalyptus wood and bark subjected to torrefaction: the potential of mass loss as a synthetic indicator, Bioresource technology 101(24) (2010) 9778-9784.
[248] F. Thurner, U. Mann, Kinetic investigation of wood pyrolysis, Industrial & Engineering Chemistry Process Design and Development 20(3) (1981) 482-488.
[249] S. Ward, J. Braslaw, Experimental weight loss kinetics of wood pyrolysis under vacuum, Combustion and flame 61(3) (1985) 261-269.
[250] P. Brachi, F. Miccio, M. Miccio, G. Ruoppolo, Isoconversional kinetic analysis of olive pomace decomposition under torrefaction operating conditions, Fuel Processing Technology 130 (2015) 147-154.
[251] P. Lv, G. Almeida, P. Perré, Torrefaction of cellulose: Validity and limitation of the temperature/duration equivalence, (2012).
[252] J. Cai, W. Wu, R. Liu, G.W. Huber, A distributed activation energy model for the pyrolysis of lignocellulosic biomass, Green Chemistry 15(5) (2013) 1331-1340.
[253] M. Ramiah, Thermogravimetric and differential thermal analysis of cellulose, hemicellulose, and lignin, Journal of applied polymer science 14(5) (1970) 1323-1337.
[254] S. Alves, J. Figueiredo, Kinetics of cellulose pyrolysis modelled by three consecutive first-order reactions, Journal of Analytical and Applied Pyrolysis 17(1) (1989) 37-46.
[255] G. Varhegyi, E. Jakab, M.J. Antal Jr, Is the Broido-Shafizadeh model for cellulose pyrolysis true?, Energy & fuels 8(6) (1994) 1345-1352.
[256] C. Di Blasi, C. Branca, F. Masotta, E. De Biase, Experimental analysis of reaction heat effects during beech wood pyrolysis, Energy & fuels 27(5) (2013) 2665-2674.
[257] T. Fisher, M. Hajaligol, B. Waymack, D. Kellogg, Pyrolysis behavior and kinetics of biomass derived materials, Journal of analytical and applied pyrolysis 62(2) (2002) 331-349.
[258] P. Rousset, I. Turner, A. Donnot, P. Perre, Choix d'un modèle de pyrolyse ménagée du bois à l'échelle de la microparticule en vue de la modélisation macroscopique, Annals of forest science 63(2) (2006) 213-229.

[259] H. Teng, Y.-C. Wei, Thermogravimetric studies on the kinetics of rice hull pyrolysis and the influence of water treatment, Industrial & Engineering Chemistry Research 37(10) (1998) 3806-3811.
[260] J. Cai, R. Liu, New distributed activation energy model: numerical solution and application to pyrolysis kinetics of some types of biomass, Bioresource Technology 99(8) (2008) 2795-2799.
[261] S. Sfakiotakis, D. Vamvuka, Development of a modified independent parallel reactions kinetic model and comparison with the distributed activation energy model for the pyrolysis of a wide variety of biomass fuels, Bioresource Technology 197 (2015) 434-442.
[262] K. Czajka, A. Kisiela, W. Moroń, W. Ferens, W. Rybak, Pyrolysis of solid fuels: Thermochemical behaviour, kinetics and compensation effect, Fuel Processing Technology 142 (2016) 42-53.
[263] E. Chornet, Compensation effect in the thermal decomposition of cellulosic materials, (1980).
[264] P. Perre, R. Remond, I. Turner, A comprehensive dual-scale wood torrefaction model: Application to the analysis of thermal run-away in industrial heat treatment processes, International Journal of Heat and Mass Transfer 64 (2013) 838-849.
[265] T.B. Reed, S. Gaur, The high heat of fast pyrolysis for large particles, Developments in thermochemical biomass conversion, Springer1997, pp. 97-103.
[266] E.R. Tinney, The combustion of wooden dowels in heated air, Symposium (International) on Combustion, Elsevier, 1965, pp. 925-930.
[267] H.-C. Kung, A.S. Kalelkar, On the heat of reaction in wood pyrolysis, Combustion and flame 20(1) (1973) 91-103.
[268] F. Beall, Differential calometric analysis of wood and wood components, Wood science and technology 5(3) (1971) 159-175.
[269] J. Wang, W. Lian, P. Li, Z. Zhang, J. Yang, X. Hao, W. Huang, G. Guan, Simulation of pyrolysis in low rank coal particle by using DAEM kinetics model: Reaction behavior and heat transfer, Fuel 207 (2017) 126-135.
[270] T. Sonobe, N. Worasuwannarak, Kinetic analyses of biomass pyrolysis using the distributed activation energy model, Fuel 87(3) (2008) 414-421.
[271] T. Cordero, J. Rodriguez-Maroto, J. Rodriguez-Mirasol, J. Rodriguez, On the kinetics of thermal decomposition of wood and wood components, Thermochimica acta 164 (1990) 135-144.
[272] F. Xu, J. Yu, T. Tesso, F. Dowell, D. Wang, Qualitative and quantitative analysis of lignocellulosic biomass using infrared techniques: a mini-review, Applied energy 104 (2013) 801-809.
[273] M.J. Prins, K.J. Ptasinski, F.J. Janssen, Torrefaction of wood: Part 1. Weight loss kinetics, Journal of analytical and applied pyrolysis 77(1) (2006) 28-34.
[274] S. Cavagnol, E. Sanz, W. Nastoll, J.F. Roesler, V. Zymla, P. Perré, Inverse analysis of wood pyrolysis with long residence times in the temperature range 210–290 C: Selection of multi-step kinetic models based on mass loss residues, Thermochimica acta 574 (2013) 1-9.
[275] P. Lv, G. Almeida, P. Perré, TGA-FTIR analysis of torrefaction of lignocellulosic components (cellulose, xylan, lignin) in isothermal conditions over a wide range of time durations, BioResources 10(3) (2015) 4239-4251.
[276] W.-H. Chen, P.-C. Kuo, A study on torrefaction of various biomass materials and its impact on lignocellulosic structure simulated by a thermogravimetry, Energy 35(6) (2010) 2580-2586.
[277] M. Poletto, A.J. Zattera, M.M. Forte, R.M. Santana, Thermal decomposition of wood: Influence of wood components and cellulose crystallite size, Bioresource Technology 109 (2012) 148-153.
[278] W. Boerjan, J. Ralph, M. Baucher, Lignin biosynthesis, Annual review of plant biology 54(1) (2003) 519-546.
[279] R.W. Whetten, J.J. MacKay, R.R. Sederoff, Recent advances in understanding lignin biosynthesis, Annual review of plant biology 49(1) (1998) 585-609.
[280] P. Rousset, C. Lapierre, B. Pollet, W. Quirino, P. Perre, Effect of severe thermal treatment on spruce and beech wood lignins, Annals of Forest Science 66(1) (2009) 1.
[281] C. Assor, V. Placet, B. Chabbert, A. Habrant, C. Lapierre, B. Pollet, P. Perre, Concomitant changes in viscoelastic properties and amorphous polymers during the hydrothermal treatment of hardwood and softwood, Journal of agricultural and food chemistry 57(15) (2009) 6830-6837.
[282] M.V. Navarro, R. Murillo, A.M. Mastral, N. Puy, J. Bartroli, Application of the distributed activation energy model to biomass and biomass constituents devolatilization, AIChE journal 55(10) (2009) 2700-2715.

[283] H. Haykiri-Acma, S. Yaman, S. Kucukbayrak, Comparison of the thermal reactivities of isolated lignin and holocellulose during pyrolysis, Fuel Processing Technology 91(7) (2010) 759-764.
[284] S.V. Vassilev, D. Baxter, L.K. Andersen, C.G. Vassileva, An overview of the composition and application of biomass ash. Part 1. Phase–mineral and chemical composition and classification, Fuel 105 (2013) 40-76.
[285] L. Febrero, E. Granada, C. Pérez, D. Patino, E. Arce, Characterisation and comparison of biomass ashes with different thermal histories using TG-DSC, Journal of Thermal Analysis and Calorimetry 118(2) (2014) 669-680.
[286] W.-H. Chen, P.-C. Kuo, Torrefaction and co-torrefaction characterization of hemicellulose, cellulose and lignin as well as torrefaction of some basic constituents in biomass, Energy 36(2) (2011) 803-811.
[287] W. Guo, C.J. Lim, X. Bi, S. Sokhansanj, S. Melin, Determination of effective thermal conductivity and specific heat capacity of wood pellets, Fuel 103 (2013) 347-355.
[288] D. Ditmars, S. Ishihara, S. Chang, G. Bernstein, E. West, Enthalpy and heat-capacity standard reference material: synthetic sapphire (a-Al2O3) from 10 to 2250 K, J Res Natl Bur Stand 87(2) (1982) 159-63.
[289] P. Perre, Coupled heat and mass transfer in biosourced porous media without local equilibrium: A macroscopic formulation tailored to computational simulation, International Journal of Heat and Mass Transfer 140 (2019) 717-730.
[290] A. Demirbas, G. Arin, An overview of biomass pyrolysis, Energy sources 24(5) (2002) 471-482.
[291] R. Kumar, V. Strezov, H. Weldekidan, J. He, S. Singh, T. Kan, B. Dastjerdi, Lignocellulose biomass pyrolysis for bio-oil production: A review of biomass pre-treatment methods for production of drop-in fuels, Renewable and Sustainable Energy Reviews 123 (2020) 109763.
[292] K. Kirtania, S. Bhattacharya, Coupling of a distributed activation energy model with particle simulation for entrained flow pyrolysis of biomass, Fuel processing technology 137 (2015) 131-138.
[293] C. Di Blasi, Modeling intra-and extra-particle processes of wood fast pyrolysis, AIChE journal 48(10) (2002) 2386-2397.
[294] P.O. Okekunle, H. Watanabe, T. Pattanotai, K. Okazaki, Effect of biomass size and aspect ratio on intra-particle tar decomposition during wood cylinder pyrolysis, Journal of Thermal Science and Technology 7(1) (2012) 1-15.
[295] A. Bharadwaj, L.L. Baxter, A.L. Robinson, Effects of intraparticle heat and mass transfer on biomass devolatilization: experimental results and model predictions, Energy & fuels 18(4) (2004) 1021-1031.
[296] D.V. Suriapparao, R. Vinu, Effects of biomass particle size on slow pyrolysis kinetics and fast pyrolysis product distribution, Waste and biomass valorization 9(3) (2018) 465-477.
[297] H. Haykiri-Acma, The role of particle size in the non-isothermal pyrolysis of hazelnut shell, Journal of analytical and applied pyrolysis 75(2) (2006) 211-216.
[298] J. Herguido, J. Corella, J. Gonzalez-Saiz, Steam gasification of lignocellulosic residues in a fluidized bed at a small pilot scale. Effect of the type of feedstock, Industrial & engineering chemistry research 31(5) (1992) 1274-1282.
[299] O. Beaumont, Y. Schwob, Influence of physical and chemical parameters on wood pyrolysis, Industrial & Engineering Chemistry Process Design and Development 23(4) (1984) 637-641.
[300] A. Demirbas, Effects of temperature and particle size on bio-char yield from pyrolysis of agricultural residues, Journal of analytical and applied pyrolysis 72(2) (2004) 243-248.
[301] T.J. Haas, M.R. Nimlos, B.S. Donohoe, Real-time and post-reaction microscopic structural analysis of biomass undergoing pyrolysis, Energy & Fuels 23(7) (2009) 3810-3817.
[302] C. Brackmann, M. Aldén, P.-E. Bengtsson, K.O. Davidsson, J.B. Pettersson, Optical and mass spectrometric study of the pyrolysis gas of wood particles, Applied spectroscopy 57(2) (2003) 216-222.
[303] R.J.M. Westerhof, Refining fast pyrolysis of biomass, (2011).
[304] O. Boutin, M. Ferrer, J. Lédé, Flash pyrolysis of cellulose pellets submitted to a concentrated radiation: experiments and modelling, Chemical Engineering Science 57(1) (2002) 15-25.
[305] M.J. Antal, E. Croiset, X. Dai, C. DeAlmeida, W.S.-L. Mok, N. Norberg, J.-R. Richard, M. Al Majthoub, High-yield biomass charcoal, Energy & Fuels 10(3) (1996) 652-658.

[306] A. Anca-Couce, R. Mehrabian, R. Scharler, I. Obernberger, Kinetic scheme of biomass pyrolysis considering secondary charring reactions, Energy Conversion and Management 87 (2014) 687-696.
[307] F. Richter, A. Atreya, P. Kotsovinos, G. Rein, The effect of chemical composition on the charring of wood across scales, Proceedings of the Combustion Institute 37(3) (2019) 4053-4061.
[308] C.A. Zaror, I.S. Hutchings, D.L. Pyle, H.N. Stiles, R. Kandiyoti, Secondary char formation in the catalytic pyrolysis of biomass, Fuel 64(7) (1985) 990-994.
[309] D.F. Arseneau, Competitive reactions in the thermal decomposition of cellulose, Canadian Journal of Chemistry 49(4) (1971) 632-638.
[310] S.R. Kersten, X. Wang, W. Prins, W.P. van Swaaij, Biomass pyrolysis in a fluidized bed reactor. Part 1: Literature review and model simulations, Industrial & engineering chemistry research 44(23) (2005) 8773-8785.
[311] Z. Cheng, W. Wu, P. Ji, X. Zhou, R. Liu, J. Cai, Applicability of Fraser–Suzuki function in kinetic analysis of DAEM processes and lignocellulosic biomass pyrolysis processes, Journal of Thermal Analysis and Calorimetry 119(2) (2015) 1429-1438.
[312] C. Couhert, J.-M. Commandre, S. Salvador, Is it possible to predict gas yields of any biomass after rapid pyrolysis at high temperature from its composition in cellulose, hemicellulose and lignin?, Fuel 88(3) (2009) 408-417.
[313] T. Hosoya, H. Kawamoto, S. Saka, Cellulose–hemicellulose and cellulose–lignin interactions in wood pyrolysis at gasification temperature, Journal of analytical and applied pyrolysis 80(1) (2007) 118-125.
[314] M.B. Pecha, J.I.M. Arbelaez, M. Garcia-Perez, F. Chejne, P.N. Ciesielski, Progress in understanding the four dominant intra-particle phenomena of lignocellulose pyrolysis: chemical reactions, heat transfer, mass transfer, and phase change, Green chemistry 21(11) (2019) 2868-2898.
[315] Y. Peng, S. Wu, The structural and thermal characteristics of wheat straw hemicellulose, Journal of Analytical and Applied Pyrolysis 88(2) (2010) 134-139.
[316] Y. Le Brech, J. Raya, L. Delmotte, N. Brosse, R. Gadiou, A. Dufour, Characterization of biomass char formation investigated by advanced solid state NMR, Carbon 108 (2016) 165-177.
[317] W.S.L. Mok, M.J. Antal Jr, P. Szabo, G. Varhegyi, B. Zelei, Formation of charcoal from biomass in a sealed reactor, Industrial & engineering chemistry research 31(4) (1992) 1162-1166.
[318] L. Basile, A. Tugnoli, C. Stramigioli, V. Cozzani, Influence of pressure on the heat of biomass pyrolysis, Fuel 137 (2014) 277-284.
[319] M. Wolfinger, J. Rath, G. Krammer, F. Barontini, V. Cozzani, Influence of the emissivity of the sample on differential scanning calorimetry measurements, Thermochimica acta 372(1-2) (2001) 11-18.
[320] M.J. Antal, M. Grønli, The art, science, and technology of charcoal production, Industrial & Engineering Chemistry Research 42(8) (2003) 1619-1640.
[321] P. Oleszczuk, W. Ćwikła-Bundyra, A. Bogusz, E. Skwarek, Y.S. Ok, Characterization of nanoparticles of biochars from different biomass, Journal of Analytical and Applied Pyrolysis 121 (2016) 165-172.
[322] B.B. Uzun, A.E. Pütün, E. Pütün, Composition of products obtained via fast pyrolysis of olive-oil residue: Effect of pyrolysis temperature, Journal of Analytical and Applied Pyrolysis 79(1-2) (2007) 147-153.
[323] K. Sun, M. Keiluweit, M. Kleber, Z. Pan, B. Xing, Sorption of fluorinated herbicides to plant biomass-derived biochars as a function of molecular structure, Bioresource technology 102(21) (2011) 9897-9903.
[324] K. Wiedner, C. Rumpel, C. Steiner, A. Pozzi, R. Maas, B. Glaser, Chemical evaluation of chars produced by thermochemical conversion (gasification, pyrolysis and hydrothermal carbonization) of agro-industrial biomass on a commercial scale, Biomass and Bioenergy 59 (2013) 264-278.
[325] R.K. Sharma, J.B. Wooten, V.L. Baliga, X. Lin, W.G. Chan, M.R. Hajaligol, Characterization of chars from pyrolysis of lignin, Fuel 83(11-12) (2004) 1469-1482.
[326] F. Kollman, W. Côté, Solid Wood, Principles of wood Science and technology, Springer New York1968.

[327] G. Almeida, D.V. Santos, P. Perré, Mild pyrolysis of fast-growing wood species (Caribbean pine and Rose gum): Dimensional changes predicted by the global mass loss, Biomass and Bioenergy 70 (2014) 407-415.
[328] P.A. John, Textbook of wood technology: structure, identification, properties, and uses of the commercial woods of the United States and Canada, McGraw-Hill series in forest resources (USA). (1980).
[329] S.B. Nordin, J.O. Nyren, E.L. Back, An indication of molten cellulose produced in a laser beam, Textile Research Journal 44(2) (1974) 152-154.
[330] A.s. Anca-Couce, A. Dieguez-Alonso, N. Zobel, A. Berger, N. Kienzl, F. Behrendt, Influence of heterogeneous secondary reactions during slow pyrolysis on char oxidation reactivity of woody biomass, Energy & fuels 31(3) (2017) 2335-2344.
[331] K. Kwiatkowski, K. Bajer, A. Celińska, M. Dudyński, J. Korotko, M. Sosnowska, Pyrolysis and gasification of a thermally thick wood particle–Effect of fragmentation, Fuel 132 (2014) 125-134.
[332] S. Wang, B. Ru, H. Lin, W. Sun, Z. Luo, Pyrolysis behaviors of four lignin polymers isolated from the same pine wood, Bioresource technology 182 (2015) 120-127.